

ADVANCES IN UNDERWATER TECHNOLOGY,
OCEAN SCIENCE AND OFFSHORE ENGINEERING
VOLUME 29

**WAVE KINEMATICS AND
ENVIRONMENTAL FORCES**

*Papers presented at a conference organized by the
Society for Underwater Technology
and held in London, U.K., March 24-25, 1993.*

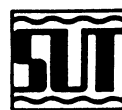


**Springer-Science
+Business Media, B.V.**

*Advances in
Underwater Technology,
Ocean Science and
Offshore Engineering*

Volume 29

*Wave Kinematics
and Environmental Forces*



***ADVANCES IN UNDERWATER TECHNOLOGY,
OCEAN SCIENCE AND OFFSHORE ENGINEERING***

- Vol. 1. Developments in Diving Technology
- Vol. 2. Design and Installation of Subsea Systems
- Vol. 3. Offshore Site Investigation
- Vol. 4. Evaluation, Comparison and Calibration of Oceanographic Instruments
- Vol. 5. Submersible Technology
- Vol. 6. Oceanology
- Vol. 7. Subsea Control and Data Acquisition
- Vol. 8. Exclusive Economic Zones
- Vol. 9. Stationing and Stability of Semi-submersibles
- Vol. 10. Modular Subsea Production Systems
- Vol. 11. Underwater Construction: Development and Potential
- Vol. 12. Modelling the Offshore Environment
- Vol. 13. Economics of Floating Production Systems
- Vol. 14. Submersible Technology: Adapting to Change
- Vol. 15. Technology Common to Aero and Marine Engineering
- Vol. 16. Oceanology '88
- Vol. 17. Energy for Islands
- Vol. 18. Disposal of Radioactive Waste in Subsea Sediments
- Vol. 19. Diverless and Deepwater Technology
- Vol. 20. Subsea International '89:
Second Generation Subsea Production Systems
- Vol. 21. NDT: Advances in Underwater Inspection Methods
- Vol. 22. Subsea Control and Data Acquisition: Technology and Experience
- Vol. 23. Subtech '89. Fitness for Purpose
- Vol. 24. Advances in Subsea Pipeline Engineering and Technology
- Vol. 25. Safety in Offshore Drilling.
The Role of Shallow Gas Surveys
- Vol. 26. Environmental Forces on Offshore Structures and their Prediction
- Vol. 27. Subtech '91. Back to the Future
- Vol. 28. Offshore Site Investigation and Foundation Behaviour
- Vol. 29. Wave Kinematics and Environmental Forces

CONFERENCE PLANNING COMMITTEE

C. Swan, *Imperial College*; R. M. Webb, *Robin Webb Consulting Limited*; S. Huntington, *HR Wallingford Ltd.*

*Advances in
Underwater Technology,
Ocean Science and
Offshore Engineering*

Volume 29

*Wave Kinematics
and Environmental Forces*

Papers presented at a conference
organized by the Society for Underwater Technology
and held in London, U.K., March 24–25, 1993.



SPRINGER-SCIENCE+BUSINESS MEDIA, B.V.

ISBN 978-90-481-4250-7 ISBN 978-94-017-3663-3 (eBook)
DOI 10.1007/978-94-017-3663-3

Printed on acid-free paper

All Rights Reserved

© 1993 Springer Science+Business Media Dordrecht

Originally published by Kluwer Academic Publishers in 1993

No part of the material protected by this copyright notice may be reproduced or
utilized in any form or by any means, electronic or mechanical
including photocopying, recording, or by any information storage and
retrieval system, without written permission from the copyright owner.

Contents

SESSION ONE: WAVE KINEMATICS	1
Technical Update and Field Data from the New Generation Microwave Directional Wave Radar	
S. J. Archer	3
Wave Kinematics – Measurement, Modelling and Application	
S. J. Buchan	19
Non-Linear Wave Current Interactions	
I. Cummins and C. Swan	35
Effects of a Shear Current on Wind Induced Waves	
A. K. Magnusson	53
Uncertainties in Prediction of Wave Kinematics in Irregular Waves	
O. T. Gudmestad and S. Haver	75
Wave Kinematics on Sheared Currents	
D. J. Skyner and W. J. Easson	101
Laboratory Wave Generation Correct to Second Order	
H. A. Schäffer	115
SESSION TWO: FLUID LOADING	
Comparison of Loads Predicted Using “Newwave” and Other Wave Models with Measurements on the Tern Structure	
J. B. Rozario, P. S. Tromans, P. H. Taylor and M. Efthymiou	143
Wave Loading Model Tests on a Gravity Base Structure	
J. J. Murray, R. G. Standing and L. M. Mak	161
Added Hydrodynamic Loading Due to Sacrificial Anodes	
M. J. Downie, B. A. Murray, P. Bettess and J. V. Haswell	191
The Vortex Induced Vibration of Marine Risers in Sheared and Critical Flows	
G. Jones and W. S. Lamb	209
Suppression of Vortex Shedding From Satellite Risers in a Current	
M. M. Zdravkovich and J. L. Baldaro	239

Review of Wave Breaking in Shallow Water	
H. N. Southgate	251
Three-Dimensional Breaking Wave Kinematics	
K. She, C. A. Greated and W. J. Easson	275
Environmental Forces at the Coastline and Implications for Coastal Defence	
N. W. Beech and J. L. Andrews	289
Full Field Study of Post Breaking Vorticity	
S. Lloyd, C. A. Greated and W. J. Easson	307
Multigrid Model of Wave-Current Interaction	
B. Li and C. A. Fleming	317
Variation of Beach Profiles in Hell's Mouth Bay, Llyn Peninsula for the Period 1979–1981	
J. Derbyshire	329

Society for Underwater Technology

The Society was founded in 1966 to promote the further understanding of the underwater environment. It is a multi-disciplinary body with a worldwide membership of scientists and engineers who are active or have a common interest in underwater technology, ocean science and offshore engineering.

Committees

The Society has a number of Committees to study such topics as:

- Diving and Submersibles
- Offshore Site Investigation and Geotechnics
- Environmental Forces and Physical Oceanography
- Ocean Resources
- Subsea Engineering and Operations
- Education and Training

Conference and Seminars

An extensive programme is organized to cater for the diverse interests and needs of the membership. An annual programme usually comprises four conferences and a much greater number of one-day seminars plus evening meetings and an occasional visit to a place of technical interest. The Society has organized over 100 seminars in London, Aberdeen and other appropriate centres during the past decade. Attendance at these events is available at significantly reduced levels of registration fees for Members or staff of Corporate Members.

Publications

Proceedings of the more recent conferences have been published in this series of *Advances in Underwater Technology, Ocean Science and Offshore Engineering*. These and other publications produced separately by the Society are available through the Society to members at a reduced cost. A careers pack 'Oceans of Opportunity' has been produced by the Society in response to the growing demand by students schools and colleges for up-to-date information.

Journal

The Society's quarterly journal *Underwater Technology* caters for the whole spectrum of the inter-disciplinary interests and professional involvement of its readership. It includes papers from authoritative international sources on such subjects as:

- Diving Technology and Physiology
- Civil Engineering
- Submersible Design and Operation
- Geology and Geophysics

Subsea Systems
Naval Architecture
Marine Biology and Pollution
Oceanography
Petroleum Exploration and Production
Environmental Data

An Editorial Board has responsibility for ensuring that a high standard of quality and presentation of papers reflects a coherent and balanced coverage of the Society's diverse subject interests; through the Editorial Board, a procedure for assessment of papers is conducted.

Endowment fund

A separate fund has been established to provide tangible incentives to students to acquire knowledge and skills in underwater technology or related aspects of ocean science and offshore engineering. Postgraduate students have been sponsored to study to MSc level and subject to the growth of the fund it is hoped to extend this activity.

Awards

An annual President's Award is presented for a major achievement in underwater technology. In addition there is a series of sponsored annual awards by some Corporate Members for the best contribution to diving operations and oceanography, and for the best technical paper in the Journal

FURTHER INFORMATION

If you would like to receive further details, please contact
Society for Underwater Technology, The Memorial Building, 76 Mark Lane,
London EC3R 7JN.
Telephone: 071-481 0750; Telex: 886481 I Mar E G; Fax: 071-481 4001.

Session 1
Wave Kinematics

TECHNICAL UPDATE AND FIELD DATA FROM THE NEW GENERATION MICROWAVE DIRECTIONAL WAVE RADAR

S. J. ARCHER

MIROS Ltd

Balgownie Technology Centre

Campus 3, Balgownie Drive

Aberdeen AB22 8GW

Scotland

ABSTRACT In 1989, a technical appraisal of the MIROS Directional Wave and Surface Current Radar was completed for a joint industry project involving BP International, Shell UK Exploration and Production, and the UK Department of Energy. The study involved contributions from three scientists working in the fields of wave measurements (M J Tucker), statistics (R G Tickell) and kinematics (J R Chaplin). The findings and recommendations of this study have now been incorporated into a new generation of Wave Radar, and this paper describes the rationale for the changes, and how they have been implemented, and presents data obtained from the Esso Odin Field using the new version of the Wave Radar where it has been trialed. The data shows that the new implementation of the design, in an equivalent configuration, has been validated against the previous design, while providing increased flexibility in configuration, and enabling all the major recommendations of the joint industry project to be realised.

INTRODUCTION

The MIROS Directional Wave and Surface Current Radar has been developed over a number of years, starting with the trial of the development prototype at Lindesnes in 1983 (Grønlie et al, 1984). Since then, over ten systems have been delivered for applications in the North Sea.

Of course, any new measurement technique has to be validated against established methods, both to confirm its calibration, and to maintain continuity between long term data sets from different sensors. In the winter of 1985/86, an early MIROS Wave Radar participated in the WADIC directional wave sensor field intercomparison (Allender et al, 1989). Over the winter of 1986/87, a MIROS Wave Radar was evaluated by Shell UK Expro on the North Cormorant platform (Dacunha and Angevaare, 1988).

Since that time, a number of improvements have been made and evaluated on the Esso Odin platform, including:

- fixed multiple antenna instead of servo controlled rotating antenna
- dual footprint to remove directional ambiguity
- updated spectra every 15 minutes (for operational users).

In 1989, a technical appraisal of the MIROS Wave Radar was completed (Archer, 1989) for a joint industry project involving BP International, Shell UK Exploration and Production, and the UK Department of Energy. The study involved contributions from three specialists working in the fields of wave measurements (M J Tucker), statistics (R G Tickell) and kinematics (J R Chaplin).

Since then, the findings and recommendations of this study have been incorporated in a new generation of Wave Radar, and this paper will describe the rationale for the changes, and will describe how they have been implemented. Finally, data obtained from the Esso Odin Field using the new version of the Wave Radar will be presented.

PRINCIPLES OF OPERATION

The principles of operation of the new Wave Radar remain unaltered from the original design (Grønlie et al, 1984). A microwave pulse is transmitted from an antenna at an elevation of about 50 m above the sea surface, and is reflected from the illuminated area ("footprint") on the sea surface which is defined by the receiver range gate and pulse length and antenna horizontal beam pattern.

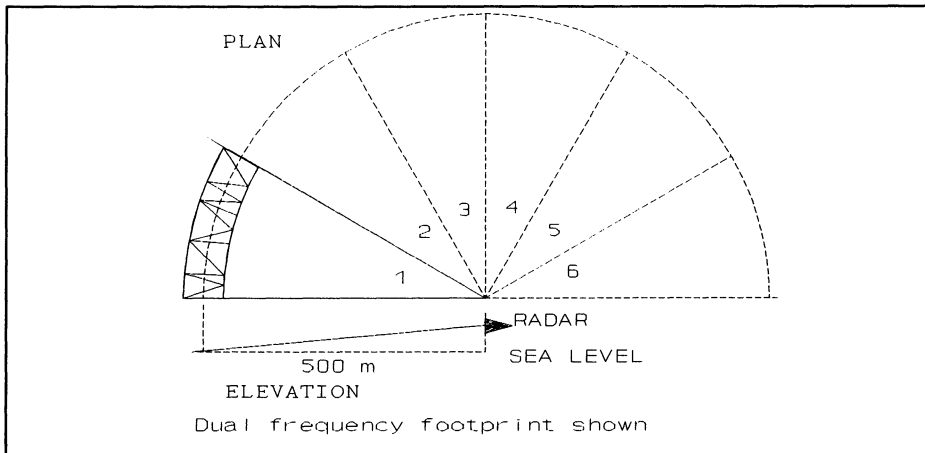


Figure 1 Wave Radar Geometry

There are two concurrent modes of operation, the pulse doppler wave mode to measure wave velocity, and the dual frequency mode to measure the surface current vector. Both modes rely on Bragg scattering of the 5.17 cm radio wavelength, which is the dominant scattering mechanism at shallow grazing angles (Tucker, 1991, Chapter 8, Section 8.2.2), from the sea surface capillary waves, resonant at wavelengths close to 2.6 cm perpendicular to the radar. These ripples travel with a phase velocity of approximately 0.24 m/s, and so can be assumed to be nearly constant relative to the local water surface between successive radar pulses (every 20 μ s). This compares to the gravity wavelengths of interest from about 15 m to 1500 m, corresponding to wave phase velocities of 4.8 m/s to 48 m/s.

Six horn antennae are arranged with boresight directions 30 degrees apart, so that the radar scans the sea surface over a total 180 degree sector. Since both approaching and receding wave energy is detected, the sea surface is effectively sampled over 360 degrees. Each antenna horizontal polar response has a two way half power beamwidth of 24 degree. The polar response pattern is used in the integration over azimuth in the transfer function between the radar backscatter and the wave power spectrum.

The vertical beamwidth has to be sufficient to allow illumination of the sea surface at the required ranges, and in practice is about 17 degrees.

PRINCIPLES OF WAVE MEASUREMENT

Pulse Doppler Wave Mode

In the pulse doppler mode, for any antenna boresight direction, a sequence of 50 ns pulses (so the footprint on the sea surface is $0.5 \times 3 \times 10^8 \times 50 \times 10^{-9} = 7.5$ m deep in range) is transmitted at a rate of 50 kHz. The pulses are Bragg reflected by the capillary waves, and are modulated in phase by the longer period gravity waves.

The doppler shift f_D of the return pulses is measured:

$$f_D = 2 \frac{u}{\lambda_R}$$

where λ_R is the radar wavelength (5.17 cm), and u is the target velocity component towards the radar.

The output is then obtained as a time series of wave particle velocity in the boresight direction.

This time series is digitally sampled (default 256 samples at a rate of 2Hz) and fourier transformed into the frequency domain to yield the wave energy spectrum (40 frequency bands each 0.0078 Hz wide from 0 to 0.3125 Hz) in that boresight direction.

By adding the spectral densities from each of the 6 boresight directions, the total energy point spectrum is obtained. The spectrum is updated every scan (6 directions \times 128 s = 768 s or 12m 48s), or after every new sampling direction (every 128 s or approximately 2 minutes).

Directional Resolution

The net component of water particle velocity in the antenna boresight direction for a plane harmonic elementary wave soon drops to zero when the ocean wavenumber forms an angle with the boresight direction greater than the directional resolution of the radar antenna. Thus, the antenna does not respond to components of waves along other boresight directions.

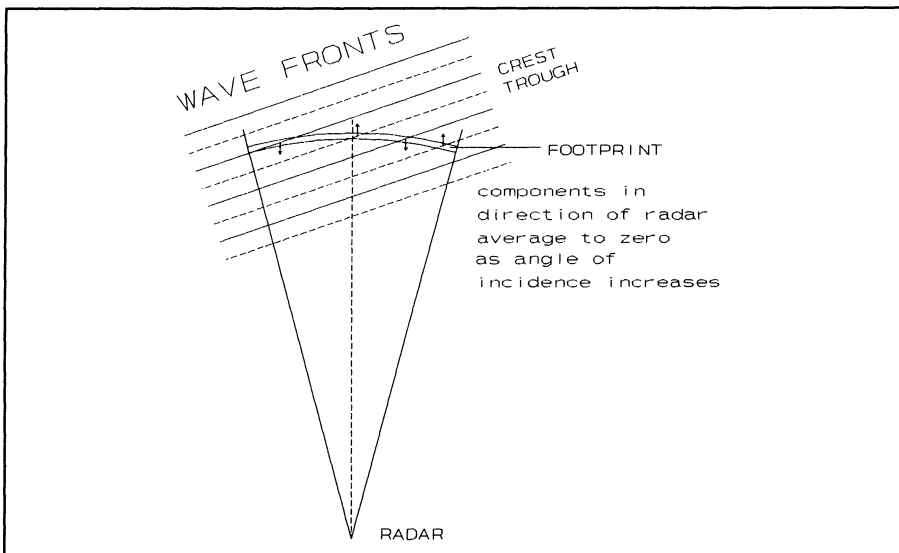


Figure 2 Antenna directional response

Resolving the Directional Ambiguity

The wave velocity time series from one boresight direction would appear the same whether the ocean wave was approaching or receding, so that there is a 180 degree ambiguity in the ocean wave direction. To resolve this ambiguity, data is collected

from two footprints which are separated by less than one half wavelength of the shortest ocean wavelength of interest (7.5 m default value). The ambiguity is then resolved for each frequency component by comparing the phase angles of the wave energy spectral densities. Thus, the directional spectra are presented as a matrix of spectral densities over 40 frequencies and 12 directions.

FREQU- ENCY	DIRECTION												ALL DIRECTIONS
	1	2	3	4	5	6	7	8	9	10	11	12	
dc													
1													
2													
3													
4													
5													
6													
7													
8													
9													
10													
11													
12													
37													
38													
39													
40													
ALL FREQUENCIES													

Figure 3 Directional wave spectral densities

PRINCIPLES OF CURRENT MEASUREMENT

Dual Frequency Mode

In the dual frequency mode, two 500 ns pulses are transmitted which differ in frequency by 10 MHz. The footprint is then 75 m deep in the boresight direction, and the difference frequency effectively couples to a 15 m long gravity wave component in the boresight direction.

This is done by multiplying the return at one frequency by the complex conjugate of

the return at the other frequency to form the power spectrum of the product signal. Only equal velocity scatterers will give coherent contributions or stable spectral components. This shows up as a line in the product power spectrum, at a frequency equal to the frequency of the particular gravity wave component.

Current "raw" data is collected as 256 complex samples at 2 Hz of the product signal. From the complex time series, the two sided power spectrum is calculated, and the presence of a coherent line in the spectrum is established using a threshold detection technique. The exact frequency is estimated by interpolation. The shift in frequency of the coherent line from the frequency expected from the wave dispersion relationship for 15 m wavelength gravity waves is proportional to the current component in that direction.

This operation is performed for each of the six boresight directions, and the current vectors averaged to find the overall least squares mean current vector.

Interpretation of Current Measurements

The surface current represents an average with respect to time (the total time to complete a scan of all six directions is $6 \times 256/2/60 = 12.8$ minutes), area (75 m deep in range by $500 \times 30 \times \pi/180 = 260$ m in azimuth) and water depth. The depth weighting is assumed to be of the form e^{-kz} where k is the wavenumber of the 15 m gravity wave, resulting in a depth average down to approximately 1.2 m.

IMPLEMENTATION OF THE NEW DESIGN

The new design differs significantly in physical layout and electronic implementation while performing the same functionality. The radio frequency and signal processing modules are now all in a single cabinet with the antenna array, forming a complete sensor assembly with processed wave and current data as output.

The main functions of the Wave Radar can be summarised as:

- collect sea surface information from the back-scattered radar signal
- process the back-scattered signals into wave and current time series
- perform power spectrum analysis
- estimate surface current components
- calculate wave spectral densities
- calculate integrated wave parameters

- estimate surface current vector
- perform real time data quality control
- generate and transmit data in a serial output format.

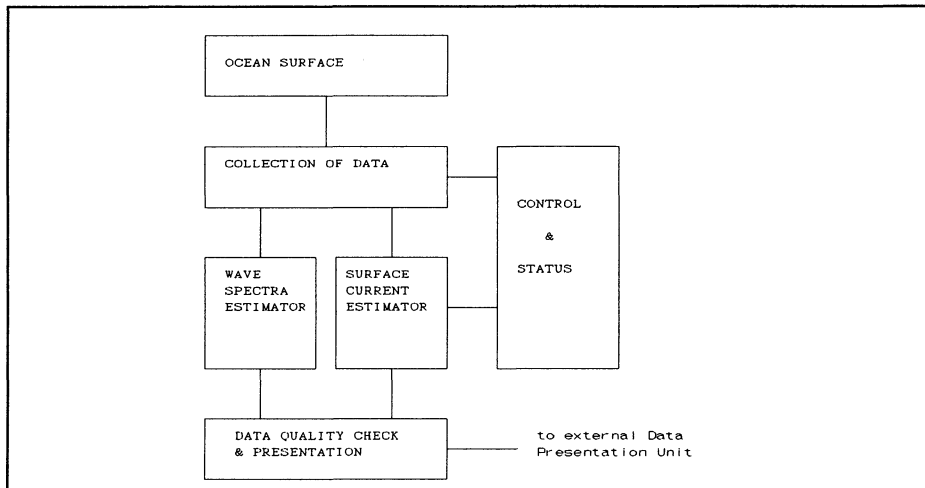


Figure 4 Wave Radar functional block diagram

Physically, the Wave Radar consists of:

- an array of 6 electronically switched horn antennae
- a microwave module
- an intermediate frequency (IF) module and digitiser
- a computer assembly and power supplies.

In the new design, the interface between the analogue and digital sections has been moved forward to the output from the pulse doppler and dual frequency demodulators, so that frequency demodulation for wave particle velocity, and cross correlation for surface current, and subsequent filtering, are performed digitally. This reduces the number of hardware components, improves reproducibility of performance, and allows higher dynamic range and truly linear detection response.

The digital processing is performed in a parallel processor controlled from the 386 industry standard architecture computer.

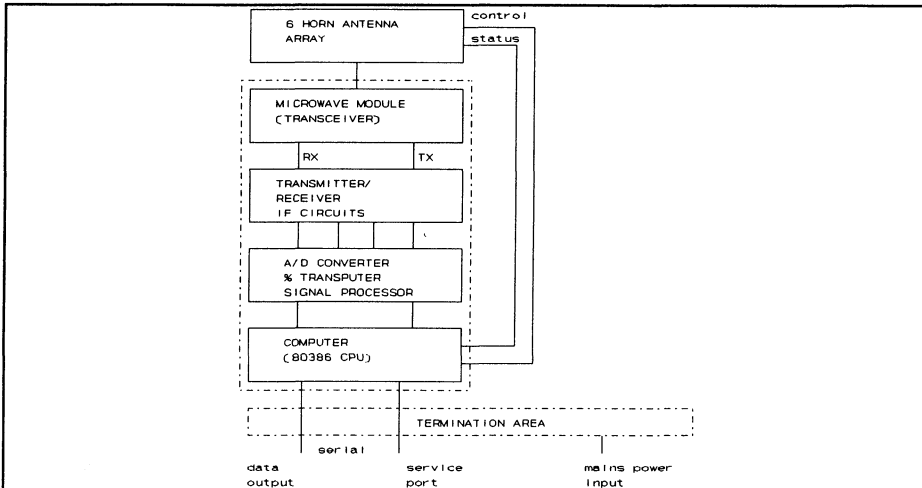


Figure 5 Wave Radar simplified block diagram

DISCUSSION OF ALGORITHMS

Digital Signal Processor

The digital signal processor performs the following tasks:

- frequency modulation detection (pulse doppler)
- cross correlation (dual frequency)
- presampling filtering.

Computer

The computer performs the following data processing tasks:

- sampling of time series
- spectrum analysis
- transformation to wave spectrum
- current component estimation
- calculation of spectral parameters

- data quality control
- generation and transmission of the data in a fixed format.

In addition, it performs the following control tasks:

- control of measurement sequence
- control and monitoring of antenna switch status (giving direction)
- control of transmitted waveform and frequency
- control of range gate delay (and hence range to sea surface footprint)
- monitoring of transmitted and reflected radar signal power
- hardware and software error monitoring.

Thus, transmitted frequency, power, pulse length, range, sampling sequence, and spectral windowing are all under software control, and can be reconfigured for special requirements.

The Wave Radar can be accessed remotely via a dedicated service port to allow monitoring of program execution, error log monitoring, or the configuration to be changed.

COMPARISON WITH TECHNICAL APPRAISAL RECOMMENDATIONS

The joint industry project identified a number of areas which could be improved, or which should be investigated further, or should be understood by workers using the data for storm studies or special applications. In general, it was agreed that the Wave Radar already provided data to a sufficient accuracy for operational purposes.

Working Principles

Tucker (Archer, 1989, Appendix C) proposed the following areas where the Wave Radar could be improved:

- the dynamic range (previously ± 6 m/s) of the doppler detector should be increased
- the output of the doppler detector should be stable if the return signal is lost

- spectral windowing should be used to minimise spectral "leakage"
- the algorithm for mean direction Dmt (equivalent to the phase of the first angular harmonic) is not properly defined unless the directional ambiguity is removed
- the algorithm for the spread parameter Spr (approximating to r.m.s. spread, but it can be erroneous in nearly unidirectional seas) should be modified
- the quality control system could be enhanced
- since the integration over direction within one antenna footprint is accurately performed, the radar elevation angle can be increased to obtain better performance in steep waves
- the two "wind noise correction" parameters should be recorded.

The combined effect of spectral leakage and the wind noise correction would be a net underestimation of significant wave height. In steep waves, a measured lower wave height has been observed in waves which are receding compared to those which are approaching (Magnusson, 1987). This may be due to shielding of the sea surface by steep waves, and a steeper elevation angle should improve performance.

The new design addresses these points as follows:

- the digital frequency modulation detector provides a dynamic range limited only by the input filter to ± 500 Hz or ± 13 m/s, and a stable output in the event of loss of return signal
- spectral windowing and the sampling parameters are all configurable to best fit the application
- the mean direction parameter is now calculated as the phase of the second angular harmonic:

$$Dmt = \arctan\left(\frac{\sum_n F_n \sin 2\theta_n}{\sum_n F_n \cos 2\theta_n}\right)$$

the revised spread parameter has not been implemented as an on-line computation, but can be estimated in post-processing from the angular harmonics of the spectral density matrix

- the quality control system has been enhanced with better hardware fault isolation, software fault detection, and parameter quality checks
- the selection of a steeper elevation angle is configurable on installation (by reducing the range gate time), and, since the transfer function is integrated across the antenna beam pattern, the directional response for long wavelength waves should not be significantly degraded
- with better spectral windowing, "wind noise" (the spectrum of the capillary wave field) can more reliably be separated from spectral "leakage", and the two correction parameters are now logged in the data output format.

Further work needs to be done to investigate the observed difference in measurements between approaching and receding waves, and the effect of a steeper grazing angle.

Further work is also needed to specify an appropriate definition for the spread parameter in terms of the available angular harmonics.

Effects Near the Breaking Limit

Chaplin (Archer, 1989, Appendix D) addressed possible problems of measurements in extreme waves, where finite amplitude and non-linear effects could introduce errors into the assumption of linear random wave theory in the transfer function between wave velocity and wave amplitude. The calculations are based on regular waves, and the effects are expected to be much less in random waves with much lower average steepness.

The relationship between wave amplitude a and horizontal velocity amplitude u is given from linear wave theory as

$$a = \frac{u\omega}{gk}$$

where ω is the radian frequency, k the wave number, and the dispersion relation is

$$\omega^2 = gk \tanh(kd)$$

The finite amplitude effect is to increase the wavelength by up to 20% in the breaking limit compared to small amplitude random wave theory. Since the wavenumber k

enters the transfer function, there could be an underestimate of wave height obtained from the wave velocity.

The wave velocity is actually measured at the instantaneous water level, and the effect of finite amplitude is to render the surface velocity amplitude greater than the velocity u at the assumed mean water level, so the wave height can be overestimated due to this effect.

The net effect of finite amplitude and instantaneous water level is that the Wave Radar would overpredict the fundamental component of surface elevation of a wave at limiting height by 4% in deep water, and by 8% when $d/L = 0.13$ (in the middle of the region known as "intermediate depth" waves).

Non-linear wave/wave interactions give rise to "tied" wave components with frequencies

$$\omega_n = n\omega_1$$

and

$$k_n = nk_1.$$

Since the dispersion relation

$$\omega_n^2 = gk_n \tanh kd$$

is used in the Wave Radar transfer function, there would be an underestimation of these tied components. The amplitudes a_n of the tied components are proportionately small (eg, for height 24 m and period 10 s, at 92% of the breaking limit, $a_1=10.3$ and $a_2=2.7$), so they are only significant in high steep waves. So for regular waves in deeper water ($d/L_o=0.5$), there is an underestimation of the fundamental component by about 10% at around 90% of the breaking limit, and worse underestimation in water of finite depth.

The presence of a current also affects the dispersion relation. In a typical situation of a current with an unknown shear profile, the inability to account for the shear could result in an overestimate of wave height if the measured current is used. Typically, this could lead to an overestimate in the fundamental component in the order of 10%, but would not be significant in the estimate of H_s . Therefore, it is recommended that no adjustment in frequency is made to the wave spectra according to the measured surface current.

These potential errors in estimation of individual wave heights will not significantly

affect the parameters obtained from the spectral moments. However, for critical work using individual waves, quantitative estimates can be made of the magnitude of non-linear behaviour, and a correction can be applied.

Linear Random Wave Theory

Tickell (Archer, 1989, Appendix E) concluded that linear random wave theory has been found to be accurate to within 10% for velocities near the spectral peak, with a tendency to overpredict (so the Wave Radar would underpredict wave height, since its fundamental measurement is the wave velocity). Also, it is the only available theory which can account for wave direction.

Bispectral analysis is proposed to investigate second order effects. The longer sampling times now available with the new Wave Radar would be needed to achieve the required spectral stability.

The raw velocity time series can still be made available for scientific work, and could be analysed directly for non-linear behaviour. Recommended studies include:

- asymmetry between crests and troughs
- asymmetries between the front and back of crests
- statistics of major events (eg, largest crest and trough, finite amplitude effects)
- apply Hilbert transform to output the envelope function of velocity amplitudes.

PRESENTATION OF RESULTS

While the new design offers increased flexibility in configuration and operation, it had to be tested in the same configuration as the previous version in order to ensure that the system had been implemented properly.

The new Wave Radar was operated on the Esso Odin Platform in 1992, and compared with wave data obtained from a Syminex vertical wave profiler on the Elf Frigg Field. The Odin Wave Radar data was sampled at 2 Hz for 256 samples in each direction. The Frigg wave parameters were calculated over a 17 minute sample by time series analysis (ie significant wave height as the mean of the highest one third zero-crossing wave heights, and mean zero-crossing period). The Frigg Platform is about 14 km from Odin. Over a three day period 9-11 October 1992, significant wave heights over 6 m were experienced, and wave heights from the two sensors were correlated, as shown in Figure 6. While a comparison with a sensor 14 km away over

such a short time is not considered conclusive, it is offered as supplementary evidence to extensive laboratory testing, that the new implementation of the Wave Radar performs the same functions in field conditions as the previous version, which itself has been extensively evaluated.

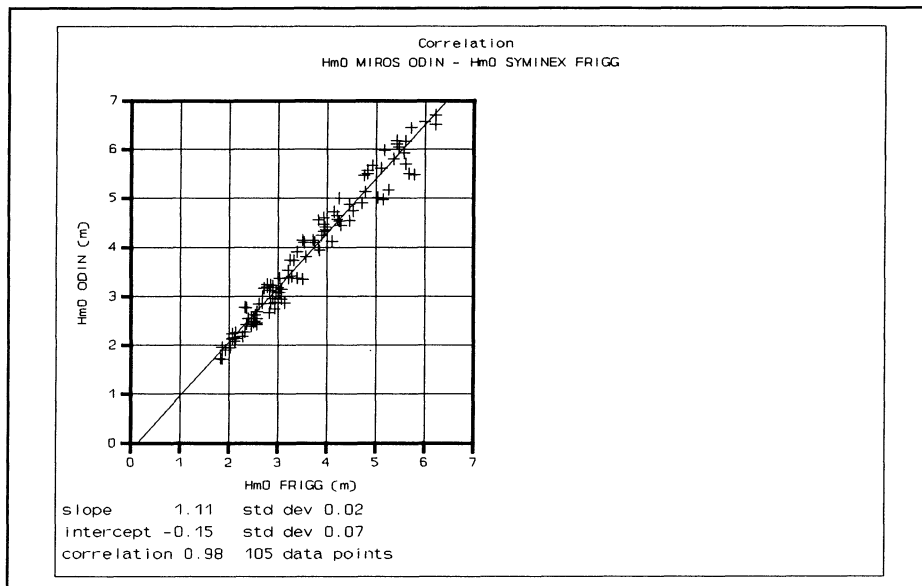


Figure 6 Wave height $Hm0$ correlation

CONCLUSIONS

The new generation Wave Radar represents a significant improvement in implementation, with simplification of components and increased flexibility in configuration. In particular, the improved automatic gain control and doppler detector mean the instrument is less affected by loss of signal in low wave/wind conditions, or by strong targets in the footprint, or by limiting of the doppler signal. In common with the previous version, the new version has been sufficiently validated for operational use, and the derived spectral parameters can be used with confidence for engineering applications. Corrections can be applied to individual spectral wave components to allow for non-linear behaviour in wave conditions near the breaking limit.

Further work is needed to test and implement an improved on-line directional spread parameter.

Further field data acquisition and detailed analyses of the data are needed to investigate differences in measurements between approaching and receding waves in high wave conditions, using a steeper grazing angle. Specialists may also wish to analyse the raw velocity time series to study non-linear effects.

REFERENCES

- Allender, J. et al. (1989) "The WADIC project: a comprehensive field evaluation of directional wave instrumentation". *Ocean Engineering* **16**, 505-536.
- Archer, S. J. (1989) "Technical Appraisal of MIROS Wave and Current Measurement System". TE/002/88/SA. MIROS Ltd, Aberdeen.
- Dacunha, N. M. C. and Angevaare, T. J. (1988) "A long term intercomparison of wave sensors in the Northern North Sea". Chapter 8 in *Oceanology 88*, Graham and Trotman, London.
- Grønlie, Ø., Brodtkorb, D. and Wøien, J. (1984) "MIROS - A microwave remote sensor for the ocean surface". Symposium on Description and Modelling of Directional Seas, Copenhagen, Denmark.
- Magnusson, A. K. (1987) "MIROS-WAVEC validation study - comparison of the measurements of sea state parameters". Det Norske Meteorologiske Institutt, Bergen, Norway.
- Tucker, M. J. (1991) "Waves in Ocean Engineering: measurement, analysis, interpretation". ISBN 0-13-932955-2. Ellis Horwood, London.

WAVE KINEMATICS - MEASUREMENT, MODELLING AND APPLICATION

S.J. BUCHAN

Steedman Science & Engineering
31 Bishop Street,
Jolimont WA 6014

ABSTRACT

Measurements of near bottom wave-induced pressures and orthogonal, horizontal velocity components, at several locations around Australia, have demonstrated that directional wave spectra and wave kinematics may be routinely monitored.

This presentation briefly addresses the measurement system, discusses various analysis techniques which have been applied to the data, and illustrate subsequent application of the information in numerical wave modelling and determination of marine engineering criteria.

Particular applications include studies on shallow water pipeline stability, nearshore wave penetration, dredge spoil dispersion and scour.

INTRODUCTION

During recent years, recognition of the importance of directional wave information in many facets of coastal and ocean engineering design has been increasing. Goda et al. (1978) have illustrated the importance of wave directionality for studies of wave diffraction and refraction in harbours; Forristall et al. (1978) have demonstrated the inadequacies of unidirectional wave theories in describing wave kinematics; and Sand et al. (1981) have discussed the applications of directional wave information to the hydrodynamics and design of offshore structures and pipelines.

Buchan et al. (1984) describes the development of a shallow water directional wave recording system, based on the Sea Data 635-12s Directional Wave Recorder. The instrument measures fluctuations in absolute pressure and horizontal current, and records the information internally on magnetic cassette. It is usually deployed in a sea bed frame.

Following Forristall et al. (1978), data processing involves the modelling of wave kinematics using linear wave theory, allowing the application of spectral analysis

techniques. The directional distribution of the sea state is described by a "spreading function". If the sea state is composed of a few resolvable, predominant wave trains, the spreading function may be satisfactorily approximated by the widely accepted cosine 2s model of Longuet-Higgins et al. (1963). Such a description of the sea state is based on only three frequency dependent parameters. These are $E(f)$, the omnidirectional energy density; $\theta(f)$, the principal direction of propagation of waves of particular frequency f ; and $s(f)$, a measure of the sharpness of the spread of wave directions about the principal direction.

Because of the directionality or "short-crestedness" of most sea states, application of unidirectional wave theory is known to cause over-estimates of wave-induced currents from surface wave measurements. Simultaneous surface wave height and near-bottom wave-induced current measurements have allowed calibration of unidirectional linear wave theory for specific oceanographic environments. Consequently surface wave data may be used to compute characteristic near-bottom wave-induced velocities.

The statistics of individual wave heights are known to approximate the Rayleigh distribution. Analysis of near-bottom wave-induced currents shows that wave-induced currents follow a similar distribution. As a result, individual current speeds may be statistically related to characteristic wave-induced velocities.

Wave-induced current velocities are of importance to littoral drift, seabed scour, sediment resuspension and lignefaction studies, fatigue analysis and risk assessment of forces on submarine pipelines and structures, and moored vessel motion studies.

This paper briefly describes a wave kinematics measurement system, discusses analysis techniques, and illustrates subsequent application of the information in numerical wave modelling and determination of marine engineering criteria.

PREAMBLE

The work described in this paper has arisen from the requirement to derive marine engineering criteria for several marginal oil field developments in shallow waters (less than 20 m) of the nearshore region of Australia's North West Shelf. For return periods of 10 years and longer, marine engineering of structures and seabed pipelines is controlled by waves generated by the severe tropical cyclones characteristic of the region.

Design in these waters is not fully supported by clear direction from currently available design codes. The shallowness of the water means that Pierson-Moskowitz and JONSWAP spectral parameterizations are less than ideal. Often exacerbating this is the presence of offshore islands or reefs, such that the ultimate design conditions (derived from directional spectral modelling of tropical cyclone wave fields) may comprise moderate wave heights of relatively long wave period (surface slopes of less than 1:15).

The marginal nature of most of these developments (low budget developments dictated by short projected field life of 3 to 10 years) means that the setting of design criteria

cannot be afforded the luxury of overconservatism, as any inflated cost of development could compromise their viability.

With waves being the controlling determinant from shallow water structures and seabed pipelines, without explicit guidance from design codes, and with the need to avoid unnecessary conservatism, wave kinematics must come under closer scrutiny.

On Australia's North West Shelf, it has become standard practice for oceanographic consultants to set design wave conditions, and for the pipeline engineer or hydrodynamicist to select the appropriate theory to describe associated wave kinematics. This is because the wave kinematics theory must be matched to the empiricism inherent in structure or pipeline loading and stability theory. However, the advice of the ocean engineer is often sought on such issues as which wave kinematics theories may be applicable, how directional spreading may be accommodated, and (more recently) whether wave irregularity (asymmetry of the front-to-back wave profile) may be of significance.

Rather than addressing these issues separately, our approach has been to try to use measured data to provide direct guidance. In particular, we have attempted to use limited wave kinematics measurements to "calibrate" more readily obtainable nondirectional surface wave data.

Our principal tool in this exercise has been the Sea Data 635-12s Directional Wave and Tide Recorder, which enables direct measurement of near-bottom wave kinematics, and subsequent determination of shallow water directional wave spectra.

INSTRUMENTATION

Hardware

The instrument measures fluctuations in absolute pressure and horizontal current velocity, at both tide and wind wave frequencies. Instrument temperature is also logged. A complete description of the instrument is given by Aubrey and Hill (1984), and a detailed analysis of sensor specifications is given by Grosskopf et al. (1983).

In operation of the 635-12s runs two separate sampling schemes in parallel. These are the mean (tide) and burst (wave) recording modes. Data from each mode are recorded in an interleaved format on a magnetic cassette tape.

In the mean mode, water pressure is integrated continuously over a specified sample interval. To conserve battery power, the mean current is computed only over every eighth mean pressure sample interval. The mean sample interval may be selected in the range 3.75 to 60 minutes. An instantaneous temperature measurement from a thermistor within the instrument housing is sampled after every 8 mean pressure samples. Data recording takes place every 8 sample intervals when an elapsed time, 8 tide measurements, a water temperature measurement, the mean current component and compass heading (instrument orientation) are recorded.

In burst mode, the instrument rapidly samples the water pressure and the two current velocity components at a preset interval in the range 0.5 to 4 seconds. The number of samples in each burst may be adjusted in steps between 64 and 2048, or alternatively the instrument may be set to run continuously. The interval between bursts may be varied from 0.5 to 24 hours. The burst samples are recorded as triplets of the water pressure, and two orthogonal horizontal velocity components.

Handling

The directional wave recorder is usually deployed in an aluminium tripod which is lowered to the sea bed by winch from a work vessel. The tripod is attached to small surface floats by a buoyant line, to facilitate recovery. Thus, deployment and retrieval operations can be carried out without diver assistance.

Within the tripod, the velocity and pressure sensors are located at 1.5 m above the base. Provided the sea bed is relatively smooth and flat (easily checked using an echo sounder), the sensors should be located above the bottom boundary layer for wave-induced currents.

Raw Data

The primary output of each burst of the 635-12s is illustrated in figure 1 which incorporates time history plots (profiles) of the raw pressure and east and north component currents, plus a cross plot of the component currents.

Inspection of the profiles facilitates convenient checking of data quality. The cross plot provides immediate confirmation of the ability of the instrument to monitor wave direction (propagation typically aligned along the major axis of the ellipse). The 180° ambiguity in propagation direction is resolved by establishing the direction of wave-induced currents under wave crests (from inspection of the raw profiles).

Also available, but not illustrated here, are mean current speed and direction, and tide height and water temperature measurements, throughout the period of a deployment.

DIRECTIONAL SPECTRAL SEA STATE REPRESENTATION

To obtain a representation of the surface sea state from subsurface measurements of pressure and velocity, an appropriate theory describing the kinematics of flow beneath surface waves must be applied. An assessment of available wave theories is presented in Forristall et al. (1978).

The simplest approach is to use linear wave theory which may be extended through spectral concepts to model irregular (i.e. aperiodic) sea. The most serious deficiency of linear theory occurs due to the non-linearity of the free surface boundary condition.

Higher order regular (periodic) and irregular (aperiodic) theories provide a better match to the free surface boundary condition, but their complexity precludes their incorporation in any practical analysis of directionally spread sea states.

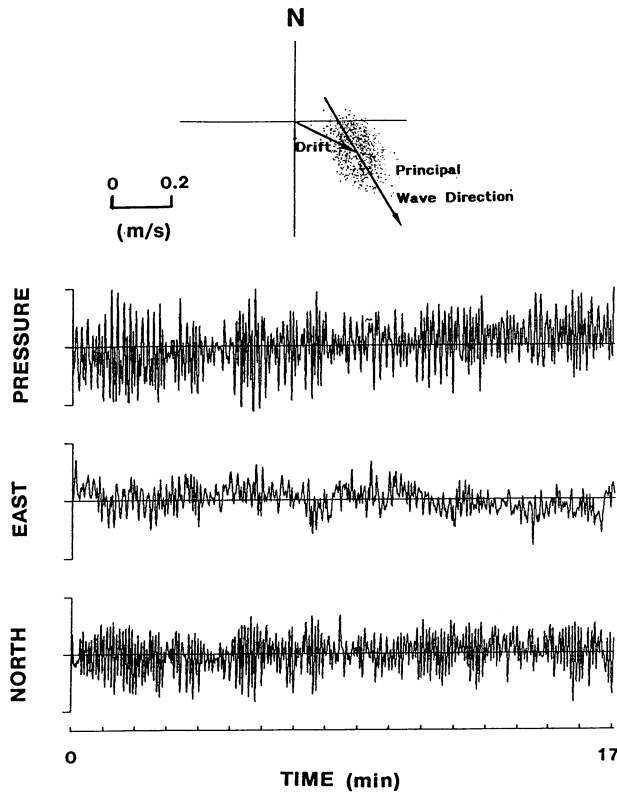


Figure 1 Raw pressure and east and north velocity component data, recorded by one burst of a Sea Data 635-12s Directional Wave and Tide Recorder.

From analysis of measurements conducted during Tropical Storm Delia in the Gulf of Mexico, Forristall et al. (1978) demonstrated that using a linear theory which accounted for the directional nature of the measured sea state provided a better representation of wave kinematics than higher-order, unidirectional wave theories.

A detailed description of linear wave theory appropriate to the 635-12s, is given in Buchan et al. (1984).

Most directional spectral wave models are parameterized in terms of the $\cos^2[(\theta - \theta_0)/2]$ spreading function, introduced by Longuet-Higgins et al. (1963). To facilitate corroboration of, or input to these models, this parametric formulation has been routinely adopted in processing of all data from the 635-12s. An example of the resulting directional spectral seastate description, from one burst of data, is illustrated in figure 2. The description is based on only three frequency dependent parameters; $E(f)$, the omnidirectional energy density; $\theta(f)$, the principal direction of wave propagation; and $S(f)$, a measure of the sharpness of spread of wave directions about the principal direction.

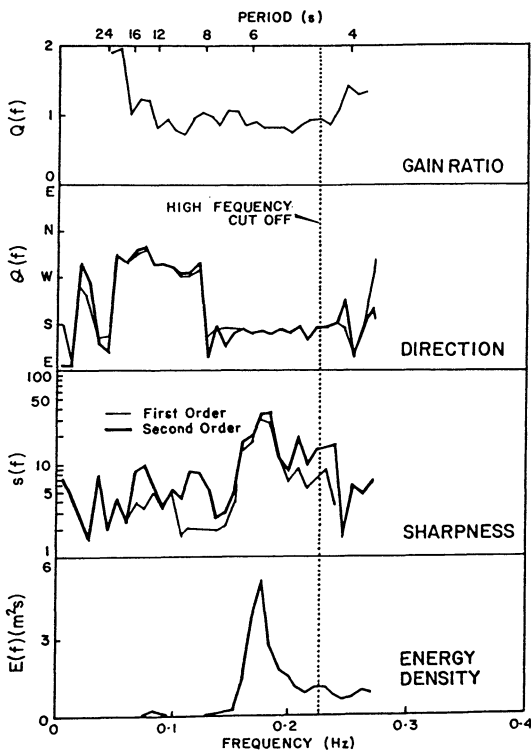


Figure 2 Example of the directional spectral information attainable from each "burst" of a Sea Data 635-12s.

Following the example of Forristall et al. (1978) the gain ratio $Q(f)$ has also been calculated. It represents the ratio of the measured pressure to velocity transfer function and that predicted by linear theory. If $Q(f)$ remains near unity, linear theory is providing a satisfactory description of wave kinematics. Figure 2 shows that $Q(f)$ departs from unity for very high frequencies where ambient turbulence contaminates the data, and for low frequencies where surface wave energy is very low.

DETERMINATION OF WAVE-INDUCED VELOCITIES

In addition to allowing determination of surface directional wave spectra, the 635-12s also provides for the direct measurement of wave-induced currents, and consequent calibration of surface wave kinematics theories (when concurrent surface wave data are available).

Measurements

Simultaneous surface wave height and near-bottom wave-induced current measurements at four difference locations were considered - Courtenay Head and Station A/B in Mermaid Sound, Dawesville near Mandurah, all in Western Australia and Streaky Bay in South Australia. These locations are situated in various water

depths at three vastly different points around the Australian coast (figure 3). Table 1 gives water depths and periods of simultaneous surface and near-bottom measurements for the four locations. Surface wave heights were measured using Datawell series 6000 FL Waverider buoys and the near-bottom wave-induced current measurements were recorded by Sea Data 635-12 Directional Wave and Tide Recorders.

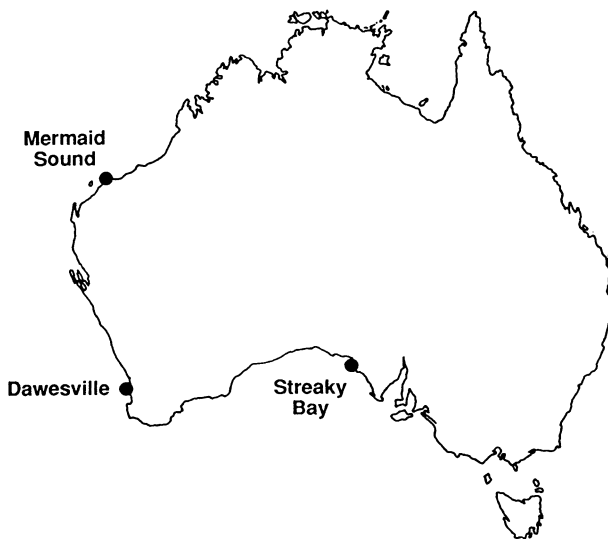


Figure 3 Wave measurement locations.

Name	Location		Depth (m)	Deployment Period
	Latitude (°S)	Longitude (°E)		
Dawesville	32°36.0'	116°37.6'	8.3	04.09.85 - 06.11.85 15.11.85 - 09.01.86
Station A/B	20°31.6'	116°43.7'	17.5	14.02.86 - 26.02.86 26.02.86 - 11.03.86
Courtenay Head	20°27.3'	116°42.7'	20.7	24.06.83 - 01.08.83
Streaky Bay	32°43.5'	133°52.0'	54.0	14.07.84 - 14.09.84

Table 1 Location and deployment details for the four 635-12s measurement locations

Surface waves were recorded as 17 minute 4 second profiles every six hours. Spectral analysis of the recorded data was carried out and wave height and period parameters were estimated as

$$H_s = 4(m_0)^{1/2}$$

$$T_z = \left(\frac{m_0}{m_2} \right)^{1/2}$$

where

$$m_p = \int_0^\infty E_w(f) f^p df ,$$

$E_w(f)$ is the surface wave spectral energy density and f is frequency.

Simultaneous measurements of the near-bottom wave-induced pressures and orthogonal horizontal velocity components, were also recorded. Spectral analysis of the measured wave-induced velocities was carried out, and for the purpose of this study, root mean square velocities, V_{rms} were calculated as follows

$$V_{rms} = (m_0)^{1/2}$$

where

$$m_0 = \int_0^\infty E_v(f) df$$

and $E_v(f)$ is the near-bottom wave-induced velocity spectral energy density.

Wave-Induced Current Statistics

The statistics of individual surface wave heights have been shown to follow very nearly the Rayleigh distribution (Longuet-Higgins, 1952) which is a special case of the Weibull distribution. On this basis, it was decided to consider the fit of a Weibull distribution to individual wave-induced current speeds.

Wave-induced current speeds were calculated from the velocity component along the major axis of the velocity ellipse (see figure 1). For each flow oscillation (between every second zero crossing) of the axial velocity component, the speed V of maximum absolute value was selected. The value of the root mean square axial velocity V'_{rms} was chosen as a characteristic velocity and the following distribution was fitted

$$P(V > x) = \exp \left(- \left(\frac{x}{V'_{rms}} \right)^a \frac{1}{b} \right)$$

The data fit this distribution very well - an example of the distribution and fitted data are shown in figure 4. Results are shown in table 2.

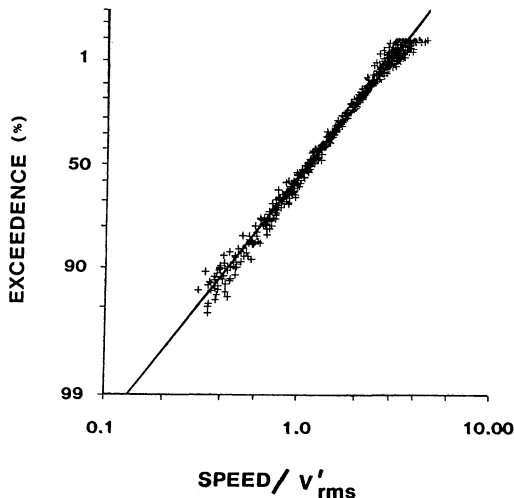


Figure 4 Weibull distribution fitted to measured maximum wave-induced speed data

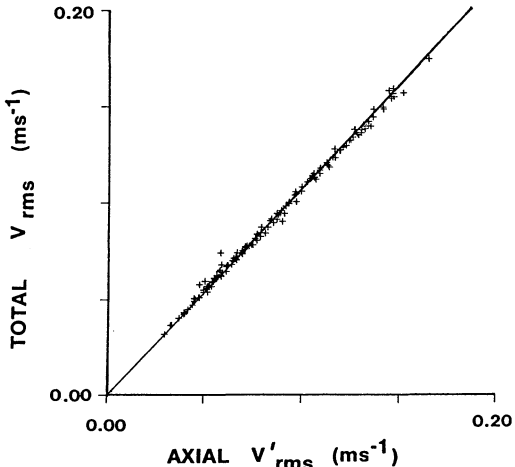


Figure 5 Linear regression of total versus axial measured wave-induced rms velocities

Location	Deployment No.	Weibull Parameters		Goodness of Fit	
		a	b	Correlation Coefficient (r)	Number of Points (n)
Dawesville	1	1.7	1.6	0.99	3111
	2	1.7	1.6	0.99	1712
Station A/B	1	2.0	1.9	0.99	259
	2	2.0	2.0	0.99	272
Courtenay Head	1	1.7	1.5	0.98	1584
Streaky Bay	1	2.0	1.9	1.00	888

Table 2 Fitted parameters for near-bottom wave-induced speed Weibull distribution

The fitted parameters a and b both range between 1.5 and 2.0 for the wide range of oceanographic locations, water depths, seasons and wave climates for which measurements were recorded. The variations in the fitted Weibull parameters appear to be relatively insensitive to any of the above factors.

In order to relate the Weibull distributed axial current speeds to the root mean square velocity, V_{rms} , calculated from the velocity spectra and hence to surface wave data, the relationship between V_{rms} and V'_{rms} was examined. A linear relationship was found to exist between these two quantities with a high degree of correlation. An illustration is presented in figure 5. Results of the linear regression for the four locations are shown in table 3.

Location	Deployment No.	Slope (m)	Regression Parameters	
			Correlation Coefficient, r	Number of Points, n
Dawesville	1	1.03	1.00	231
	2	1.03	1.00	213
Station A/B	1	1.03	1.00	93
	2	1.02	1.00	97
Courtenay Head	1	1.12	0.99	223
Streaky Bay	1	1.07	1.00	162

Table 3 Linear regression parameters for V_{rms} versus V'_{rms}

Wave-Induced Velocities from Surface Waves

It has been shown previously (Forristall et al., 1978; van Heteren et al., 1985) that the use of unidirectional linear theory to estimate near-bottom currents from surface wave leads to overestimates. This is a result of the directionality of the surface wave field which is not accounted for. Rather than attempt to use a more complex directional wave theory, we have approached the problem by quantifying the overestimate and thereby calibrating linear theory.

Direct computation of velocity spectra from measured near-bottom wave-induced velocities was accomplished using spectral techniques. Inferred spectra of the near-bottom wave-induced velocities were calculated from measured surface wave spectra using linear theory

$$E_v(f) = 2\pi f \frac{\cosh kz_v}{\sinh kd} E_w(f)$$

where d is the water depth, k is wave number and z_v is the height of the velocity sensor above the sea bed.

A least squares regression was then used to estimate the ratio of inferred to measured "velocity squared" ordinates (i.e. spectral ordinate units of $(\text{m s}^{-1})^2 \text{ Hz}^{-1}$) and hence the ratio of inferred to measured velocities for the four measurement locations, from all simultaneously recorded spectra, at each spectral frequency (e.g. figure 6).

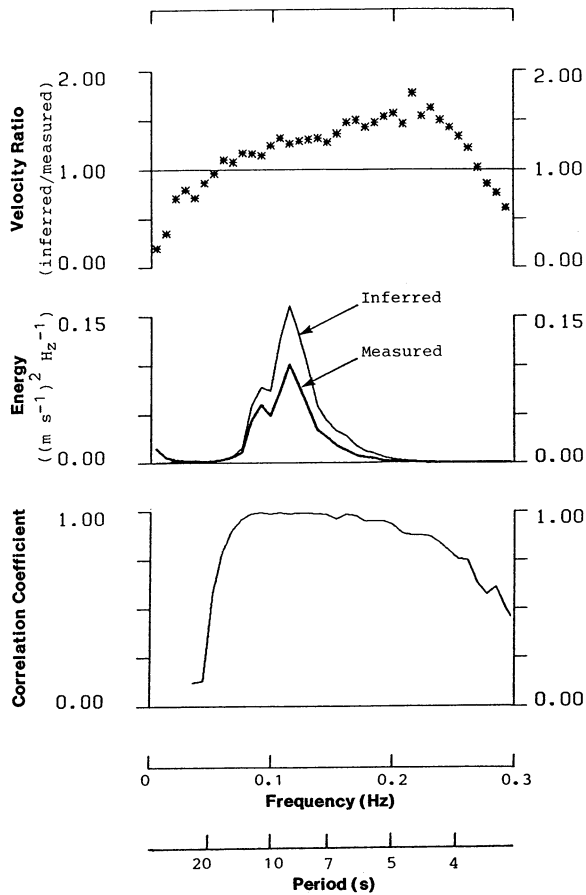


Figure 6 Comparison of measured near-bottom wave-induced velocity spectra with those inferred by linear theory.

Considering only the frequency range where significant correlation occurs (say > 0.75), the results show that linear theory over-estimates velocities from between 10% and 70%. This varies from location to location, and across frequencies for a particular location.

Implications for Wave Kinematics Computations

Measurements of near-bottom wave-induced currents are more difficult to make than standard surface wave measurements. Consequently, while suitable amounts of

nondirectional surface wave information may be available for many marine developments, wave kinematics measurements are very scarce.

The methodology described above provides a means of calibrating long-term surface wave measurements with short-term near-bottom wave-induced velocity measurements, thereby facilitating more accurate determinations of fatigue analysis and risk assessment of forces on submarine pipelines and structures.

The mechanism is as described below.

- (i) A deployment mean calibration of measured and inferred velocity spectra is conducted, as illustrated in figure 6. This establishes a transfer function of surface wave spectra to near-bottom velocity spectra.
- (ii) The near-bottom wave-induced velocity measurements are used to define the axial V'_{rms} versus total V_{rms} relationship, as illustrated in figure 5.
- (iii) The near-bottom current speed distribution may then be established from a fitted Weibull distribution, as illustrated in figure 4.

Even without site-specific deployments of the 635-12s, the results of the comparison studies conducted at several shallow water locations around Australia, indicate that improved estimates of near-bottom wave-induced velocities may be obtained from surface wave measurements, simply by using linear wave theory and the relatively insensitive parameterizations presented in tables 2 and 3, together with sensible estimates of the linear theory calibration factor (~ 10% reduction for strongly directional storm waves and swell, ranging up to 25% for confused sea states).

APPLICATIONS OF MEASURED WAVE KINEMATICS

Estimation of Shallow Water Directional Wave Spectra

Figure 2 illustrates the estimation of directional wave spectra from near-bottom measurements of wave kinematics.

These estimates may be used in calibration of, or input to, directional spectral wave models of storm wave propagation and swell penetration in the shallow water regions of Australia's North West Shelf.

Seabed Pipeline Stability and Fatigue Studies

The methodology outlined in the previous section allows improved analyses of pipeline stability and fatigue to be conducted using nondirectional surface wave data. This approach has been adopted in flow line design in shallow water and fields south of Barrow Island. It has allow been applied to wastewater discharge lines off Perth.

For fatigue studies in particular, all that is required is an input surface wave significant wave height and average zero crossing period percentage joint occurrence matrix.

Sediment Transport Studies

Figure 1 also demonstrates the applicability of the 635-12s in sediment transport studies.

Rather than relying on the uncertain combination of theoretically derived wave-induced currents with drift currents, this instrument directly measures the absolute, instantaneous, near-bottom current. It also measures the period of near-bottom wave-induced oscillations. According to Seymour (1985), both quantities are necessary in the assessment of the exceedence of sediment resuspension thresholds.

Such information has been applied in the assessment of dispersion of dredge spoil from dump sites, created by the deepening of the Port Hedland shipping channel in the north of Western Australia.

Again, the methodology of the previous section allows extension of surface wave data in providing improved estimates of sediment resuspension. Such as practice was adopted for dredge spoil resuspension studies conducted in Mermaid Sound (near Station A/B, refer figure 3).

Ship Motion Studies

The 635-12s can be directly employed to monitor low frequency swell-induced current motions which may cause problems with handling of moored vessels. This may be particularly important if a vessel is moored near a node of a standing wave motion (seiche) which may have little surface elevation signature, but still cause substantial mooring problems.

Such measurements have been conducted in Cockburn Sound south of Fremantle, and in Esperance Harbour.

CONCLUSIONS

The Sea Data 635-12s Directional Wave Recorder provides a convenient, reliable means of measurement of subsurface wave-induced motions, and of shallow water directional wave climate.

Measurements of near-bottom currents show that wave-induced velocities follow the Weibull distribution. The same parameters for the Weibull distribution, with only minor variations, apply to four different locations around the Australian coastline in a variety of wave climates, water depth and seasons.

Linear theory, applied to surface wave measurements, over-estimates the near-bottom wave-induced currents for the four locations investigated by some 10% to 70%.

These results agree with those of other workers in this field and allow characteristic near-bottom velocities to be calculated from surface wave measurements. From the characteristic velocity, maximum instantaneous speed statistics can be calculated using the Weibull distribution.

Application of these results potentially includes littoral drift, liquefaction, sea scour and sediment transport studies, fatigue analysis, and risk assessment of forces on submarine pipelines and structures.

ACKNOWLEDGMENTS

The authors wish to thank the Joint Venture participants and the management of Woodside Offshore Petroleum Pty Ltd for permission to publish material presented in this paper. The participants in the North West Shelf Joint Venture are Woodside Petroleum Ltd (through subsidiaries), Shell Development (Australia) Proprietary Limited, BHP Petroleum Pty Ltd, BP Developments Australia Ltd, California Asiatic Oil Company, and Japan Australia LNG (MIMI) Pty Ltd.

We also wish to thank the Department of Marine and Harbours of Western Australia for permission to use data measured off Dawesville, Western Australia.

Data measurements undertaken off Streaky Bay in South Australia were supported by funding from the Marine Sciences and Technologies Grants Scheme of the Commonwealth of Australia.

REFERENCES

- Aubrey, D.G. and W. Hill (1984). Performance of bottom-mounted directional wave gauges. Conference Record, Oceans '84, Marine Technology Society, IEEE Ocean Engineering Society, Washington D.C.
- Borgman, L.E. (1979). Directional wave spectra from wave sensor. In Ocean Wave Climate edited by M.D. Earle and A. Malahoff. Marine Science, 8, 269-300. Plenum Press (N.Y.).
- Buchan, S.J., R.K. Steedman, S.A. Stroud and D.G. Provis (1984). A Shallow Water Directional Wave Recorder. 19th Coastal Engineering Conference, ASCE, September 1984.
- Forristall, G.Z., E.G. Ward, V.J. Cardone and L.E. Borgman (1978). The directional spectra and kinematics of surface gravity waves in tropical storm Delia. J. Phys. Oceanogr., Vol. 8, 888-909.
- Goda, Y., T. Takayama and Y. Suzuki (1978). Diffraction diagrams for directional random waves. Proc. 16th Coastal Eng. Conf. Hamburg. Published by ASCE, New York.

- Grosskopf, W.G., D.G. Aubrey, N.G. Mattie and M. Mathiessen (1983). Field intercomparison of nearshore directional wave sensors. IEEE J. Oceanic Eng., OE-8, 254-271.
- Longuet-Higgins, M.S., 1952. On the statistical distributions of sea waves. J. Mar. Res., Vol. XI, No. 3, 245-265.
- Longuet-Higgins, M.S., D.E. Cartwright, and N.D. Smith (1963). Observations of the directional spectrum of sea waves using the motions of a floating buoy. Ocean Wave Spectra, Prentice-Hall Inc. (NY), pp. 111-136.
- Mitsuyašu, J., F. Tasai, T. Suhara, S. Mizuno, M. Ohkusu, T. Honda and K. Rikiishi (1975). Observations of the directional spectrum of ocean waves using a cloverleaf buoy. J. Phys. Oceanogr., Vol. 5, 750-760.
- Sand, S.E., O. Brink-Kjaer and J.B. Nielson (1981). Directional numerical models as a design basis. ARAE International Symposium, Wave and Wind Directionality with Applications to the Design of Structures. Paris.
- Seymour, R.J. (1985). Threshold effects on sediment transport by waves. J. Waterway Port Coastal & Ocean Eng., Vol. III, No. 2, 371-387.
- van Heteren, J. and M.J.F. Stive (1985). Kinematics and directionality of waves in the surf zone. Report WWKZ-84.S013, Rijkwaterstaat, Netherlands.

NON-LINEAR WAVE CURRENT INTERACTIONS.

I. CUMMINS¹ and C. SWAN²
Department of Civil Engineering,
Imperial College,
London, UK.

This paper considers the description of a two dimensional wave train propagating on an arbitrary current. The bi-linear numerical model, first proposed by Dalrymple (1974), has been extended to incorporate a five layered description of the flow field. This model allows an accurate representation of a strongly sheared current, and at the same time minimises the discontinuity in the vorticity profile. A variety of wave-current combinations are investigated, and it is shown that the time-averaged vorticity profile is an important parameter in determining the non-linearity of the wave form. In particular, the presence of a strongly sheared current at the water surface is shown to produce a significant increase in both the crest elevation and the wave induced velocity field. These changes cannot be predicted by a simple Doppler shifted solution based on an "equivalent" uniform current.

1. INTRODUCTION

The interaction between waves and currents is an important feature of most marine environments, and should be taken into account when describing the combined flow field. Even in the simplest of situations, involving a linear wave and a uniform current, the combined kinematics cannot be represented by the linear sum of the wave and the current components. In all cases the wave form travels on top of the current profile. This creates an apparent Doppler shift which produces a change in the dispersive characteristics of the wave form. If the current profile is non-uniform (or depth varying) then the interactive process may become highly non-linear and lead to the formation of a rotational wave component. Under these conditions the fluid velocity in the vicinity of a strongly sheared current may be much larger than

¹ Research student, ² Lecturer.

the linear sum of the wave and the current components. This may have important implications for the structural design of an individual member subject to increased local velocities.

If the current profile is sheared in the vicinity of the water surface the total overturning moment experienced by a structure can only be determined after the inclusion of the wave-current interaction. Furthermore, the water surface elevation is dependent upon the non-linearity of the wave motion. The interaction with a current profile may therefore produce an increase in the crest elevation (for a given wave height) and a corresponding reduction in the "air gap" separating the lowest layers of the structure and the water surface.

The present paper will consider the equilibrium conditions resulting from the combination of waves and currents. The non-linearity of the interaction will be described together with the characteristics of the combined flow field. This paper will not consider the initial propagation of the wave onto the current profile. This forms part of a transient condition in which there is a transfer of energy between the various components of the flow field. This problem has already been considered by a number of authors including Longuet-Higgins and Stewart (1960, 1961), Bretherton and Garrett (1968), Brink-kjær and Jonsson (1975) and Skop (1987a). A full discussion of these matters is given in the review articles by Peregrine (1976) and Jonsson (1990).

2. PREVIOUS WORK

The combination of waves and currents has been the focus of sustained research over a large number of years. Much of this work has considered the interaction with a uniform current ($U(z)=U_0$) since this provides a good approximation to both the large scale ocean currents and the majority of tidal flows. Under these conditions a Doppler shifted solution results. To a first approximation the phase velocity c , measured relative to a stationary observer, is given by:-

$$c = \frac{\sigma}{k} - \left[\frac{g}{k} \tanh(kh) \right]^{1/2} + U_0 \quad (1)$$

Where h is the water depth, g is the gravitational constant, σ is the wave frequency and k is the wave number defined by $2\pi/\lambda$, where λ is the wavelength. Fenton (1985) considered this problem and presented an "alternative Stokes theory". This is valid to a fifth order of wave steepness and gives explicit solutions for both the underlying kinematics and the dispersion equation.

A second situation which has been widely investigated involves the propagation of waves on a linear shear current. Tsao (1959) considered this case and found that because the current varies linearly with depth, the vorticity distribution is uniform, and consequently the oscillatory component of the flow field remains irrotational. Kishida and Sobey (1988) also considered this case and showed that the dispersive characteristics of the wave form are dependent upon the shear of the current profile. At a second order of wave steepness the dispersion equation is given by:-

$$c = \frac{\sigma}{k} - \left[\frac{g}{k} \tanh(kh) \right]^{1/2} + U_s - U'_s \frac{\tanh(kh)}{k} \quad (2)$$

where the subscript s denotes the value at the water surface, and the prime defines the gradient in the z direction.

This result was also obtained by Skop (1987b). Using an approach first proposed by Stewart and Joy (1974) he obtained a first approximation to the dispersion equation in finite depth and suggested that equation (2) provides a good approximation to a number of simple wave-current interactions. This work was further extended by Kirby and Chen (1989). They developed a second approximation to the dispersion equation for arbitrary currents in finite depth and showed that the expansions are valid for large currents having weak vorticity.

The importance of the vorticity distribution has been further investigated by Swan (1990, 1992). The first of these papers presents an experimental investigation, while the second describes a stream function solution for waves on a strongly sheared current. This latter formulation is presented in the form of a simple analytical expansion and gives explicit solutions for both the dispersion equation and the underlying kinematics. At a second order of wave steepness the dispersion equation is given by:-

$$\begin{aligned} c = & \left[\frac{g}{k} \tanh(kh) \right]^{1/2} + U_s - U'_s \frac{\tanh(kh)}{k} \\ & + U''_s \frac{3}{2k^2} - U'''_s \frac{3\tanh(kh)}{k^3} + \frac{F_a}{2\cosh^2(kh)} \end{aligned} \quad (3)$$

where the prime again denotes the z derivatives taken at the water surface and F_a is a constant for a given wave-current interaction. This result clearly demonstrates the importance of the vorticity distribution occurring at the water surface.

The solution presented by Swan (1992) showed that the wave induced kinematics (u, v) are also dependent upon the

vorticity distribution, and that significant departures from the established irrotational solutions can arise. However, it is difficult to quantify the effect of the wave-current interaction within the confines of a truncated series expansion. The order of approximation is inevitably determined by the complexity of the algebraic expansions rather than a clear understanding of the non-linearity of the combined flow field. The present paper will address this point.

A brief description of the numerical model is presented in section 3. This model is used to investigate a variety of wave-current interactions, and a full description of the resulting flows is given in section 4. At the end of the paper some concluding remarks are presented, and guidance is given on the appropriateness of the various wave-current solutions.

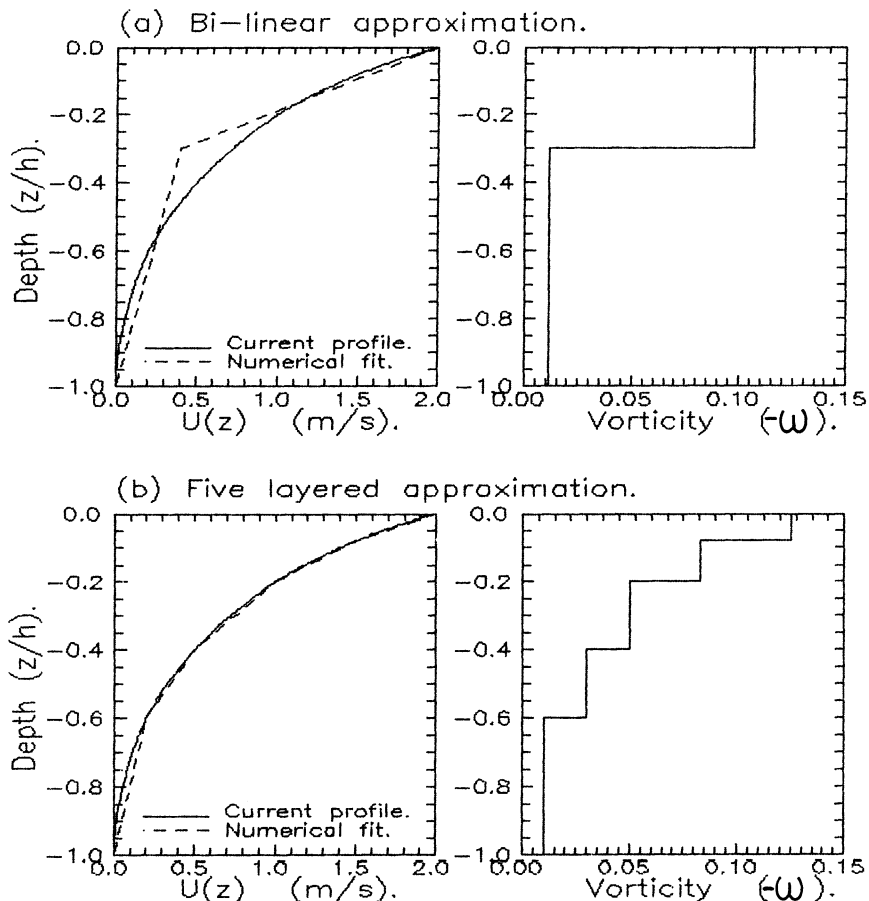


Figure 1. Modelling the current profile.

3. NUMERICAL MODEL

The multi-layered model proposed by Dalrymple and Heideman (1989) represents a natural extension of the two layered, or bi-linear model proposed by Dalrymple (1974). If a current profile is highly sheared (figure 1) a bi-linear approximation provides a poor representation of the velocity distribution. Furthermore, the gradient of the linear shear will, by necessity, be very different in the two layers and consequently this description introduces a large discontinuity in the vorticity profile (figure 1a).

These difficulties may be overcome by the introduction of a multi-layered flow field (figure 1b). In the present investigation a five layered model, shown on figure 2, was found to provide an adequate compromise between the description of the flow field and the increased computational requirements associated with array sizes and processing times.

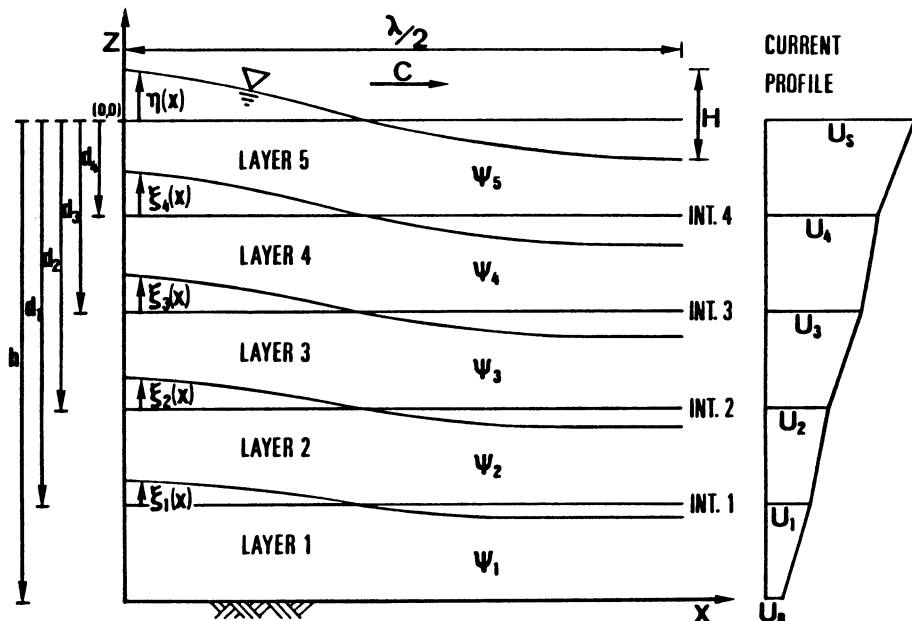


Figure 2. Solution domain.

The numerical model provides a two dimensional representation of an established wave-current interaction. It is therefore assumed that the wave motion consists of a regular wave train propagating without change of form in a homogenous, incompressible fluid of constant depth. The current profile $U(z)$ is assumed to be steady and is aligned in

the plane of the wave motion. If the effects of viscosity are ignored, the wave train may be brought to rest by the translation of the co-ordinate axes. Within this steady frame of reference a stream function $\Psi(x, z)$ may be defined such that the velocity components in the (x, z) directions are given by:-

$$\begin{aligned}\frac{\partial \Psi}{\partial z} &= -(U+u-c) \\ \frac{\partial \Psi}{\partial x} &= v\end{aligned}\quad (4)$$

Where U is the current velocity, (u, v) are the wave induced velocity components, and c is the phase velocity defined by an appropriate dispersion equation.

Within the frame of reference described in figure 2, the equations of motion may be simplified to give:-

$$\begin{aligned}(U+u-c) \frac{\partial(U+u-c)}{\partial x} + v \frac{\partial(U+u-c)}{\partial z} &= -\frac{1}{\rho} \frac{\partial P}{\partial x} \\ (U+u-c) \frac{\partial v}{\partial x} + v \frac{\partial v}{\partial z} &= -\frac{1}{\rho} \frac{\partial P}{\partial z} - g\end{aligned}\quad (5)$$

After substituting for the stream function Ψ and eliminating the pressure P , equations (5) may be integrated to give a governing equation of the form:-

$$\nabla^2 \Psi = f(\Psi) \quad (6)$$

Where $f(\Psi)$ defines the vorticity distribution which is constant within each fluid layer. To satisfy equation (6) the stream function Ψ_i , where $i=1, 2, \dots, 5$ for each of the fluid layers (figure 2), must be given by a general solution:-

$$\begin{aligned}\Psi_i &= cz - U_{(i-1)}z - \frac{(U_i - U_{i-1})}{(d_{i-1} - d_i)}(z^2/2 + d_{i-1}z) \\ &+ \sum_{n=1}^N \left[X_i(n) \sinh\left(\frac{2\pi nz}{\lambda}\right) + Y_i(n) \cosh\left(\frac{2\pi nz}{\lambda}\right) \right] \cos\left(\frac{2\pi nx}{\lambda}\right)\end{aligned}\quad (7)$$

Where λ represents the unknown wavelength, and N is the order of the approximation which corresponds to the number of harmonics within the series solution. The first term in equation (7) corresponds to the current profile while the second describes the resulting wave motion. The unknown coefficients $X_i(n)$ and $Y_i(n)$ are determined from the usual boundary constraints.

(a) Bed Conditions

If the bed is impermeable then the fluid velocity perpendicular to the bed must be zero.

$$\frac{\partial \Psi_1}{\partial x} = 0 \quad \text{on } z = -h \quad (8)$$

(b) Internal Conditions

The velocities and pressures must be continuous throughout the entire water depth,

$$\begin{aligned} & \left(\frac{\partial \Psi_{i+1}}{\partial z} - \frac{\partial \Psi_i}{\partial z} \right)_{z=d_i+\xi_i} \\ & \left(\frac{\partial \Psi_{i+1}}{\partial x} - \frac{\partial \Psi_i}{\partial x} \right)_{z=d_i+\xi_i} \quad \text{for } i = 1, 2, 3, 4 \end{aligned} \quad (9)$$

and there should be no mean displacement of the interface positions.

$$\int_{x=0}^{\lambda/2} \xi_i(x) dx = 0 \quad \text{for } i = 1, 2, 3, 4 \quad (10)$$

(c) Surface Conditions

If $z=\eta(x)$ defines the water surface, then the conditions require that there should be no change in the mean water level,

$$\int_{x=0}^{\lambda/2} \eta(x) dx = 0 \quad (11)$$

and the difference between the crest and the trough elevations should be equal to the specified wave height, H .

$$H = \eta(x=0) - \eta(x=\lambda/2) \quad (12)$$

Two further conditions must be satisfied at the water surface. The kinematic condition requires that the water surface is a streamline, and the dynamic condition requires the pressure normal to the water surface to be constant. The first condition is satisfied exactly by specifying $\Psi=\text{constant}$ on $z=\eta$. The application of Bernoulli's equation along this streamline gives the required dynamic condition:-

$$\eta(x) + \frac{1}{2g} \left[\left(\frac{\partial \Psi_s}{\partial x} \right)^2 + \left(\frac{\partial \Psi_s}{\partial z} \right)^2 \right] = \text{constant on } z=\eta(x) \quad (13)$$

Equations (8)-(13) provide the 16 conditions required for a unique solution of the five layered model shown on figure 2. To achieve a solution an initial estimate is made for the unknown parameters and the errors in the boundary conditions are minimised with respect to the wavelength λ and the coefficients of the individual harmonics, $X_1(n)$ and $Y_1(n)$. The minimisation technique uses a number of Lagrange multipliers within a matrix solution. This approach is similar to that proposed by Dean (1965).

The procedure described above is valid for a wide range of wave-current interactions. However to achieve convergence the scheme requires a good initial estimate for the unknown parameters and these are difficult to identify for a steep wave on a strongly sheared current. To overcome this difficulty an iterative approach was adopted in which the estimates for an N^{th} order approximation were obtained from an $(N-1)^{\text{th}}$ order solution. In some cases it was also necessary to reduce the number of fluid layers before an initial estimate of the input parameters could be obtained. Having achieved convergence for a 3 layered model, the input for the five layered model was obtained by linear interpolation. Using these techniques a converged solution for the five layered model was identified for all (non-breaking) wave-current combinations.

4. NON-LINEARITY

The wave steepness expressed in terms of a/k , where a is the surface amplitude and k is the wave number, is often used to express the non-linearity of a wave form. Indeed, many wave solutions are based upon a series expansion in which the wave steepness is adopted as an appropriate expansion parameter. However, with the combination of waves and currents it is not immediately apparent that the wave steepness will provide a satisfactory measure of the non-linearity. To investigate this point we must reconsider the surface boundary conditions. The non-linearity associated with a wave arises from both the kinematic and the dynamic boundary conditions. In the present solution the kinematic condition is satisfied exactly and hence the error in the dynamic boundary condition will provide a direct measure of the non-linearity. Re-arranging equation (13) gives:-

$$\eta(x) + \frac{1}{2g} \left[\left(\frac{\partial \Psi_s}{\partial x} \right)^2 + \left(\frac{\partial \Psi_s}{\partial z} \right)^2 \right] - Q = \epsilon_1(x) \quad \text{on } z=\eta(x) \quad (14)$$

Where Q is a constant so that the average value of the error $\epsilon_1(x)$ is zero.

$$Q = \frac{2}{\lambda} \int_{x=0}^{\lambda/2} \eta(x) + \frac{1}{2g} \left[\left(\frac{\partial \Psi_s}{\partial x} \right)^2 + \left(\frac{\partial \Psi_s}{\partial z} \right)^2 \right] dx \quad (15)$$

Taking the root mean square of $\epsilon_1(x)$ and non-dimensionalising with respect to the wave height gives:

$$\sqrt{\epsilon_1^2}/H = \left[\frac{2}{H^2 \lambda} \int_{x=0}^{x=\lambda/2} (\epsilon_1(x) - Q)^2 dx \right]^{1/2} \quad (16)$$

This approach was first suggested by Dean (1970), and will be used as an appropriate measure of the non-linearity in the following discussion.

5. RESULTS AND DISCUSSION

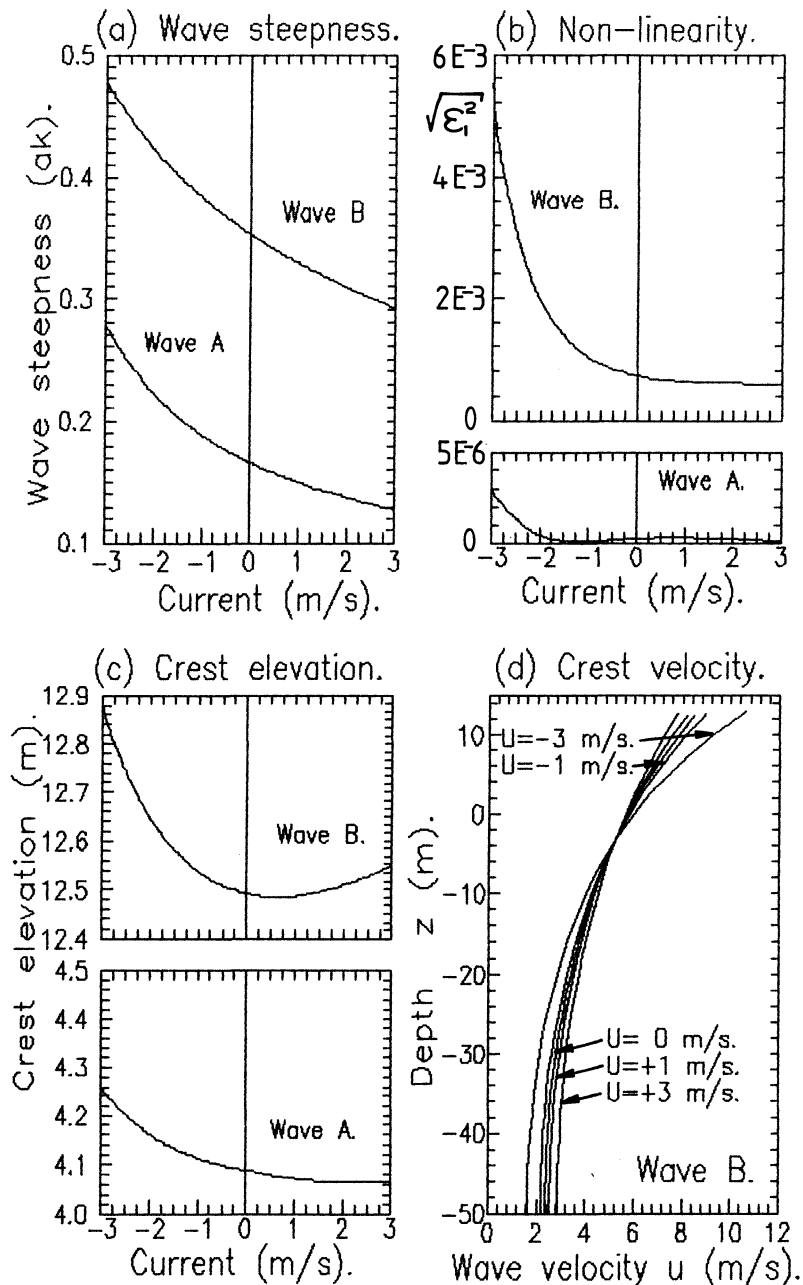
To clarify the separate effects of the surface current and the vorticity distribution the discussion will consist of two parts. The first considers the interaction with a uniform current ranging from +3 m/s to -3 m/s, and the second considers the effect of the vorticity distribution for a given surface current. In each case the interaction with two wave forms will be considered:

Table 1. Wave characteristics.

	Wave period	Wave height	water depth	Wave steepness
Wave A.	10.0s	7.5m	50.0m	0.166
Wave B.	12.0s	20.0m	50.0m	0.353

Using the classification code proposed by Dean (1970), wave A is approximately linear, and wave B represents a steeper fifth order wave form.

Figures 3a-3d concern the interaction of waves A and B with six different uniform currents ($U=-3, -2, -1, +1, +2, +3$ m/s) and shows that the wave characteristics are largely dependent upon the changes in the wave length. This change is associated



Figures 3a-3d. Interaction with a uniform current.

with the Doppler shift identified in equation 1. An adverse current ($U < 0$) shortens the wave length and therefore increases the wave steepness, while a favourable current stretches the wave form and reduces the wave steepness. Figure 3b shows that the non-linearity of the waveform, expressed in terms of $\sqrt{\epsilon_1^2}$, directly reflects these changes in the wave steepness.

Figure 3c gives the variation in the crest elevation (η_{max}) for a given wave height. It shows that as each wave form steepens on an adverse current the crest elevation increases. However, as the wave steepness reduces on a favourable current, the crest elevation of the steepest wave (wave B) begins to increase. This is inconsistent with the usual interpretation of non-linearity and wave steepness and indicates that the higher order interactions are becoming significant despite the reduction in the wave steepness. The horizontal component of the oscillatory velocity occurring beneath the crest of wave B is given on figure 3d. These values are consistent with the changes in the wave length. A shorter wave ($U = -3$ m/s) has larger near surface velocities which decay more rapidly with depth; while a longer wave ($U = +3$ m/s) has smaller near surface velocities which decay more slowly.

To assess the effect of the vorticity distribution the wave forms described in table 1 are combined with the current profiles shown on figure 4.

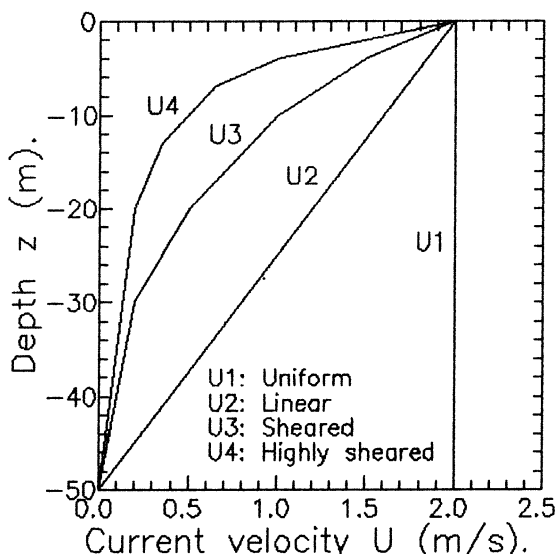


Figure 4. Sheared current profiles.

The surface vorticity ω_s associated with these profiles is given in table 2.

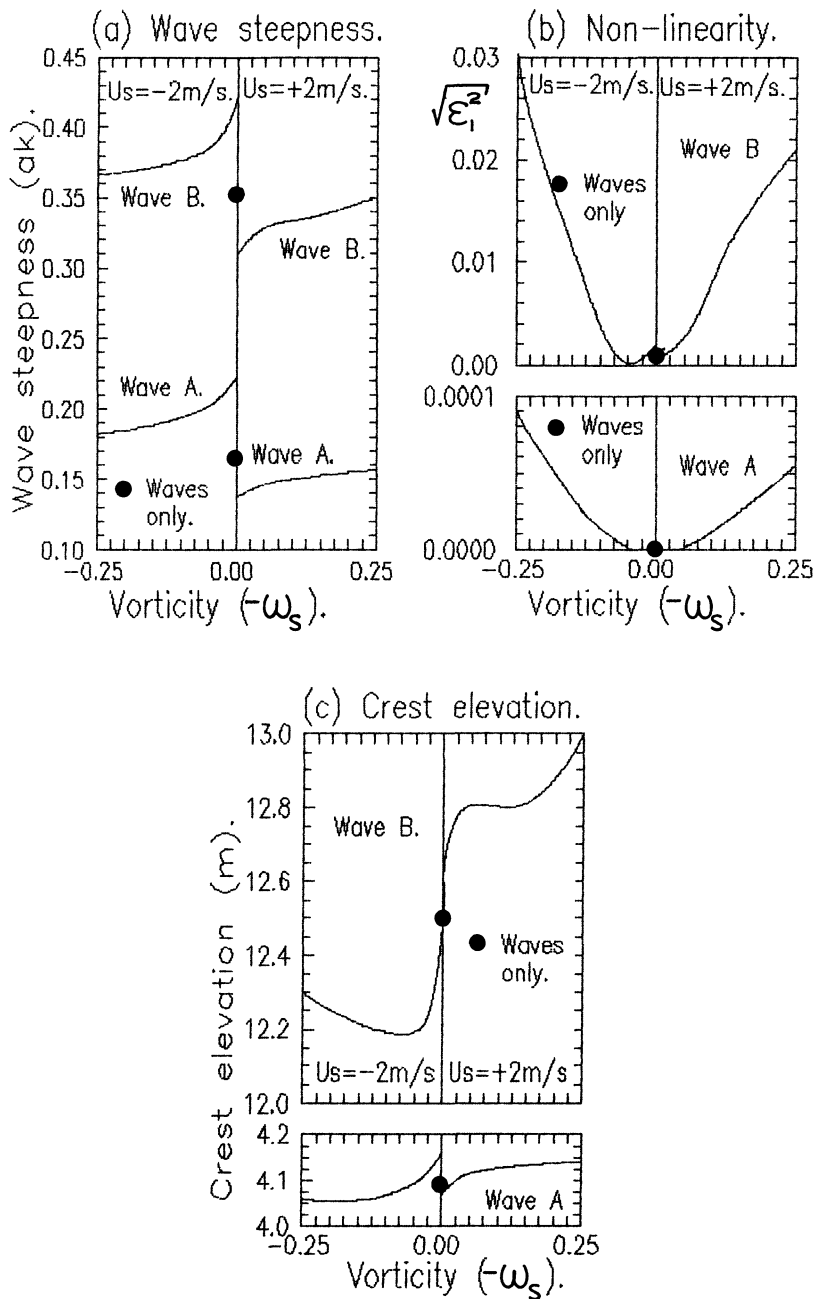
Table 2 Surface vorticity.

	U1	U2	U3	U4
ω_s	0.0 s ⁻¹	± 0.04 s ⁻¹	± 0.125 s ⁻¹	± 0.250 s ⁻¹

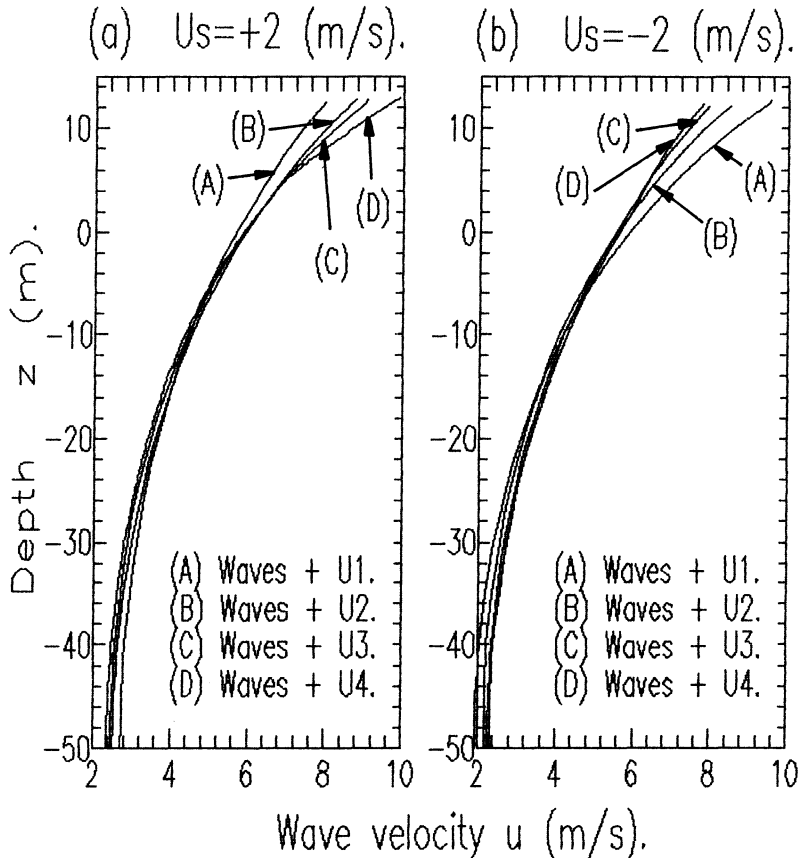
The interaction with both the "favourable" currents ($U>0$) and the "adverse" currents ($U<0$) is shown on figures 5a-5c. Convention dictates that a vorticity distribution is positive if it causes an anti-clockwise rotation of the fluid particles ($\omega = -dU/dz$). Unfortunately, this means that a positively sheared current ($dU/dz > 0$) has negative vorticity. To avoid confusion the horizontal abscissa in figures 5a-5c is expressed in terms of $(-\omega_s)$, so that an increase in the positive x direction indicates an increase in the positive shear.

Figure 5a considers the wave steepness and shows that for a given value of the surface current a positive shear increases the wave steepness, while a negative shear reduces the wave steepness. This highlights the importance of the depth variation indicated in equation (3). The non-linearity of the wave form shown on figure 5b does not, however, follow an identical trend to the wave steepness. For example, an increase in the positive shear does not increase the wave steepness beyond the waves only value (indicated by ● on figure 5a). In contrast, the non-linearity is increased well beyond the waves only value. This suggests that a combination of waves and currents may reduce the wave steepness, but increase the non-linearity. This is contrary to the normal expectation, and makes it very difficult to determine the appropriate order for a given wave current interaction. This point is further complicated in the case of an adverse current ($U_s < 0$), where an increase in the negative shear actually reduces the wave steepness below the uniform current case, but leads to an increase in the non-linearity.

Figure 5c considers the variation in the crest elevation. The positive shear within a favourable current produces an increase in the crest elevation, while negative shear within an adverse current produces a reduction in the crest elevation. In both cases the vorticity distribution has the opposite effect to that which is predicted by the Doppler shifted solution which is appropriate for waves on a uniform current.



Figures 5a-5c. Interaction with a sheared current.



Figures 6a-6b. Wave induced crest kinematics (Wave B).

The oscillatory flow resulting from the wave-current combinations discussed above are shown on figures 6a-6b. The first figure considers the interaction with a positively sheared favourable current ($U_s > 0$) and shows that the amplitude of the oscillatory velocity (u) is directly related to the gradient of the current profile. An increase in the time averaged vorticity distribution occurring at the water surface produces a corresponding increase in the local amplitude of the oscillatory motion. As a result, the existing irrotational solutions underestimate the maximum value of the near surface kinematics. Figure 6b considers an adverse current with negative shear. In this case the vorticity distribution has the opposite effect and leads to a reduction in the near surface kinematics. In both of these cases a simple Doppler shifted solution cannot predict the underlying kinematics.

6. CONCLUSIONS.

The equilibrium conditions associated with the combination of waves and currents has been considered using a five layered model. This approach allows a satisfactory description of a strongly sheared current and at the same time minimises the discontinuities in the vorticity profile. Several combinations of waves and currents have been considered, and it has been found that the time averaged vorticity distribution associated with the current has a significant effect upon the underlying flow field. For example, a positive shear in the vicinity of the water surface produces an increase in the local amplitude of the oscillatory motion. This cannot be predicted by an irrotational solution and is entirely distinct from the Doppler shift associated with the surface current.

Furthermore, if the current is highly sheared the wave steepness does not provide an adequate representation of the non-linearity of the wave form. An increase in the positive shear was found to produce a reduction in the wave steepness, but an increase in the crest elevation and the crest velocity. This effect is associated with the development of a rotational wave component which can only be identified within a full non-linear wave-current interaction. Under these circumstances the flow field cannot be described by a simple Doppler shifted solution based upon an equivalent uniform current.

7. ACKNOWLEDGEMENTS.

The authors are grateful to the Science and Engineering Research Council (SERC) for their financial support of the first author during his doctoral studies.

8. REFERENCES.

- Bretherton, F.P. & Garrett, C.J.R. (1968) "Wave trains in inhomogeneous moving media", Proc. R. Soc. London, Ser.A, Vol. 302, pp. 529-554.
- Brink-Kjær, O. & Jonsson, I.G. (1975) "Radiation stress and energy flux in water waves on a shear current", Tech. Univ. Denmark, Inst. Hydrodyn. and Hydraul. Eng., Prog. Rep. no. 36, pp. 27-32.
- Dalrymple, R.A. (1974) "Water waves on a bi-linear shear current", Proc. 14th Conf. Coastal Eng., ASCE, Hamburg, pp. 626-641.

Dalrymple, R.A. & Heideman, J.C. (1989) "Nonlinear water waves on a vertically sheared current", Proc. I.M.P. Forum. Paris 1989.

Dean, R.G., (1965) "Stream function representation of non linear ocean waves", J. Geophys. Res., Vol. 70(18), pp. 4561-4572.

Dean, R.G., (1970) "Relative validities of water wave theories". Proc. ASCE J. Waterw. Harbors Coastal Engng. Div. Vol. 96, pp 105-119.

Fenton, J.D. (1985) "A fifth-order Stokes theory for steady waves", J. Waterway, Port, Coastal and Ocean Eng. Div. ASCE, Vol. 111, pp 216-234.

Jonsson, I.G. (1990) "Wave-current interactions", The Sea, Vol. 9, Ocean Eng. Science, Chap. 1.1.3.

Kirby, J.T., & Chen, T.-M. (1989) "Surface waves on vertically sheared flows: Approximate dispersion relations", J. Geophys. Res., Vol 94, pp. 1013-1027.

Kishida, N. & Sobey, R.J. (1988) "Stokes theory for waves on linear shear current", J. Eng. Mech., ASCE, Vol. 114, pp. 1317-1334.

Longuet-Higgins, M.S. & Stewart, R.W. (1960) "Changes in the form of short gravity waves on long waves and tidal currents", J. Fluid Mech., Vol. 8, pp. 565-583.

Longuet-Higgins, M.S. & Stewart, R.W. (1961) "The changes in amplitude of short gravity waves on steady non-uniform currents", J. Fluid Mech., Vol. 10, pp. 529-549.

Peregrine, D.H. (1976) "Interaction of water waves and currents", Adv. Appl. Mech., Vol. 16, pp. 9-117.

Skop, R.A. (1987a) "An approach to the analysis of the interaction of surface waves with depth-varying current fields", Appl. Math. Modelling, Vol. 11, pp. 432-437.

Skop, R.A. (1987b) "An approximate dispersion relation for wave-current interactions", J. Waterway, Port, Coastal and Ocean Eng. Div. ASCE, Vol. 113, pp. 187-195.

Stewart, R.H. & Joy, H.W. (1974) "HF radio measurements of surface currents", Deep-Sea Res., Vol. 21, pp. 1039-1049.

Swan, C. (1990) "An experimental study of waves on a strongly sheared current profile", Proc. 22nd. Int. Conf. Coastal Eng. Delft 1990, Vol. 1, pp 489-502.

Swan, C. (1992) "A stream function solution for waves on a strongly sheared current", Proc. 23rd. Int. Conf. Coastal Eng. Venice 1992.

Tsao, S. (1959) "Behaviour of surface waves on a linearly varying flow", Moskow. Fiz.-Tech. Inst. Issl. Mekh. Prikl. Mat., Vol 3, pp. 66-84.

EFFECTS OF A SHEAR CURRENT ON WIND INDUCED WAVES.

A.K. Magnusson

The Norwegian Meteorological Institute

Allegaten 70, N-5007 Bergen

Norway

ABSTRACT

A third generation wave model has been run with constant wind speed over a numerical coastal current. It is seen that the traditional kinematical results (with no sources and sinks of energy) of current refraction are overruled by the dynamical action of the wind, except for a transition zone at the shear zone of the current.

INTRODUCTION

Wave theory has been a research topic for at least a century. Since the second World War, it has been a skill to forecast ocean waves, and since oil industry started offshore, it has also been useful to hindcast them for design purposes. Wave models have reached a relatively high level of confidence. But even if results are good overall, it is important to work towards better theories to be able to also model the unpredicted happenings that occur on the ocean surface now and then. There are still situations where validation against measurements are showing bad results.

The kinematics of monochromatic waves is well known. Kinematics of waves describing a sea state by a sum of Fourier components are similar. Geometrical optics approximation can for example be applied for varying currents and depths (Mei, 1989, Jonsson, 1990). The method of characteristics or ray tracing techniques have been used by many to calculate and visualize bottom and current refraction effects (see for example M.Mathiesen, 1985, I.G. Jonsson, 1990). This method can demonstrate where there are possibilities of convergence or divergence of energy, but the method applies only for swell propagation since no wind action is taken account of.

This article shows results from part of a Phd work dealing with the study of effects of currents in a third generation wave model, aiming at defining these effects both qualitatively and quantitatively, and especially studying the importance of the interplay between the dynamics and the kinematics. Neither currents nor winds are affected in any way by the waves in this study. The model used is the model "WAVEWATCH", made and described by Tolman (1989) as Phd work. He demonstrated the impact of tidal currents on waves in the southern North Sea as recorded by instruments. Effects of the Gulf Stream on waves have also been modelled, demonstrating different impacts on swell and on high wind waves. In the storm situation over a Gulf stream ring, refraction causes considerable variations in significant wave height and short-crestedness, but is hardly affecting the mean wave direction. The effect is spacially limited in the storm situation, whereas the impact of the gulf ring is more pronounced for swell.

The value of taking account of current effects in wave models has been put in doubt, especially given the reason that modelled current fields are not yet good enough to take account of. But while waiting for better current fields and larger and faster computers, there is a good justification in studying further the interplay of waves, currents and winds. An increasing number of wave observations, more reliable measuring devices and numerical models have together given indications that the theories now used in the wave models to model sources and sinks for wave energy could be improved. Wave models are based on empirical studies, based again on early measurements. Now that we start to get longer time series of measurements, we see that the empirical formulae used to model energy sources and sinks as well as nonlinear wave-wave interactions could be improved, not only by tuning constants, but also in taking account of currents (among other things).

BASIC EQUATIONS. KINEMATICAL RESULTS.

A wave motion can be described by the form $a \cdot \exp(i\phi)$, where a is the wave amplitude and $\phi(r, t)$ is the phase function. The wavenumber k and the radian frequency σ are then defined in terms of the phase function:

$$\mathbf{k} = \nabla \phi \quad ; \quad \sigma = -\frac{\partial \phi}{\partial t} \quad (1)$$

so that the wave motion is described by $a \cdot \exp(\mathbf{k} \cdot \mathbf{r} - \sigma \cdot t)$.

Wave number and radian frequency are related to wave length L and wave frequency f or period T by

$$k = \frac{2\pi}{L} ; \quad \sigma = 2\pi f = \frac{2\pi}{T}$$

From (1) we have

$$\nabla \times \mathbf{k} = 0 \quad (2)$$

and the conservation of crest equation

$$\frac{\partial \mathbf{k}}{\partial t} + \nabla \sigma = 0 \quad (3)$$

This equation is a kinematical conservation equation for the density of waves. The rate of change of wave-number (the number of waves per unit length) is balanced by the convergence of the frequency, the number of wave crests passing per unit time, or the flux of waves.

The phase speed is given by

$$c_p = \frac{\sigma}{k} \quad (4)$$

and the group velocity is

$$c_g = \frac{\partial \sigma}{\partial k} \quad (5)$$

The dispersion relation relating the radian frequency to the wave number can be deduced from basic linearized hydrodynamic equations for an incompressible and nonrotational fluid, together with specific boundary conditions. For surface waves in water of depth d we have

$$\sigma^2 = g k \tanh k d \quad (6)$$

where g is gravity. For deep water ($k d \gg 1$) we get

$$\sigma^2 = g k \quad (7)$$

If the medium in which the waves are propagating is moving with a velocity $\mathbf{U}(X, t)$, the original waves described by $a \exp(i(\mathbf{k} \cdot \mathbf{x} - \sigma t))$ will be subject to a translation of coordinates such that $X = \mathbf{x} + \mathbf{U} \cdot t$, where X is a horizontal coordinate in a fixed frame of reference and x is a horizontal coordinate in a frame moving with the current

speed $\mathbf{U}(\mathbf{X}, t)$. In the fixed frame of reference, the absolute phase will be

$$\phi_a = \mathbf{k} \cdot (\mathbf{X} - \mathbf{U} \cdot t) - \sigma \cdot t$$

or rewriting

$$\phi_a = \mathbf{k} \cdot \mathbf{X} - (\sigma + \mathbf{k} \cdot \mathbf{U}) \cdot t = \mathbf{k} \cdot \mathbf{X} - \omega \cdot t$$

where

$$\omega = \sigma + \mathbf{k} \cdot \mathbf{U} \quad (8)$$

ω is the absolute frequency. The intrinsic frequency σ is the frequency seen by an observer moving with the current $\mathbf{U}(\mathbf{X}, t)$. Equation (8) is often referred to as the doppler equation, where σ is the doppler shifted frequency.

The group velocity in the fixed frame of reference becomes

$$c_{ga} = \frac{\partial \omega}{\partial \mathbf{k}} = c_g + \mathbf{U} \quad (9)$$

By this equation we can see that waves having in still water a given direction, will be subject to a change of direction "towards" the direction of the current (for those components which are not in the same direction of the current). The doppler equation shows also that in case of counter-current, the frequency in the fixed frame of reference will be smaller than in the frame moving with the current (that is, wave periods become longer). Conservation of crest equation becomes

$$\frac{\partial \mathbf{k}}{\partial t} + \nabla \omega = 0 \quad (10)$$

Combinations of the above equations and simplifications for ideal cases can give educative solutions. For example, for stationary conditions, equation (10) becomes

$$\nabla \omega = \nabla \cdot (\sigma + \mathbf{k} \cdot \mathbf{U}) = 0 \quad (11)$$

From this equation, as described in Phillips (1980), we can see that waves which initially propagate in a medium at rest and then enter a moving medium, will have a longer wave period (in the absolute frame of reference) in the counter current than in the region without current.

Another way of combining these equations leads to the so called ray equations, see for example Mathiesen (1985), which are a set of ordinary differential equations for

respectively the position vector \mathbf{r} , wave number \mathbf{k} and wave frequency ω as functions of depth, current speed, σ and \mathbf{k} .

The method of integrating ray equations along the wave paths (rays) has been widely used to show convergence zones along coastal areas or in shallow regions. Dynamics are usually taken care of by conservation of the wave action $A(\mathbf{k}, \mathbf{x}, t) = F(\mathbf{k}, \mathbf{x}, t)/\sigma$, F being the local wave energy density (see for ex. Phillips, 1980, Mathiesen, 1985)

$$\frac{\partial A}{\partial t} + \nabla \cdot [(\mathbf{c}_g + \mathbf{U}) \cdot A] = 0 \quad (12)$$

which reduces to the equation for conservation of energy

$$\frac{\partial F}{\partial t} + \mathbf{c}_g \cdot \nabla F = 0 \quad (13)$$

when there is no current and no depth refraction.

The difference between the kinematical point of view and the more dynamical interpretation used in wave models is that the right hand side of these conservation equations are not zero. Rates of change of energy or wave action are dependent of wind input, energy dissipation and non-linear wave-wave interactions. To the authors knowledge, the wave model by Tolman discussed hereafter was the first full wave model taking account of current effects. This model is though only a tool to get closer to understanding the effects of currents in a growing sea. Hopefully, with more reality than pure kinematics.

DESCRIPTION OF MODEL.

The wave model used in this work is made by Tolman (1990) and is using same theory as in the third generation wave model WAM (The WAMDI group, 1990). Numerical schemes are different, and currents are taken into account both in the propagation and in the wind input term. The driving equation in the model, with all terms included, is the wave action conservation equation:

$$\frac{\partial A}{\partial t} + \nabla \cdot [(\mathbf{c}_g + \mathbf{U}) \cdot A] + \frac{\partial}{\partial \omega} (c_\omega \cdot A) + \frac{\partial}{\partial \theta} (c_\theta \cdot A) = \frac{S}{\sigma} \quad (14)$$

where

$A(\omega, \theta, \mathbf{x}, t) = F(\omega, \theta, \mathbf{x}, t)/\sigma$ is the wave action
 $F(\omega, \theta, \mathbf{x}, t)$ is the 2 dimensional (frequency-direction)
variance density spectrum

- c_g is energy/action propagation velocity in x_1 - x_2 space
 (frame of reference moving with the current velocity U)
 c_θ is propagation velocity in the direction space
 c_ω is propagation velocity in the frequency space
 S is the source and sink functions for wave variance.

$$c_g = \frac{\partial \sigma}{\partial k} = n \cdot \frac{\sigma}{k} \quad \text{with} \quad n = \frac{1}{2} + \frac{kd}{\sinh(2kd)} \quad (15)$$

The 2nd term on the left side of the wave conservation equation (15) includes depth and current shoaling due to spacial variations of $(U+c_g)$ in the propagation direction of wave energy.

The 3rd term represents refraction.

$$c_\theta = \frac{d\theta}{dt} = -\frac{1}{k} \left[\frac{\partial \sigma}{\partial d} \frac{\partial d}{\partial m} + \mathbf{k} \cdot \frac{\partial U}{\partial m} \right] \quad (16)$$

where m is the coordinate perpendicular to the propagation direction of wave energy θ . The change of direction is represented here by a transport of wave action in the θ -space.

The 4th term represents the change of absolute frequency due to instationarity of currents and depth (in case of tidal variations).

$$c_\omega = \frac{d\omega}{dt} = \frac{\partial \sigma}{\partial d} \frac{\partial d}{\partial t} + \mathbf{k} \cdot \frac{\partial U}{\partial t} \quad (17)$$

In this work, $c_\omega = 0$ because of constant currents and depths.

On the right hand side of equation (15), we have the source function :

$$S(i, x, t) = \text{Sin}'(i, x, t) + Sds(i, x, t) + Snl(i, x, t) \quad (18)$$

where $i = (\omega, \theta)$. For brevity of notation the dependence of F and S on x and t are omitted in the following. The three source functions are a wind input source term (Sin'), a dissipation term (Sds) and a term that takes care of the nonlinear interactions (Snl). The wind input source term is an expression for the exponential wind growth based on Miles theory and on the observations of Snyder et al (1981), rescaled with friction velocity U_* (Komen et al, 1984, WAMDI group, 1988). Without current it has the form:

$$\sin(i) = 0.25 \rho_r [28.U_*/(\sigma/k).\cos(\theta-\theta_w)-1].\sigma F(i) \quad (19)$$

with $U_* = U_{10} \cdot [0.8 + 0.065 \cdot U_{10}] \cdot 10^{-3}$ (20)

U_{10} is the wind speed at 10m above the water surface, θ_w is its direction, and ρ_r is the relative density between air and water (ρ_a / ρ_w).

The current influence is taken into account by replacing U_{10} in the above equation by a wind speed (U_{10r}) relative to the coordinate system moving with the current, that is,

$$U_{10r} = U_{10} - U \quad (21)$$

Dissipation takes place by wave breaking and white capping as well as by bottom friction. The source term taking care of this is the same as in the WAM model (see f.ex Tolman, 1990). The nonlinear source term is also the same. At this stage, little is known about the current effect on these energy "sources", so the source terms are put in the equations without any changes.

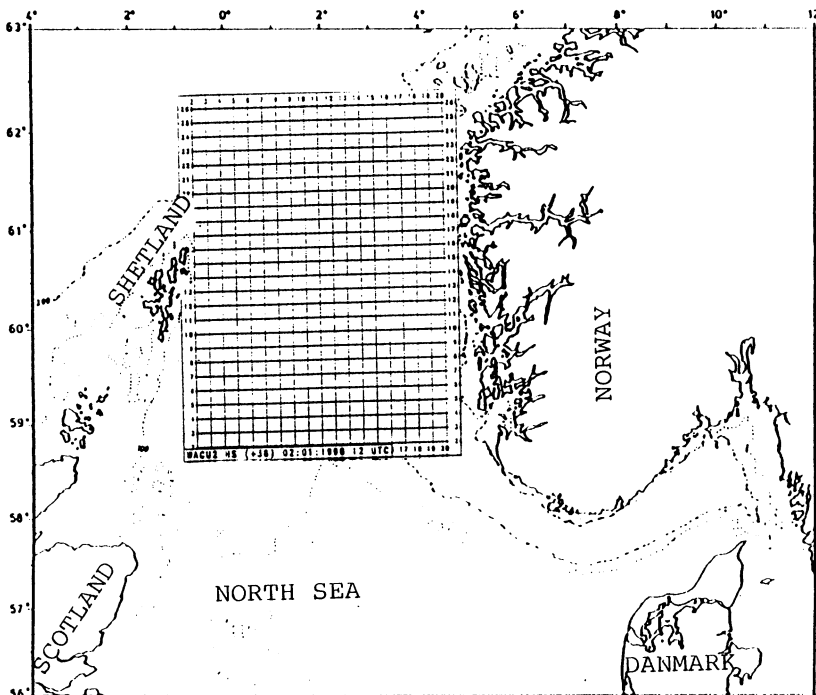


Figure 1 Dimensions of the model grid compared to the North sea.

MODEL SETUP

In view of implementing this model to the North Sea Basin and looking for effects of the Norwegian coastal current, the model was tested on a square grid. Dimensions of the grid basin compared to the North Sea can be seen in figure 1. Spacial resolution is 15km, total lengths of the basin are 300 and 390 km.

The current applied is uniform in the y direction (North), but is a function of x (west-east direction) (see figure 2). There is no current in the western part of the basin, while it is either +1 or -1 m/s within the simulated coastal current. The current gradient is linear, with a variation from 0 to 1 m/s over 2 grid intervals (30 km).

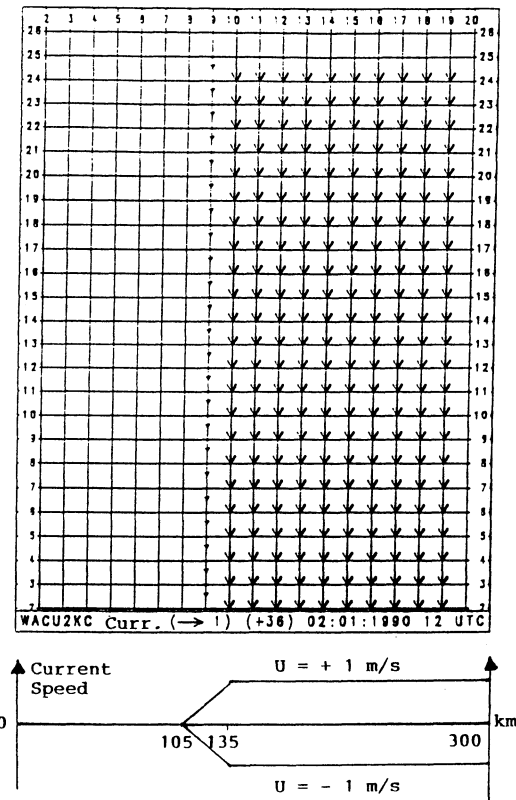


Figure 2 The model grid with arrows of the counter coastal current case. Bottom, plot of the two different coastal currents applied (speed across the basin). The current is constant northward.

Input to the grid is a constant wind over the basin during 36 hours, from southwest, showing the growth of waves from 0.9 meters to approximately fully developed sea.

Results from the two current situations are compared to results from a run without any current. The propagation of swell in this basin with and without the 2 types of current is also investigated, showing expected kinematical results. Comparison indicates the relative effects of kinematics and dynamics in windsea-current interaction. The effect of using a relative wind speed is also investigated.

A description of the model runs is summarized in Table 1.

Table 1. Run specification.

Name	Nx	Ny	Lx	Ly	Δx	Δt	T	U=	U=	U_{10}/DD	B.C.	Dynamics included?
			km	km	km	sec	hrs	-1m/s	+1m/s	m/s deg.	HMO/DDM	
Run0	21	27	300	390	15	600	36	-	-	0	2.3/ 45°	No
Run0c	=	=	=	=	=	=	=	x	-	0	=	No
Run2	=	=	=	=	=	=	=	-	-	14.1/45°	0.9/ 45°	Yes
Run2k	=	=	=	=	=	=	=	-	x	=	=	Yes
Run2kc	=	=	=	=	=	=	=	x	-	=	=	Yes
Run1kc	=	=	=	=	=	=	=	-	-	U_{10r}	=	Yes

Δx , Δt : space and time steps in the model

T : Total integration time

Lx, Ly : Dimensions of the basin

U : current speed, with a negative sign indicating a counter current to incoming or produced waves.
The spacial distribution of the current is indicated in Figure 2.

U_{10} : wind speed

U_{10r} : =14.9m/s : relative wind speed (equation 21).

DD : wind direction (meteorological convention).

B.C. : Boundary Conditions

HMO (Hs) : significant wave height

DDM : mean wave direction (oceanographic convention).

The east boundary is land, and there is deep water (depth = 1000m) elsewhere.

The names of the runs are used in plots.

As initial conditions, a wave spectrum is given for all sea grid points at time zero. At the boundary points, this initial condition is held constant during time integration. The spectrum given is the fully developed Pierson-Moskowitz spectrum, with mean frequency 0.3 Hz and 45° mean direction (same direction as the wind). Oceanographic convention is used for the current and wave directions (i.e. directions

they are travelling to). The significant wave height for the initial and boundary conditions is 0.9 m. The boundary conditions simulate in this way that waves with $HMO=0.9$ m continuously enter the area while there is a wind blowing over the basin.

RESULTS

Swell propagation.

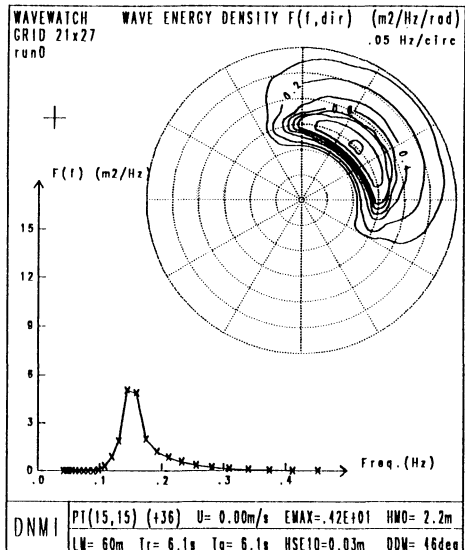
Before discussing the growing sea case, it is important to show what the model gives when waves only propagate through a given current field. To show this, the model is run with no wind, no source functions acting, and with boundary conditions constant with incoming waves of 2.3 m significant wave height, in the NE direction.

Figure 3.a. shows the 1- and 2-dimensional spectrum at grid point (19,23) for Run0, after 36 hours of time integration. Waves coming into the basin from 2 borders (south and west) go northeastward through the grid and are only subject to propagation. The fact that the eastern border is land gives a "slanting fetch" effect. That is, less energy is propagated from east compared to the west side at this grid point. Therefore, the wave mean direction gradually slightly changes downstream towards east (from 45 deg to 48 deg at this particular grid point). Significant wave height (HMO) is 2.1m, that is, the wave height is slightly reduced compared to the incoming waves because of the slanting fetch effect.

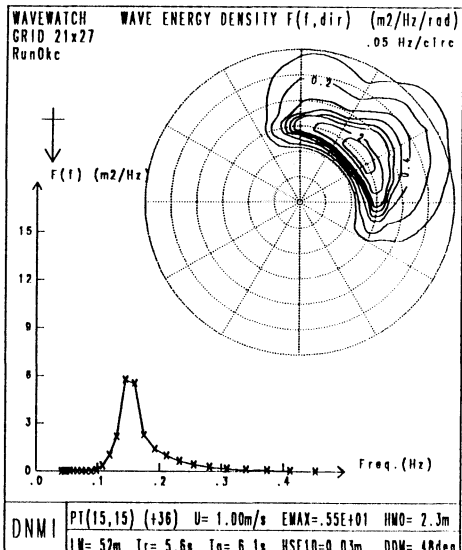
Figure 3.b shows 1-D spectra (D: dimensional) from run0 and run0kc (southward current), and the 2-D plot of the difference between each 2-D spectra. Parameters on the bottom of the figure refer to Run0kc. We see that the mean direction of the waves in the counter current case (southward current) has veered southward, to the right (49deg), which is the expected kinematical result: waves veer in the direction of the current. Wave height has increased by 10% compared to the no current run, wave length and relative period are reduced. The 2-D plot gives an idea of where in the frequency/direction space the energy has moved: Energy has in total moved to the right of the mean direction, and at the same time the energy has increased and spread out to lower and higher frequencies.

Full model equations:

When there is wind forcing, the picture is quite different. Figures 4(a-c) are similar to Fig 3.(a-b). Fig. 4.a shows the spectrum at grid point (15,15), the other two plots



(a)

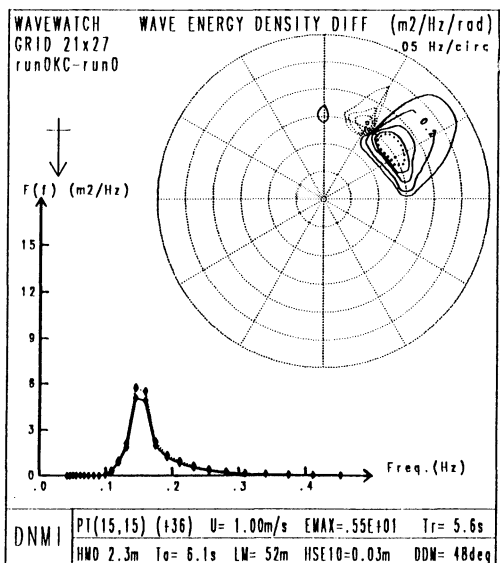


(b)

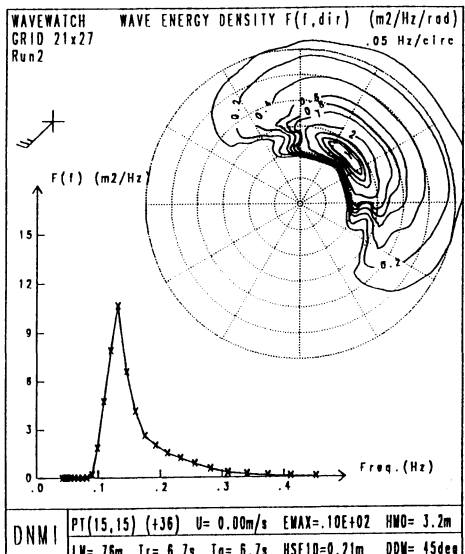
Figure 3 (a) (up, left) shows the 1-and 2-dimensional wave spectra at grid point (15,15) for Run0 (no wind, no current, only propagation). (b) (up, right) As for (a), for Run0kc showing the effect of a counter-current on a propagating swell. (c) shows the difference between the above 2-D spectra. Negative difference (loss of energy) are figured with dotted isolines, gain of energy with full lines.

Negative difference (loss of energy) are figured with dotted isolines, gain of energy with full lines.

Parameters given in the difference plot as well as the wind and current vectors (top left) refer to the first Run-name in the top left of each figure. Wave periods are given in the absolute (Ta) and relative (Tr) coordinate systems. Emax is the maximum energy density ($\text{m}^2/\text{Hz}/\text{rad}$) in the spectra. HsE10 is a wave height calculated from the energy at frequencies lower than 0.1 Hz. Mean wave direction is given in the oceanographic convention.



(c)



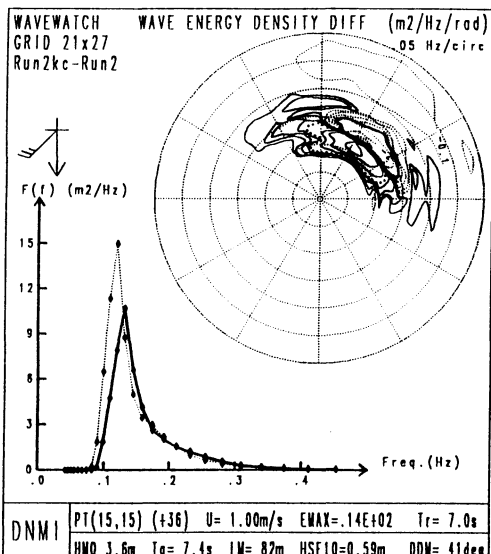
(a)

Figure 4

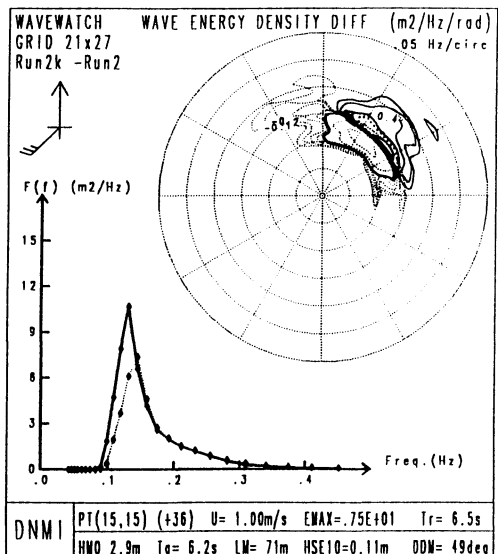
(a, left) 1-D and 2-D spectra at grid point (15,15) of Run2 (wind: $(u,v)=(10,10)\text{m/s}$) after 36 hours.

(b, bottom left) Effect of a counter-current on the 2-D spectra (difference of 2-D spectra). Negative differences (loss of energy) are figured with dotted isolines, gain of energy with full lines. 1-D spectra of run2 and Run2kc (reference run in full line (Run2))

(c) Difference between run with a "with"-current and without any current. Further details, see figure 3.



(b)



(c)

show the difference spectra of the runs with southward and northward current respectively (both compared to the no-current results as indicated in title in plot, f.ex. Run2kc-Run2). With no current, mean wave direction is 45° and significant wave height is 3.2 m. The 2-D plots at this point with either current cases are very similar to the plot with no current. That is why they are not shown here. The difference plot are much more interesting. We can see, especially compared to the swell case, that the energy is displaced in the frequency-direction domain in a quite different manner when there is wind, dissipation and non-linear interaction acting on the waves. The most interesting effect is that mean direction has veered in the opposite direction. The 2-D difference plot is much more diffuse than in the swell case. Energy has moved left (in counter current case), which means that energy has turned "upcurrent", in particular for frequencies higher than the peak frequency. That is: the dynamics in the model has overruled the kinematics.

Relative wind, no current refraction:

The above results indicate that the method of using a wind relative to the moving coordinate system in the input source function S_{in} may be responsible for the effects seen. An interesting question is if one could use a relative wind in a model to simulate the current effects instead of using the more costly way of implementing the current effect in the equations. The wind input in the model is given as

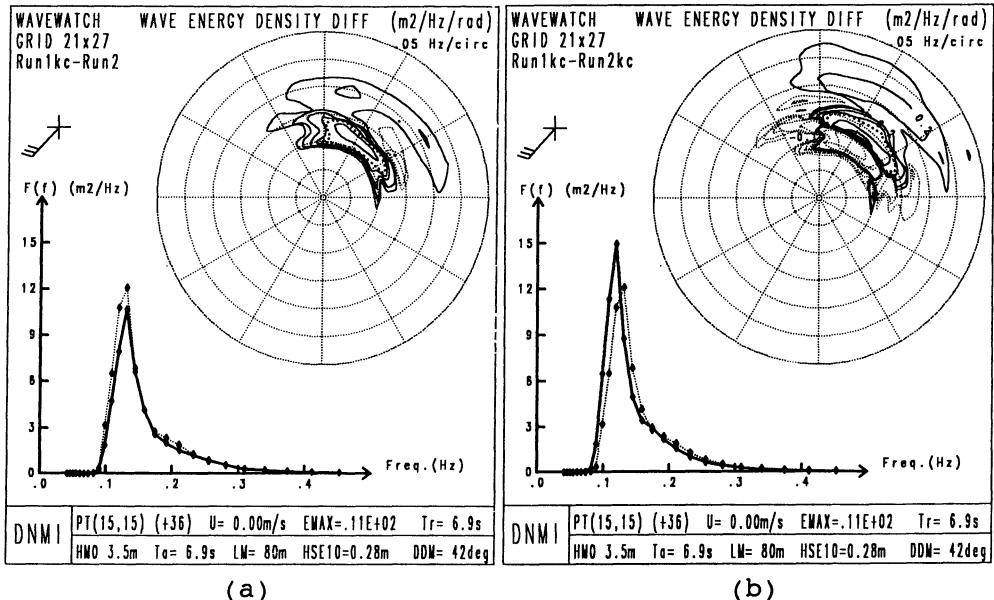
$$U_{10} = (u, v) = (10, 10) \text{ m/s.}$$

The relative wind $U_{10r} = U_{10} - U$ will in the counter-current of -1m/s have components:

$$\begin{aligned} u_r &= 10 - 0 = 10 \text{ m/s} \\ v_r &= 10 - (-1) = 11 \text{ m/s} \end{aligned}$$

So that the wind speed increases from $14.14 \text{ m/s } (= (10^2 + 10^2)^{0.5})$ to 14.87 m/s ($= (10^2 + 11^2)^{0.5}$) and the wind direction changes from 45° to 42.3° in the meteorological convention. That is, a veering towards north.

The effect of the implementation method used for the wind can be seen in Figures 5(a-b). 2-D difference plots of the run at grid point (15,15) show comparison between the relative wind run (Run1kc) and the run with no current (Fig. 5.a), and between Run1kc and the run with a counter-current Run2kc (Fig. 5.b).



Figur 5 (a) Difference between spectra at point (15,15) between Run1kc and Run2, showing effect of intensified wind speed but without any current refraction. (b) Difference between Run1kc and Run2kc, showing effect of current refraction on the spectrum.

The wind arrow in the top left corner shows that the wind has increased and there is no current applied in Run1kc. The method of changing the input wind by applying the source functions in the moving coordinate system seems to cause the wave direction change observed in the counter-current case. The total energy is approximately the same (3.5 m and 3.6 m) but the distribution of energy in the frequency domain is quite different. The conclusion for this test is that energy for lower frequencies would be underestimated if relative winds are used with no current refraction. Run2kc, with current effects, gives about 8% longer wave periods than the runs without currents.

Table 2 summarizes the parameters at grid point (15,15) after 36 hours with the different runs in this test, that is: swell propagation, wind sea with and without counter-current and run with relative wind speed.

Table 2. Wave parameters at grid point (15,15) for different runs. HsE10 is a "wave height" calculated from the wave spectrum at frequencies above 0.1 Hz.

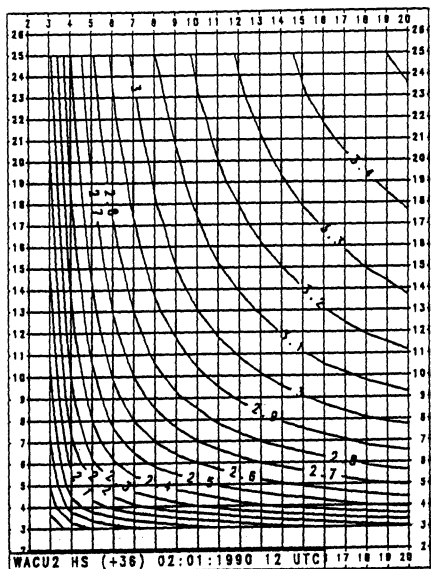
	U10 m/s	U m/s	Hs m	HsE10 m	Tr sec	Ta sec	Lm m	DDm deg
Run0	0	0	2.2	0.03	6.1	6.1	60	46
Run0kc	0	-1	2.3	0.03	5.6	6.1	52	48
Run2	14.14	0	3.2	0.21	6.7	6.7	76	45
Run2k	"	+1	2.9	0.11	6.5	6.2	71	49
Run2kc	"	-1	3.6	0.59	7.0	7.4	82	41
Run1kc	14.87	0	3.5	0.28	6.9	6.9	80	42

Figures 6 (a,d and g) show contours of significant wave height (isolines every .1 m), mean wave period (isolines every .1 sec) and mean wave length (isolines every 2 m) in the model basin (in the absolute coordinate system) with the given wind after 36 hours in Run2. Figures 6 (b,e and h) show the differences in these parameters after runs with current refraction (Run2kc, southward current case), and Figures 6 (c,f and i) show the equivalent (Run2 as reference) when running the model with relative winds and no current refraction.

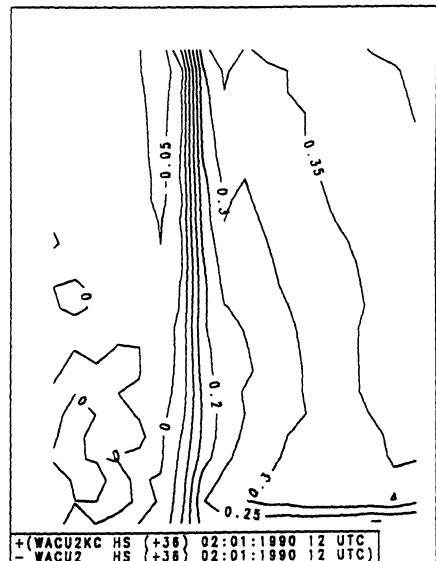
In the NE corner of the basin, the wave height has increased from 3.5 m in the run with no current with .4 m in Run2kc and with approximately .33 m in Run1kc. The difference is not very significant compared to measuring errors, but the mean period and wave lengths are almost not changed in run1kc which simulates an equivalent current.

We see that a counter current of 1m/s increases significant wave height, mean period and mean wave length with about 10%. Relative winds increase wave height with about 8% (roughly), wave periods less than 3% and wave length with about 6%.

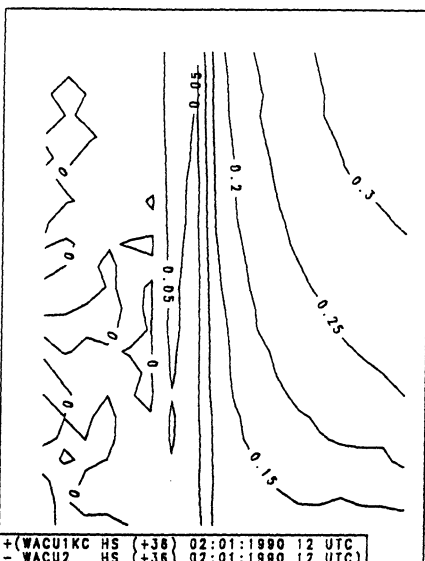
Figure 7.a and b show mean direction for grid line 23 (330 km north), across the basin, for different runs. Fig.7.a demonstrates direction changes for the swell propagations. The mean wave direction is around 45° across the basin, but is weekly influenced by slanting fetch effects as the wave direction increases slightly towards east in the eastern part of the basin (when DDM increases from 45°, the direction veers from NE towards E). But when swell is propagated trough the region with a counter current present, a direction change of 10° is observed in the current gradient region, while well within the coastal



(a)

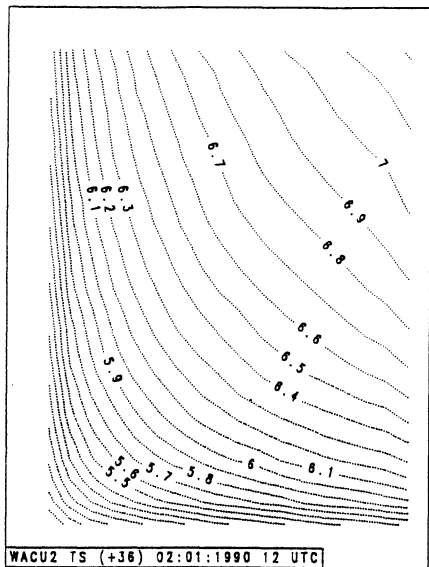


(b)



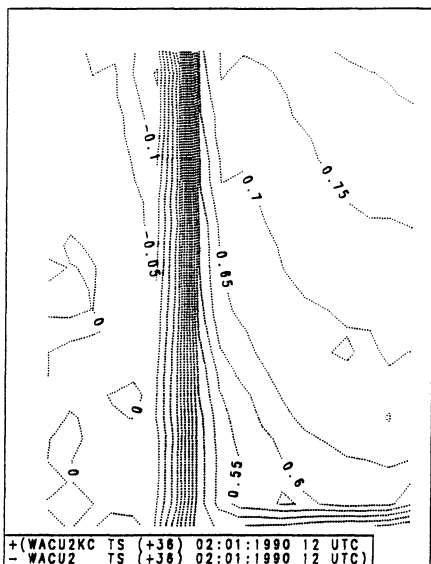
(c)

Figure 6 (a) Surface map with contours of significant wave height (HS) after 36 hours of model run with constant wind speed 14.1 m/s from South West. (b) Differences in HS between the run with Southward current and the reference run without current (Run2kc - Run2). (c) Differences in HS after a run with a "relative wind speed" and no current refraction.

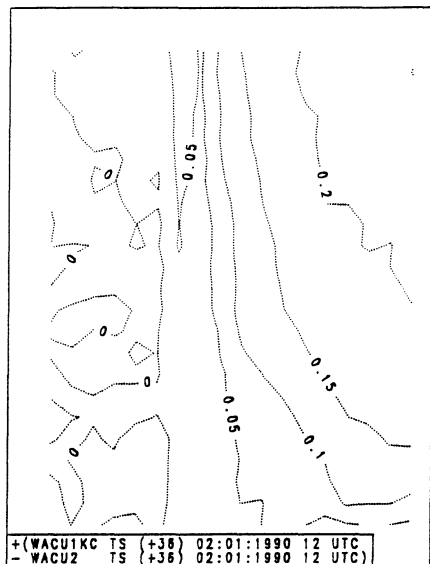


(d)

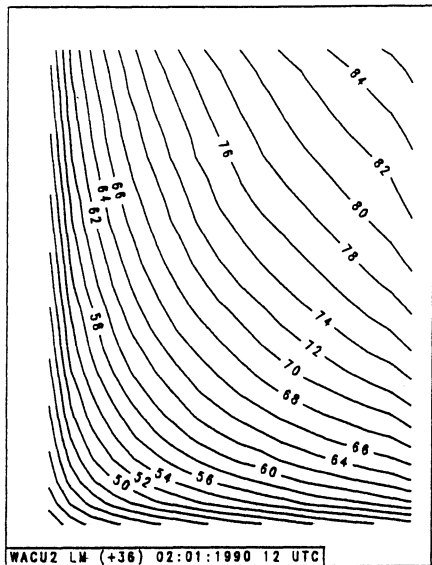
Figure 6 (d-f) Same as for (a-c) but showing the absolute mean wave period.



(e)

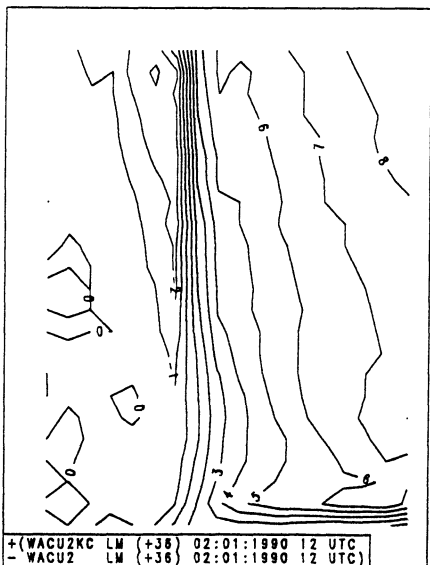


(f)

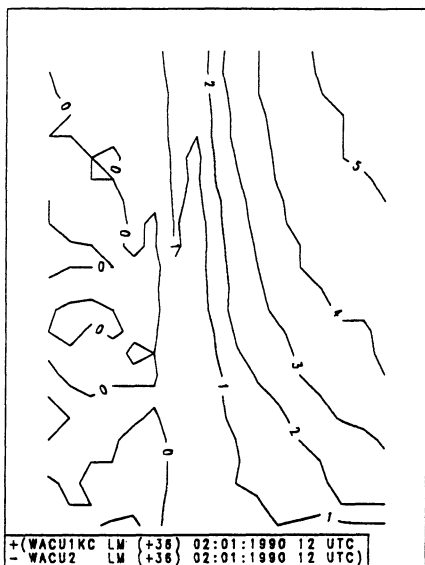


(g)

Figure 6 (g-i) Same as for (a-c) but showing the mean wave length.

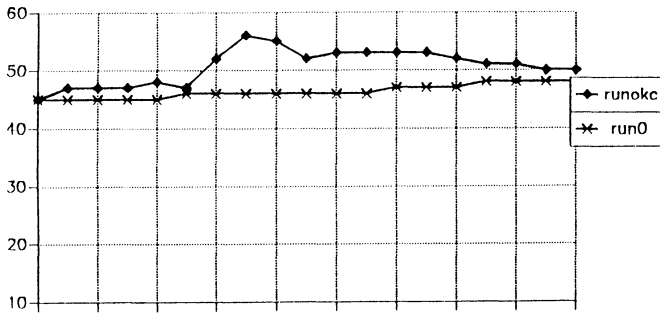


(h)

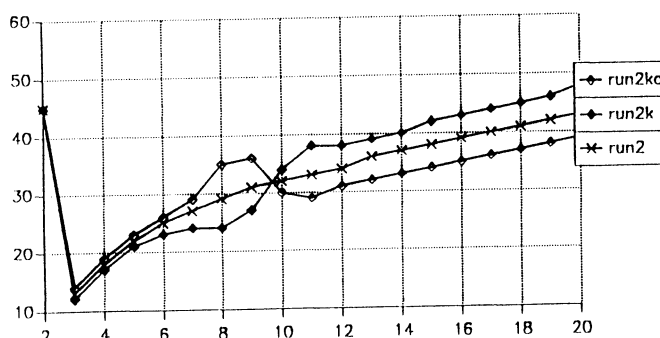


(i)

current, slanting fetches again take over slowly.



(a)



(b)

Figure 7 Mean wave directions across the basin at grid line 23 (330 km north) (a) Only propagation cases: Run0 and Run0kc. (b) Wind driven sea cases: Run2, Run2kc and Run2k.

Fig 7.b shows the refraction when there is wind wave growth in the case of both following and counter current. The center line is the mean wave direction across the basin, and we see it is very influenced by slanting fetch. The boundary condition at grid line 2 (west boundary) is demonstrated here with a mean direction of 45° , but because more energy comes from the right hand side of the wind direction after the wind has blown towards NE during 36 hours, the mean direction of waves near the east boundary is northward. Nevertheless, relative comparison with the mean direction across the basin in the 2 current cases show

interesting results. We see that the direction veers as with only propagation in the model (Fig.7.a) in the current gradient region. But within the "coastal current", the direction change is almost as due to the change of wind direction produced by the change of coordinates (using relative wind).

This is the most important result so far: It is seen that within the current gradient, kinematics are more important than dynamics, whereas the opposite prevails within the current region. A future paper is planned where a discussion about how large the impact (space and time relaxation) from the frontal zones of currents can be.

CONCLUSIONS

The series of numerical wave model runs have demonstrated that currents of the order of 1 m/s indeed have considerable impact on the growth of waves. The differences in significant wave height are of the order of 10%, for absolute wave periods and wave lengths a little less. The change of direction is not large in these runs, only 10°, which is hardly measurable by standard measuring devices. These effects might though have considerable impact if we have an increasing wind situation. The wave growth is dependent on the actual wave spectra. In a strong current, the spectra can be changed and consequently the wave growth. Further study is required to analyze this effect.

Nonetheless, this study has demonstrated effects in the gradient zone that are very interesting. The example shown here shows a refraction effect as is expected by standard kinematical results, but only limited in the gradient zone. Outside, the dynamics take over. Further study on the extent of the gradient effect is under progress. Results are probably valuable for the understanding of SAR imaging of ocean waves from space.

REFERENCES

Komen, G.J., S. Hasselmann, and K. Hasselmann (1984) "On the existence of a fully developed windsea spectrum", Journal of Physical Oceanography, 14, 1271-1854.

Jonsson, Ivar G. (1990) "Wave Current Interactions". The Sea: Ocean Engineering Science, Vol.9, Chapt. 3. Wiley & Sons.

Phillips, Owen M. (1980) The Dynamics of the Upper Ocean. 2nd edition, Cambridge University Press.

Mathiesen, Martin (1985) "Computer Modelling of Depth and Current Refraction" Report No. STF60 A85067, Norwegian Hydrotechnical Laboratory, Trondheim, Norway.

Mei Chiang C. (1989) The Applied Dynamics of Ocean Surface Waves, Advanced Series on Ocean Engineering - Volume 1, World Scientific, Singapore.

Tolman, Hendrik (1989) "The Numerical Model WAVEWATCH: a third generation model for hindcasting of wind waves on tides in shelf seas". Communications on hydraulic and geotechnical engineering. TU Delft, Report no. 89-2.

Tolman, Hendrik (1990) "The influence of Unsteady Depths and Currents of Tides on Wind-Wave Propagation in Shelf Seas" Journal of Physical Oceanography, Vol. 20, No. 8.

WAMDI group, (1988): The WAM model - A third generation ocean wave prediction model, J. Phys. Oceanography. 18, 12, 1775-1810.

ACKNOWLEDGEMENTS

This work is funded by the norwegian research foundation NAVF for a Phd thesis. Numerical calculations were performed on the IBM 3090 at IBM's scientific centre in Bergen. I am indebted to Hendrik Tolman who gave me his model for research purposes.

UNCERTAINTIES IN PREDICTION OF WAVE KINEMATICS IN IRREGULAR WAVES

OVE T. GUDMESTAD¹ and SVERRE HAVER²

¹ Statoil a.s, Boks 300, 4001 Stavanger, Norway

² Statoil a.s, Ranheimsvn. 10, 7004 Trondheim, Norway

ABSTRACT

Irregular water wave kinematics have recently been measured in the wave flume at Norwegian Hydrodynamics Laboratories (NHL) in Trondheim, using Laser Doppler Velocimetry (LDV) equipment (Skjelbreia et al., 1989 and 1991). The use of Wheeler stretching theory to estimate water wave kinematics in irregular waves is recommended to represent the best fit to the measurements. Reviewing available literature on water wave kinematics, Gudmestad (1992) arrives at the same conclusion.

Uncertainties in the estimate of water wave kinematics is, however, shown to represent one of the main sources of uncertainties for the calculation of forces on slender structures like jackups in relatively deep water. The need to further determine the uncertainty in the water wave kinematics prediction is pointed out (Haver and Gudmestad, 1992).

The data from the NHL tank tests have recently been reassessed and revised estimates of the uncertainties in wave kinematics are presented. Both the deviation from Wheeler theory and the spreading of the results have been estimated as function of depth below the surface. The influence of the revised estimates of the uncertainty in water wave kinematics on the overturning moment of a drag dominated structure is reviewed.

INTRODUCTION

In determining the response of offshore structures, it is of utmost importance to determine, in the most correct manner, all factors which contribute to the total force acting on these structures. Applying the Morison formula (Morison et. al., 1950) to calculate forces on offshore slender structures, uncertainties related to the understanding of the wave climate, the hydrodynamic force coefficients and the kinematics of ocean waves represent the most important contributions to the uncertainties in the prediction of the total forces on these structures (Haver and Gudmestad, 1992).

Traditional calculation of forces on offshore structures involves the use of regular waves with the following non-linearities incorporated

- use of regular wave theories incorporating higher order terms
- use of Morison equation having a nonlinear drag term
- inclusion of the effect of the free surface by integrating all contributions to total forces and moments from the sea floor to the free surface of the waves

In order to describe the sea more realistically, the ocean surface is to be described as an irregular sea surface represented by its energy spectrum. The associated decomposition of the sea surface is given as a linear sum of linear waves. The total force is found by integrating the contribution from all components in the wave spectrum to the free surface. The kinematics of each component must therefore be determined. It can easily be shown, however, that the higher frequency wave components obtain unrealistic high velocity values above the free surface when a linear Airy velocity profile is assumed (Gudmestad, 1990). This problem has been given particular attention by the oil industry which is constantly improving its models for calculation of forces on offshore structures.

A real sea surface may deviate from the Gaussian surface obtained from the superposition of Airy waves. The effect of a possible deviation from the Gaussian assumption is herein assessed by showing results for various values of the coefficient of skewness.

During the last years it has become evident that accurate prediction of the kinematics of ocean waves play an important role in reducing the uncertainty in the calculation of the loading on offshore structures (Bea et al., 1988 and Haver and Gudmestad, 1992). Of particular importance is the trend to go to very slender and more cost efficient jacket structures, like Statoil's Veslefrikk jacket, the trend to utilize jackups for increasingly deep water as well as the search for cost efficient complicant towers for very deep waters. These structures are all

drag dominated and the uncertainty in wave kinematics (wave velocity) prediction play an important role for safe and accurate design of these structures as shown in Fig. 1 (Litton and Mitwally, 1991).

KINEMATICS OF OCEAN WAVES

Regular water wave kinematics is normally predicted by use of linear Airy wave theory or one of the higher order classic wave theories (Skjelbreia and Hendrikson, 1960). Fenton (1985) has, however, pointed out that a consistent treatment of the mean fluid velocity under the waves should be given particular attention, and it can be argued that this effect is important in order to understand the measured kinematics under regular waves in a wave tank (Gudmestad, 1992).

The kinematics of each wave components in irregular seas can not, on the other hand, be predicted by linear wave theory as discussed in the Introduction. Several engineering approximations have therefore been suggested to describe the wave velocity in the irregular wave situation. Amongst the most common methods are (Gudmestad, 1992)

- Vertical extension to the wave crest of the velocity found by Airy theory at the mean water level (Vertical stretching of Airy theory)
- Wheeler stretching of Airy velocity (Wheeler, 1970)
- Use of a constant velocity gradient above the depth - Δ below mean water level (Delta stretching)

These approximations have all in common that they do not satisfy the Laplace equation nor the nonlinear boundary conditions at the free surface. These approximations cannot therefore fully represent the hydrodynamics of the flow problem. In this respect, a method proposed by Zhang (Zhang et al., 1991) whereby the nonlinear interaction between high and low frequency waves be taken into consideration, shows considerable promise for understanding of irregular wave kinematics.

State of art for prediction of kinematics (wave velocity) in irregular waves is at present represented by use of Wheeler stretching method. The selection of this method is supported by several measurement programmes in the open sea and in laboratory. A summary of recent literature and experiments is presented by Gudmestad (1992). Although the Wheeler stretching method is shown to best represent the kinematics of irregular water waves, all experiments show that this method may underpredict the kinematics somewhat around the free surface (Gudmestad, 1992). In order to design safe structures, it is therefore of major importance to estimate the uncertainty in the kinematics predicted by using the Wheeler method. Such uncertainty measures have been proposed by Bea (1990),

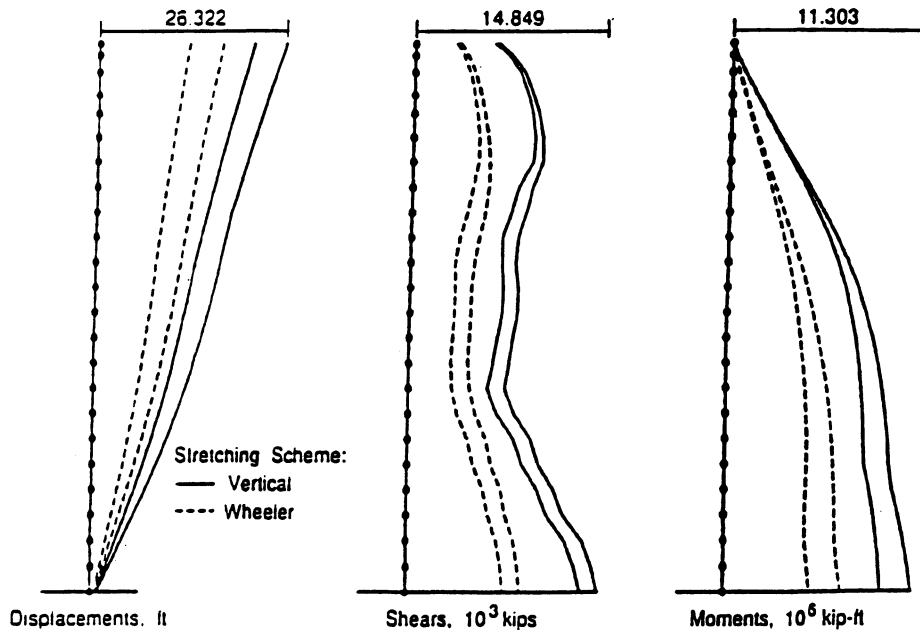


Fig. 1. Bounds of Maximum Displacements for a 2000 ft compliant tower using different stretching schemes. (Litton and Mitwally, 1991)

Table 1 Wave situations analyzed (Ref. Skjelbreia et. al., 1989, 1991)

Case	Type of wave	T_p (s)	H_s (m)	d (m)	H_s/gT_p^2	d/gT_p^2
3(I165a)	Irregular	1.65	0.17	1.3	0.0064	0.049
4(I165b)	Irregular	1.65	0.17	0.6	0.0064	0.022
6(I24)	Irregular	2.4	0.25	1.3	0.0044	0.023

Gudmestad (1992) and recently by Haver and Gudmestad (1992). Reviewing in details a series of measurements carried out at NHL, Trondheim (Skjelbreia et al., 1989 and 1991) we are, however, in position to present a more accurate prediction of the uncertainty of using the Wheeler method.

The Wheeler method represents a stretching of the wave velocity calculated at the mean water line by use of linear Airy theory to the free surface of the wave:

$$U_{wh}(z) = \omega A \frac{\cosh k \left(\frac{z + D}{1 + A/D} \right)}{\sinh k D} ; \quad z \leq A \quad (1)$$

where ω is the wave frequency, k is the wave number, D is the mean water depth and A is the wave crest height.

The wave velocity measurements at NHL, presented by Skjelbreia et al. (1989 and 1991), support the use of this method for each wave component within an irregular sea state. The NHL measurements of the wave velocity in a closed wave flume can be presented as shown in Figures 2, 3 and 4 for three wave situations (Table 1), where measurements of the horizontal velocity beneath the crests of the waves are compared to the predicted velocities found by the Wheeler method. A considerable scatter in the data is seen for all depths (location) under the wave crests within the flume.

The highest velocity values are associated with the highest wave crests. These highest values of the velocity give rise to the largest forces acting on an offshore structure. The mean of the highest measured velocity values are estimated from Figures 2 to 4 for each location where kinematics measurements were taken in the NHL measurements (Skjelbreia et al., 1991). The range of variation of the measurements are also estimated. All curves are shown in Figures 2 to 4. The range of variation plotted is suggested to represent ± 2 standard deviations for the measured data.

In the wave tank, a return flow will always occur from the beach of the tank. Although the return flow in the NHL experiments was estimated to be about 5% (Skjelbreia et al., 1989), the flow can influence the measured velocity values significantly. An estimate of the return flow is given in Figure 5 for wave case 6, (conf. Table 1). The estimated return flow is the differences between the average observed flow under the waves and the predicted average flow below the waves (Cieslikiewicz and Gudmestad, 1992). The mean value of measured kinematics and the range of variation have been adjusted to take into account the estimated return flow and the resulting estimates have been given by dotted lines in Figures 2 to 4.

Fig. 2 Measurement of horizontal velocity beneath crests compared against Wheeler's method for Case 3 (Table 1) of NHL's measurements (Skjelbreia et al. 1989, 1991).

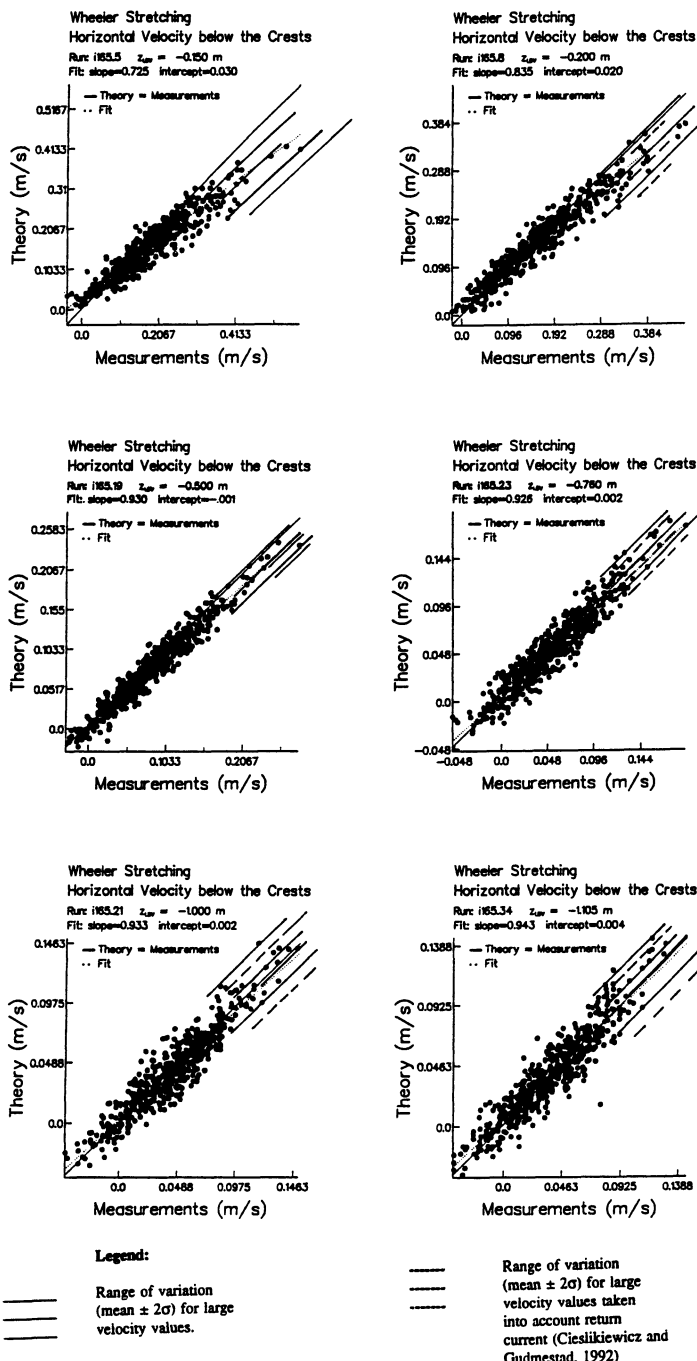


Fig. 2 Cont.

Measurement of horizontal velocity beneath crests compared against Wheeler's method for Case 3 (Table 1) of NHL's measurements (Skjelbreia et al., 1989, 1991).

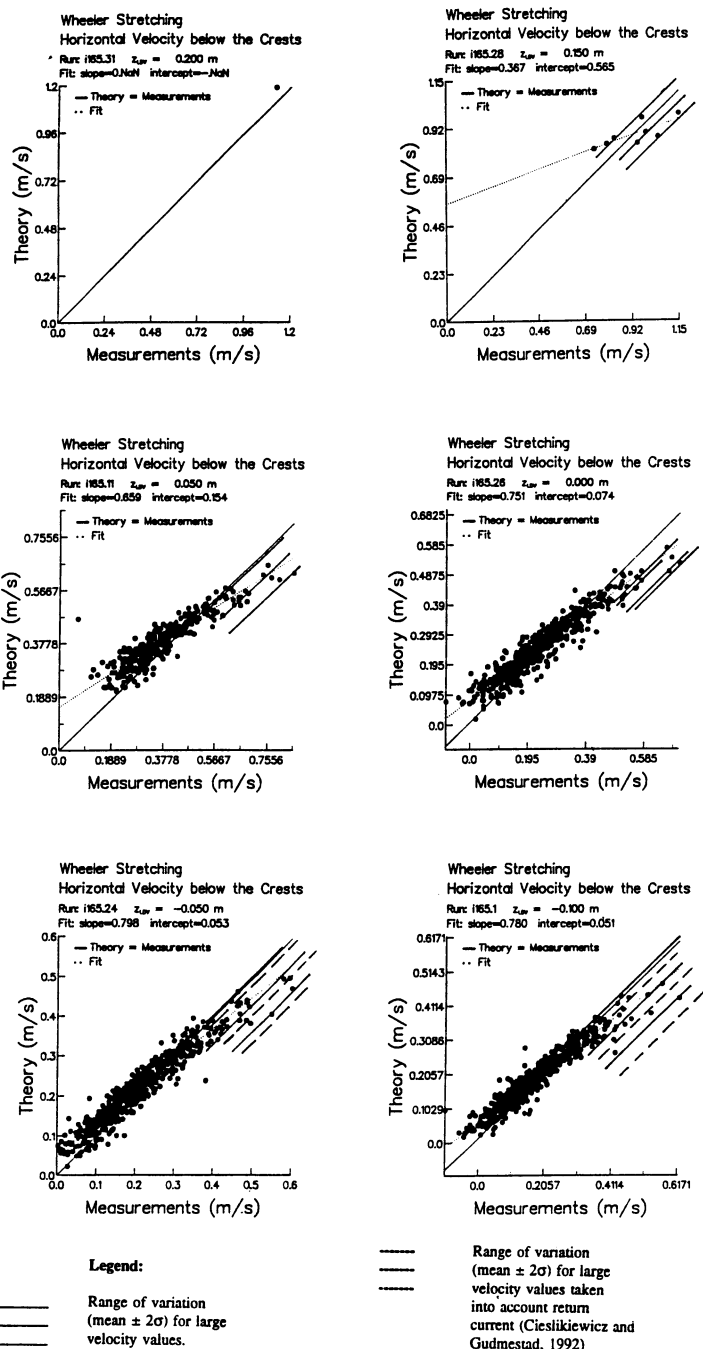


Fig. 3 Measurements of horizontal velocity beneath crests compared against Wheeler's method for Case 4 (Table 1) of NHL's measurements (Skjelbreia et al., 1989, 1991).

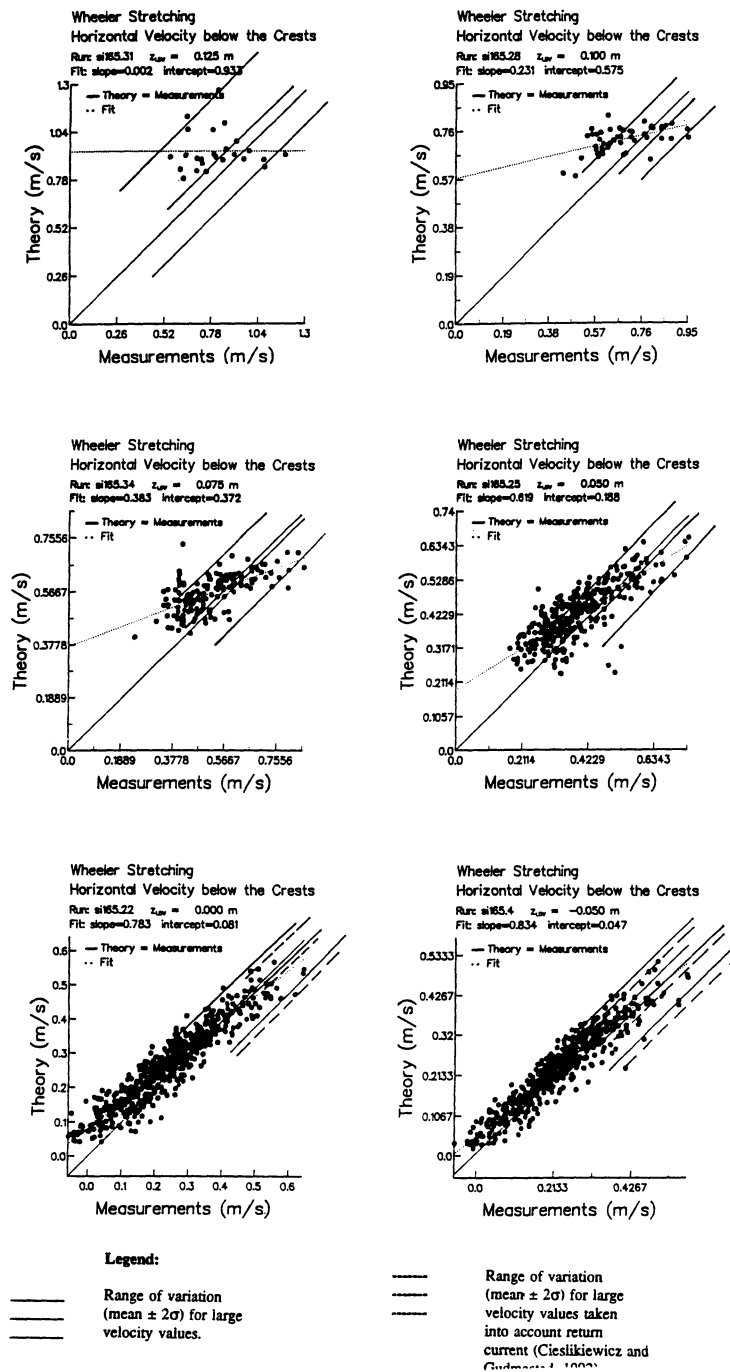


Fig. 3 Cont.

Measurements of horizontal velocity beneath crests compared against Wheeler's method for Case 4 (Table 1) of NHL's measurements
(Skjelbreia et al., 1989, 1991).

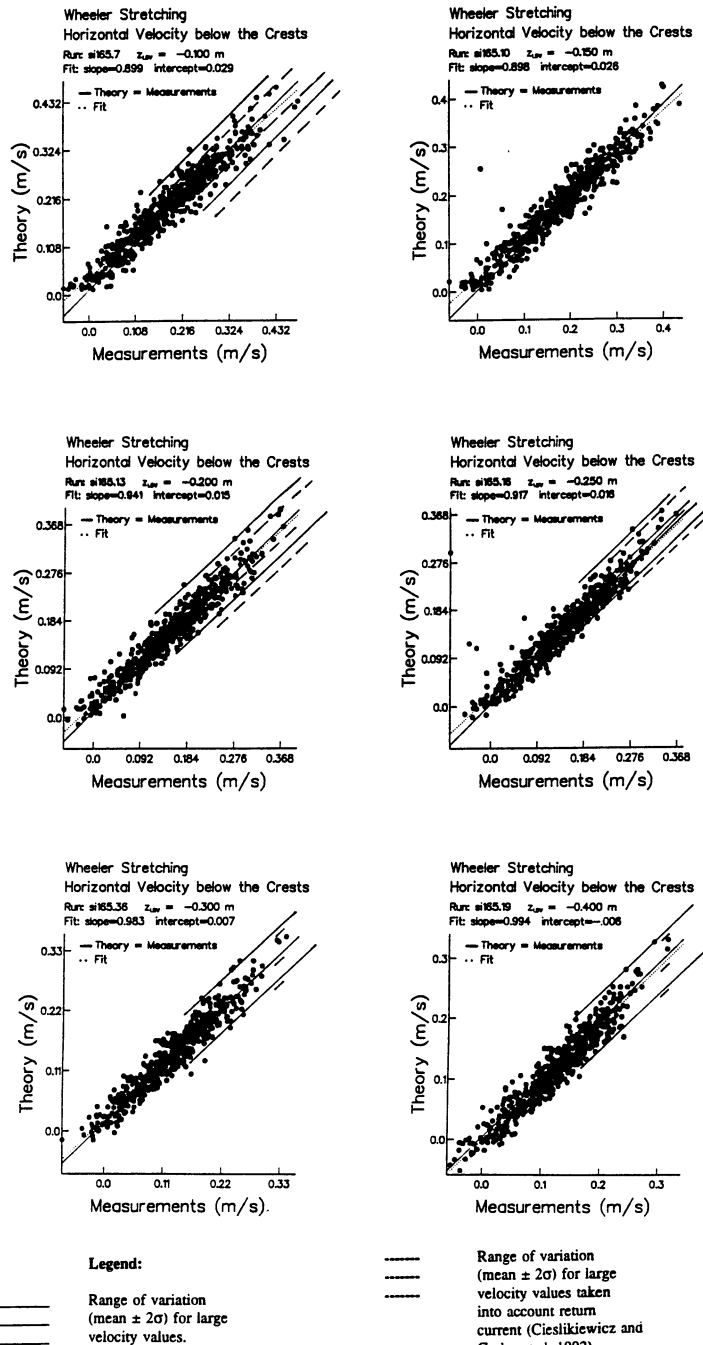


Fig. 4 Measurements of horizontal velocity beneath crests compared against Wheeler's method for Case 6 (Table 1) of NHL's measurements (Skjelbreia et al., 1989, 1991).

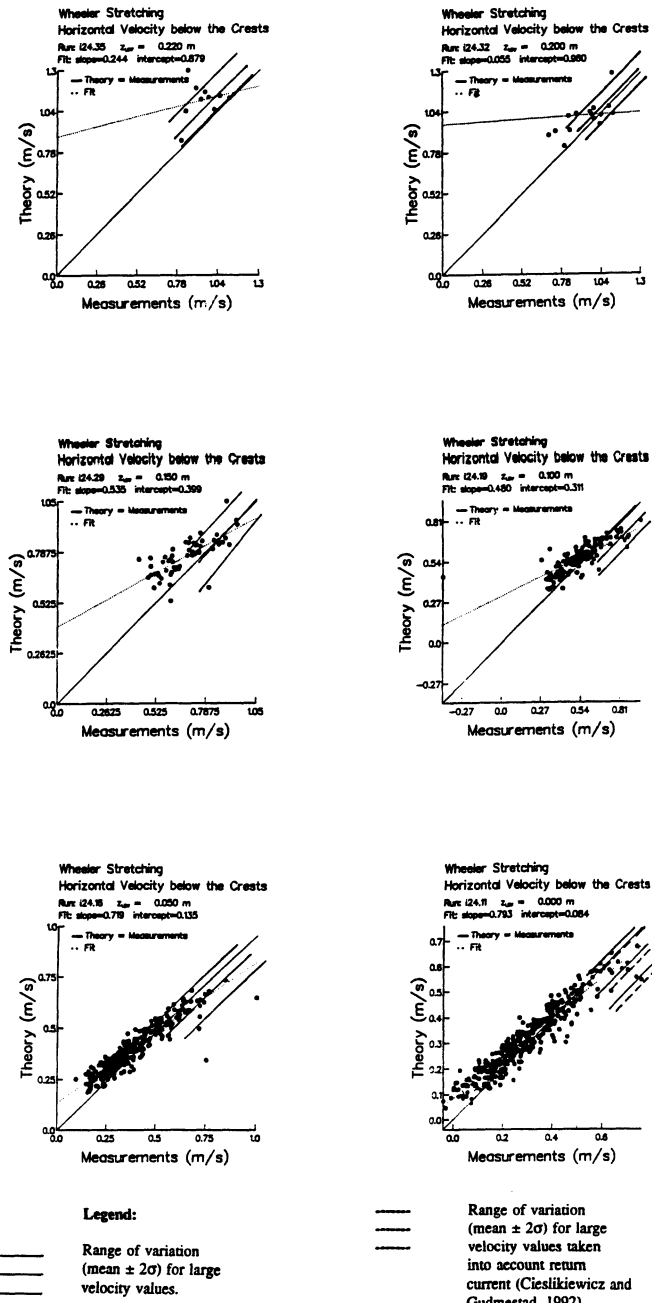
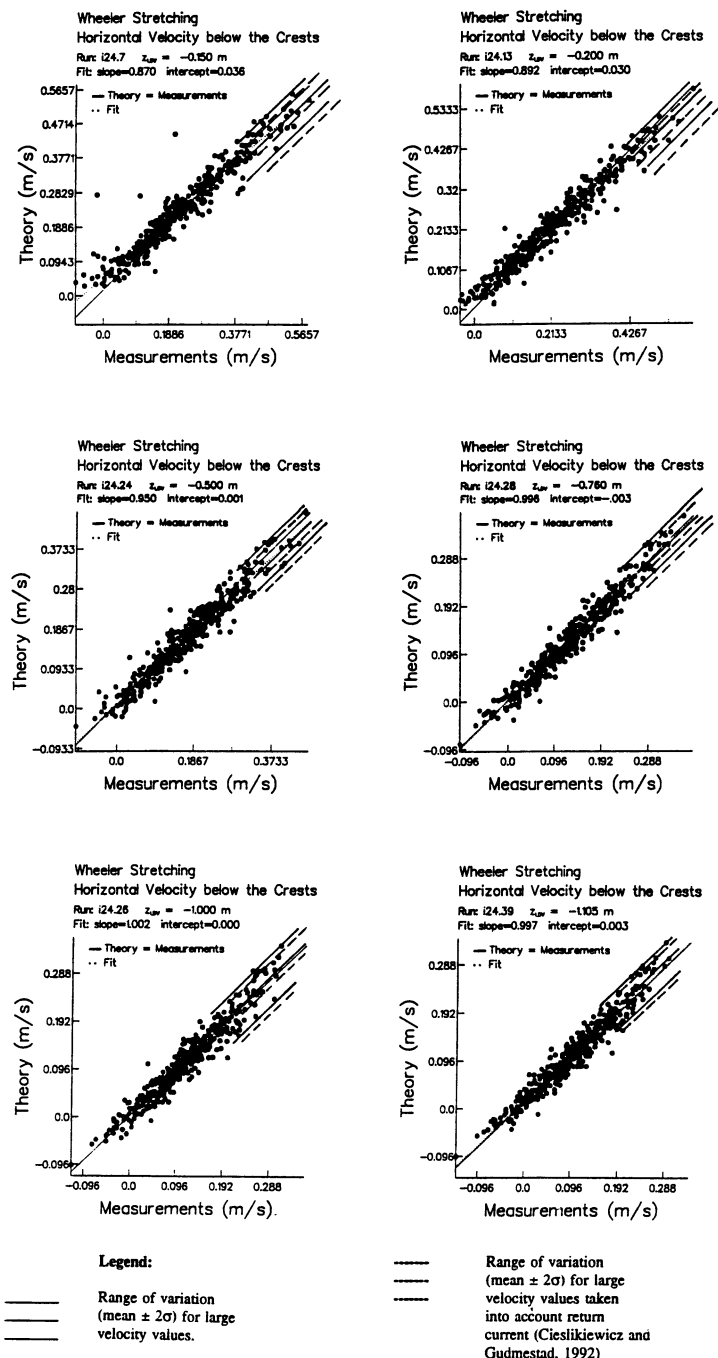


Fig. 4 Cont.

Measurements of horizontal velocity beneath crests compared against Wheeler's method for Case 6 (Table 1) of NHL's measurements (Skjelbreia et al., 1989, 1991).



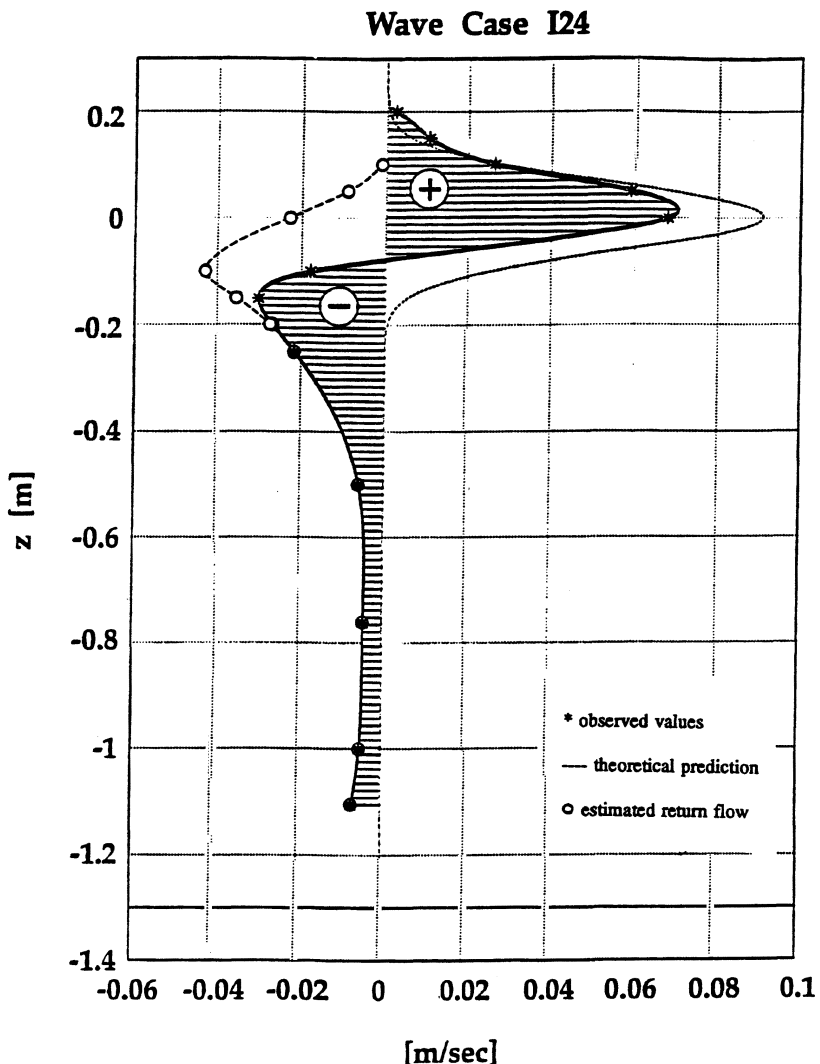


Fig. 5. Mean value of horizontal velocity as function of elevation z for Wave Case 6 (I24) of NHL's measurements. (Ref. Cieslikiewicz and Gudmestad, 1992).

Based on data from Figures 2 to 4, the ratios of the velocity estimated by the Wheeler method and the velocity measured have been plotted in Figures 6 to 8 for the wave cases under consideration. Note that the correction due to the return flow in the wave tank has been incorporated. From these plots, the following relation between the prediction of the Wheeler method and measurements of the velocity in the NHL tank is suggested for the wave cases considered;

$$\begin{aligned} w_f(z) &= 1.2 \left(1 + 0.16 \left(\frac{z}{D} \right) \right), \quad -D \leq z < 0 \\ w_f(z) &= 1.2 \left(1 - 0.16 \left(\frac{z}{A} \right) \right), \quad 0 \leq z \leq A \end{aligned} \quad (2)$$

with the range of variation given

$$2\sigma \sim 15 \text{ to } 20\%$$

$$\sigma \sim 7.5 \text{ to } 10\% \quad (3)$$

Further analysis of the NHL measurements (Skjelbreia et al., 1989 and 1991) should be done to confirm above formula. It is of particular interest to refine the formula for different wave steepness situations.

Although an accurate estimate of the uncertainty in applying the Wheeler stretching method is presented, this does not relieve us from continuous work to improve the understanding of wave kinematics. A particular effort should be carried out to develop theories which match with measurements and which are derived from the basic principles of hydrodynamics rather than from engineering approximations to the problem.

An attempt to correct the Wheeler stretching method to account for inconsistencies regarding fulfillment of hydrodynamic equations has been presented by Gudmestad and Connor (1986). Their Figure 1 indicates adjustments of the Wheeler theory as proposed by Equation (2) above.

EFFECTS OF WAVE KINEMATICS ON THE PREDICTED STRUCTURAL RESPONSE

The previous chapter has indicated that the Wheeler approach for calculation of wave kinematics appears to underestimate the horizontal particle velocity somewhat. A depth dependent correction formula, Eq. (3), is suggested together with a measure of the uncertainties related to the adequacy of the Wheeler method. In order to assess the importance of these kinematic-induced inaccuracies and uncertainties for structural load calculations, the overturning moment of a drag dominated structure is considered. With respect to effects of kinematic-induced uncertainties this should represent a worst case response quantity.

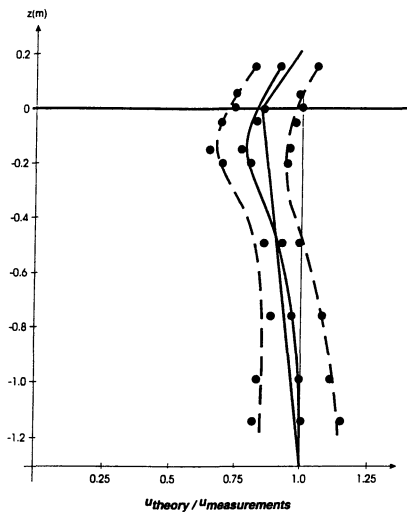


Fig. 6. Velocity as predicted by Wheeler method (u_{theory}) vs. measured velocity. Case 3 of NHL measurements (see Table 1).

○ measurements
 — mean
 --- mean $\pm 2\sigma$
 — suggested modification of Wheeler method (Eq. 2)

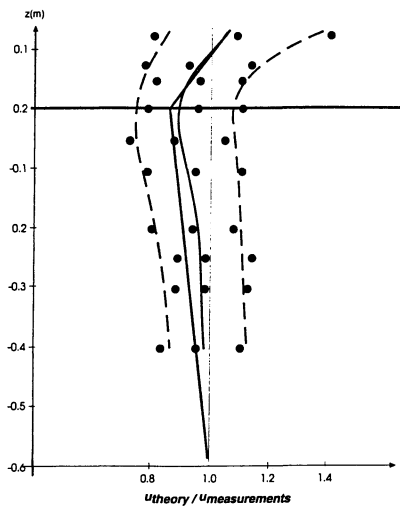


Fig. 7. Velocity as predicted by Wheeler method (u_{theory}) vs. measured velocity. Case 4 of NHL measurements, see Table 1.

+ measurements
 — mean
 --- mean $\pm 2\sigma$
 — suggested modification of Wheeler method (Eq. 2)

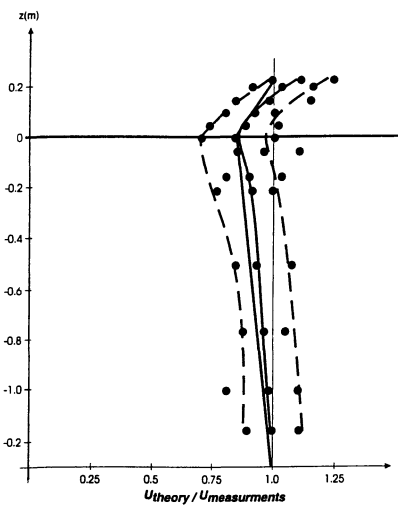


Fig. 8. Velocity as predicted by Wheeler method (u_{theory}) vs. measured velocity. Case 6 of NHL measurements, See Table 1.

○ measurements
 — mean
 --- mean $\pm 2\sigma$
 — suggested modification of Wheeler method (Eq. 2)

The hydrodynamic loading on the platform is approximated by first of all establishing an analytical expression for the overturning moment obtained for one vertical platform leg and, thereafter, a qualitatively representative load level

is obtained by scaling the one-leg-moment properly. The effect of wind is accounted for by calculating the overturning moment corresponding to a resulting wind exposed area of 1600 m². The center of gravity for the wind force is assumed to be 40 m above mean water level.

In connection with the calculation of the overturning moment for a single leg the following assumptions are made;

- the wave profile is locally modelled as a sinusoidal profile
- the wave induced speed (velocity) is calculated according to Wheeler's approach, Eq. (1). This speed is then modified by multiplying it with the depth dependent factor $w_f(z)$ given by Eq. (2).
- the current profile is linear with depth, i.e.:

$$u(z) = a_c + b_c z \quad (4)$$

The coefficients are given by;

$$a_c = (2 - c_c) \bar{u} \quad (5a)$$

$$b_c = 2 (1 - c_c) \bar{u}/D \quad (5b)$$

where \bar{u} is the depth averaged current speed and c_c is a coefficient specifying the part of the current profile which is modelled by a slab profile ($c_c = 1.0$ yields a uniform slab current profile).

Using the drag term of the Morison equation, (Sarpkaya and Isaacson, 1981), the hydrodynamic overturning moment (quasistatic) on a single pile is given by

$$M_{pile} = \rho r c_d \int_{-D}^A (w_f(z) U_{wh}(z) + a_c + b_c z)^2 (D + z) dz \quad (6)$$

where ρ is the density of the sea water, r is the leg radius and c_d is the drag coefficient.

The wind induced moment is herein calculated as follows;

$$M_{wind} = \frac{1}{2} c_p \rho_a \partial_p c_z^2 w^2 (D + h_{Ap}) \quad (7)$$

where c_p is a pressure coefficient, ρ_a is density of air, a_p is wind exposed area (projected), c_z is a height correction factor for the wind speed, w is the 1-hour mean wind speed at 10 m above mean sea level, and h_{Ap} is the height from the mean water level to the center of gravity for the wind force.

We aim towards a response level which is qualitatively representative for a jack-up type structure. A dynamic amplification factor is therefore applied to the hydrodynamic moment. The dynamic amplification factor is herein assumed to be given by;

$$DAF = \exp(a_{DAF} (t_o/T_p)^2) \quad (8)$$

where t_o is the natural period, T_p is the spectral peak period of the sea state and a_{DAF} is a proper amplification coefficient. Herein $a_{DAF} = 1.346$ is selected.

The resulting overturning moment is then given by;

$$M = c_{pl} DAF \cdot M_{pile} + M_{wind} \quad (9)$$

where 10.0 is adopted for the scaling factor, c_{pl} , between overturning moment on a pile and the platform overturning moment. The expression for M_{pile} after the solving the integral in Eq. (6) is simple but rather lengthy and it is therefore not explicitly included in the paper. The nice thing about the analytical expression is that we have a closed form expression between the overturning moment and the environmental and structural variables and coefficients that causes this moment. This makes it in principle rather easy to estimate the probability of exceeding various moment levels. Herein this is done by using the First Order Reliability Method - technique (FORM), see e.g. Madsen et al. (1986). The present application of FORM is very similar to the approach previously applied when estimating the base shear of a jack-up (Haver and Gudmestad , 1992).

The main assumptions of the present approach are that the annual largest overturning moment occurs as the annual largest wave passes the structure and, furthermore, that the annual largest wave occurs during the peak of the annual largest storm.

Assuming the sea surface to be modelled by a Gaussian process, the conditional distribution function for the largest wave during the storm peak given the storm

peak characteristics can be determined theoretically. The distribution functions for the storm peak characteristic of the annual largest storm can be estimated from measurements. Herein we will consider the wave conditions for the Statfjord area. Probabilistic models and corresponding parameters are given in Haver and Gudmestad (1992).

In this paper we will also demonstrate the effect of introducing a non-Gaussian sea surface. A non-Gaussian value for the wave crest is obtained by the Hermite transformation developed by Winterstein (1988). Herein a non-Gaussian sea surface is specified by introducing a positive coefficient of skewness instead of zero which is the Gaussian value. The coefficient of curtosis is kept at its Gaussian value. The actual transformation is also given by Haver and Winterstein (1990).

Another source of uncertainty that is compared to the uncertainties related to the wave kinematics is the current profile. The sensitivity to the current level is investigated by varying \bar{u} , while the sensitivity to the shape of the profile is considered by varying the coefficient c_c , see Eq. (5). The wind is assumed to be constant throughout this study.

NUMERICAL RESULTS

The numerical results are obtained using the storm wave climate described for the Statfjord area, Haver and Gudmestad (1992). The water depth for the platform location is selected to be 100 m. The depth is assumed to be deterministic. The wind is also kept constant and a value of 40 m/s is selected for the 1-hour mean wind 10 m above mean sea level. The various constants adopted for this study are; $\rho = 1026 \text{ kg/m}^3$, $r = 0.7 \text{ m}$, $c_d = 1.0$, $c_p = 1.0$, $\rho_a = 1.3 \text{ kg/m}^3$, $a_p = 1600 \text{ m}^2$, $c_z = 1.22$ and $h_{Ap} = 40 \text{ m}$.

At first the effects of the proposed speed correction factor, Eq. (2), are compared to various current formulations and to various formulations of the sea surface process with respect to skewness. The probability of exceeding large moment levels are shown for the different cases in Fig. 9. It is seen that the suggested speed correction, (Eq. 2), yields a stronger effect than does a shift from a slab profile for the current to a linear shear profile with a bottom speed being equal to one third of the surface speed. For the initial case the 100-year moment is seen to be 1950 MNm. By changing the current profile to a linear profile this value increases with about 10%. The speed correction, on the other hand, causes the 100-year value to increase by nearly 20%. It is also seen that the speed correction in effect corresponds to increasing the surface skewness from the Gaussian value (0.0) to a value in between 0.1 and 0.2.

The randomness in the moment shown in Fig. 9 is caused by the randomness in the wave conditions as this particular site (Statfjord). So far we have assumed that the various statistical parameters and physical coefficients are perfectly

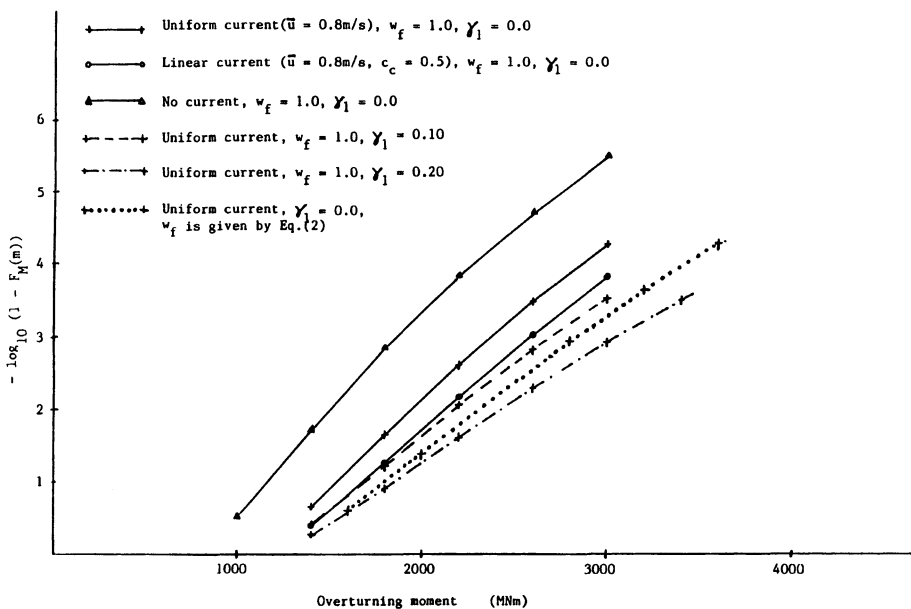


Fig. 9. Probability of exceedance for fixed parameter cases.

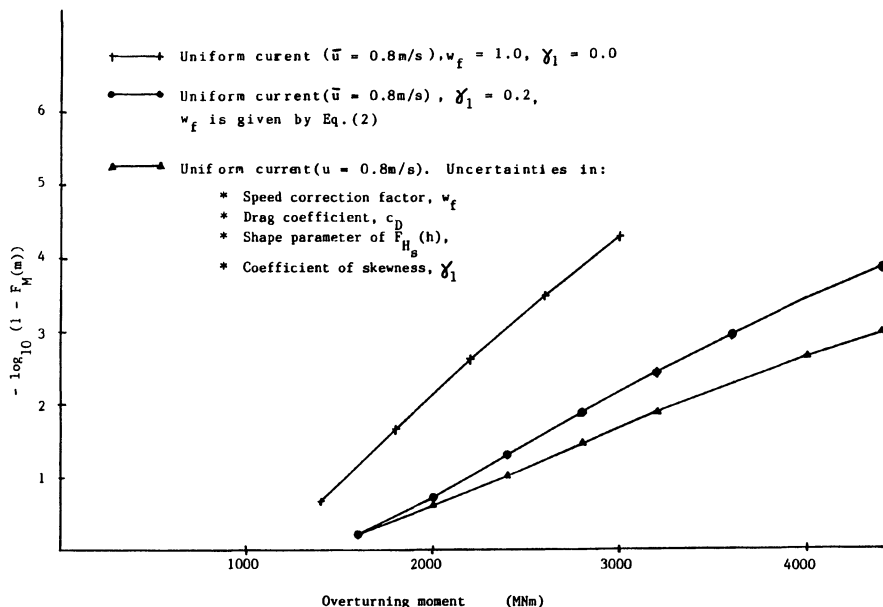


Fig. 10. Probability of exceedance for fixed parameters and uncertain parameters

known. In reality uncertainties are related to the chosen values and it is of some interest to see the effect of these uncertainties on the estimated exceedance probability. Furthermore, the FORM technique does also provide us with a measure of the relative importance of the randomness of the various variables and parameters/coefficients.

For the actual water depth the extreme sea state is likely to be significantly skewed. For the base case with fixed parameters a coefficient of skewness of 0.2 is therefore adopted. The resulting effect of both the skewness correction and the speed-correction factor (Eq. 2) is shown in Fig. 10. It is seen that these corrections increases the 100-year value by about 50%. Based on previous studies, Haver and Winterstein (1990) and Haver and Gudmestad (1992), we know which parameters are most important with respect to the effects of the associated uncertainties. These parameters are listed in Table 2 together with their respective mean and coefficient of variation. The properties of the speed correction factor, $w_f(z)$, is discussed in an earlier chapter of this paper, while properties of the shape parameter involved in the storm wave climate for Statfjord are given in Haver and Gudmestad (1992). The choice of characteristics for the drag coefficient, c_d , and the coefficient of skewness, γ_1 , is of course subjective. However, we expect these characteristics to reflect a reasonable level of uncertainties.

The effect of introducing uncertain parameters is demonstrated in Fig. 10. It is seen that the probability of exceeding a large level is increased by a factor in the range 4 - 10 depending on the moment level.

The relative importance of the various sources of uncertainties are given by Table 3. It is seen that the most important sources of randomness are the inherent randomness associated with variation of the annual largest storm and the largest storm wave. However, it is also seen that the indicated variability in the speed correction factor suggest that this parameter with respect to randomness is of an importance which is comparable with the drag coefficient. It should also be noted that the uncertainties related to the probabilistic modelling of the annual largest storm increases somewhat with increasing moment level.

Finally, we will consider the importance of the variability of the speed correction factor relative to possible uncertainties related to the current profile. For this purpose a linear current profile with $\bar{u} = 0.4$ m/s and $c_c = 0.75$ is adopted as the fixed case current profile. The fixed parameters are as for the previous example. (See the mean values given in Table 2). An uncertain current profile is then obtained by introducing \bar{u} as a variable being uniformly distributed from 0 to 0.8 m/s, and c_c as uniformly distributed between 0.5 and 1.0. The randomness for the other parameters are as for the previous example. The exceedance probabilities are shown in Fig. 11. The effects of uncertainties are now slightly stronger than for the case shown in Fig. 10 due to the uncertain

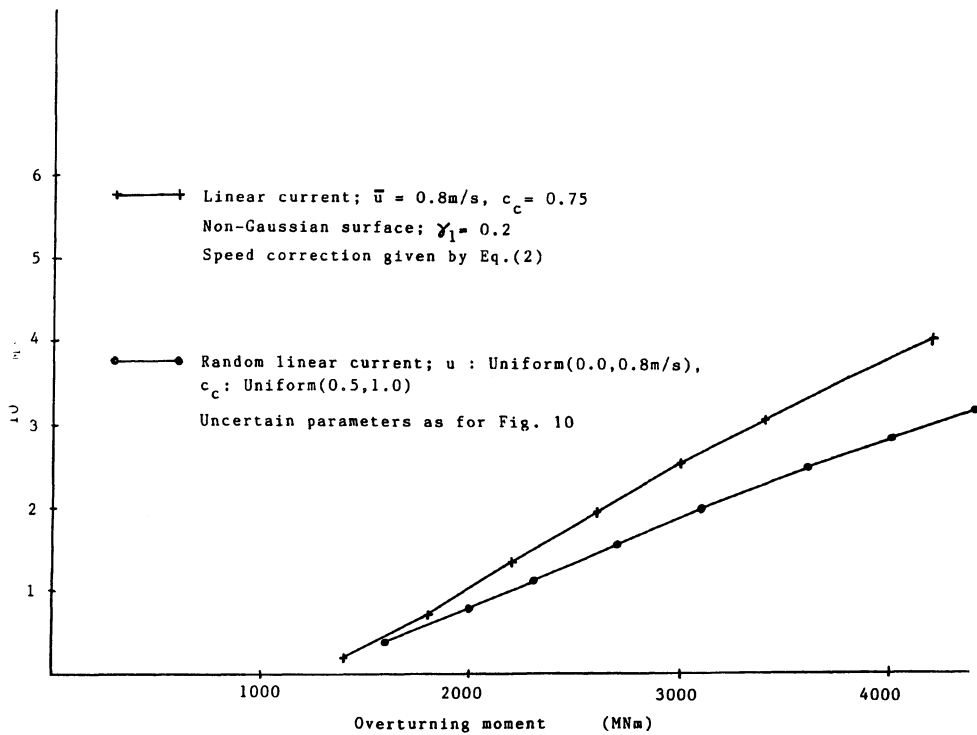


Fig. 11. Probability of exceedance for fixed parameters and uncertain parameters including an uncertain current profile.

Table 2 Parameters introduced as uncertain parameters in the structural response prediction

Parameter	Mean	Coefficient of variation	Distribution
Wheeler factor, $w_f(z)$	Eq. (2)	7.5%	Normal
Shape parameter of $F_{Hs}(h)$, γ	2.00	32.5%	Log normal
Drag coefficient c_d	1.00	15%	Normal
Coefficient of skewness, γ_1	0.20	25%	Normal

current profile. However, the difference is rather small bearing in mind the very extreme variability that is introduced for the current profile.

Relative importance factors are shown in Table 4. It is seen that the results remind us very much of those shown by Table 3. The introduction of current as an uncertain phenomenon does not change the relative importance of the variability of the speed correction factor. It is seen that even with rather conservative modelling of the uncertainties related to the current field, uncertainties related to the wave kinematics seem to be much more important regarding estimation of exceedance probabilities of structural loads.

CONCLUSIONS

The use of Wheeler stretching method for prediction of wave kinematics in irregular seas is recommended to represent state of the art although it has been concluded from several measurements that this method slightly underpredicts the measured kinematics around the mean water line.

A new review of data from a water velocity measurement program at NHL in Trondheim has made it possible to suggest a quantitative revision of the Wheeler stretching velocity profile by multiplying Wheeler estimated velocities by a factor $w_f(z)$ given in Equation 2 as a function of the depth below the wave crest.

The numerical studies of a jack-up indicate that for drag dominated structures it is very important to account for the suggested speed (velocity) correction w_f . This appears to yield a more important correction than possible moderate adjustments of the current profile provided the depth integrated current level is held constant. The variability associated with the predicted kinematics is of an importance comparable to the variability/uncertainty in the drag coefficient. Even with a rather conservative modelling of the uncertainties related to the current profile, the variability in the wave kinematics is a more important contribution to the exceedance probability. It should be stressed, however, that this is the case for the overturning moment of a jack-up. For base shear, the sensitivity of the results to the wave kinematics will be somewhat reduced (Haver and Gudmestad, 1992).

Further analysis of data as well as further theoretical development is, however, encouraged in order to reduce the uncertainty in predicted velocity as well as the uncertainty in the drag coefficient, contributing to uncertainty in force prediction on slender offshore structures.

Table 3 Importance factors for the case with uncertain parameters for two moment levels

Variable/Parameter	Moment level (MNm)	
	2800	4400
Annual max. significant wave height, $H_{s,1}$	37%	45%
Spectral peak period of the storm, T_p	4%	2%
Largest wave crest of the storm, A	29%	30%
Speed correction factor, w_f	12%	8%
Shape parameter of storm distribution for H_s , γ	2%	5%
Drag coefficient, c_d	14%	9%
Coefficient of skewness, γ_1	2%	2%

Table 4 Importance factors for the case with uncertain parameters and uncertain current profile

Variable/Parameter	Moment level (MNm)	
	2700	4000
Annual max. significant wave height, H_{s1}	34%	41%
Spectral peak period of storm, T_p	4%	2%
Largest weave crest of the storm, A	27%	29%
Speed correction factor, w_f	11%	8%
Shape parameter of storm distribution for the significant wave height, γ	2%	4%
Dray coefficient, c_d	12%	9%
Coefficient of skewness, γ_1	2%	2%
Depth integrated current, \bar{u}	8%	4%
Profile parameter, c_c	0	0

ACKNOWLEDGEMENTS

The authors will express thanks to Statoil for permission to publish this paper. Furthermore, the participation of all partners supporting the NHL measurement program during the years 1988 - 1990 should be acknowledged: Statoil, Exxon, Amoco, Conoco, Mobil and the Norwegian Council for Scientific and Industrial Research (NTNF).

REFERENCES

- Bea, R.G., (1990), "Effects of water wave kinematics uncertainty on design criteria for offshore structures". In: Tørum, A. and Gudmestad, O.T. (editors), "Water Wave Kinematics", pp. 103-159, Kluwer Acad. Publishers, Dordrecht.
- Bea, R.G., Litton, R.W., Pawsey, S.F., (1988), "Hydrodynamic effects on design of offshore platforms (HEDOP): In "Technology Assessment and Research Program for Offshore Minerals Operations", 1988 report, OSC study MMS 88-0057, US Department of the Interior Minerals Management Service, Washington D.C., pp. 85-90.
- Cieslikiewicz, W. and Gudmestad, O.T., (1992), "Mass transport within the free surface zone of water waves". Subm. to Wave Motion.
- Fenton, J.D., (1985), "A fifth order Stokes theory for steady waves". J. of Waterway, Port, Coastal and Ocean Engineering, Vol. III, No. 2, pp. 216-234.
- Gudmestad, O.T., (1990), "A new approach for estimating irregular deep water wave kinematics". Applied Ocean Research, Vol. 12, No. 1, pp. 19-24.
- Gudmestad, O.T., (1992), "Measured and predicted deep water wave kinematics in regular and irregular seas". Accepted for publication in Journal of Marine Structures.
- Gudmestad, O.T. and Connor, J.J., (1986), "Engineering approximations to nonlinear deepwater waves". Applied Ocean Research, Vol. 8, No. 2, pp. 76-88.
- Haver, S. and Gudmestad, O.T., (1992), "Uncertainties related to the kinematics of ocean waves and their effect on structural reliability". Proc. ISOPE, San Francisco, (1992), ISOPE, Golden Colorado, Vol. 3, pp. 444-453.

Haver, S. and Winterstein, S. (1990) "The Effects of a Joint Description of Environmental Data on Design Loads and Reliability", Proc. OMAE, Houston, 1990.

Litton, R. and Mitwally, H., (1991), "Hydrodynamic Effects on Design of Offshore Platforms (HEDOP) Phases IIa and IIb", in "Technology Assessment and Research Program for Offshore Mineral Operations". 1991 report, OSC study MMS 91-0057, US Department of the Interior Minerals Management Service, Washington D.C., pp. 57-60.

Madsen, H. Krenk, S. and Lind, N. (1986): "Structural Safety", Prestige Hall, Inc., Englewood Cliffs, New Jersey.

Morison, J.R., O'Brian, M.P., Johnson, J.W. and Schaaf, S.A., (1950), "The forces exerted by surface waves on piles". Petroleum Transactions, AIME, Vol. 189, pp. 149-157.

Sarpkaya, T. and Isaacson, M. (1981): "Mechanics of Wave Forces on Offshore Structures", Van Nostrand Reinhold Company.

Skjelbreia, J., Berek, E., Bolen, J.K., Gudmestad, O.T., Heideman, J., Ohmart, R.D., Spidsoe, N. and Tørum, A., (1991), "Wave Kinematics in irregular waves". Proceedings Mechanics and Artic Engineering, OMAE, Stavanger, (1991), ASME, New York, pp. 223-228.

Skjelbreia, J., Tørum, A., Berek, E., Gudmestad, O.T., Heideman, J. and Spidsoe, N., (1989), "Laboratory Measurements of Regular Wave and Irregular Wave Kinematics". E&P Forum, report 3 12/56. "Wave and Current Kinematics and Loading", IFP, Paris.

Skjelbreia, J and Hendrikson, J.A., (1960), "Fifth order gravity wave theory". Proceedings 7th Coastal Engr. Conference, The Hague, Council of Wave Research, The Engineering Foundation, Richmond, USA, Chapter 10, pp. 184-196.

Wheeler, J.D., (1970), "Method for calculating forces produced by irregular waves". Journal of Petroleum Technology, March 1970, pp. 359-367.

Winterstein, S.R. (1988): "Nonlinear Vibration Models for Extremes and Fatigue", Journal of Engineering Mechanics, ASCE, 114 (10), October 1988.

Zhang, J., Randall, R.E. and Spell, C.A., (1991), "On wave kinematics approximate methods". Proceedings Offshore Technology Conference, OTC 6522, (1991), Offshore Technology Conference, Houston, pp. 231-234.

WAVE KINEMATICS ON SHEARED CURRENTS

D.J.SKYNER and W.J.EASSON

Department of Mechanical Engineering
University of Edinburgh
Mayfield Road, Edinburgh, EH9 3JL
Scotland

ABSTRACT: Whole-field kinematic measurements are presented for steep, steady waves travelling on strongly sheared currents, concentrating on the region between trough and crest level. For slab currents, the crest kinematics and wave parameters were found to be correctly obtained by using Doppler shifting and standard wave theories. When the current was sheared, the crest kinematics were found to be well predicted by adding the results of an irrotational model to the stretched current profile, although this approach did not yield good predictions in the trough. The average shear was found to be reduced, in the presence of waves, from the undisturbed value, in agreement with the findings and predictions of other authors.

INTRODUCTION

It has recently been accepted that large waves require the use of high order theories for the prediction of their internal kinematics, and such predictions, in the absence of current, have been extensively verified by laboratory studies. On a uniform current the combined wave-current kinematics can be calculated by changing reference frame to one moving with the current and using a high-order model, after Doppler shifting the wave frequency. Several authors have recently tackled the problem of steep waves on currents with linear and bi-linear profiles [Dalrymple and Heideman,1989, Eastwood and Watson,1989], and programs are now being developed for the prediction of the kinematics in the presence of currents with arbitrary profiles [Chaplin,1990, Thomas,1990].

Whilst numerical solutions are available from several sources, experimental studies are still comparatively rare. Swan [1990] produced moderate amplitude waves on strongly sheared currents and addressed some of the difficulties posed by Dalrymple and Heideman in their cautionary note on tank testing. Other notable experiments

include those of Thomas [1990], where good agreement was obtained between laboratory measurements and numerical predictions for weakly sheared currents, and Kemp and Simons [1983] whose study concentrated on the effects near the bed.

EXPERIMENTAL MEASUREMENTS

In the present study, experiments were performed in a purpose built wave flume, capable of producing forward or reverse currents with various profiles. The experimental arrangement is shown in figure 1. The main current condition selected for the experimental programme was strongly sheared in the direction of wave propagation, and was generated by introducing a flow opposed to the waves along the bottom half of the flume. In the subsequent analysis, the bulk value of the current was altered to yield the desired profile in the chosen reference frame, and the wave frequency modified with the appropriate Doppler shift.

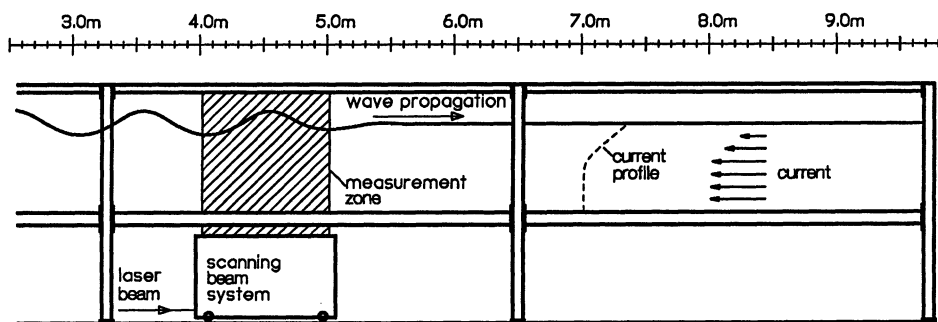


Figure 1: Wave flume used for the kinematic measurements of wave/current interaction, showing a reverse current with forward shear

In the experimental test sequence, steep waves were run onto the current and kinematic measurements made once the waves were steady and before reflections came back. The combined kinematics were measured by the method of Particle Image Velocimetry (PIV), in which small seeding particles are multiply exposed and recorded onto film. Further details of the use of the technique in this and other hydrodynamic studies are described in [Greated, 1992].

RESULTS OF THE EXPERIMENTAL STUDY

In this section, the experimentally obtained wave kinematics are presented and compared to numerical predictions. Initially, the experimentally obtained kinematics of steep waves, in the absence of a current, are checked for consistency against a high-order steady wave model. Then the kinematics measured with waves riding on a uniform current are compared with numerical predictions after suitable shifting of the frequency. Next the combined kinematics of steep waves and strongly currents are plotted along with the results of adding the predictions from the irrotational model to the stretched current profile. Such comparisons are present under the crest in all cases, and under the whole wave in a case which was studied in more detail.

Comparison between Experimental and Numerical Kinematics in the Absence of Current

Before attempting comparisons for the cases of waves combining with currents, the experimental measurements of steep, steady waves, in the absence of current, were checked against numerical predictions. This has a major benefit: if the two approaches are found to be consistent then some confidence in the quality of the experiments and the correctness of the assumptions in applying the model is gained. In the tests, care was taken to ensure that the measurements were accurate, and that the waves were as steady as possible and free from reflection. An overall assessment of these effects is obtained by checking against a suitable numerical model.

The kinematic measurements were conducted, in the absence of current, for six waves with similar parameters, of height and wavelength, to those used in the tests with currents. The main parameters of the waves are summarised in dimensionless form in table 1, for these six waves, together with the wave & current combinations.

The experimental measurements of the horizontal velocity component under the crest are plotted in figure 2 for the wave cases in the absence of current, along with the numerical predictions. The plots for cases 0 to 3 are the averages of two repeats of the same wave cycle in the wavetrain. The variation between the repeats is smaller than the symbols marking the data points. Of the cases for which measurements were also made later in the wavetrain the agreement for case 3 was better, and for case 0 worse, probably due to reflection.

The discrepancies range from about 1% for the central waves case, to about 4% in the worst case, with these errors being defined from the differences and absolute velocities

Case	Current	Top shear $\frac{\partial u}{\partial z} \sqrt{\frac{\lambda}{g}}$	h/λ	H/λ	$\frac{h}{gT^2}$	%age of limiting steepness
0	No current		0.2970	0.0825	0.0489	58.8%
1	No current		0.4741	0.0563	0.0764	34.9%
2	No current		0.4615	0.0823	0.0765	52.4%
3	No current		0.4467	0.1064	0.0764	70.0%
4	No current		0.6471	0.0800	0.1101	51.0%
5	No current		0.6198	0.1018	0.1101	67.7%
6	Uniform, reverse	(0.094)	0.4213	0.0752	0.0703	48.6%
7	Uniform, forward	(0.028)	0.3178	0.0569	0.0474	37.2%
8	Uniform, forward	(0.022)	0.4839	0.0574	0.0738	33.7%
9	Weak shear	0.053	0.3138	0.0870	0.0503	59.7%
10	Weak shear	0.044	0.4545	0.0536	0.0732	33.3%
11	Weak shear	0.045	0.4438	0.0794	0.0731	50.4%
12	Weak shear	0.046	0.4190	0.0989	0.0705	64.4%
13	Weak shear	0.038	0.6250	0.0779	0.1040	48.7%
14	Weak shear	0.039	0.5952	0.0984	0.1018	63.3%
15	Strong shear	0.226	0.2717	0.0751	0.0419	53.7%
16	Strong shear	0.175	0.4518	0.0535	0.0728	33.2%
17	Strong shear	0.183	0.4121	0.0729	0.0671	46.4%
18	Strong shear	0.184	0.4098	0.0976	0.0687	63.6%
19	Strong shear	0.159	0.5515	0.0686	0.0906	42.8%
20	Strong shear	0.156	0.5725	0.0929	0.0970	59.4%

Table 1: Non-dimensionalised wave parameters. Note that T has been obtained from H and λ using irrotational theory

near the crest. These discrepancies should be borne in mind when assessing the later comparisons.

The Checking of Doppler Shifting on a Uniform Current

If waves travel on a uniform current, or if waves on otherwise still water are viewed by a moving observer, then their frequency is modified according to Doppler theory [Doppler, 1842].

Consider a steady wave with wavelength λ . If this wave has frequency f_1 when observed in a given frame of reference S_1 , then an observer in a second frame of reference S_2 , moving with velocity u , measured in the direction of wave propagation and relative to S_1 , will measure an apparent frequency f_2 , given by the Doppler formula

$$f_2 = f_1 - \frac{u}{\lambda} \quad (1)$$

Experiments were performed on currents whose profiles were approximately uniform in the top half of the water depth. Horizontal velocity profiles beneath the crest are plotted for the reverse current cases in figure 3 and the forward current cases in figure 4. Each plot shows the experimental measurements, the *almost* uniform current profiles and velocity profiles generated numerically by Doppler shifting the frequency to the frame of reference moving with the current. Also shown is the combined profile obtained by adding the numerical values to the (stretched) current profile.

The horizontal lines in the plots represent the scatter found between repeats of the same cycle of the wave in each wavetrain and between earlier and later cycles.

It can be seen that the crest kinematics are reasonably well predicted within the value of the experimental errors, for the reversing current. The agreement is less good for the forward current cases, particularly above the trough level. This may be due to interaction between the wave and current generation being advected down to the measurement zone, or may be due to the turbulence present in the current.

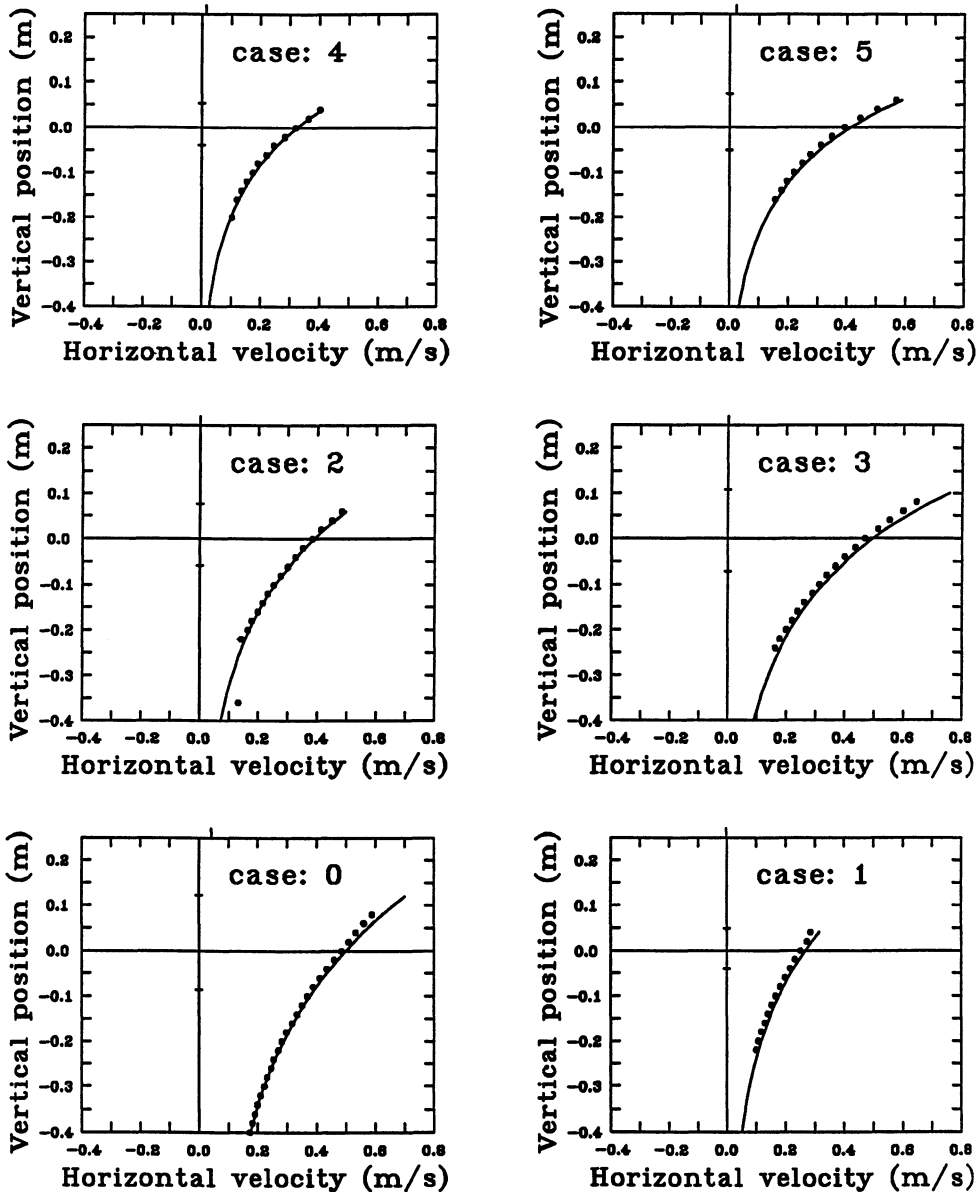


Figure 2: Horizontal velocity profiles under the crest, in the absence of current. -•- experimental data, with scatter, — prediction from irrotational numerical model. Water depth = .75m

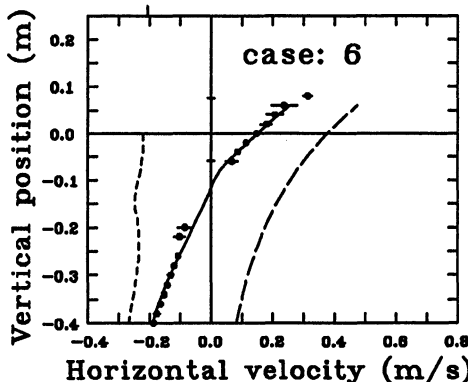


Figure 3: Horizontal velocity profiles under the crest, for waves on a uniform, reverse current. -•- experimental data, with scatter, - - - undisturbed current, — — irrotational numerical model, — prediction from numerical model and stretched current profile

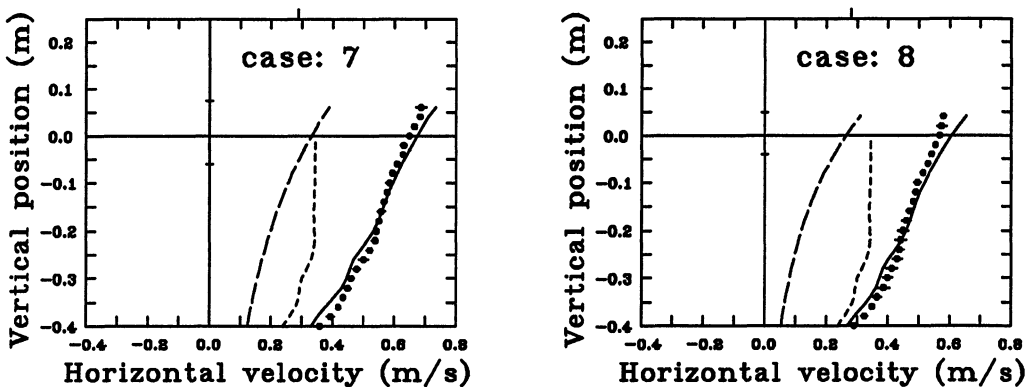


Figure 4: Horizontal velocity profiles under the crest, for waves on a uniform, forward current. -•- experimental data, with scatter, - - - undisturbed current, — — irrotational numerical model, — prediction from numerical model and stretched current profile

Waves on Sheared Currents

Tests were conducted with weakly and strongly sheared currents, over similar ranges of wave frequency and wave steepness to those used in the earlier, shear-free cases. The dimensionless parameters of the wave/current cases studied have been summarised in table 1.

EFFECT OF SHEARED CURRENTS ON VELOCITY PROFILES UNDER THE CREST

The experimentally measured velocity profiles under the crest for weakly and strongly sheared current conditions are plotted in figures 5 and 6, along with numerical predictions. Each graph contains the undisturbed current profile, the velocity profile under the crest for the combined flow, a numerically generated profile for an irrotational wave with the same height and wavelength, and the numerical data combined with the stretched current profile. The results presented in figures 5 and 6 have been shifted by $.2\text{ms}^{-1}$ for the weakly sheared current, and by $.3\text{ms}^{-1}$ for the strongly sheared current.

The experimental values were obtained by averaging over repeats of the same waves in the train. The horizontal lines in each plot represent the experimental scatter.

The numerically generated velocity data was for waves with the same height and wavelength as those measured experimentally. This approach is slightly different from that adopted for the cases in the absence of current and on uniform currents, where the current velocity was used to obtain the appropriate wave parameters, given the wave frequency and height in the laboratory frame of reference. The approach differs because the velocity value which should be used for the Doppler shift on a sheared current is not known. A treatment using the value of the current at the surface for the Doppler shifting was attempted for the sheared current cases, yielding plots which are almost identical to those shown in figures 5 and 6.

The current profile under the crest was obtained by linearly stretching the undisturbed current profile to the surface. No modification to conserve mass has been applied. A slightly less arbitrary scheme for stretching the current profile, based on the water orbital excursions at each level was attempted, but the difference from the linear stretching was negligible.

In the graphs there is good agreement in all cases, with the predicted values for the combined wave and current velocities lying within the experimental scatter.

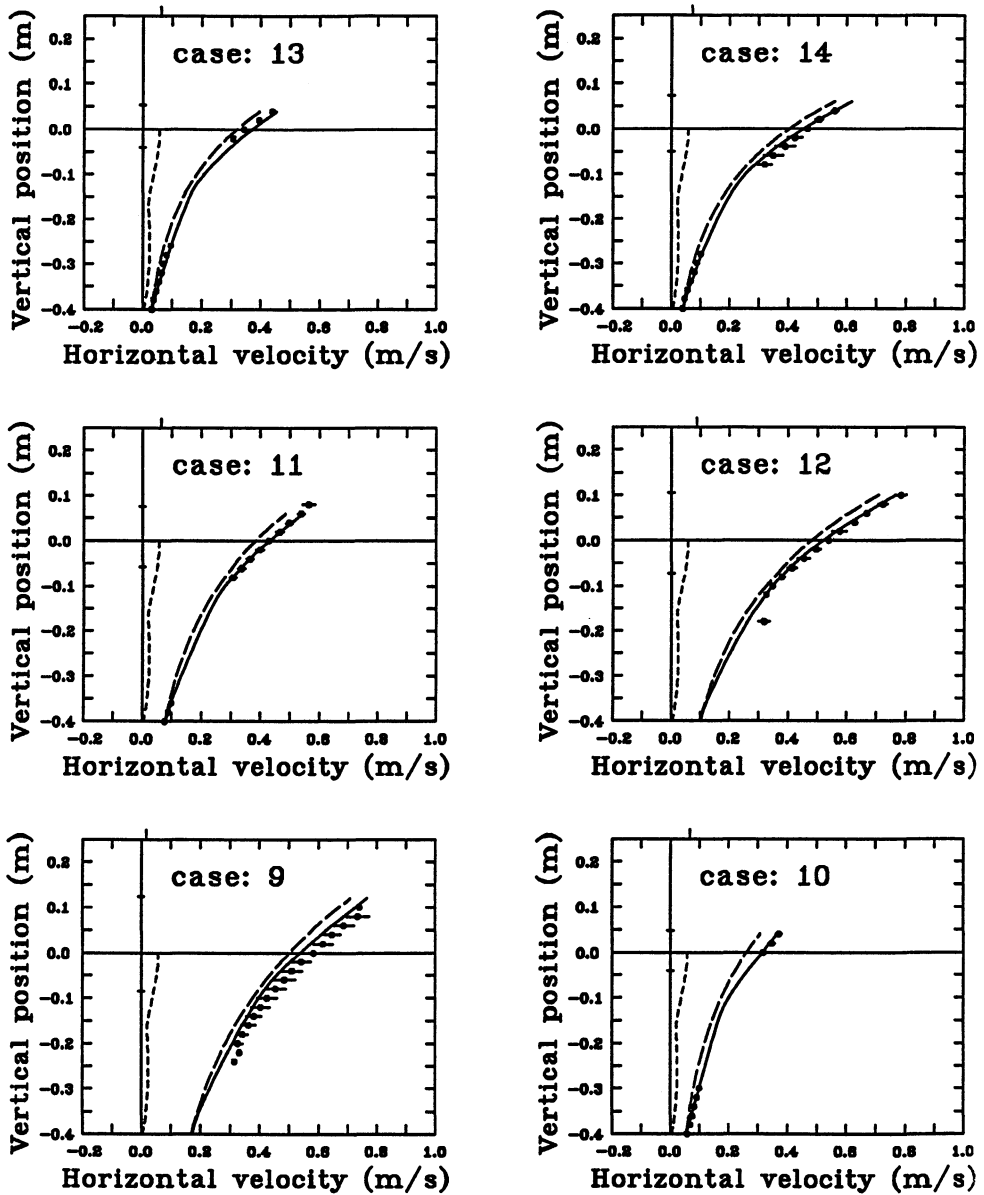


Figure 5: Horizontal velocity profiles under the crest, for waves on a weakly sheared current. -•- experimental data, with scatter, - - - undisturbed current, - - - irrotational numerical model, — prediction from numerical model and stretched current profile

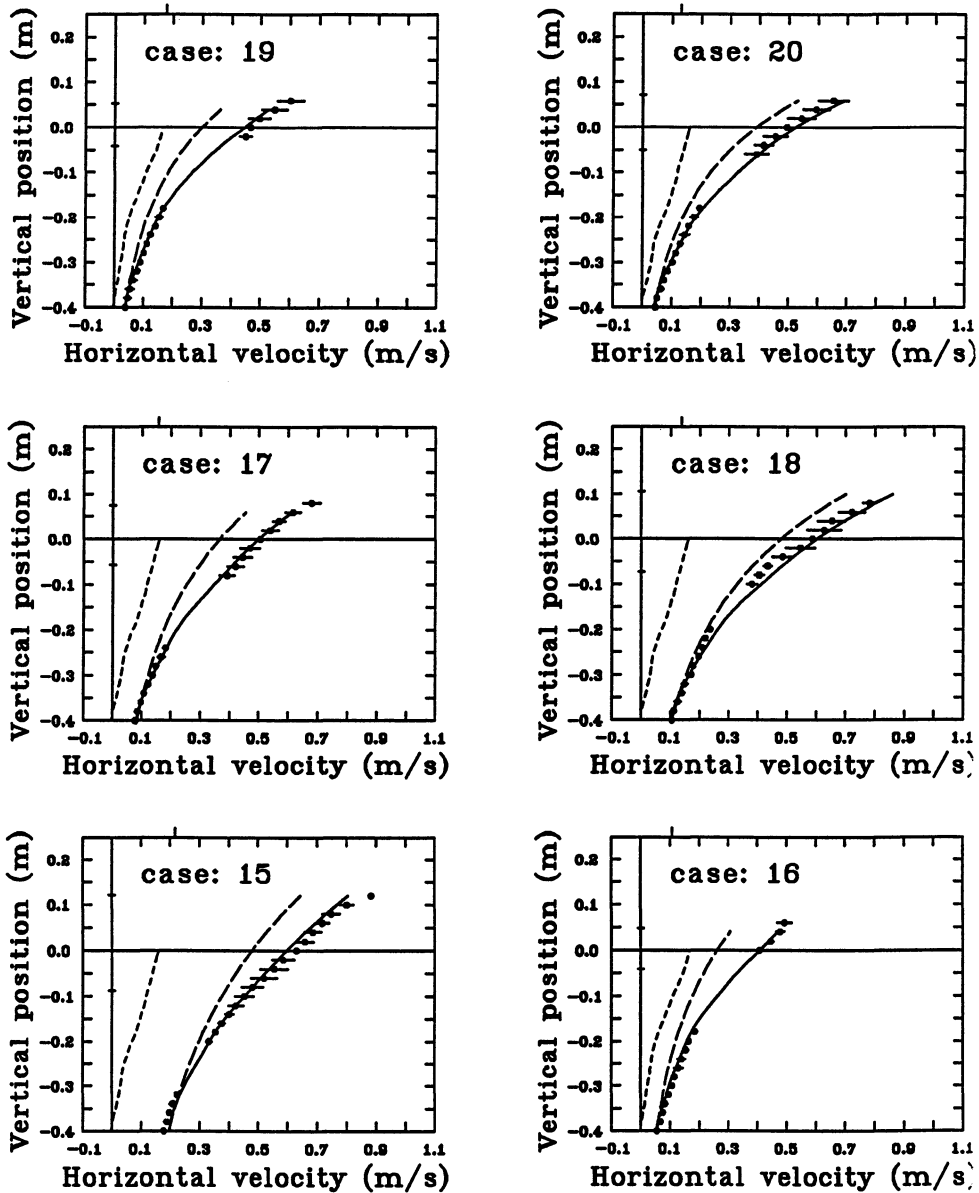


Figure 6: Horizontal velocity profiles under the crest, for waves on a strongly sheared current. -•- experimental data, with scatter, - - - undisturbed current, — irrotational numerical model, — prediction from numerical model and stretched current profile

EFFECT OF SHEARED CURRENTS ON VELOCITY PROFILES UNDER THE WHOLE WAVE

While the horizontal velocities near the crest lead to the highest loadings and are therefore the most important for design purposes, the velocity field throughout a complete wave cycle or wavelength is also of interest. For the more central wave/current cases, the wave kinematics were analysed in greater detail, and composite velocity fields constructed over a complete wavelength. Velocity data was then generated with a Chaplin's irrotational numerical model [Chaplin,1980], with the same wave height and wavelength as those measured experimentally. This numerical data was then subtracted, point by point, from the experimental values to yield the underlying current.

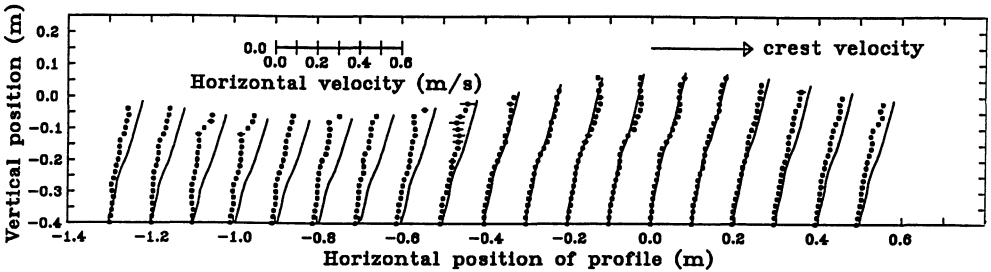


Figure 7: Underlying current at various phases of a wave, in the absence of current.
 -•— experimental data, with predictions from irrotational numerical model subtracted,
 — stretched current profile.

In order to check the sensitivity of this method, the procedure was first tried for one of the waves in the absence of current (case 2), where the underlying current should be zero. The residual current obtained after subtracting the numerical data is plotted in figure 7 at various positions within the wave. In this case experimental data was only available over three-quarters of a wavelength, but since this includes both trough and crest, and the wave is expected to be symmetric, there is no loss of information.

The agreement between the experimental and numerical velocity data in this irrotational case is good, except very near the water surface where some overprediction is apparent. The maximum velocity in the crest is plotted for comparison with these small discrepancies.

Figure 8 shows the results for a similar treatment to one of the wave cases on the strongly sheared current (number 17). Again the numerical data has been subtracted to leave the residual current, which is plotted by averaging bands within the wave-

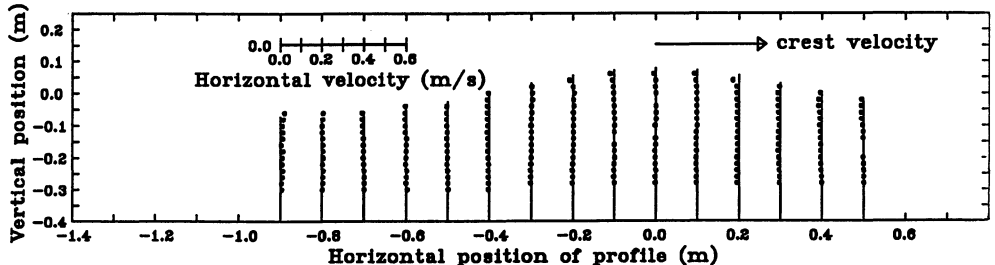


Figure 8: Underlying current at various phases of a wave, on a strongly sheared current. -•- experimental data, with predictions from irrotational numerical model subtracted, — stretched current profile.

length. For comparison, the stretched current profile is also plotted at each position.

In the whole of the crest region, the estimated residual current matches the stretched current profile, as expected from the crest profiles shown earlier. However, in the trough, stretching predicts an increase in shear, which is not supported by these experimental results. If anything, the shear is reduced in the trough compared to the value in the undisturbed current. Similar trends were found for the wave/current cases with similar steepness at higher and lower frequency.

CONCLUSIONS

There was good agreement for the crest kinematics of the waves in the absence of currents. In the presence of uniform currents, the kinematics were reasonably well predicted by the irrotational numerical model, after Doppler shifting the wave frequency. When sheared currents were present, there was fair agreement between the measured crest kinematics and the estimate obtained by combining the stretched current profile with the prediction of the irrotational model.

While the kinematics of a medium amplitude wave, in the absence of current, were well predicted over a complete wavelength, in the strongly sheared case the predictions obtained using current stretching were poor in the trough region. There was some evidence that the underlying current had constant shear throughout the wavelength.

The success of current stretching in the crest seems a little fortuitous. No combination of current profile stretching and mass conservation can predict the experimental values

satisfactorily over the whole wave, although the good agreement near the crest may be adequate for design purposes. The behaviour presented through the wave cycle should be predictable by the full numerical treatments.

References

- [1] Chaplin, J.R. *Developments of Stream Function Wave Theory*. 1980. Coastal Engineering 3, 179-205.
- [2] Chaplin, J.R. *The Computation of Non-Linear Waves on a Current of Arbitrary Non-Uniform Profile*. 1990. OTH 90 327, HMSO.
- [3] Dalrymple, R.A. and Heidemann, J.E. *Non-linear Water Waves on a Vertically-Sheared Current Wave and Current Kinematics and Loading*. 1989. E&P Forum, Report No. 3.12/156, 69-92.
- [4] Eastwood, J.W. and Watson, C.J.H. *Implications of Wave-Current Interaction for Offshore Design Wave and Current Kinematics and Loading*. 1989. E&P Forum, Report No. 3.12/156, 93-112.
- [5] Kemp, P.H. and Simons, R.R. *The Interaction of Waves and a Turbulent Current: Waves Propagating against the Current*. 1983. Journal of Fluid Mechanics, 130, 73-89.
- [6] Skyner, D.J., Easson, W.J. and Greated C.A. *The Internal Kinematics of Steep Waves on Sheared Currents — An Experimental Study*. 1992. OTH 92 366.
- [7] Swan, C. *An Experimental Study of Waves on a Strongly Sheared Profile*. 1990. Proc. 22nd Int. Conf. on Coastal Eng., ASCE, 1, 489-502.
- [8] Thomas, G.P. *Wave-current Interactions: an Experimental and Numerical Study, Part 2: Non-Linear waves*. 1990. Journal of Fluid Mechanics, 216, 505-536.

LABORATORY WAVE GENERATION CORRECT TO SECOND ORDER

HEMMING A. SCHÄFFER
Danish Hydraulic Institute
Agern Allé 5, DK-2970 Hørsholm
Denmark

ABSTRACT Through the eighties the theory for second order irregular wave generation was developed within the framework of Stokes wave theory. This pioneering work, however, is not fully consistent. Furthermore, due to the extensive algebra involved, the derived transfer functions appear in an unnecessarily complicated form. The present paper develops the full second order wavemaker theory (including superharmonics as well as subharmonics) valid for a variety of different types of wave board motion. In addition to the well known transfer functions some new terms evolve. These are related to the first order local disturbances (evanescent modes) and accordingly they are significant when the wave board motion makes a poor fit to the velocity profile of the desired progressive wave component. This is typically the case for the high-frequency part of a primary wave spectrum when using a piston type wavemaker. The transfer functions are given in a relatively simple form by which the computational effort is reduced substantially. This enhances the practical computation of second order wavemaker control signals for irregular waves, and no narrow band assumption is needed. The software is conveniently included in a PC-based wave generation system - the DHI Wave Synthesizer. The validity of the theory is analysed in a number of laboratory wave tests, covering the superharmonic generation for regular waves.

1. INTRODUCTION

First order wavemaker theory corresponding to linearized Stokes theory has long been well established (Havelock, 1929, Biesel, 1951, Ursell et al., 1960, and others, cf. the review by Svendsen, 1985) and we shall devote this introduction to second order theories of wave generation.

The first step towards the development of wavemaker theory is of course the knowledge of the underlying wave theory. Already in 1847 Stokes gave results for regular waves in terms of a perturbation series using the wave steepness as the small ordering parameter. For regular waves only the sum frequencies appear (since the difference frequencies vanish) and Stokes found the resulting superharmonics.

Presumably the first approach to second order wavemaker theory was given by Fontanet (1961) for regular waves. Using a Lagrangian description he found the spurious superharmonics generated by a purely sinusoidal oscillation of the

wave board and gave directions as how to suppress these by adding a superharmonic component to the wavemaker control signal.

Recently Hudspeth and Sulisz (1991) derived the complete second order lagrangian theory for regular waves with special emphasis on Stokes drift and return flow in wave flumes. The theories of Fontanet (1961) and Hudspeth and Sulisz (1991) appear to be the most complete theoretical developments yet.

Madsen (1971) developed an approximate theory for the suppression of spurious superharmonics in regular waves generated in fairly shallow water.

Buhr Hansen et al. (1975) chose an emperical approach to persue the second order control signal for regular waves. The second order regular wave field generated by a first order control signal has further been studied by Flick and Guza (1980).

For irregular waves both sum and difference frequencies appear in the interaction terms at second order. Longuet-Higgins and Stewart (1962,1964) derived results for the subharmonics with the restriction of only slightly different frequencies (narrow band restriction) in the interacting wavelets. Without this restriction Ottesen-Hansen (1978) gave similar results in a more suitable form i.e. using a transfer function giving the second order contribution in terms of the interacting first order wavelets. A generalization including both subharmonics and superharmonics for directional waves was given by Sharma and Dean (1979), see also Dean and Sharma (1981).

Neglecting the local disturbance terms in the first order solution Flick and Guza (1980) gave an approximate theory for the generation of spurious long waves by a first order bichromatic control signal under the narrow band assumption.

Without this assumption Sand (1982) calculated the second order subharmonic control signal for a piston type wavemaker needed to suppress spurious long wave generation. A more detailed description of the theory was given by Barthel et al. (1983), who also extended the theory to include a rotating wave board motion, restricting the centre of rotation to a point at or below the bottom. This is, however, an inconvenient restriction, since many wavemakers are equipped with a hinge situated above the bottom. Sand and Donslund (1985) gave the required theoretical extension.

For irregular waves a technique for the synthesis of wave maker control signals based on the narrow band assumption for the first order carrier waves has further been used by Klopman and Leeuwen (1990) and by Bowers (1988) (discussed by Mansard et al., 1989) for subharmonic frequencies. This approximation allows for an efficient time-domain computation of the second order control signal.

For irregular waves Mansard and Sand (1986a,b) derived the wavemaker theory for the superharmonics valid for translatory as well as rotating wave boards. For a directional wavemaker Suh and Dalrymple (1987) developed part of the theory for the spurious superharmonic and subharmonic second order waves generated by a first order wavemaker control signal.

In the present paper the full second order wavemaker theory is rederived in a unifying and compact form that includes both superharmonics and subharmonics and covers a variety of different types of wave board motion †. No narrow band approximation is applied.

† Inconsistencies in the previous derivations are pointed out concurrently using footnotes.

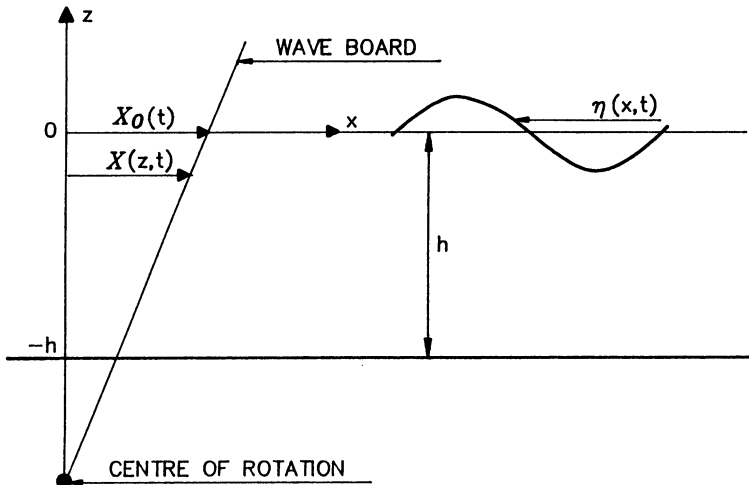


Figure 1 Definition sketch (the waveboard motion indicated corresponds to type (b) in Fig. 2).

In order to facilitate and reduce the theoretical calculations a complex representation is chosen although the resulting transfer functions are also given in real form.

2. GENERAL THEORY

2.1. Governing equations

The classical method of perturbation theory in combination with Taylor expansions of the boundary conditions at the free surface and at the wave board leads to a boundary value problem for the first and second order wave contributions, respectively (Stokes, 1947, Laitone, 1961, Flick and Guza, 1980, and others). Let $(u, w) = (\dot{\Phi}_x, \dot{\Phi}_z)$ define the velocity potential $\Phi = \Phi(x, z, t)$ in a Cartesian coordinate system (x, z) , cf. Fig. 1, and let $\eta = \eta(x, t)$, $X = X(z, t)$, g , h , and t denote surface elevation, wave board position, acceleration of gravity, still water depth, and time, respectively, then the relevant boundary value problems may be written

$$\Delta\Phi = 0 \quad \text{everywhere} \quad (1a)$$

$$\Phi_{tt} + g\Phi_z = R \quad \text{for } z = 0 \quad (1b)$$

$$\Phi_x = Q \quad \text{for } x = 0 \quad (1c)$$

$$\eta = -\frac{1}{g}(\Phi_t + P) \quad \text{for } z = 0 \quad (1d)$$

$$\Phi_z = 0 \quad \text{for } z = -h \quad (1e)$$

where R , Q , and P are given below. The elevation, potential, and wave board position (see (5)) correct to second order are given by

$$\eta = \epsilon\eta^{(1)} + \epsilon^2\eta^{(2)} \quad (2a)$$

$$\Phi = \epsilon\Phi^{(1)} + \epsilon^2\Phi^{(2)} \quad (2b)$$

$$X_0 = \epsilon X_0^{(1)} + \epsilon^2 X_0^{(2)} \quad (2c)$$

where ϵ is a small ordering parameter, and (1) covers the first order problem for $(\Phi, \eta) = (\Phi^{(1)}, \eta^{(1)})$, where

$$R^{(1)} = 0 \quad (3a)$$

$$Q^{(1)} = f(z)X_{0t}^{(1)} \quad (3b)$$

$$P^{(1)} = 0 \quad (3c)$$

and the second order problem for $(\Phi, \eta) = (\Phi^{(2)}, \eta^{(2)})$, where †

$$R^{(2)} = -\left\{(\Phi_x^{(1)})^2 + \Phi_z^{(1)2}\right\}_t + \eta^{(1)}(\Phi_{tt}^{(1)} + g\Phi_z^{(1)})_z \quad (4a)$$

$$Q^{(2)} = \begin{cases} -X_0^{(1)}\{f(z)\Phi_{xx}^{(1)} - \frac{1}{h+\ell}\Phi_z^{(1)}\} + f(z)X_{0t}^{(2)} & \text{for } -(h-d) \leq z \leq 0 \\ 0 & \text{for } -h \leq z < -(h-d) \end{cases} \quad (4b)$$

$$P^{(2)} = \frac{1}{2}\left(\Phi_x^{(1)2} + \Phi_z^{(1)2}\right) + \eta^{(1)}\Phi_{zt}^{(1)} \quad (4c)$$

The position of the wave board is

$$X(z, t) = f(z)X_0(t) \quad (5)$$

where $f(z)$ describes the type of wavemaker:

$$f(z) = \begin{cases} 1 + \frac{z}{h+\ell} & \text{for } -(h-d) \leq z \leq 0 \\ 0 & \text{for } -h \leq z < -(h-d) \end{cases} \quad (6)$$

Here $z = -(h + \ell)$ gives the centre of rotation ($-h < \ell \leq \infty$) and $d \geq 0$ describes elevated wavemakers i.e. the last case in (6) is only relevant for $d > 0$. For $\ell = -d$ or ($d = 0, \ell \geq 0$) equation (6) reduces to types of wavemakers considered in previous references. The present extension is made mainly because it covers wavemakers of the piston type (i.e. $\ell = \infty$), where the piston does not reach the bottom (i.e. $d > 0$), cf. Fig. 2, which shows the possible combinations. It is emphasized that solutions for such discontinuous $f(z)$ should be used with

† For wave boards hinged above the bottom $Q = 0$ must be required specifically below the hinge. The consequence of this fact was not fully drawn in Sand and Donslund (1985) and Sand and Mansard (1986a,b).

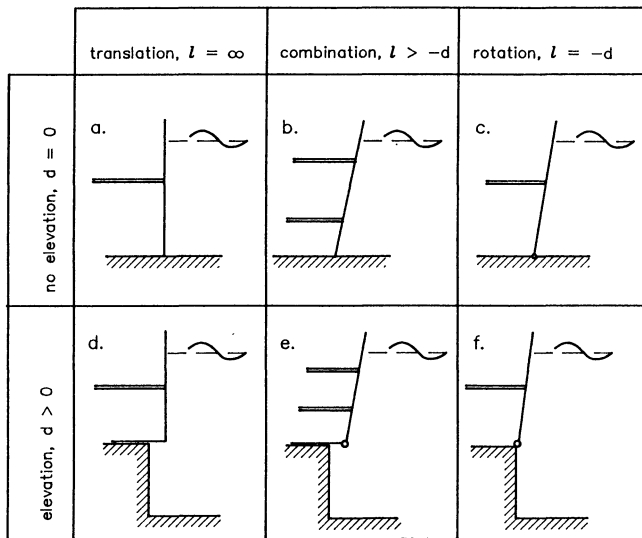


Figure 2 Different types of waveboard motions: (a) translatory (piston type) (b) combined (c) rotational (d) translatory, elevated (e) combined, elevated (f) rotational, elevated.

extreme care, since separated flow (which is not considered in the present theory) is inevitable around angular points.

As described in detail by Barthel et al. (1983), the second order problem is conveniently separated into three contributions

$$\Phi^{(2)} = \Phi^{(21)} + \Phi^{(22)} + \Phi^{(23)} \quad (7a)$$

$$\eta^{(2)} = \eta^{(21)} + \eta^{(22)} + \eta^{(23)} \quad (7b)$$

and the respective boundary value problems are given by (1), where for $(\Phi, \eta) = (\Phi^{(21)}, \eta^{(21)})$:

$$R^{(21)} = - \left\{ \left(\Phi_x^{(1)}{}^2 + \Phi_z^{(1)}{}^2 \right)_t + \eta^{(1)} (\Phi_{tt}^{(1)} + g \Phi_z^{(1)})_z \right\} \quad (8a)$$

$$Q^{(21)} = \text{arbitrary (i.e. condition disappears)} \quad (8b)$$

$$P^{(21)} = \frac{1}{2} \left(\Phi_x^{(1)}{}^2 + \Phi_z^{(1)}{}^2 \right) + \eta^{(1)} \Phi_{zt}^{(1)} \quad (8c)$$

for $(\Phi, \eta) = (\Phi^{(22)}, \eta^{(22)})$:

$$R^{(22)} = 0$$

$$Q^{(22)} = \begin{cases} -X_0^{(1)} \{ f(z) \Phi_{xx}^{(1)} - \frac{1}{h+\ell} \Phi_z^{(1)} \} - \Phi_x^{(21)} & \text{for } -(h-d) \leq z \leq 0 \\ -\Phi_x^{(21)} & \text{for } -h \leq z < -(h-d) \end{cases} \quad (9a)$$

$$P^{(22)} = 0$$

and for $(\Phi, \eta) = (\Phi^{(23)}, \eta^{(23)})$:

$$R^{(23)} = 0 \quad (10a)$$

$$Q^{(23)} = f(z) X_{0t}^{(2)} \quad (10b)$$

$$P^{(23)} = 0 \quad (10c)$$

Here $\Phi^{(21)}$ gives the bound waves due to the interaction between first order wavelets, $\Phi^{(22)}$ describes the free waves due to the wavemaker leaving its mean position and due to $\Phi^{(21)}$ mismatching the boundary condition at the wavemaker, and $\Phi^{(23)}$ gives the free waves generated by the second order wave board motion. If the control signal for the wavemaker is based on first order theory alone then the resulting second order waves are given by $\Phi^{(2)} = \Phi^{(21)} + \Phi^{(22)}$ i.e. the spurious free waves from $\Phi^{(22)}$ are not eliminated. Let subscript 0 (on Φ and η) denote the progressive part of a wave field then the objective for second order wavemaker theory is to determine $X_0^{(2)}(t)$ as to produce free waves $\eta_0^{(23)}$ which eliminate these spurious free waves $\eta_0^{(22)}$ by requiring

$$\eta_0^{(22)} + \eta_0^{(23)} = 0 \quad (11)$$

or equivalently

$$\Phi_0^{(22)} + \Phi_0^{(23)} = 0 \quad (12)$$

2.2. First order solution

The first order solution was obtained by Biesel (1951), Ursell et al. (1960), Flick and Guza (1980), Sand and Donslund (1985), and others. Here the solution will be given in a slightly more general version as regards the type of wave board motion, and in the compact notation provided by a complex representation.

Let the first order paddle position for each of the wavelets constituting the first order spectrum be given by

$$X_0^{(1)} = \frac{1}{2} \{ -iX_a e^{i\omega t} + \text{c.c.} \} \quad (13)$$

where X_a is the constant complex first order wave board amplitude at still water level and where c.c. denotes the complex conjugate of the preceding term, then

the solution to the first order problem (1) and (3) may be expressed as

$$\Phi^{(1)} = \frac{1}{2} \left\{ \frac{igX_a}{\omega} \sum_{j=0}^{\infty} c_j \frac{\cosh k_j(z+h)}{\cosh k_j h} e^{i(\omega t - k_j z)} + \text{c.c.} \right\} \quad (14a)$$

$$\eta^{(1)} = \frac{1}{2} \left\{ X_a \sum_{j=0}^{\infty} c_j e^{i(\omega t - k_j z)} + \text{c.c.} \right\} \quad (14b)$$

which includes both the wanted progressive-wave term and the local disturbances which are due to the mismatch between the shape of the progressive-wave velocity profile and the shape function $f(z)$. This solution obviously satisfies the bottom boundary condition (1e), and the free surface boundary condition (1b) is easily shown to require

$$\omega^2 = gk_j \tanh k_j h \quad (15)$$

This is the linear dispersion relation generalized to complex wavenumbers, and it has one real solution, say k_0 , and an infinity of purely imaginary solutions (k_1, k_2, \dots) , where $ik_j > 0$, $j = 1, 2, \dots$. In order not to confuse k_0 with the deep water wave number we shall omit the subscript on k when $j = 0$ appears explicitly (and only when it is the only index).

It may seem artificial to retain imaginary wavenumbers instead of letting k_j , $j = 1, 2, \dots$ be the real solutions to $-\omega^2 = gk_j \tan k_j h$. However, this choice gives a considerable reduction of the algebra involved at a later stage, and it assures the analogy between the treatment of the progressive-wave term ($j = 0$) and the local disturbances ($j = 1, 2, \dots$).

The coefficients c_j are determined by requiring the solution to satisfy the boundary condition at the wavemaker. This is done by inserting (3b) and (14a) in (1c), multiplying the equation by $\cosh k_l(z+h)$ and integrating the result over the depth. Due to the orthogonality relation

$$\int_{-h}^0 \cosh k_j(z+h) \cosh k_l(z+h) dz = \begin{cases} \frac{1}{2k_j} (k_j h + \sinh k_j h \cosh k_j h) & \text{for } l = j \\ 0 & \text{for } l \neq j \end{cases} \quad (16)$$

which may readily be verified, only the term $j = l$ remains in the infinite series, and the resulting equation is solved for c_j to obtain

$$c_j = \sinh k_j h \frac{\Lambda_1(k_j)}{\Lambda_2(k_j)} \quad (17a)$$

where

$$\begin{aligned} \Lambda_1(k_j) &\equiv k_j \int_{-h}^0 f(z) \cosh k_j(z+h) dz \\ &= \sinh k_j h - \frac{d+\ell}{h+\ell} \sinh k_j d + \frac{1}{h+\ell} \frac{\cosh k_j d - \cosh k_j h}{k_j} \end{aligned} \quad (17b)$$

$$\Lambda_2(k_j) \equiv k_j \int_{-h}^0 \cosh^2 k_j(z+h) dz = \frac{1}{2} (k_j h + \sinh k_j h \cosh k_j h) \quad (17c)$$

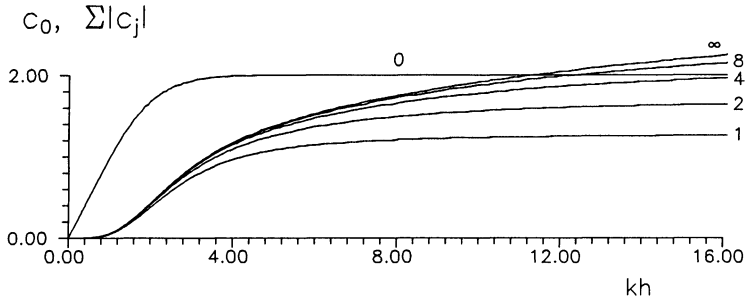


Figure 3 The Biesel transfer function c_0 with the sum of the local disturbance transfer functions c_j from $j = 1$ retaining 1,2,4,8, and “ ∞ ” terms in the series, respectively. The results shown are valid for a piston type wavemaker.

For $j = 0$ this gives the real quantity c_0 which is known as the Biesel transfer function in terms of which the complex amplitude A of the progressive part of the first order wavefield in (14) may be related to the complex amplitude X_a of the first order paddle position through

$$A = c_0 X_a \quad (18)$$

the elevation for the progressive part of the first order waves being

$$\eta_0^{(1)} = \frac{1}{2} \{ A e^{i(\omega t - kx)} + \text{c.c.} \} \quad (19)$$

With $A = a - ib$ (13) and (19) may be written $X_0^{(1)} = c_0(a \sin \omega t - b \cos \omega t)$ and $\eta_0^{(1)} = a \cos(\omega t - kx) + b \sin(\omega t - kx)$.

For $j = 1, 2, \dots$ c_j is purely imaginary and $ic_j > 0$, $j = 1, 2, \dots$

Before we proceed to the second order solution we shall illustrate the magnitude of the local disturbances at the wave board. This is relevant for the importance of the interaction terms at second order and for special applications of first order theory like active absorption relying on wave gauges in conjunction with the wave board. For a piston type wave wavemaker Fig. 3 compares the Biesel transfer function c_0 with the sum of the local disturbance transfer functions c_j from $j = 1$ retaining 1,2,4,8, and “ ∞ ” terms in the series, respectively. While c_0 practically reaches its asymptotic value of 2 at the traditional deep water limit $kh = \pi$ the sum of the local disturbance coefficients increase continuously with increasing kh . It appears that for $kh > 11.5$ the amplitude of the local disturbance at the wave board exceeds the amplitude of the emitted progressive wave. This demonstrates the problems of generating deep water waves with a piston type wavemaker, since pronounced local disturbances will significantly increase the nonlinear wave interaction.

It turns out that the maximum slope of the local disturbance at the wave board is somewhat smaller than the maximum slope of the emitted progressive wave. In fact it can be shown theoretically that

$$k_0 h c_0, \sum |k_j h c_j|$$

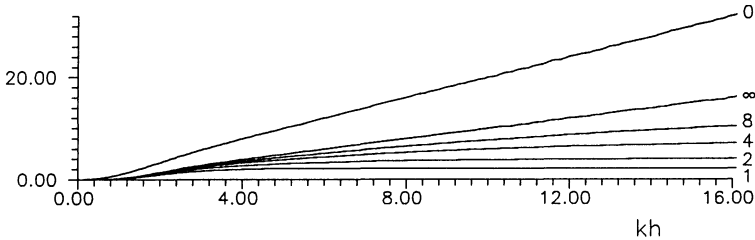


Figure 4 The maximum surface slopes equivalent to the representation of surface elevations in Fig. 3.

$$\sum_{j=0}^{\infty} k_j h c_j = \omega^2 \frac{h}{g} \quad (20)$$

by which the ratio of maximum slopes for a piston type wavemaker becomes

$$\frac{1}{k h c_0} \sum_{j=1}^{\infty} |k_j h c_j| = \frac{1}{2} \left(1 - \frac{k h}{\sinh k h \cosh k h} \right) \quad (21)$$

approaching $1/2$ in in the deep water limit. Fig. 4 shows the maximum surface slopes equivalent to the representation of surface elevations in Fig. 3. The reason for showing the result of retaining 1,2,4, and 8 terms, respectively in summation in Fig. 4 is to illustrate the slow rate of convergence compared with the curves in Fig. 3. It can be shown that (piston type wavemaker)

$$k_j h c_j \propto \frac{1}{j^2} \quad \text{for } j \gg 1 \quad (22)$$

while

$$c_j \propto \frac{1}{j^3} \quad \text{for } j \gg 1 \quad (23)$$

This gives an immense difference of convergence rate as can be seen by computing $\sum_{j=1}^{\infty} 1/j^N$, which to single precision requires $2^{24/N}$ terms i.e. 4096, 256, 64, and 28 terms for $N = 2, 3, 4$, and 5, respectively. The inconveniently slow rate of convergence characterized by $N = 2$ reappears in the new second order terms found below, whereas the well known series term exhibits the the faster convergence rate corresponding to $N = 3$. The problem of slow convergence requires

special attention in the computation of the second order transfer functions; It can be shown numerically that the accuracy obtained by straight forward summation of well over a hundred terms can be obtained using an order of magnitude fewer terms together with the knowledge of the asymptotic rate of convergence.

The significance of the local disturbances in the nonlinear interaction will be treated later.

2.3. Second order solution

Interactions between two wavelets of generally different frequencies ω_n and ω_m constitute the basis of the second order spectrum. The summation indices for the series (14) giving the first order solution for ω_n and ω_m are denoted j and l , respectively, and if $S^{(21)}$ stands for each of the quantities $R^{(21)}$, $\Phi^{(21)}$, $P^{(21)}$, and $\eta^{(21)}$, then $S_{jnlm}^{(21)+}$ and $S_{jnlm}^{(21)-}$ denote the complex superharmonic and subharmonic contributions, respectively, for the interaction between each pair of terms drawn from the two series, i.e.

$$S^{(21)} = \frac{1}{2} \left\{ \sum_{j=0}^{\infty} \sum_{l=0}^{\infty} [S_{jnlm}^{(21)+} + S_{jnlm}^{(21)-}] + \text{c.c.} \right\}; \quad S^{(21)} = \begin{cases} R^{(21)} \\ \Phi^{(21)} \\ P^{(21)} \\ \eta^{(21)} \end{cases} \quad (24)$$

Using (15) to eliminate any appearing $\tanh k_j h$ -term (8a) and (14) yield after straight forward but lengthy algebra

$$\begin{aligned} R_{jnlm}^{(21)\pm} &= \delta_{nm} \left\{ i X_n X_m^{-: *} c_{jn} c_{lm}^{-: *} e^{i(\theta_{jn} \pm \theta_{lm}^{-: *})} \right. \\ &\quad \left[\omega_n \omega_m \mp \frac{g^2 k_{jn} k_{lm}^{-: *}}{\omega_n} \pm \frac{1}{2} \left(\omega_m^3 - \frac{g^2 k_{lm}^2}{\omega_m} \right) \right] + \widehat{lmjn}^{-: *} \Big\} \quad (25a) \\ &= \delta_{nm} H_{jnlm}^{\pm} i X_n X_m^{-: *} c_{jn} c_{lm}^{-: *} e^{i(\theta_{jn} \pm \theta_{lm}^{-: *})} \end{aligned}$$

where

$$\delta_{nm} \equiv \begin{cases} \frac{1}{2} & \text{for } n = m \\ 1 & \text{for } n \neq m \end{cases} \quad (25b)$$

$$\theta_{jn} \equiv \omega_n t - k_{jn} x; \quad \theta_{lm} \equiv \omega_m t - k_{lm} x \quad (25c)$$

and \widehat{lmjn} means "the preceding term permuting l and j as well as m and n ". This symbol is used throughout even in cases where l or j are explicitly given as zero. Furthermore

$$H_{jnlm}^{\pm} \equiv (\omega_n \pm \omega_m) \left(\pm \omega_n \omega_m - \frac{g^2 k_{jn} k_{lm}^{-: *}}{\omega_n \omega_m} \right) + \frac{\omega_n^3 \pm \omega_m^3}{2} - \frac{g^2}{2} \left(\frac{k_{jn}^2}{\omega_n} \pm \frac{k_{lm}^2}{\omega_m} \right) \quad (25d)$$

and the symbol $^{-: *}$ introduced for brevity is defined by

$$Z^{-: *} = \begin{cases} Z & \text{for superharmonics} \\ Z^* & \text{for subharmonics} \end{cases} \quad (26)$$

where $*$ denotes complex conjugation, i.e. $-:*$ is to be interpreted as complex conjugation in case of subharmonics, while being ignored for superharmonics. Furthermore the complex identity

$$\{Z_1 e^{iz_1} + c.c.\} \{Z_2 e^{iz_2} + c.c.\} = \left\{ Z_1 Z_2 e^{i(z_1+z_2)} + Z_1 Z_2^* e^{i(z_1-z_2^*)} \right\} + c.c. \quad (27)$$

where z_1, z_2, Z_1, Z_2 are complex numbers has been used. This identity reveals the origin of the distinction (26) between the superharmonics and the subharmonics used in (25). (Note that originally the term \widehat{lmjn} in (25a) would appear without the conjugation symbol. However, it is seen that (24) still holds irrespective of whether or not the complex conjugation is imposed on a term in $R_{jnlm}^{(21)\pm}$, and accordingly $\widehat{lmjn}^{-:*$ may well be used instead of \widehat{lmjn} .)

It follows that the solution to (1a) and (8a) is †

$$\Phi_{jnlm}^{(21)\pm} = \frac{R_{jnlm}^{(21)\pm}}{D_{jnlm}^\pm} \frac{\cosh(k_{jn} \pm k_{lm}^{-:*)}(z+h)}{\cosh(k_{jn} \pm k_{lm}^{-:*)}h) \quad (28a)}$$

where

$$D_{jnlm}^\pm \equiv g(k_{jn} \pm k_{lm}^{-:*)} \tanh(k_{jn} \pm k_{lm}^{-:*)}h - (\omega_n \pm \omega_m)^2 \quad (28b)$$

For $(j, l) = (0, 0)$ equation (28) is real and it is consistent with Dean and Sharma (1981).

We now turn to the corresponding surface elevation. From (8c) and (14) we obtain

$$\begin{aligned} P_{jnlm}^{(21)\pm} &= \delta_{nm} \left\{ X_n X_m^{-:*)} c_{jn} c_{lm}^{-:*)} e^{i(\theta_{jn} \pm \theta_{lm}^{-:*)}} \right. \\ &\quad \left[\frac{g^2 k_{jn} k_{lm}^{-:*)}}{4\omega_n \omega_m} \mp \frac{1}{4} \omega_n \omega_m - \frac{1}{2} \omega_m^2 \right] + \widehat{lmjn}^{-:*)} \} \quad (29a) \\ &= \delta_{nm} L_{jnlm}^\pm X_n X_m^{-:*)} c_{jn} c_{lm}^{-:*)} e^{i(\theta_{jn} \pm \theta_{lm}^{-:*)}} \end{aligned}$$

where

$$L_{jnlm}^\pm \equiv \frac{1}{2} \left\{ \frac{g^2 k_{jn} k_{lm}^{-:*)}}{\omega_n \omega_m} \mp \omega_n \omega_m - (\omega_n^2 + \omega_m^2) \right\} \quad (29b)$$

which by (1d) yields

$$\eta_{jnlm}^{(21)\pm} = G_{jnlm}^\pm X_n X_m^{-:*)} c_{jn} c_{lm}^{-:*)} e^{i(\theta_{jn} \pm \theta_{lm}^{-:*)}} \quad (30a)$$

† In the previous papers on the subject involving more than one primary frequency only the contribution from the progressive first order waves i.e. $(j, l) = (0, 0)$ has been considered. It appears that all contributions (j, l) enter the transfer functions used for second order wave generation.

where

$$G_{jnlm}^{\pm} \equiv \frac{\delta_{nm}}{g} \left\{ (\omega_n \pm \omega_m) \frac{H_{jnlm}^{\pm}}{D_{jnlm}^{\pm}} - L_{jnlm}^{\pm} \right\} \quad (30b)$$

For $(j, l) = (0, 0)$ this gives the progressive part of the second order bound wave, and G_{0n0m}^{\pm} can be shown to equal the transfer functions G_{nm}^{\pm} given by Ottesen-Hansen (1978) and Sand and Mansard (1986a,b), and we have †

$$\eta_0^{(21)\pm} = \frac{1}{2} \left\{ G_{nm}^{\pm} A_n A_m^{-:\ast} e^{i(\theta_{0n} \pm \theta_{0m})} + \text{c.c.} \right\} \quad (31)$$

With $A_n = a_n - ib_n$ and $A_m^{-:\ast} = a_m \mp ib_m$ (31) may be written $\eta_0^{(21)\pm} = G_{nm}^{\pm} \{(a_n a_m \mp b_n b_m) \cos(\theta_{0n} \pm \theta_{0m}) + (\pm a_n b_m + a_m b_n) \sin(\theta_{0n} \pm \theta_{0m})\}$.

It should be emphasized that in the present formulation of second order wavemaker theory the above calculations of $\eta^{(21)}$ and G_{jnlm}^{\pm} are not needed.

The remaining contributions at second order, $\Phi^{(22)}$ and $\Phi^{(23)}$, represent free waves, and the analogy to the first order solution is evident, since the function Q cf. (3b), (9b), (10b), gives the only deviation from the first order problem. Thus, following the same procedure as for the first order waves only now for superharmonic and subharmonic frequencies, we have

$$\Phi^{(22)} = \Phi^{(22)+} + \Phi^{(22)-} \quad (32a)$$

$$\eta^{(22)} = \eta^{(22)+} + \eta^{(22)-} \quad (32b)$$

$$\Phi^{(22)\pm} = \frac{1}{2} \left\{ \frac{ig A_n A_m^{-:\ast}}{h(\omega_n \pm \omega_m)} \sum_{j=0}^{\infty} c_j^{(22)\pm} \frac{\cosh K_j^{\pm}(z+h)}{\cosh K_j^{\pm} h} e^{i((\omega_n \pm \omega_m)t - K_j^{\pm} z)} + \text{c.c.} \right\} \quad (32c)$$

$$\eta^{(22)\pm} = \frac{1}{2} \left\{ \frac{A_n A_m^{-:\ast}}{h} \sum_{j=0}^{\infty} c_j^{(22)\pm} e^{i((\omega_n \pm \omega_m)t - K_j^{\pm} z)} + \text{c.c.} \right\} \quad (32d)$$

† In the papers by Sand (1982), Barthel et al. (1983), and Sand and Donslund (1985), the transfer function G_{nm}^- for the second order surface elevation as found by Ottesen-Hansen (1978) was used in connection with $\Phi^{(21)-}$ as if $\eta^{(21)-}$ was a free wave i.e. (1d) was solved for $\Phi^{(21)-}$ neglecting that $P^{(21)-} \neq 0$, cf. (8c). In terms of the quantities defined above, the term L_{0n0m}^- (L_{nm}^- for short) was retained in the transfer function for $\Phi^{(21)-}$. This was corrected for the superharmonics cf. Sand and Mansard (1986a,b) and Mansard, Sand, and Klinting (1987) by introducing a so-called U^{\pm} -factor, which may be shown to satisfy

$$U^{\pm} = \frac{g(k_n \pm k_m) \tanh(k_n \pm k_m) h}{(\omega_n \pm \omega_m)^2} \frac{G_{nm}^{\pm} + \delta_{nm} L_{nm}^{\pm}/g}{G_{nm}^{\pm}}$$

In the present formulation $H_{jnlm}^{\pm}/D_{jnlm}^{\pm}$ is used directly in the resulting transfer function without using the more complicated G_{nm}^{\pm} and U^{\pm} -factors.

which includes the progressive-wave term as well as the local disturbances. Here K_j^\pm is the solution to

$$(\omega_n \pm \omega_m)^2 = g K_j^\pm \tanh K_j^\pm h \quad (33)$$

which is the linear dispersion relation generalized to complex wavenumbers, cf. (15) and the discussion there. Using (32c) and (9b) in (1c) and multiplying the resulting equation with $\cosh K_l^\pm(z + h)$, integration from $z = -h$ to $z = 0$ gives the coefficients $c_j^{(22)\pm}$ by virtue of orthogonality, exactly as in the first order case. Let index p take the place of index j then we get

$$\begin{aligned} c_p^{(22)\pm} = \delta_{nm} \frac{h(\omega_n \pm \omega_m) \cosh K_p^\pm h}{g c_{0n} c_{0m} \Lambda_2(K_p^\pm)} & \left\{ \pm \frac{g}{2\omega_n} \sum_{j=0}^{\infty} \frac{c_{jn} k_{jn}}{\cosh k_{jn} h} \Gamma_4(k_{jn}, K_p^\pm) + \widehat{lmjn} \right. \\ & \left. - \sum_{j=0}^{\infty} \sum_{l=0}^{\infty} c_{jn} c_{lm}^{-*} \frac{k_{jn} \pm k_{lm}^{-*}}{\cosh(k_{jn} \pm k_{lm}^{-*})h} \frac{H_{jnlm}^\pm}{D_{jnlm}^\pm} \Gamma_1(k_{jn} \pm k_{lm}^{-*}, K_p^\pm) \right\} \end{aligned} \quad (34)$$

where

$$\Gamma_1(\kappa_1, \kappa_2) \equiv \int_{-h}^0 \cosh \kappa_1(z + h) \cosh \kappa_2(z + h) dz \quad (35a)$$

and

$$\Gamma_4(\kappa_1, \kappa_2) \equiv \kappa_1 \Gamma_2(\kappa_1, \kappa_2) + \frac{1}{h + \ell} \Gamma_3(\kappa_1, \kappa_2) \quad (35b)$$

where

$$\Gamma_2(\kappa_1, \kappa_2) \equiv \int_{-h+d}^0 f(z) \cosh \kappa_1(z + h) \cosh \kappa_2(z + h) dz \quad (35c)$$

and †

$$\Gamma_3(\kappa_1, \kappa_2) \equiv \int_{-h+d}^0 \sinh \kappa_1(z + h) \cosh \kappa_2(z + h) dz \quad (35d)$$

The functions $\Gamma_1 \dots \Gamma_4$ are evaluated in the appendix. Using $\Gamma_1(k_{jn} \pm k_{lm}^{-*}, K_p^\pm)$ as given in (A9) eq. (34) reduces to

$$\begin{aligned} c_p^{(22)\pm} = \delta_{nm} \frac{h(\omega_n \pm \omega_m) \cosh K_p^\pm h}{g c_{0n} c_{0m} \Lambda_2(K_p^\pm)} & \left\{ \pm \frac{g}{2\omega_n} \sum_{j=0}^{\infty} \frac{c_{jn} k_{jn}}{\cosh k_{jn} h} \Gamma_4(k_{jn}, K_p^\pm) + \widehat{lmjn} \right. \\ & \left. - \frac{\cosh K_p^\pm h}{g} \sum_{j=0}^{\infty} \sum_{l=0}^{\infty} c_{jn} c_{lm}^{-*} \frac{k_{jn} \pm k_{lm}^{-*}}{(k_{jn} \pm k_{lm}^{-*})^2 - K_0^{\pm 2}} H_{jnlm}^\pm \right\} \end{aligned} \quad (36)$$

† Here lower bound of the integral for Γ_3 must be taken as $-h + d$ (instead of just $-h$), cf. (9b) and the footnote in connection with (4b). In the integral for Γ_2 , however, either lower bound may be used since $f(z) \equiv 0$ for $-h \leq z < -h + d$.

The denominator D_{jnlm}^\pm and thereby one explicit shallow water singularity has now vanished from the expression.

We now turn to $\Phi^{(28)}$. Let the second order paddle position be given by

$$X_0^{(2)\pm} = \frac{1}{2} \left\{ -i\mathcal{F}^\pm \frac{A_n A_m^{-*}}{h} e^{i(\omega_n \pm \omega_m)t} + \text{c.c.} \right\} \quad (37)$$

and let

$$\Phi^{(28)} = \Phi^{(28)+} + \Phi^{(28)-} \quad (38a)$$

$$\eta^{(28)} = \eta^{(28)+} + \eta^{(28)-} \quad (38b)$$

then

$$\Phi^{(28)\pm} = \frac{1}{2} \left\{ \frac{ig\mathcal{F}^\pm A_n A_m^{-*}}{h(\omega_n \pm \omega_m)} \sum_{j=0}^{\infty} c_j^{(28)\pm} \frac{\cosh K_j^\pm(z+h)}{\cosh K_j^\pm h} e^{i((\omega_n \pm \omega_m)t - K_j^\pm z)} + \text{c.c.} \right\} \quad (38c)$$

$$\eta^{(28)\pm} = \frac{1}{2} \left\{ \mathcal{F}^\pm \frac{A_n A_m^{-*}}{h} \sum_{j=0}^{\infty} c_j^{(28)\pm} e^{i((\omega_n \pm \omega_m)t - K_j^\pm z)} + \text{c.c.} \right\} \quad (38d)$$

where

$$c_j^{(28)\pm} = \sinh K_j^\pm h \frac{\Lambda_1(K_j^\pm)}{\Lambda_2(K_j^\pm)} \quad (39)$$

cf. (17). From (11) or (12) we obtain the transfer function

$$\mathcal{F}^\pm = -\frac{c_0^{(22)\pm}}{c_0^{(28)\pm}} \quad (40)$$

Note that this only assures that the progressive-wave terms ($j = 0$) in (32) and (38) cancel, i.e. the local disturbances ($j = 1, 2, \dots$) still remain. From (36) and (39) we further get

$$\begin{aligned} \mathcal{F}^\pm = & \frac{\delta_{nm} K_0^\pm h}{c_{0n} c_{0m} \Lambda_1(K_0^\pm)(\omega_n \pm \omega_m)} \left\{ \mp \frac{g}{2\omega_n} \sum_{j=0}^{\infty} \frac{c_{jn} k_{jn}}{\cosh k_{jn} h} \Gamma_4(k_{jn}, K_0^\pm) + \widehat{l m j n} \right. \\ & \left. - \frac{\cosh K_p^\pm h}{g} \sum_{j=0}^{\infty} \sum_{l=0}^{\infty} c_{jn} c_{lm}^{-*} \frac{k_{jn} \pm k_{lm}^{-*}}{(k_{jn} \pm k_{lm}^{-*})^2 - K_0^{\pm 2}} H_{jn lm}^\pm \right\} \end{aligned} \quad (41)$$

which is the main result of this theory.

Sand (1982), Barthel et al. (1983), Sand and Donslund (1985) and Mansard and Sand (1986a,b) used three transfer functions denoted F_{11} , F_{12} , and F_{23} . These functions all eliminate free waves which otherwise would have been emitted from the wave paddle due to the interaction between the following combinations of two first order terms (the terms referenced are in (41))

- (i): progressive wavelet and progressive wavelet (F_{11} or the first term in the double summation, $j = l = 0$)
- (ii): component of paddle position and progressive wavelet (F_{12} or the first term in the single summation, $j = 0$)
- (iii): component of paddle position and local disturbance wavelet (F_{23} or the rest of the single summation, $j = 1, 2, \dots$)

In addition to these terms (41) comprises two additional qualitatively different terms both related to the local first order disturbances. These terms are present in order to eliminate the emission of free waves due to the interaction between the first order terms

- (iv): progressive wavelet and local disturbance wavelet (F_{13} and F_{24} defined below or $j = 0, l = 1, 2, \dots$ and vice versa in the double summation)
- (v): local disturbance wavelet and local disturbance wavelet (F_{22} defined below or the rest of the double summation, $j = 1, 2, \dots, l = j = 1, 2, \dots$)

Except for the corrections given previously as footnotes the function \mathcal{F}^\pm (excluding the new terms) is consistent with the findings in the above referenced papers.

The terms mentioned under (iv) and (v) are included in the analysis for regular waves given by Fontanet (1961) and Hudspeth and Sulisz (1991) and also recognized although not included by Suh and Dalrymple (1987).

With $A_n = a_n - ib_n$ and $A_m^{-:*=} = a_m \mp ib_m$ we have in a real representation

$$\begin{aligned} X_0^{(2)\pm} = & \frac{\Re\{\mathcal{F}^\pm\}}{h} \{ (a_n a_m \mp b_n b_m) \sin(\omega_n \pm \omega_m)t + (\mp a_n b_m - a_m b_n) \cos(\omega_n \pm \omega_m)t \} \\ & - \frac{\Im\{\mathcal{F}^\pm\}}{h} \{ (\mp a_n b_m - a_m b_n) \sin(\omega_n \pm \omega_m)t - (a_n a_m \mp b_n b_m) \cos(\omega_n \pm \omega_m)t \} \end{aligned} \quad (42)$$

The new term (iv) mentioned above makes it tedious to derive the real and imaginary parts of the transfer function (41), since the complex term $k_{jn} \pm k_{lm}^{-:*=}$ in this case is neither real nor purely imaginary. It is recommended to use the relatively simple complex formulation for practical application and to let a computer separate the complex result whenever appropriate in the actual implementation. However, we shall derive $\Re\{\mathcal{F}^\pm\}$ and $\Im\{\mathcal{F}^\pm\}$ for the sake of comparison with F_{11} , F_{12} , and F_{23} .

$\Re\{\mathcal{F}^\pm\}$ and $\Im\{\mathcal{F}^\pm\}$ may be split up into three contributions

$$\Re\{\mathcal{F}^\pm\} = \mp (F_{11}^\pm + F_{12}^\pm + F_{13}^\pm) h \quad (43)$$

and

$$\Im\{\mathcal{F}^\pm\} = (F_{22}^\pm + F_{23}^\pm + F_{24}^\pm) h \quad (44)$$

where the factor h is included for historical reasons.

In addition to the well known transfer functions F_{11}^\pm , F_{12}^\pm , and F_{23}^\pm three new functions F_{13}^\pm , F_{22}^\pm , and F_{24}^\pm appear (The succession of indices as well as the sign convention has been chosen to match the definitions of the old functions F_{11}^\pm , F_{12}^\pm , and F_{23}^\pm). Remembering that c_{jn} (c_{lm}) and k_{jn} (k_{lm}) are real for $j = 0$ ($l = 0$) and purely imaginary for $j = 1, 2, \dots$ ($l = 1, 2, \dots$) we get

$$F_{11}^\pm = B^\pm \frac{k_{0n} \pm k_{0m}}{(k_{0n} \pm k_{0m})^2 - K_0^{\pm 2}} H_{0n0m}^\pm \quad (45)$$

$$F_{12}^\pm = \frac{\delta_{nm} K_0^\pm h}{c_{0m} \Lambda_1(K_0^\pm)(\omega_n \pm \omega_m)} \left\{ \mp \frac{g}{2\omega_n} \frac{k_{0n}}{\cosh k_{0n} h} \Gamma_4(k_{0n}, K_0^\pm) + \widehat{lm0n} \right\} \quad (46)$$

$$\begin{aligned} F_{13}^\pm = B^\pm \sum_{j=1}^{\infty} \frac{\frac{c_{jn}}{c_{0n}}}{(k_{jn}^2 + k_{0n}^2 - K_0^{\pm 2})^2 - 4k_{jn}^2 k_{0m}^2} & \left\{ k_{jn} (k_{jn}^2 - k_{0m}^2 - K_0^{\pm 2}) \Re\{H_{jn0m}\} \right. \\ & \left. \pm k_{0m} (-k_{jn}^2 + k_{0m}^2 - K_0^{\pm 2}) i\Im\{H_{jn0m}\} \right\} \\ & + \widehat{lm0n} \end{aligned} \quad (47)$$

and

$$iF_{22}^\pm = B^\pm \frac{1}{c_{0n} c_{0m}} \sum_{j=1}^{\infty} \sum_{l=1}^{\infty} c_{jn} c_{lm}^{-*:} \frac{k_{jn} \pm k_{lm}^{-*:}}{(k_{jn} \pm k_{lm}^{-*:})^2 - K_0^{\pm 2}} H_{jn0m}^\pm \quad (48)$$

$$iF_{23}^\pm = \frac{\delta_{nm} K_0^\pm h}{c_{0n} c_{0m} \Lambda_1(K_0^\pm)(\omega_n \pm \omega_m)} \left\{ \mp \frac{g}{2\omega_n} \sum_{j=1}^{\infty} \frac{c_{jn} k_{jn}}{\cosh k_{jn} h} \Gamma_4(k_{jn}, K_0^\pm) + \widehat{lmjn} \right\} \quad (49)$$

$$\begin{aligned} iF_{24}^\pm = B^\pm \sum_{j=1}^{\infty} \frac{\frac{c_{jn}}{c_{0n}}}{(k_{jn}^2 + k_{0n}^2 - K_0^{\pm 2})^2 - 4k_{jn}^2 k_{0m}^2} & \left\{ k_{jn} (k_{jn}^2 - k_{0m}^2 - K_0^{\pm 2}) i\Im\{H_{jn0m}\} \right. \\ & \left. \pm k_{0m} (-k_{jn}^2 + k_{0m}^2 - K_0^{\pm 2}) \Re\{H_{jn0m}\} \right\} \\ & + \widehat{lm0n} \end{aligned} \quad (50)$$

where

$$B^\pm \equiv \frac{\delta_{nm} K_0^{\pm 2}}{(\omega_n \pm \omega_m)^3} \quad (51)$$

and from (25d)

$$\Re\{H_{jn0m}\} = \pm(\omega_n \pm \omega_m) \omega_n \omega_m + \frac{\omega_n^3 \pm \omega_m^3}{2} - \frac{g^2}{2} \left(\frac{k_{jn}^2}{\omega_n} \pm \frac{k_{0m}^2}{\omega_m} \right) \quad (52a)$$

$$i\Im\{H_{jn0m}\} = -(\omega_n \pm \omega_m) \frac{g^2 k_{jn} k_{0m}}{\omega_n \omega_m} \quad (52b)$$

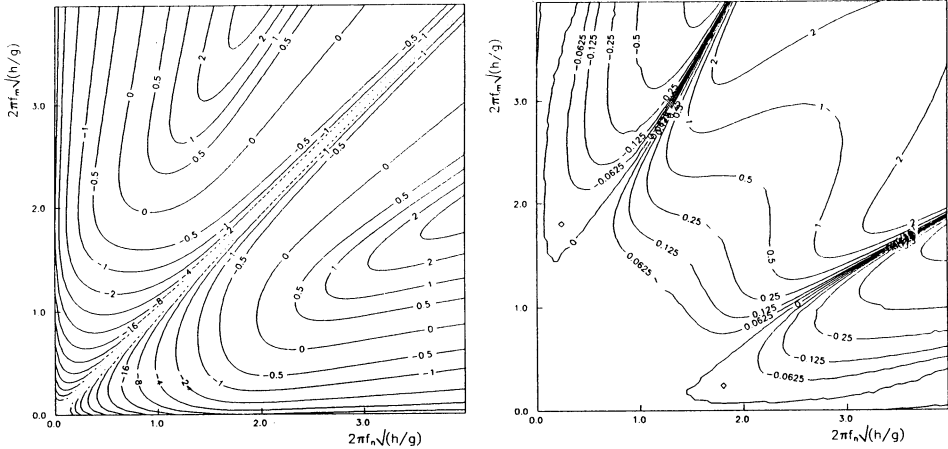


Figure 5 Components of subharmonic complex transfer function $\mathcal{F}^-/\delta_{nm}$ versus dimensionless first order frequencies $2\pi f_n \sqrt{h/g}$ and $2\pi f_m \sqrt{h/g}$ for a piston type wavemaker. (a): $\Re\{\mathcal{F}^-\}/\delta_{nm}$; Contour lines are a subset of $(0, \pm 1/2, \pm 1, \pm 2, \pm 4, \dots)$ (b): $\Im\{\mathcal{F}^-\}/\delta_{nm}$; Contour lines are a subset of $(0, \pm 1/16, \pm 1/8, \pm 1/4, \pm 1/2, \pm 1, \pm 2, \pm 4, \dots)$

3. PISTON TYPE WAVEMAKER

Using the results for Γ_4 from the appendix in (37b) gives

$$\begin{aligned} \mathcal{F}^\pm = & \frac{\delta_{nm} K_0^{\pm 2} h}{c_0 c_{0m} (\omega_n \pm \omega_m)^3} \left\{ \mp g \frac{\omega_n^2 - (\omega_n \pm \omega_m)^2}{2\omega_n} \sum_{j=0}^{\infty} c_{jn} \frac{k_{jn}^2}{k_{jn}^2 - K_0^{\pm 2}} + \widehat{lmjn} \right. \\ & \left. + \sum_{j=0}^{\infty} \sum_{l=0}^{\infty} c_{jn} c_{lm}^{-:*\!} \frac{k_{jn} \pm k_{lm}^{-:*\!}}{(k_{jn} \pm k_{lm}^{-:*\!})^2 - K_0^{\pm 2}} H_{jn lm}^\pm \right\} \quad (53) \end{aligned}$$

For a piston wavemaker Fig. 5a,b show the real and imaginary parts of the subharmonic complex transfer function $\mathcal{F}^-/\delta_{nm}$ versus dimensionless first order frequencies $2\pi f_n \sqrt{h/g}$ and $2\pi f_m \sqrt{h/g}$. Fig. 6a,b show the equivalent for the superharmonics.

The simplification of F_{11}^\pm , F_{13}^\pm , F_{22}^\pm , and F_{24}^\pm lies implicitly in the first order transfer functions, see (17). F_{12}^\pm and F_{23}^\pm reduce to

$$F_{12}^\pm = \mp B^\pm \left\{ \frac{g}{c_{0m}} \frac{\omega_n^2 - (\omega_n \pm \omega_m)^2}{2\omega_n} \frac{k_{0n}^2}{k_{0n}^2 - K_0^{\pm 2}} + \widehat{lm0n} \right\} \quad (54)$$

and

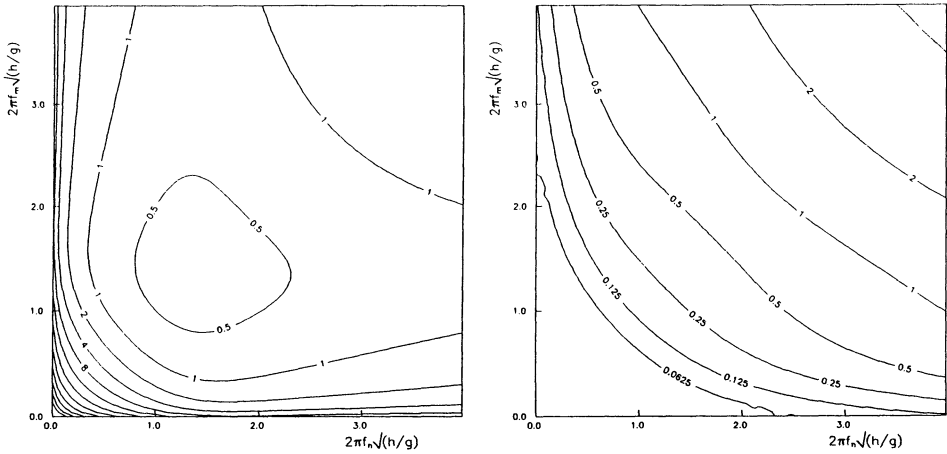


Figure 6 Components of superharmonic complex transfer function $\mathcal{F}^+/\delta_{nm}$ versus dimensionless first order frequencies $2\pi f_n \sqrt{h/g}$ and $2\pi f_m \sqrt{h/g}$ for a piston type wave-maker. (a): $\Re\{\mathcal{F}^+\}/\delta_{nm}$; Contour lines are a subset of $(0, \pm 1/2, \pm 1, \pm 2, \pm 4, \dots)$ (b): $\Im\{\mathcal{F}^+\}/\delta_{nm}$; Contour lines are a subset of $(0, \pm 1/16, \pm 1/8, \pm 1/4, \pm 1/2, \pm 1, \pm 2, \pm 4, \dots)$

$$iF_{23}^\pm = \mp B^\pm \frac{1}{c_{0n} c_{0m}} \left\{ g \frac{\omega_n^2 - (\omega_n \pm \omega_m)^2}{2\omega_n} \sum_{j=1}^{\infty} c_{jn} \frac{k_{jn}^2}{k_{jn}^2 - K_0^{\pm 2}} \pm \widehat{lmjn} \right\} \quad (55)$$

Note that for the subharmonics the factor $\omega_m^2 - (\omega_m - \omega_n)^2$ in the \widehat{lmjn} -term in F_{12}^\pm and F_{23}^\pm vanishes for $\omega_n = 2\omega_m$ (if $\omega_n < \omega_m$ is chosen this appears for $\omega_m = 2\omega_n$ in the previous term) and the series-term vanishes except for the first term ($j = 0$) where $k_{0m} - K_0^- = 0$. In this special case the Γ_4 -part of the expression (cf. (37b)) should be replaced by $\Lambda_1(k_{0m})$ (cf. (A11) in the appendix) or equivalently $(\omega_m^2 - (\omega_m - \omega_n)^2)/(k_{0m}^2 - K_0^2)$ should be recognized as cc_g (where we have locally defined c and c_g as the phase velocity and group velocity for $\omega = \omega_m$) using the identity $cc_g = \omega^4/(gk^3 c_0)$ (where c_0 is the Biesel transfer function). This way it may easily be shown that the contribution $g(\omega_m^2 - (\omega_m - \omega_n)^2)/(2\omega_m) \sum_{l=0}^{\infty} c_{lm} k_{lm}^2 / (k_{lm}^2 - K_0^2)$ should be replaced by $\omega_m^3/(2k_{0m})$ for $\omega_m = \omega_n/2$.

4. EXPERIMENTAL VERIFICATION

A variety of experiments have been made with a piston type wavemaker. At present only the tests for regular waves have been analysed and experimental results for wave groups and irregular waves will be published later.

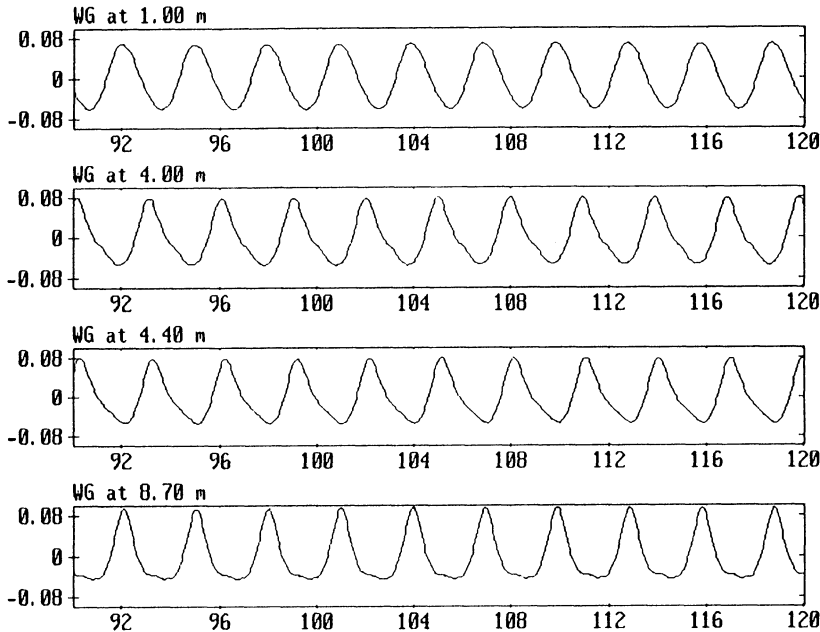


Figure 7 Time series of surface elevation at different positions in the flume ($x = 0$ at wavemaker) using a FIRST ORDER control signal ($h = 0.70m$, $T = 3.0s$, and $H = 0.14m$).

The experimental facility used is a 20m flume, 1.0m deep and 0.60m wide, equipped with a piston type wavemaker in one end ($x = 0$) and an efficient absorber in the other end. For a depth of $h = 0.70m$, a period of $T = 3.0s$ and a height of $H = 0.14m$ Figs. 7 and 8 show time series of surface elevation at different positions in the flume using first order and second order control signals, respectively. The use of first order wavemaker theory (Fig. 7) gives a spurious, free superharmonic, progressive wave generated in addition to the natural, forced superharmonic. These two superharmonic wave components progress at different celerities creating an interference pattern resulting in different wave shapes throughout the flume, the repetition length (in this case) theoretically predicted to be 19.1m. Close to the wavemaker (WG at 1.00m in Fig. 7) the two superharmonics almost cancel and the elevation becomes nearly sinusoidal, which is not a stable form for this rather nonlinear wave. Further down the flume this results in vertical assymetry or secondary peaks in the troughs. The use of second order wavemaker theory solves these problems, see Fig. 8.

This test was used by Sand and Mansard to successfully verify their version of second order wavemaker theory. The difference between the two theories is small for this rather shallow water example, but it is indeed significant in deeper water.

A detailed analysis was made using the following two steps for the surface elevation time series measured at each wave gauge (positions 1.00, 4.00, 4.40, and

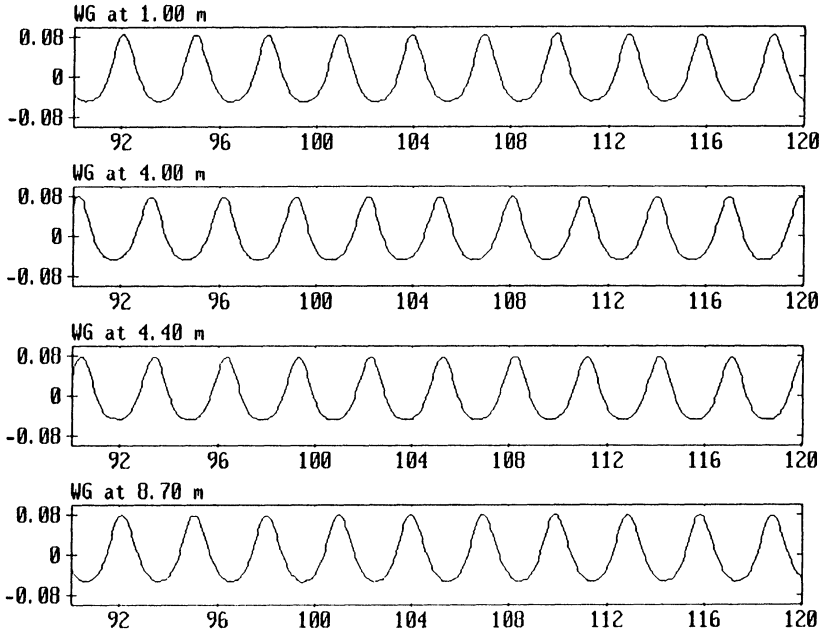


Figure 8 Time series of surface elevation at different positions in the flume ($x = 0$ at wavemaker) using a SECOND ORDER control signal ($h = 0.70m$, $T = 3.0s$, and $H = 0.14m$).

8.70m from the wavemaker): 1) Band pass filtering around the primary frequency and the superharmonic frequency, respectively and 2) zero-crossing of the filtered time series in order to obtain the respective wave heights.

For a wide range of periods, $T = 3.0, 2.0, 1.2$, and 0.8 s corresponding to water depth to wave length ratios, $h/L = 0.09, 0.15, 0.32$, and 0.7 . The values of the complex transfer function \mathcal{F}^+ for these periods are $(1.53, 0.00)$, $(0.40, 0.03)$, $(0.18, 0.15)$, and $(0.29, 0.41)$. If the new terms corresponding to F_{13}^+ , F_{22}^+ and F_{22}^+ are neglected these values become $(1.46, -0.02)$, $(0.25, -0.07)$, $(-0.17, -0.13)$, and $(-0.44, -0.20)$. As expected the new terms are important except near the shallow water limit. Even in the intermediate water depth (represented here by $T = 1.2\text{s}$) the new terms change the original values by roughly -100% .

Fig. 9 compares the experiments with theory. The solid curves are theoretical results and the experiments are given by white squares in case of first order generation and black squares in case of second order generation.

For the primary wave the constant wave height given by the solid line gives the specified wave height and the experimental values are seen to be somewhat smaller.

For the superharmonic the constant bound-wave height given by the straight lines are the theoretical values based on the specified primary wave height and

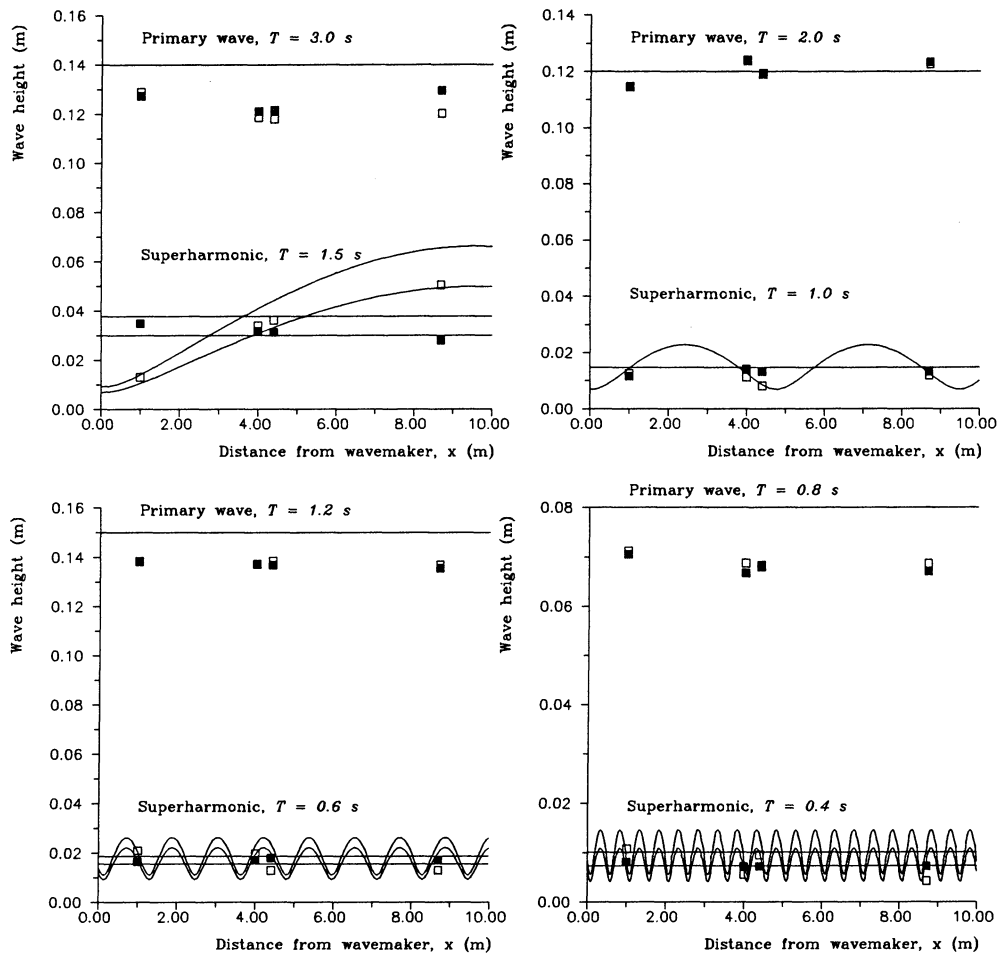


Figure 9 Wave heights for the primary wave and the superharmonic using first order control signal (white squares) and second order control signal (black squares), respectively. Theory is indicated by the curves and the straight lines. For the superharmonic these give the second order theory for generation correct to first order (curves) and to second order (lines), respectively. The theory of the superharmonic is shown both for the specified and for the actually measured primary wave height (spatial mean). Water depth is $h = 0.70\text{m}$.

the spatial mean of the measured primary wave heights, respectively. The black squares are expected to lie between these two lines and the agreement is satisfac-

tory.

The oscillating curves give the second order theoretical height of the interference wave pattern of bound and free superharmonic components resulting from first order wave generation. Again, the upper curve is based on the specified primary wave height whereas the lower one is based on the spatial mean of the measured primary wave heights. The white squares are expected to lie between the two oscillating curves. The agreement is generally good.

The experiments clearly show how second order wave generation gives waves of constant form as opposed to first order generation (the black squares are far closer to being constant than the white squares). This conclusion holds even in deep water.

Acknowledgements. Jesper Skourup checked the theoretical development, Peter Hyllested made the necessary extensions of the DHI Wave Synthesizer, and Niels Mathiesen assisted with the experiments.

References

- Barthel, V., Mansard, E.P.D. Sand, S.E., and Vis, F.C., 1983. Group bounded long waves in physical models. *Ocean Engrg.* **10**(4), 261–294.
- Biesel, F., 1951. Etude théorique d'un type d'appareil à houle. *La Houille Blanche* **6**(2), 152–165.
- Bowers, E. C. 1989. Wave grouping and harbour design. *Proc. Instn Civ. Engrs., Part 2*, **85**, 237–258.
- Buhr Hansen, J., Schiolten, P., and Svendsen, I.A., 1975. Laboratory generation of waves of constant form. Series Paper **9**, Inst. of Hydrodyn. and Hydraulic Engrg. (ISVA), Tech. Univ. of Denmark, 56 pp.
- Dean, R.G. and Sharma, J.N., 1981. Simulation of wave systems due to nonlinear directional spectra, *Proc. Int. Symp. Hydrodynamics in Ocean Engrg., The Norwegian Inst. of Techn.* **2**, 1211–1222.
- Flick, R.E. and Guza, R.T., 1980. Paddle generated waves in laboratory channels. *J. WatWays, Port, Coastal Ocean Div., ASCE* **106**(WW1), 79–97.
- Fontanet, P., 1961. Théorie de la génération de la houle cylindrique par un batteur plan. *La Houille Blanche* **16**(1), 3–31 (part 1) and 174–196 (part 2).
- Hudspeth, R. T. and W. Sulisz, 1990. Stokes drift in two-dimensional wave flumes. *J. Fluid Mech.* **230**, 209–229.
- Klopman, G. and Van Leeuwen, P. J., 1990. An efficient method for the reproduction of non-linear random waves. *Proc. 22nd Int. Conf. Coastal Engrg., Delft, The Netherlands, 1990, ASCE, New York, 1991*, **1**, 478–488.
- Madsen, O. S., 1971. On the generation of long waves. *J. Geophys. Res.* **76**, 8672–8673.
- Mansard, E. P., Barthel V., Funke, E. R., Klinting, P., and Jensen, O. J., 1989. Wave grouping and harbour design - discussion of Bowers (1988). *Proc. Instn Civ. Engrs., Part 2*, **87**, 135–142.

- Ottesen Hansen, N.-E., 1978. Long Period waves in natural wave trains. *Prog. Rep.* 46, Inst. of Hydrodyn. and Hydraulic Engrg. (ISVA), Tech. Univ. of Denmark, 13-24.
- Sand, S.E., 1982. Long wave problems in laboratory models. *J. WatWays, Port, Coastal Ocean Div., ASCE* 108(WW4), 492-503.
- Sand, S.E. and Donslund, B., 1985. Influence of wave board type on bounded long waves. *J. Hydraulic Res.* 23(2), 147-163.
- Sand, S.E. and Mansard, E.P.D., 1986a. Description and reproduction of higher harmonic waves. National Research Council of Canada, Hydraulics Laboratory Tech. Rep. TR-HY-012.
- Sand, S.E. and Mansard, E.P.D., 1986b. Reproduction of higher harmonics in irregular waves. *Ocean Engrg.* 13(1), 57-83.
- Sharma, J.N., 1979. Development and evaluation of a procedure for simulating a random directional second-order sea surface and associated wave forces. Ph.D. Dissertation, University of Delaware, 139 pp.
- Suh, K. and R. A. Dalrymple, 1987. Directional wavemaker theory: A spectral approach. Proc. IAHR-Seminar *Wave analysis and generation in laboratory basins*, Lausanne, Switzerland, 1987, 389-395.
- Svendsen, I. A., 1985. Physical modelling of water waves. *Physical Modelling in Ocean Engineering*, Dalrymple, R. A., ed., Rotterdam, A. A. Balkema.
- Stokes, G.G. 1847. On the theory of oscillatory waves, *Trans. Camb. Phil. Soc.* 8, 441-455.

Appendix

The functions $\Gamma_{1\dots 4}$ (see (35)) are evaluated in this appendix.

In order to reduce the computational cost for the case of irregular waves it is important to avoid terms like $\sinh(k_{0n} \pm k_{0m})h$, since these would have to be computed $\propto N^2$ times, where N is the number of frequencies representing the first order spectrum, whereas terms like $\sinh k_{0n}h$ need only be computed $\propto N$ times, provided the sufficient computer memory is available. Three forms of each of the functions $\gamma_{1\dots 3}$ (see below) are given. The first one is the standard form for the relevant integral, the second form is suited for the general wave board type, whereas the last form is preferable for $d = 0$.

For $\kappa_1 \neq \kappa_2$ we get

$$\begin{aligned}\Gamma_1(\kappa_1, \kappa_2) &\equiv \int_{-h}^0 \cosh \kappa_1(z+h) \cosh \kappa_2(z+h) dz \\ &= \gamma_1(\kappa_1, \kappa_2; h)\end{aligned}\tag{A1}$$

where

$$\begin{aligned}
\gamma_1(\kappa_1, \kappa_2; r) &\equiv \frac{\sinh(\kappa_1 - \kappa_2)r}{2(\kappa_1 - \kappa_2)} + \frac{\sinh(\kappa_1 + \kappa_2)r}{2(\kappa_1 + \kappa_2)} \\
&= \frac{1}{\kappa_1^2 - \kappa_2^2} \left\{ \kappa_1 \sinh \kappa_1 r \cosh \kappa_2 r - \kappa_2 \cosh \kappa_1 r \sinh \kappa_2 r \right\} \\
&= \frac{\cosh \kappa_1 r \cosh \kappa_2 r}{\kappa_1^2 - \kappa_2^2} \left\{ \kappa_1 \tanh \kappa_1 r - \kappa_2 \tanh \kappa_2 r \right\}
\end{aligned} \tag{A2}$$

and

$$\begin{aligned}
\Gamma_2(\kappa_1, \kappa_2) &\equiv \int_{-h+d}^0 f(z) \cosh \kappa_1(z+h) \cosh \kappa_2(z+h) dz \\
&= \gamma_1(\kappa_1, \kappa_2; h) - \frac{d+\ell}{h+\ell} \gamma_1(\kappa_1, \kappa_2; d) \\
&\quad - \frac{1}{h+\ell} \left\{ \gamma_2(\kappa_1, \kappa_2; h) - \gamma_2(\kappa_1, \kappa_2; d) \right\}
\end{aligned} \tag{A3}$$

where

$$\begin{aligned}
\gamma_2(\kappa_1, \kappa_2; r) &\equiv \frac{\cosh(\kappa_1 - \kappa_2)r}{2(\kappa_1 - \kappa_2)^2} + \frac{\cosh(\kappa_1 + \kappa_2)r}{2(\kappa_1 + \kappa_2)^2} \\
&= \frac{1}{(\kappa_1^2 - \kappa_2^2)^2} \left\{ (\kappa_1^2 + \kappa_2^2) \cosh \kappa_1 r \cosh \kappa_2 r - 2\kappa_1 \kappa_2 \sinh \kappa_1 r \sinh \kappa_2 r \right\} \\
&= \frac{\cosh \kappa_1 r \cosh \kappa_2 r}{(\kappa_1^2 - \kappa_2^2)^2} \left\{ (\kappa_1^2 + \kappa_2^2) - 2\kappa_1 \kappa_2 \tanh \kappa_1 r \tanh \kappa_2 r \right\}
\end{aligned} \tag{A4}$$

and

$$\begin{aligned}
\Gamma_3(\kappa_1, \kappa_2) &\equiv \int_{-h+d}^0 \sinh \kappa_1(z+h) \cosh \kappa_2(z+h) dz \\
&= \gamma_3(\kappa_1, \kappa_2; h) - \gamma_3(\kappa_1, \kappa_2; d)
\end{aligned} \tag{A5}$$

where

$$\begin{aligned}
\gamma_3(\kappa_1, \kappa_2; r) &\equiv \frac{\cosh(\kappa_1 - \kappa_2)r}{2(\kappa_1 - \kappa_2)} + \frac{\cosh(\kappa_1 + \kappa_2)r}{2(\kappa_1 + \kappa_2)} \\
&= \frac{1}{\kappa_1^2 - \kappa_2^2} \left\{ \kappa_1 \cosh \kappa_1 r \cosh \kappa_2 r - \kappa_2 \sinh \kappa_1 r \sinh \kappa_2 r \right\} \\
&= \frac{\cosh \kappa_1 r \cosh \kappa_2 r}{\kappa_1^2 - \kappa_2^2} \left\{ \kappa_1 - \kappa_2 \tanh \kappa_1 r \tanh \kappa_2 r \right\}
\end{aligned} \tag{A6}$$

and

$$\begin{aligned}
\Gamma_4(\kappa_1, \kappa_2) &\equiv \kappa_1 \Gamma_2(\kappa_1, \kappa_2) + \frac{1}{h+\ell} \Gamma_3(\kappa_1, \kappa_2) \\
&= \kappa_1 \left\{ \gamma_1(\kappa_1, \kappa_2; h) - \frac{d+\ell}{h+\ell} \gamma_1(\kappa_1, \kappa_2; d) \right\} \\
&\quad - \frac{1}{h+\ell} \frac{\kappa_2}{(\kappa_1^2 - \kappa_2^2)^2} \left(2\kappa_1 \kappa_2 (\cosh \kappa_1 h \cosh \kappa_2 h - \cosh \kappa_1 d \cosh \kappa_2 d) \right)
\end{aligned}$$

$$- (\kappa_1^2 + \kappa_2^2)(\sinh \kappa_1 h \sinh \kappa_2 h - \sinh \kappa_1 d \sinh \kappa_2 d) \Big) \\ (A7)$$

The case of $\kappa_1 = \kappa_2 = \kappa$ may occur in Γ_4 and we get

$$\Gamma_4(\kappa, \kappa) = \frac{1}{2} \left\{ \kappa h + \sinh \kappa h \cosh \kappa h - \frac{d + \ell}{h + \ell} (\kappa d + \sinh \kappa d \cosh \kappa d) \right. \\ \left. - \frac{\kappa}{h + \ell} \frac{h^2 - d^2}{2} \right\} \quad (A8)$$

With reference to (34a) we only need Γ_1 for $(\kappa_1, \kappa_2) = (k_{jn} \pm k_{lm}^{-*}, K_p^\pm)$. In terms of D_{jnlm}^\pm defined in (28b) we get

$$\Gamma_1(k_{jn} \pm k_{lm}^{-*}, K_p^\pm) = \frac{\cosh(k_{jn} \pm k_{lm}^{-*})h \cosh K_p^\pm h}{g((k_{jn} \pm k_{lm}^{-*})^2 - K_p^{\pm 2})} D_{jnlm}^\pm \quad (A9)$$

In the special case of a piston type wavemaker ($d = 0, \ell = \infty$) application of the dispersion relations (29) and (33) brings $\Gamma_4(k_{jn}, K_p^\pm)$ in a very simple form:

$$\Gamma_4(k_{jn}, K_p^\pm) = k_{jn} \frac{\cosh k_{jn} h \cosh K_p^\pm h}{g(k_{jn}^2 - K_p^{\pm 2})} (\omega_n^2 - (\omega_n \pm \omega_m)^2) \quad (A10)$$

Finally we note that for the piston type wavemaker

$$\Gamma_4(\kappa, \kappa) = \Lambda_2(\kappa) \quad (A11)$$

where Λ_2 is given by (17b).

Session 2

Fluid Loading

COMPARISON OF LOADS PREDICTED USING "NEWWAVE" AND OTHER WAVE MODELS WITH MEASUREMENTS ON THE TERN STRUCTURE

J.B. Rozario, P.S. Tromans, P.H. Taylor and M. Efthymiou*

Shell Research B.V.
Postbus 60
2280 AB Rijswijk
The Netherlands

* Shell U.K. Exploration and Production
1, Altens Farm Road
Nigg, Aberdeen AB9 2HY
Scotland

Global wave loads measured on the Tern platform during a very severe storm have been compared with predictions made on the basis of three different models for wave kinematics. The first is the "Newwave" theory, a broadband-based, probabilistic-based model for the extreme waves of a random seastate. The second model involves complex time-domain simulation of random directional seas. Both these theories are used with the Morison equation and realistic force coefficients to predict global forces. The third wave model is the Stokes fifth-order theory with artificial values for the force coefficients, as used in conventional design practice.

Both the Newwave theory and the random directional simulations lead to predicted base shear forces that are comparable to the measured values over a wide range. If non-linear effects in the ocean surface are accounted for, then the Newwave theory predicts the base shear generated by the largest wave of the storm with a very high degree of accuracy. In contrast, calculations based on the Stokes kinematics of conventional design practice overpredict the measured loads over the whole range studied.

It appears that Newwave is the most suitable available wave theory for routine use in the design and analysis of structures such as Tern.

INTRODUCTION

The computation of wave forces on offshore, space-frame structures involves two steps. The first is the determination of fluid kinematics around the structure associated with waves and currents. The second stage is the calculation of forces on the platform generated by the fluid motion. Thus, realistic predictions of global

loads require realistic, verified theories for the kinematics of the flow beneath the surface waves.

In mid 1989 a structural monitoring system was put into operation by Shell U.K. Exploration and Production on the Tern platform. The platform is located in the UK sector of the northern North Sea, as shown on Figure 1, and stands in a water depth of 167 m.

The platform comprises a piled steel space-frame sub-structure and a module support frame (MSF), which carries the topside facilities including drilling, process and accommodation packages. The jacket was designed for an estimated 100-year wave of 30.5 m (see Figure 2).

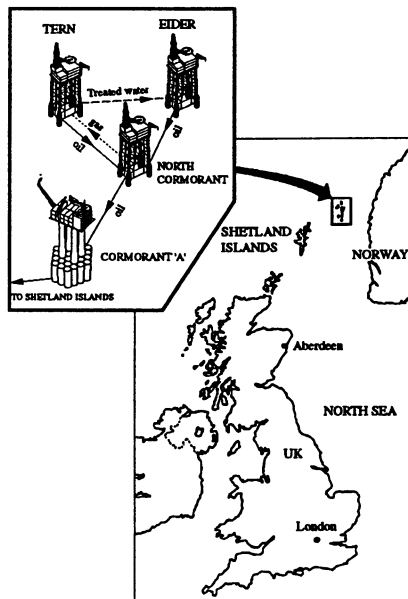


Figure 1 Platform location

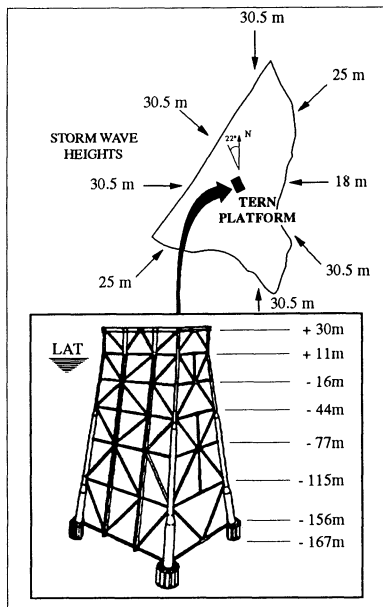


Figure 2 Jacket and MSF configuration and storm wave heights

The monitoring system on Tern (see Figure 3) consists of 68 strain gauges positioned near the base of the four corner legs, a wind sensor placed on top of the derrick, two wave-height sensors at different locations, and two water-particle velocity meters attached to the jacket at elevations of -13 m and -41 m. The strain gauge readings are used to establish the axial load, bending moment (in two orthogonal directions) and shear force (in two orthogonal directions) for every instrumented brace and leg. These member forces are then combined to give base shear and overturning moments for the entire structure. Four accelerometers were also installed to monitor the dynamic behaviour of the structure. The specific objective of the system was to measure both the platform's global storm loading and environmental conditions at the same time. Such simultaneous measurements offer the opportunity to test various techniques for predicting fluid loads.

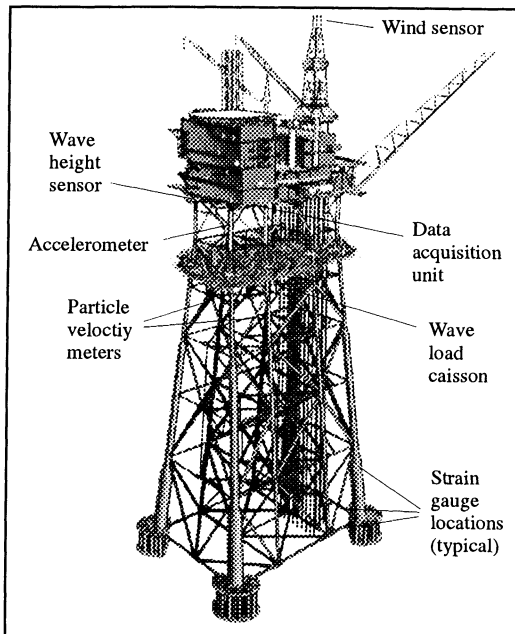


Figure 3 Structural monitoring system

Shell has developed two broadband models of wave kinematics that reflect the random, broadband nature of real seas. These are the 'Random Directional Wave Force' (RDWF) [1] and 'Newwave' [2] theories. Both models, which are incorporated in the simulation program DYNAL/DYNSCRN, make use of Morison's equation and realistic force coefficients. Work on wave load prediction and on the comparing, testing and refining of both theories is discussed in Refs. 1 to 13. In particular, Elzinga and Tromans [13] have already made some comparisons between measured and predicted forces on Tern for a storm with a significant wave height of 12 m. They found good agreement between regression lines derived from measured data and values predicted using Newwave and RDWF, essentially showing both methods to be unbiased predictors.

In this paper we briefly revisit their results to compare them with predictions made using conventional design practice. However, our main interest is with the previously unreported global load measurements taken during a storm on January 1st 1992. With a significant wave height of 13.7 m and a maximum individual wave height of 25.5 m, this is a much more severe storm than any previously analysed or recorded and approaches the 100-year storm condition. Moreover, the storm included some rather high crests and, hence, steep waves, which test

the capability of the wave models to deal with non-linearity. In the present paper we shall concentrate on these high crests. The comparisons made cannot be extensive, but they are sufficient to indicate trends.

THE WAVE MODELS

The ocean surface

In conventional design and assessment practices, wave loads on fixed offshore structures are calculated using a deterministic, periodic, unidirectional wave theory such as Stokes'. In fact, the variation of the ocean surface is a random process, with wave energy travelling in many directions. It is therefore better represented by the sum of numerous linear waves, each having a different amplitude, frequency, direction of travel and random phase. Thus, the surface elevation is

$$\eta(x,y,t) = \sum_n \sum_i c_{n,i} \cos(k_n x \cos\theta_{n,i} + k_n y \sin\theta_{n,i} - \omega_n t + \varepsilon_{n,i}), \quad (1)$$

where n, i are large and the expected value of amplitude $c_{n,i}$ is given by

$$\langle c_{n,i}^2/2 \rangle = f(\omega_n, \theta_{n,i}) S(\omega_n) \Delta\omega \Delta\theta \quad (2)$$

For component n, i , k_n is the wavenumber, $\theta_{n,i}$ is the direction relative to the mean wave direction, ω_n is the frequency, and $\varepsilon_{n,i}$ is the random phase angle. $S(\omega_n)$ is the surface energy spectrum and $f(\omega_n, \theta_{n,i})$ is a frequency dependent spreading function. The monitoring system on Tern provides sufficient information to specify $f(\omega_n, \theta_{n,i})$ and $S(\omega_n)$.

The random directional wave force theory

The random directional wave force (RDWF) model in the DYNAL/DYNSCRN program makes use of Eqs. (1) and (2) together with randomly selected values of c_n and ε_n to generate random time series of ocean surface elevation around the structure. Selection of c_n values requires the specification of $S(\omega_n)$ and $f(\omega_n, \theta_{n,i})$. In the present studies the empirical spectrum, derived from the surface elevation, is used for $S(\omega_n)$, while $f(\omega_n, \theta_{n,i})$ is obtained by matching cosine-2S functions to measurements of surface elevation and particle velocities [14]. Linear theory can be used to deduce water-particle kinematics [8, 9]. The theory yields realistic results for the kinematics well below the ocean surface. However, near the mean water level the linear values are modified using the 'delta stretching' technique (see Figure 4) as described by Rodenbusch and Forristall [9].

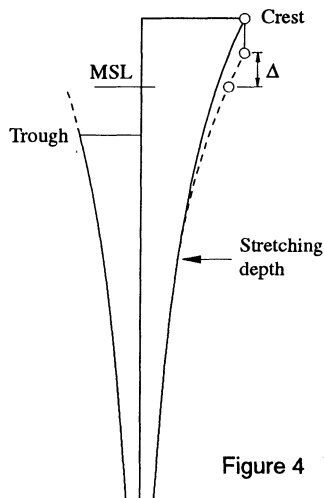


Figure 4 Wave kinematic profile -
Delta Stretch

The resultant velocities and accelerations are substituted into the Morison equation to obtain local and global forces on a hydrodynamic model of the structure. The force coefficients we use with the Morison equation are dependent on the roughness of the members and the ratio of water-particle amplitude to member diameter; they are based on the large-scale laboratory and field measurements by Rodenbusch and Källström [11]. The RDWF model has already been extensively tested against laboratory and field measurements and shown to provide realistic predictions of the sea surface and water-particle kinematics and of forces on space frame structures [1, 8, 9, 13]. Just as in the real sea, extreme waves appear infrequently in a time series. As a consequence, if extreme waves are to be captured, RDWF calculations involve a high cost both in computer time required for the many hours of simulation and in "human" time required for the subsequent analysis of the results [3].

The hydrodynamic model of the Tern substructure consists of 1171 members and 585 joints. Marine growth in agreement with surveys was assumed to be present on the members between - 2.3 m and - 40.0 m.

The comparison of measured and predicted loads is facilitated if loads are calculated for the actual, or a close approximation to the actual, motion of the water particles around the platform during the measurements. This can be achieved by "conditioning" the simulated time histories of surface elevation and water-particle velocity. In a "conditioned" simulation the program minimises the error between measured and simulated time series through a repeated procedure of adjusting phases, directions and amplitudes of wave components [1, 9]. In the present study the surface elevation and the water-particle velocities measured at - 41 m in the X and Y directions have been used as the conditioning variables.

The Newwave theory

In the RDWF theory extreme waves arise on the rare occasions when the many wave components in Eq. (1) come into phase. In the Newwave theory, the expected kinematics under the extreme waves of a seastate [4] is derived directly from an analysis of the problem in the probabilistic domain. For a nearly unidirectional sea, the surface elevation becomes

$$\eta(x,y,t) = A \sum_n d_n \cos(k_n x - \omega_n t), \quad (3)$$

where $d_n = 4 S(\omega_n) \Delta\omega / H_s^2$, A is the crest elevation and H_s is the significant wave height. For the present studies the spectrum has been assumed to be JONSWAP with a spreading function independent of frequency. The surface profile is plotted in Figure 5. The theory is described further by Tromans et al. [2] and has already received some testing against offshore experience [6, 7, 13].

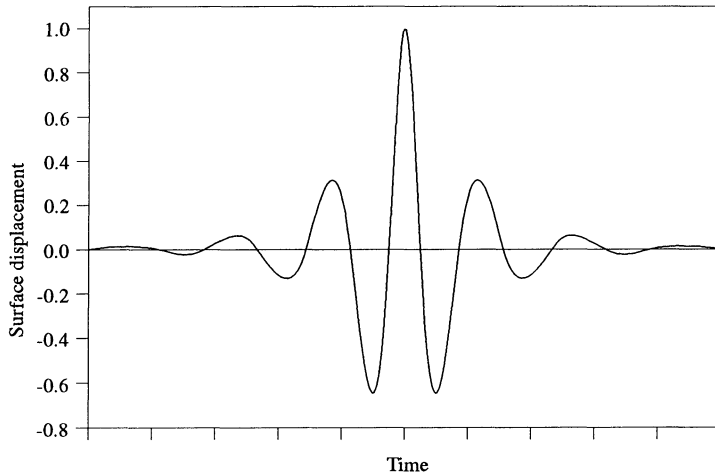


Figure 5 Newwave surface history, normalised with respect to crest elevation

The Newwave theory describes some other features of ocean waves. In addition to the deterministic kinematics (the expected kinematics given, for example, by Eq. (3)), there is also a random part. This random part is a source of uncertainty in the force associated with a wave crest, particularly with the lower crests. However,

as crest elevation increases the random part becomes less significant compared with the expected (or deterministic) part, which eventually totally dominates [2, 4].

As formulated in Eq. (3), the Newwave theory, like RDWF theory, is based on a linear model. However, second-order corrections to the ocean surface can be accounted for in a simple way [5] by applying the equation

$$A_2 = A_1 (1 + A_1 \cdot k_p \cdot 0.52) ,$$

where A_1 is the linear crest elevation, A_2 is the second-order crest elevation, k_p is the wavenumber corresponding to the peak in the wave spectrum. The factor 0.52, instead of 0.5, reflects the broadbandness.

Calculations indicate that global loads derived with Newwave including second-order corrections are the same as those derived with the equivalent linear Newwave [5]. Thus, loads under the non-linear wave can be obtained by estimating the second-order correction to crest elevation, subtracting this from the measured crest elevation and using the resultant value to calculate the equivalent linear Newwave. This equivalent linear NEWWAVE is then used in the wave load calculation.

Newwave was applied to generate loads on the basis of the same hydrodynamic model of the Tern structure and force coefficients as were used in the RDWF analysis. However, unlike the RDWF analysis, which requires the simulation of many hours of seastate, Newwave theory involves the simulation of just one wave group. Thus, Newwave theory offers a fast and powerful tool for predicting extreme wave loading on offshore structures.

Conventional practice using Stokes kinematics

Wave loads were also calculated using the conventional design practice, that is, with Stokes fifth-order kinematics, assuming a drag coefficient of 0.7 and an inertia coefficient of 2.0 for all members, regardless of surface roughness and fluid motion. The wave period was set to the peak period of the measured spectrum.

RESULTS

A comparison between measured and predicted forces on Tern has already been reported [13]. For the one-hour seastate with 12 m significant wave height, the comparison was made for the waves ranked in the highest 1/3 on the basis of RDWF simulated peaks in base shear. Good agreement was found between measured values and predictions based on RDWF and Newwave for this

seastate. In Figure 6 we have added some results obtained from conventional practice using Stokes kinematics. For this comparison, the Stokes wave was specified by setting its crest elevation equal to the measured value. The overprediction by conventional practice under these conditions is clear.

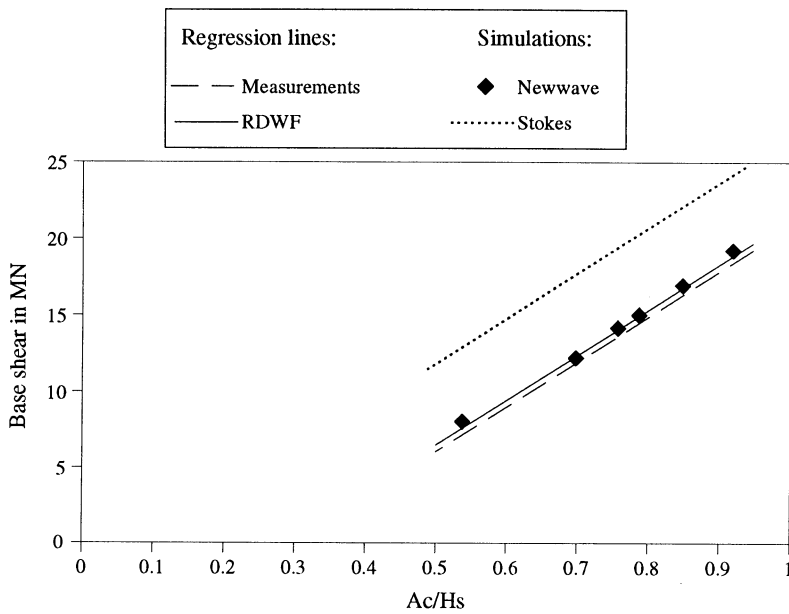


Figure 6 Comparison between Newwave, Stokes and RDWF predictions and measured base shear

For the remainder of this paper we analyse global load measurements taken on January 1st 1992 in a sea with a significant wave height of 13.7 m and a highest crest of over 16 m (a maximum individual wave height of 25.5 m). This is a much more severe storm than any previously analysed or recorded and approaches the 100-year storm condition. Moreover, the storm was of a slightly low zero-crossing period (11.1 seconds) and included some rather high crests and, hence, steep waves, which test the capability of the wave models to deal with non-linearity. Rather than analyse a large number of waves, we shall concentrate on the very largest waves of the sea. These are the most important for testing a proposed extreme design model and, according to the Newwave theory, should be more consistent in their kinematics and hence in their resultant loading of the platform. Moreover, to minimise the effects of measurement uncertainty, we shall restrict

our analysis to those waves for which the two wave height sensors gave consistent crest elevations.

We begin with conditioned simulations generated using the random directional wave model. Figures 7 and 8 show measured and conditioned time series of surface elevation and horizontal water-particle velocity for a segment including the highest crest of the storm. As in previous analyses [13], the conditioned simulations successfully reproduce the measured time series.

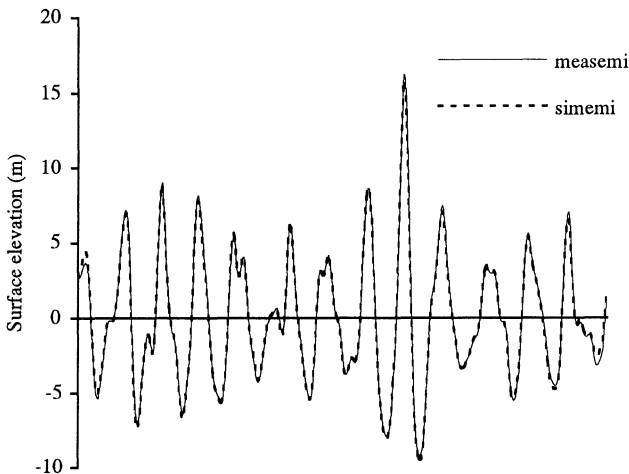


Figure 7 Comparison between measured and simulated surface elevation

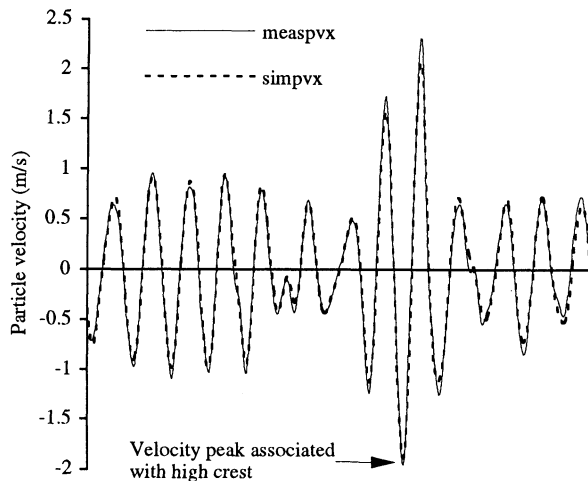


Figure 8 Comparison between measured and simulated horizontal particle velocity. (note: -ve velocities are associated with +ve crests)

Figure 9 shows the conditioned simulation of base shear for the same interval. Surprisingly, the load associated with the extreme crest is overpredicted by roughly one third.

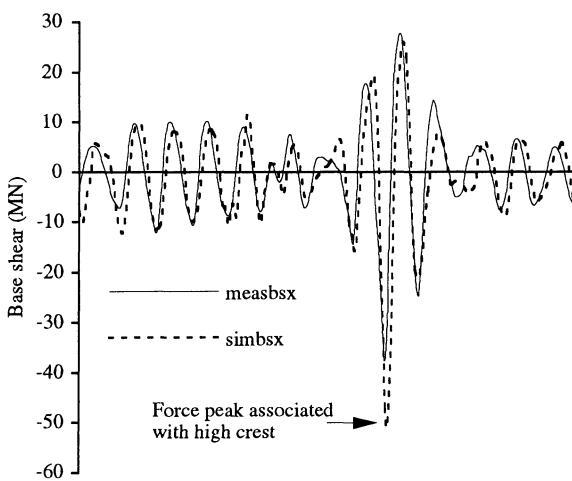


Figure 9 Comparison between measured and simulated base shear. (note: -ve base shear is associated with +ve crest)

This is shown more clearly in Figure 10, where some of the measured and conditioned peaks in base shear forces are plotted against the corresponding crest elevations (normalised with respect to significant wave height). The lower values are reasonably consistent, but the highest values diverge significantly. In Figure 10 we have added two lines calculated with Newwave, one under the assumption of linear crests and the other taking second-order effects on crest elevation into account as described earlier. The results based on linear Newwave theory are consistent with all the RDWF conditioned simulations and the lower measured values. Again, the load under the highest crest is significantly overpredicted. Accounting for non-linearity in the crest elevation has very little consequence on the Newwave results for the lower crests. However, it significantly reduces the predicted base shear under the highest crest. This reduction brings the predicted value into close agreement with the measured value. Newwave with second-order corrections appears therefore to be in good agreement with the measurements over the whole range. Similar trends are found in plots of the overturning moment.

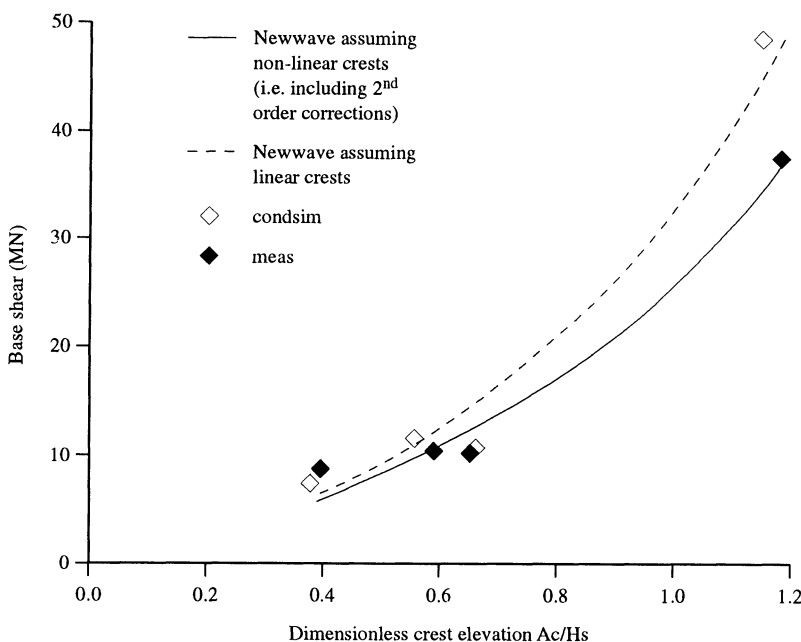


Figure 10 Comparison between Newwave, conditioned simulation and measured base shear

The question now arises of how to match the characteristics of the largest irregular wave in the measured record to an equivalent regular Stokes wave. For the largest wave in the January storm, this was done in two ways: we matched either the crest elevation or the wave height (extreme crest and following trough). Note the matching of crest elevation is consistent with present design practice (see Appendix A). The comparisons are shown in Figure 11.

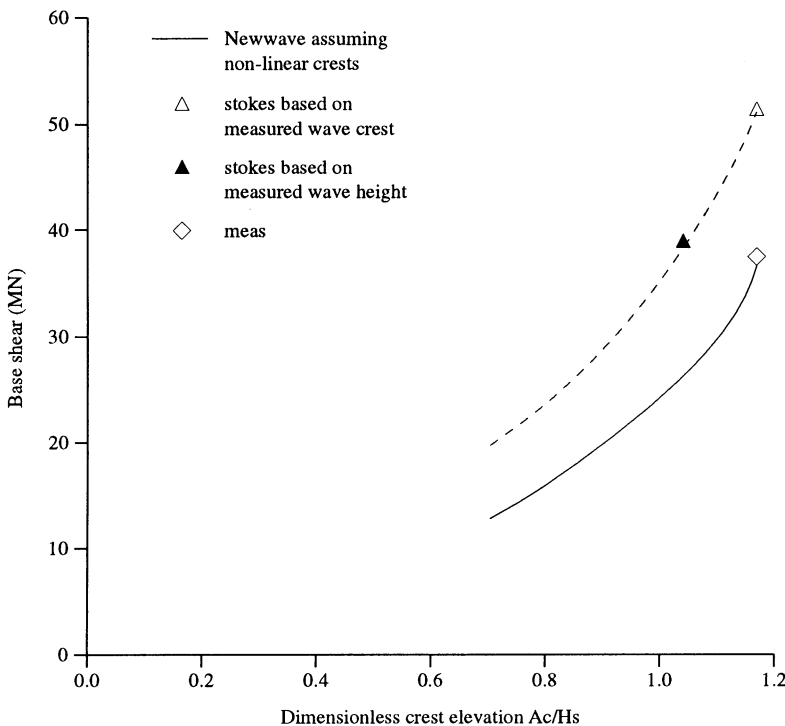


Figure 11 Comparison between stokes, Newwave and measured base shear

Matching the wave height gives a closer agreement to the measured extreme force (and the non-linear version of Newwave), but the Stokes crest is then much smaller than the measured crest elevation. This ambiguity in the use of Stokes theory will always exist. No such problem is encountered in the use of Newwave, which is a better model for an extreme wave in a random sea, as can be seen by comparing the surface elevations for Newwave (Figure 5) and the measured elevation close to the extreme wave (Figure 7).

DISCUSSION

We shall discuss the results in the context of the physical insights provided by Newwave. Firstly, Newwave indicates that for the lower crests in a given seastate there is more uncertainty in force because the random part of the kinematics is more important than the deterministic part. This uncertainty is always a problem in offshore measurement programmes. However, Newwave predicts the force associated with the expected kinematics. The agreement between the predictions and the regression line through the measured values of base shear force supports this (see Figure 6).

Since there are not many very high waves in one hour of a particular seastate, it is difficult to make a statistical study of measured loads associated with very high crests. Fortunately, this is not necessary. According to Newwave theory, the uncertainty in kinematics and, hence, in the load associated with a given crest height becomes smaller as the crest elevation increases. Thus, for the very high crest it is possible to make a direct comparison of measured and predicted wave load. In fact, for the one very high crest discussed here the agreement between measured base shear force and the Newwave prediction is excellent, so long as non-linear effects in crest elevation are accounted for.

The ultimate objective of this study is to develop better methods for calculating extreme fluid loading on offshore structures. In practical design or reassessment the first step is an analysis of the oceanographic statistics to produce a design extreme wave height or, in the case of Newwave, a design extreme crest elevation [12]. The oceanographic statistics of extreme waves within a stationary seastate are described in a straightforward and accurate way by a Rayleigh distribution of their equivalent linear crest elevation. Newwave theory, whether linear or second-order corrected, is conveniently specified by its equivalent linear crest elevation. There is no need to account for wave surface non-linearity in generating the oceanographic statistics. In view of its accuracy and general convenience, Newwave provides an excellent theory of wave kinematics for use in a newly proposed "total loading package" [12] for improved design and assessment practices - at least for drag dominated, space-frame structures in environments similar to the northern North Sea.

CONCLUSIONS

On the basis of the measurements obtained so far, we conclude that, for drag-dominated, space-frame structures subject to extreme environments such as the northern North Sea,

1. Newwave, taking second-order corrections into account, successfully predicts the loads generated by measured waves on a major steel fixed platform.
2. For design purposes, the Newwave theory is the most suitable predictor of extreme forces whenever crest elevation is derived from a linear statistical model.

It is desirable to continue the programme of comparisons between predictions based on Newwave and measurements in order to further validate the theory. In particular, although Newwave has been demonstrated to be a useful model for waves in deep water, shallow-water effects remain to be addressed.

REFERENCES

- [1] Rodenbusch, G. (1986), "Random directional wave force on template off-shore platforms", OTC 5098 Proceedings of the 18th Annual O.T.C., Houston, Texas.
- [2] Tromans, P.S., Anaturk, A.R., and Hagemeijer, P. (1991), "A new model for the kinematics of large ocean waves - Application as a design wave", Proceedings of the ISOPE-91 Conference, Edinburgh, Scotland.
- [3] Hagemeijer, P.M. (1989), "A comparison between deterministic and probabilistic fluid load models for a jacket structure", OMAE Conference, The Hague.
- [4] Tromans, P.S. (1993), "Large ocean waves", to be submitted to Ocean Engineering.
- [5] Taylor, P.H. (1992), "On the kinematics of large ocean waves", BOSS '92 Conference, (Volume 1 pg. 134), London.
- [6] Van de Graaf, J.W., and Tromans, P.S. (1991), "Statistical verification of predicted loading and ultimate strength against observed damage for an off-shore structure", OTC 6573, Proceedings of the 23rd Annual O.T.C., Houston, Texas.
- [7] Tromans, P.S. and van de Graaf, J.W. (1992), "A substantiated risk assessment of an off-shore jacket structure", OTC 7075, Proceedings of the 24th Annual O.T.C., Houston, Texas.
- [8] Forristall, G.Z., Ward, E.G. and Cardone, V.J. (1980), "Directional wave spectra and wave kinematics in hurricanes Carmen and Eloise", Proceedings of the 17th Coastal Engineering Conference, ASCE, Sydney, Australia.
- [9] Rodenbusch, G. and Forristall, G.Z. (1986), "An empirical model for random directional wave kinematics near the free surface", OTC 5097 Proceedings of 18th Annual O.T.C., Houston, Texas.

- [10] Taylor, P.H. (1991), "Current blockage : reduced forces on off-shore space-frame structures", OTC 6519, Proceedings of the 23rd Annual O.T.C., Houston, Texas.
- [11] Rodenbusch, G. and Källström, C. (1986), "Forces on a large cylinder in random 2-Dimensional flow", OTC 5096, Proceedings of the 18th Annual O.T.C., Houston, Texas.
- [12] Tromans, P.S., van de Graaf, J.W., Efthymiou, M., Taylor, P.H., and Vanderschuren, L. (1992), " Extreme storm loading on fixed offshore platforms", BOSS '92 Conference, (Volume 1 pg. 325), London.
- [13] Elzinga, T. and Tromans, P.S. (1992), "Validation of 'Newwave' theory and RDWF predictions against measured global loading on a North Sea jacket", BOSS '92 Conference, (Volume 1 pg. 495), London.
- [14] Forristall, G.Z., Ward, E.G. , Cardone, V.J., and Borgmann, L.E. (1978), "Directional spectra and wave kinematics of surface gravity waves in tropical storm Delia", Journal of Physical Oceanography, September.

APPENDIX A MATCHING OF STOKES AND MEASURED WAVES FOR THE COMPARISON OF MEASURED AND PREDICTED LOADING

Conventional practice for the design of offshore structures has been largely developed on the basis of practical experience. Although it is overall a very safe practice, its details are not easily related to physical reality. Considerable care is therefore required in comparing elements of the practice against offshore measurements. In this Appendix, we address the problem of how the Stokes wave, used in conventional design practice, should be matched to a measured wave in order to compare predicted and measured forces. Since design codes have generally been written in terms of wave height, it is tempting to match the Stokes wave to the observed wave by its height. This, however, is incorrect.

Design loads are conventionally calculated using a Stokes wave to represent the "most probable extreme wave" in a 3 hour interval (typically the 100 year sea state). If the sea state consists of 1,000 waves (say), the most probable extreme is the one in 1,000 wave. The height of this wave is obtained by assuming a Rayleigh distribution.

The Rayleigh distribution is valid for **crest** elevations of the larger waves of a linear Gaussian sea. It is valid for the **heights** of the larger waves only when the sea is narrow banded. This arises because the wave height of a narrow banded wave is twice the linear crest elevation. Since Stokes is a periodic (very narrow banded) wave theory, the use of the Rayleigh distribution for Stokes wave height is reasonable.

In contrast, the real sea is broadband; in particular the highest crests are not preceded by troughs of equal magnitude. The Rayleigh distribution is therefore not a valid description of the wave **height** statistics of measured waves.

However, the linear **crest** elevations of the larger waves in a random sea state satisfy the Rayleigh distribution. Thus, the real wave with the same probability (average frequency) of exceedance as the theoretical Stokes wave is one with the same crest elevation.

The conclusion is that, for the purpose of testing the accuracy of conventional design practice, the theoretical Stokes wave should be matched to the measured wave on the basis of crest elevation.

WAVE LOADING MODEL TESTS ON A GRAVITY BASE STRUCTURE

J.J. Murray*, R.G. Standing and L.M. Mak***

* Institute for Marine Dynamics
St. John's, Newfoundland, Canada

**BMT Fluid Mechanics Limited
Teddington, Middlesex, UK

A series of model tests was carried out on a 1:40 scale model of a gravity base structure (GBS). The model was instrumented to measure global horizontal loads and overturning moments about its base, and local pressures and water elevations at a number of locations on the model structure. The model was subjected to a series of regular and irregular waves. Groups of high waves were also selected from the irregular spectra and run in isolation. The objective was to compare the structure's response to this group to that from the same group found in the full length spectrum. This is referred to as the snapshot technique. Generation of model waves is complicated by wave reflections from the test facility boundaries. The snapshot technique was found to be useful in determining the amount of reflection buildup during an irregular run. In regular waves a technique was developed to minimize these effects. Providing quantitative data from such test programs is particularly complicated by the non-linear nature of the wave loading mechanisms such as steep and breaking waves, slamming and wave impact. The paper focuses primarily on techniques of data acquisition and analysis.

INTRODUCTION

The gravity base structure (GBS) is a large heavy structure which rests on the ocean floor and remains stable under its own weight with the topsides facility supported some safe distance above the sea level. Such structures are generally constructed of concrete and have greater capital costs than other fixed bottom structures such as the jacket type. However, the GBS presents an alternative design for more hostile environmental conditions such as ice infested waters where local oil storage is required but cannot be accommodated by a jacket structure.

Mobil Oil Canada proposed to develop the Hibernia Field off the coast of Canada using a gravity base structure. A preliminary design of the structure proposed by Mobil Canada in 1985, illustrated in Figure 1, consists of a concrete caisson extending from the ocean floor to a distance of 5 meters above the water surface. This large caisson supports four columns which in turn support the topside facilities.

The Ocean Engineering Laboratory of the Institute for Marine Dynamics (IMD) carried out a series of tests on this GBS model [1]. The primary objective of the test program described in this document was to investigate and evaluate techniques associated with model testing of gravity base structures for purposes of engineering design. The test program addressed aspects of GBS model testing such as:

- the quality of waves being generated in the test facility,
- design procedures for the model and instrumentation,
- reduction and analysis of the test data.

The effects of the test facility's boundaries on the model waves are a concern because of the physical size of the model. During a test run waves are diffracted and reflected from the model. Although these waves are genuine in the development of the diffraction process, they impinge on the wavemakers and other facility boundaries and are reflected back to the model itself, thus affecting the measured loads. It is necessary to identify data from the acquired time series which has the minimum reflection from the boundaries.

An accurate assessment of global loading is important when considering interactions between the structure foundation and the surrounding soil. Local pressure measurements, on the other hand, provide design information for structural members which are required to withstand impact forces over small areas. The model assembly is an integrated system of transducers and the geometrically scaled model itself. The measurement and interpretation of the loads is potentially complicated by the dynamic responses of the model and its force transducers. Such dynamic responses are the property of the model (including transducers) and do not represent those of the full scale structure. It is necessary to design the model and its transducer systems so they measure accurately up to the highest loading frequency of interest.

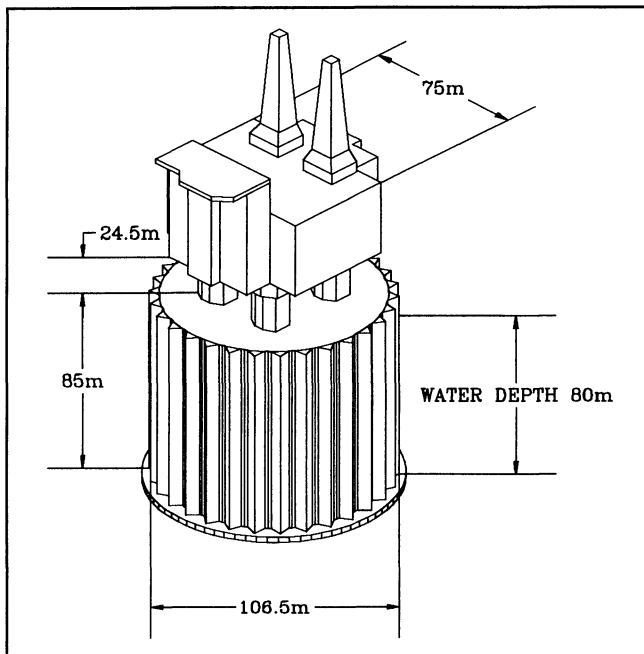


Figure 1. GBS Structure

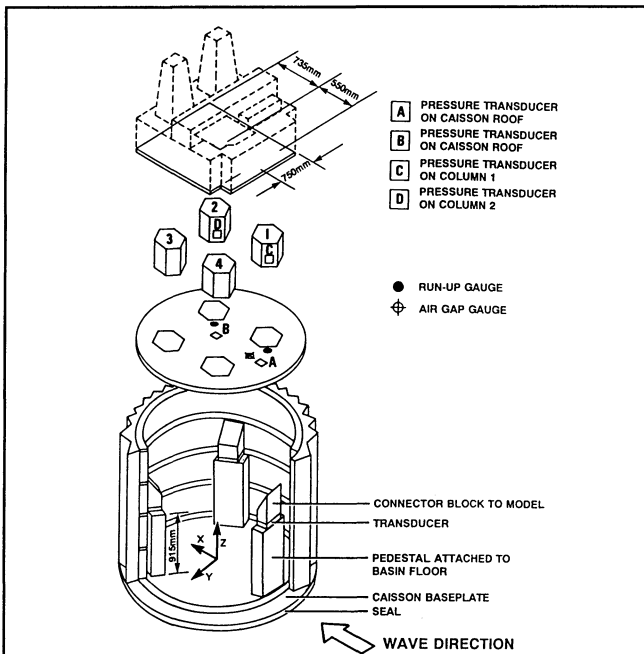


Figure 2. Instrumentation Layout

to the designer without any effect from the dynamic response of the instrumentation.

Wave runup is the height to which water will runup a column of the GBS. Air gap is a measure of the clearance between the top of the caisson and the underside of the deck at distances far away from the columns. Runup is of particular importance because it identifies the maximum height to which water will impart local loading on the structure. The amount of spray or water associated with the disintegration of a breaking wave may be difficult to measure when considering the highest part of a wave crest and the load imparted on the structure by the water. The surface tension affects the amount of spray associated with a breaking wave. Modelled waves will have less spray than the full scale waves they represent. Loads associated with runup are dependent on a number of factors such as, air content and compressibility and acceleration of the fluid. The GBS test program measured runup on two columns and air gap at one location between the caisson roof and deck underside.

The response of a gravity base structures can be very complex due to the nonlinear nature of both the waves and the responses to be quantified. In presenting the test results, the main objective is to provide the designers with germane and lucid information about the behaviour of the structure. The program was focused on the techniques of model testing rather than providing any assessment of the GBS design. Test results are presented and discussed in relation to the above outlined aspects of the test program.

MODEL DESIGN AND CONSTRUCTION

A 1:40 scale model of the GBS illustrated in Figure 1 was used in the model test program. This model was equipped with the necessary instrumentation to make the following measurements:

- global loading and overturning moments,
- local loading on the caisson roof,
- local loading on the columns,
- deck clearance and wave runup on the columns.

The instrumentation layout for the model assembly is shown

in Figure 2. This arrangement was accepted following structural analysis.

Design criteria for instrumentation to measure global loading were concerned with providing an instrument capable of measuring the maximum load to within 2 % resolution. Also, to ensure that the dynamic response of the model/dynamometer assembly would not affect the measurements of the global loads and overturning moments, a target natural frequency for this assembly 10 times above the maximum wave frequency was imposed.

Global Load Measurement

Two numerical models were used to estimate the global load for purposes of instrumentation design. One was based on the classical linear diffraction theory by McCamy and Fuchs (MCF) for fixed bottom cylinders and the second was based on the boundary integral method using Green's functions. In addition to the global loads and overturning moments on the GBS caisson, the hydrodynamic added mass and damping effects of the caisson were also determined from the boundary integral method.

The McCamy and Fuchs model assumed the GBS to be a cylinder with a radius of 50 m, while the boundary integral method accounted for the teeth around the outside of the model by using 880 square panels to represent the wetted surface of the caisson. The design water depth was 80 m. The design wave height was 30 m.

A comparison of normalized horizontal loads computed by the two methods is shown in Figure 3. The results show little difference between the two methods for periods up to approximately 13 seconds. Above this period, the MCF method shows a trend with smaller estimates of horizontal loads and overturning moments than the boundary integral method. These differences may be due to modelling the teeth on the caisson, or to numerical errors in computing the diffraction loads using the boundary integral method. In any case the difference is not significant for practical purposes. The design global loads and overturning moments used for the GBS model design are given in Table 1.

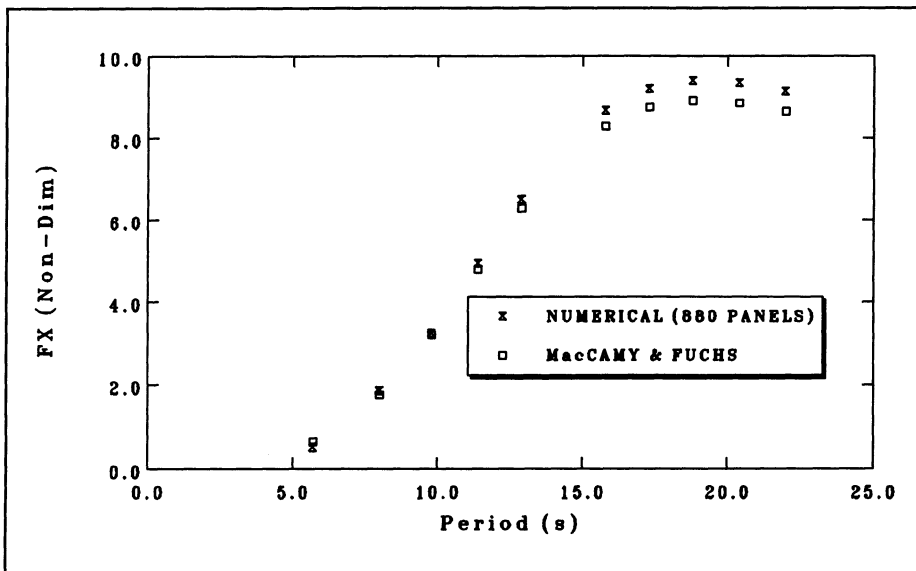


Figure 3. Comparison of Computed Horizontal Loads

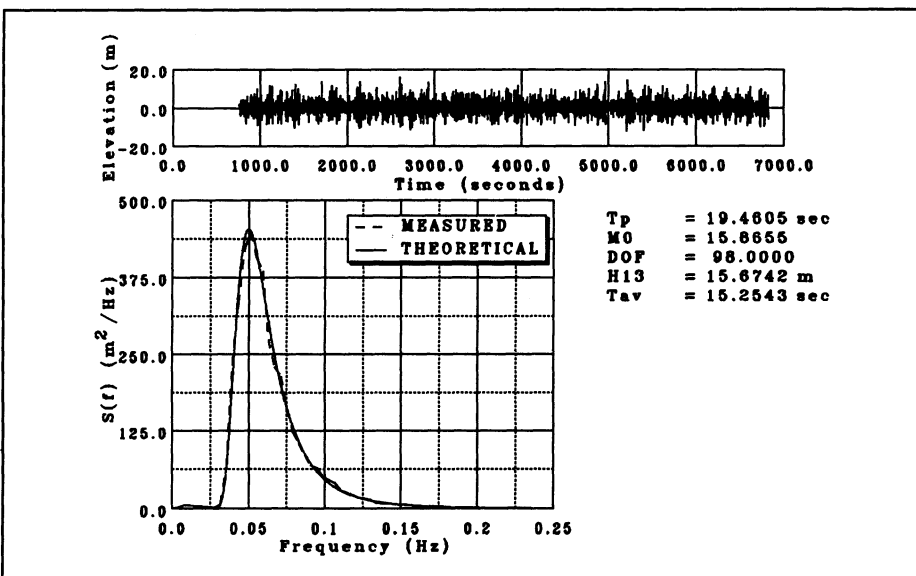


Figure 4. Irregular Wave Spectrum

PARAMETER	
Max F_x	1,800 MN
Max M_y	72.3 E03 MN-m
Global Load Resolution	2 %
Max Local Pressure	250 KPa
Min Natural Frequency	3.0 Hz

TABLE 1. STRUCTURAL DESIGN CRITERIA FOR MODEL DESIGN

Local Loading

Local pressures were measured at a number of locations around the GBS using matrices of flush mounted pressure transducers. A total of four matrices were attached to the model. The pressure transducers in a matrix were arranged similar to the five-side of a die.

In order to size these transducers, the pressure was estimated using the expression,

$$P = 0.5 * C_s * \rho * U^2 \quad (1)$$

where, C_s is the slamming coefficient and, U , is the impact velocity of the water. This impact velocity was computed from linear wave potential assuming the incident wave was undisturbed.

The likely conservatism or otherwise of equation (1) depends on the maximum frequencies of interest and therefore whether very large, but of short duration, forces are significant. With regard to the selection of pressure transducers and associated instrumentation, a more conservative estimate is prudent in order to avoid the transducer or the instrumentation's amplifiers.

A C_s value between 4.1 and 6.4 is common. However, as reported in [2], choice of this value can lead to underestimations of pressures in the order of 50% to 90%. Therefore, a more conservative value of C_s equal to 12 was used. A local design pressure of 250 KPa was chosen.

Wave Runup and Deck Clearance Gauges

Both wave runup and deck clearance were measured using capacitance type gauges. Wave runup is the elevation that water will reach on the columns between the top of the caisson and the underside of the deck. Deck clearance is the air gap under the deck at distances sufficiently far away from the columns. In total, 2 runup gauges and 1 deck clearance gauge were used. Their locations are illustrated in Figure 2.

Caisson Seal

Global loading was effectively measured with respect to earth. The caisson maintains contact only with the three transducers on the pedestals and is isolated from the basin floor. A gap at the caisson base is large enough to allow the model to be displaced as required by the transducers. It was, therefore, necessary to seal the gap between the bottom of the caisson and the basin floor. Details of the seal used on the model are found in [3].

Structural Analysis

As part of the model design procedure, an extensive structural analysis was carried out on the model and the load cell assembly to ensure adequate structural rigidity such that the natural frequencies of the model assembly when surrounded by water were not near those in the wave frequency range. A detailed description of the analysis procedures and results are found in [4].

The natural frequencies of the model assembly were predicted using two finite-element idealizations; one, referred to as the flexible F-E model, modelled the caisson, columns and topsides as flexible members mounted on a rigid foundation via springs (representing the load cell stiffness), the other, referred to as the rigid F-E model, assumes the model to be rigid and mounted on the same foundation using the same effective spring stiffness. Both methods were used to predict the responses in air and when surrounded with fluid.

A comparison between the natural frequencies , predicted by the two F-E models in air is given in Table 2. The flexible F-E model identified the first mode corresponded to a twisting oscillation about the vertical axis (yaw), and the second and third modes as coupled horizontal translation

(surge and sway) and rotation about a horizontal axis (pitch and roll), respectively. The rigid F-E model again identified the lowest natural frequency to be in the rotational direction about the vertical Z-axis, but the frequency was estimated to be 11.6 Hz as compared to 6.5 Hz predicted using the flexible model. Such a discrepancy is expected since the flexible case permits local deformation in the GBS structure at locations such as the connections to the load cells.

The natural frequencies of the GBS were estimated in water by accounting for the hydrodynamic added mass effect. For Mode 1 in air (yaw), the added mass effect was very small and did not significantly change the natural frequency, whereas the added mass effects for Modes 2 and 3 (coupled surge, sway, pitch and roll) were significant. Following adjustments for the added mass effects, the mode of the lowest natural frequency in water corresponded to modes 2 and 3 in air. Therefore, the lowest natural frequency of the model in water was estimated by the rigid finite-element model to be 4.7 Hz (29.7 Hz model scale) and 2.9 Hz (18.34 Hz model scale) by the fully flexible model. The minimum allowable natural frequency was 3.0 Hz (18.9 Hz model scale). The value of 2.9 Hz was acceptable.

MODE NUMBER	FLEXIBLE MODEL (Hz)	RIGID MODEL (Hz)
1	6.5	11.6
2	7.7	12.1
3	7.7	12.1
4	10.6	15.8
5	10.6	15.8
6	12.6	25.5

TABLE 2. COMPARISON OF NATURAL FREQUENCIES IN AIR PREDICTED BY FLEXIBLE MODEL AND RIGID MODEL

The differences between the natural frequencies estimated using the rigid and flexible model are quite large. This may

explain why, when models are designed assuming rigid components, they are often more flexible when built than their design predicts. The result is they have lower natural frequencies. Careful design, taking into account the flexibility of the model itself, as well as that of the transducers, is important when designing a complex model of this type, particularly when impact or other short-duration forces are being measured.

Structural analysis did not include the effects of the seals since it was assumed that stiffness and damping contributions to the full model assembly were negligible. This was in fact one of the requirements of these sealing devices.

MODEL SETUP - STATIC AND VIBRATION TESTS

Static calibrations were carried out on the GBS assembly with and without the seals attached to determine the stiffness effects of the seal by comparing measurements of the applied loads with the seal attached to those without the seal attached. The accuracy of the three load cell dynamometer was first determined by applying known loads to the caisson over a range of elevations.

A difference of approximately 2 % between the applied and measured loads was found without the seal attached. Comparison of the no seal condition to the seal attached condition demonstrate the effect of the seal stiffness on the dynamometer. Calibration results showed an average difference in stiffness of 0.6 % between seal attached and the no seal condition.

Vibrations tests were also carried out on the model assembly both in air and in water to identify the natural frequencies. Once again results were compared to those obtained from the case with no seal attached. The objective was to determine the damping effects of the seal and to confirm the predefined natural frequencies of the model assembly. The condition of no seal attached show a natural frequency in air of 4.4 Hz and a damping ratio of approximately 5 %, which is acceptable for structural damping. The damping effects increased to a ratio of 6.6% when the seal was attached.

The added mass was estimated from the change in frequency

determined from the decay time trace. The predicted added mass in the horizontal direction was 3.27E08 kg (full scale). This compared to a measured value of 2.47E08 kg. The measured natural frequency in the horizontal direction of the model in water was 3.4 Hz as compared to a predicted value, using the flexible model, of 2.9 Hz. The difference in natural frequencies may be attributed to differences in added mass. However, the measured natural frequency agreed well with the predictions based on the flexible model, demonstrating the value of the flexible model analysis.

The vibrations tests confirmed that the natural frequency of the model dynamometer assembly to be approximately ten times the maximum frequency of the wave load, and the assembly's damping characteristics had negligible effect on the response within the range of wave loading.

TEST FACILITIES

Offshore Engineering Basin

The Offshore Engineering Basin facility is a reinforced concrete structure 75 m long, 32 m wide with a wall height of 4 m. Water levels may be varied up to a depth of 3.5 m. Waves are generated by 192 segmented wave machines, of wet back design. Each segment is 2 m high by 0.5 m wide. The wavemakers can operate in five modes of articulation: flapper, piston and 3 different combinations of flapper and piston. These modes optimize segment motion for generating waves in deep, shallow and intermediate water depths, respectively. Passive absorption is accomplished using expanded metal sheets of varying porosities and spacings.

The data acquisition system uses Neff Instruments 620-500 buffered and unbuffered analog subsystems. Attached to these are Neff 620-100 analog to digital converters with 15 bit conversion accuracy and 50 kHz throughput. Neff 620-300 signal conditioners are used as a front end for conditioning load transducers. The acquisition computer is a VAX 3200. The 620-500 buffered system provides for data acquisition and data throughput independent of the computer's real time clock.

Wave Calibration

The model test program consisted of a total of 82 regular

waves and 6 irregular waves. In addition to the full length irregular wave spectra, the model was subjected to 15 snapshots selected from the irregular wave runs. The snapshot is a sequence of waves, chosen from the full length sequence, and run in isolation. These waves were calibrated in the basin without the model installed.

All irregular waves were calibrated using the Random Fourier Coefficient Method. This technique is analogous to white noise filtering in the time domain using a modified form of the JONSWAP spectrum as the filter shape. The repeat period of each spectrum was 6071 seconds. Figures 4 shows a sample of a calibrated wave spectrum.

The measured spectrum is smoothed using 100 degrees of freedom in a frequency band of 0.0084 Hz. Therefore each component compared to the target spectrum is the average of 50 complex spectral components within this bandwidth.

TEST PROGRAM

Runs in Small Amplitude Regular Waves

Following installation and setup testing of the model, a number of small amplitude waves were run such that they did not break over the caisson roof. The purpose of these runs was two fold; first to test the method intended to select the data for analysis, and second to compare the measured wave loads on the caisson to numerical predictions to further verify the dynamometer calibration.

Figure 5 compares measured load from small amplitude waves to those predicted by the MCF model. In the figure, the loads determined by using the group velocity to identify the data with minimum reflection effects from the facility boundaries. The group velocity was used to predict the time taken for waves reflected from the model to reach the boundaries and travel back to the model again. The data used in this case is labelled (Interval 1). Data chosen from other portions of the time trace are labelled (Interval 2). Interval 1 begins after the starting transient has died out and ends when the wave, reflected from the model to the wavemaker, travels back to the model again. Interval 2 begins at the end of Interval 1 and continues to the end of the record.

Time traces of the loads, particularly at the lower periods,

showed a distinct change in the time trace between Interval 1 and Interval 2. This technique is very useful since the data selection can be programmed into the analysis procedure without having to visually inspect each time trace.

There is less scatter between the predicted and measured loads when using the group velocity technique up to a period of approximately 13 seconds. The good agreement below this period does however give confidence to the dynamometer measurements. A more detailed analysis of the results involved in this part of the test program can be found in [5].

Tests in Regular Waves

The model was subjected to a total of 82 regular waves ranging in periods from 5.7 to 28.0 seconds, and in heights from 3 m to 30 m. Data acquisition in regular waves commenced as soon as the wavemakers were started and continued for a duration of 120 seconds. Thus, the still water condition prior to each run was included in the data acquisition. All channels were sampled at 200 Hz.

Irregular Wave Tests

In the irregular wave tests, the model was subjected to a total of 6 spectra. As in the case of the regular wave runs, data acquisition started at the still water condition. Acquisition continued for a duration of 1080 seconds to ensure that a full repeat period of the wave spectrum was acquired. All channels were sampled at 200 Hz.

Snapshot Tests

In addition to the irregular wave runs, the model was subjected to a total of 15 snapshots, selected by visual observation from the highest groups in the incident wave train.

The snapshot, introduced in [6], is generated by selecting a wave group from the full length time history. The spectral components of the group are identified and each is assigned a relative phase component, bases on its celerity, such that the resulting sequence conforms to the required group at the specified location in the basin. The leading and following ends of the group are ramped up and down respectively to

avoid spurious components caused by abrupt motions of the wavemaker.

DATA ANALYSIS TECHNIQUES

The main objective of data analysis is to reduce and present the test data in a format useful to the designer. The non-linear nature of the responses to wave loading makes analysis best suited to a statistical approach. Presentation of results is focused on comparing responses found in regular waves to those found in irregular waves in the form of ranked plots. Irregular wave data are also presented in the form of Weibull cumulative distributions. Snapshots are also used in the analysis of the irregular wave results.

Ranked Plots

The ranked plot method, used in [7], compares wave heights to peak force values by ranking both in descending order and plotting the forces against the heights on linear scales. A straight line can be fit through these data. These fitted lines were then used to interpolate or extrapolate the peak force that occurred with the same probability as the design wave height. The procedure can be statistically justified even though the largest peak force may not be necessarily associated with the largest wave height. This is because, on average, the probability of the largest force occurring is the same as the largest wave. Only the two probability distributions were compared.

Weibull and Rayleigh Distributions

The logarithmic form of the Weibull cumulative distribution, p , states that the probability of observing a quantity, such as wave height or load, etc., that is less than a quantity, X , is described by the expression,

$$\ln(-\ln(1-p)) = C \ln(X-A) - C \ln(B) \quad (2)$$

- A - location parameter, chosen as the minimum value of interest,
- B - scale parameter,
- C - shape parameter.

Parameter A was set equal to the minimum value in the data. A measure of the Weibull fit was determined by the computing

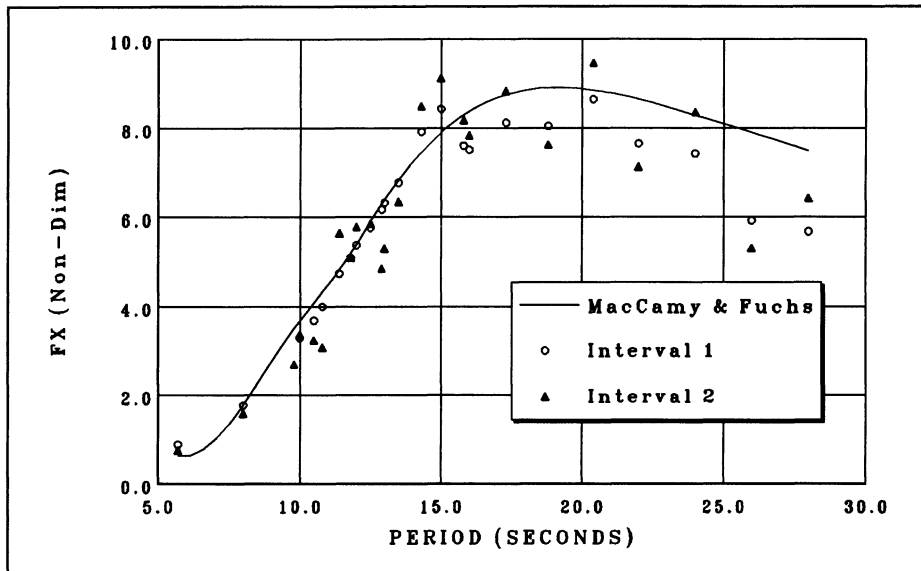


Figure 5. Small Amplitude Wave Loads

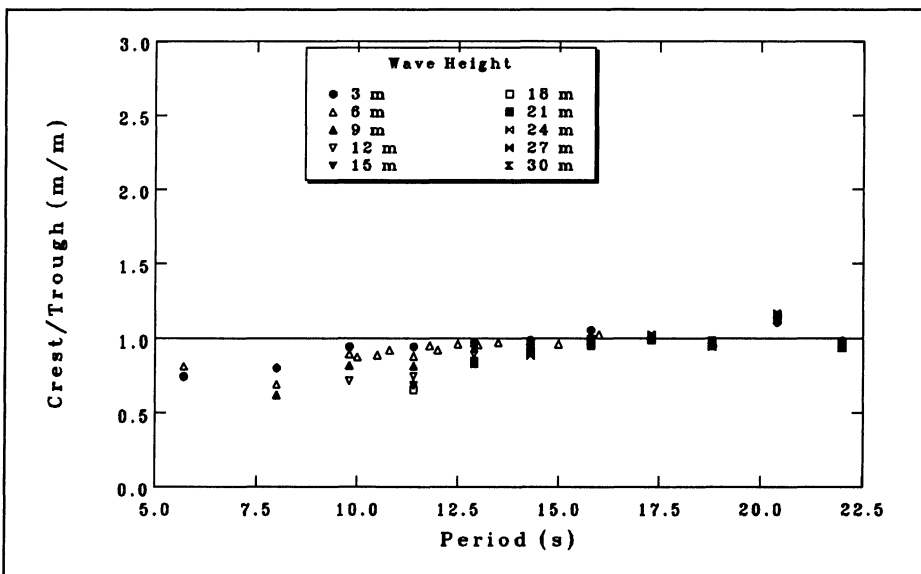


Figure 6. Load Crest to Trough Ratio

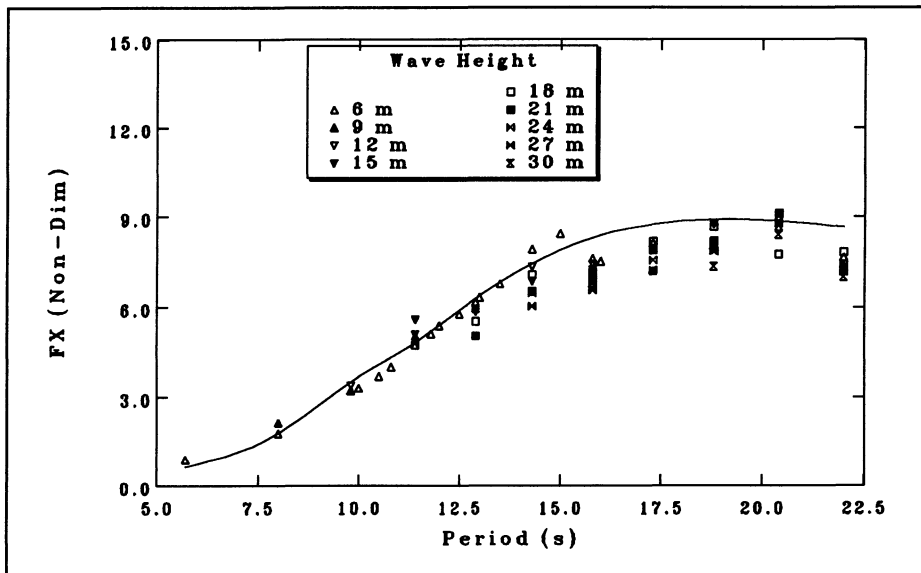


Figure 7. Normalized Horizontal Loads

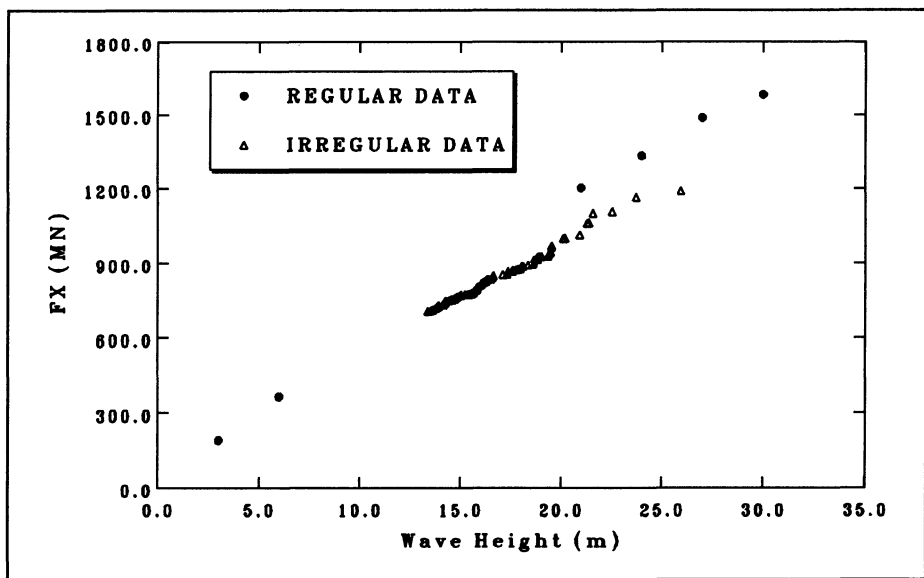


Figure 8. Ranked Plot of Horizontal Load

the least-squares *goodness-of-fit* parameter, R2. This is the only assessment of the validity of the distribution used in this fitting procedure.

The Rayleigh probability density function, R(X), is given by the expression,

$$R(X) = \frac{1}{\alpha^2} X e^{-(X^2/2\alpha^2)} \quad (3)$$

Data presented in the Weibull model follow a Rayleigh distribution when: A = 0.00, B = $\sqrt{2}\alpha$, and C = 2. Using this relationship, data can be directly compared to the Rayleigh distribution on the Weibull plot.

TEST RESULTS AND DISCUSSION

Global Loads and Overturning Moments

In the shorter wave period range, horizontal global loading in regular waves showed a non-sinusoidal nature with a flat crest and a more sinusoidal trough in the time trace. In regular waves of higher periods, the crest of the time trace is large in magnitude than the trough. The flatter crest is due to overtopping on the caisson roof, while on the reverse cycle the trough of the wave maintains contact with the caisson, thus resulting in a larger load in this direction. In longer waves, the loads imparted to the columns on top of the caisson are more significant, thus the crest of the loading time trace is larger than the trough.

Figure 6 shows the ratio of the magnitudes of the loads measured at the crest of the time trace to the load measured at the trough (negative direction) of the time trace. Horizontal forces, normalize with respect to the wave height are shown in Figure 7. The solid line in the Figure 7 indicated the value predicted using the MCF model.

The maximum horizontal global load measured on the GBS model in regular waves was lower than the predicted design value, giving a maximum measured value of 1580 MN as compared to a predicted value of 1800 MN. Similar differences were found

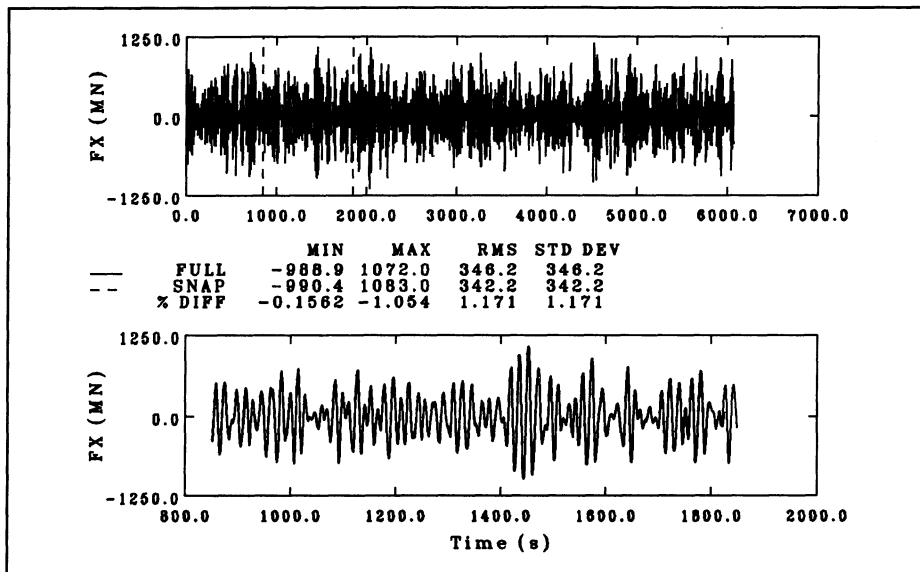


Figure 9. Snapshot of Horizontal Load

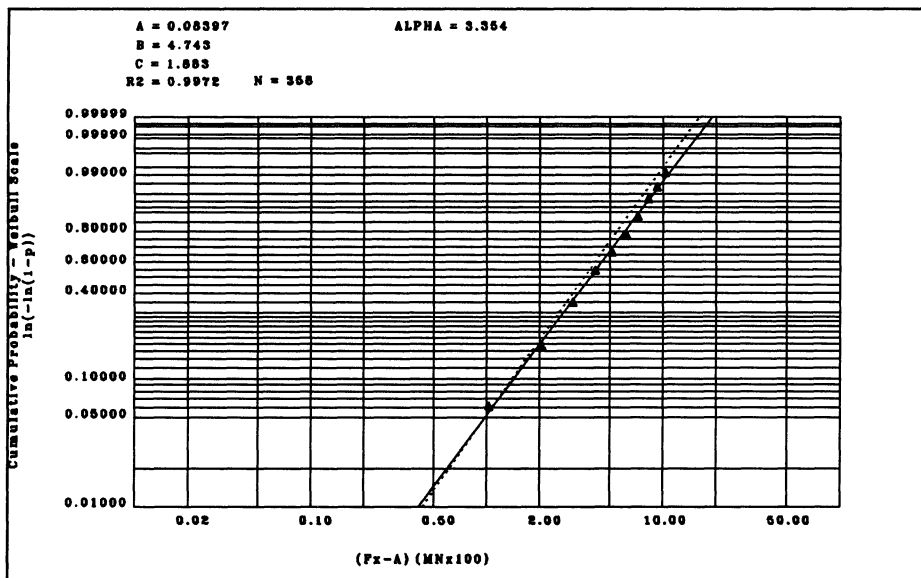


Figure 10. Weibull Plot of Horizontal Load

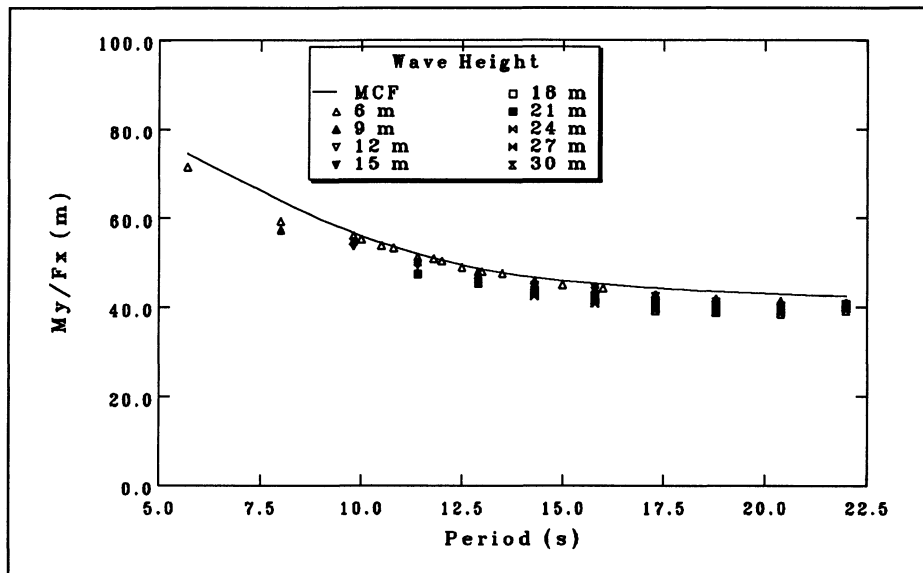


Figure 11. Moment Arm

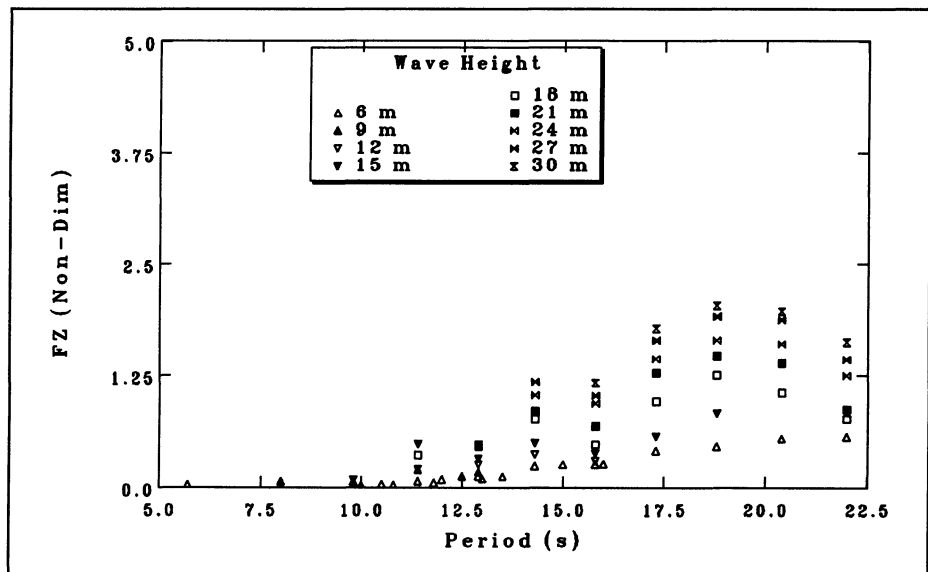


Figure 12. Normalized Vertical Loads

in the overturning moments results. The main reason for these discrepancies is related to the simplified numerical model used to predict the loads and moments. Design loads were estimated using linear diffraction theory by modelling the GBS as an infinitely high cylinder with a radius of 50 m. Loads on the columns were not included in this analysis.

A sample of a ranked plot of the horizontal force is given in Figure 8. The loads given in these ranked plots are maximum load values found from the time traces regardless of the direction of loading. In general, ranked plots comparing horizontal forces measured in regular and irregular waves, showed regular wave results to be larger than those measured in irregular waves. The only exception is the comparison between regular wave loads at a period of 20.4 seconds and the irregular loads found from the spectrum having a peak period of 20 seconds.

A sample of a snapshot of a horizontal load is given in Figure 9. There are very small differences between the snapshot and the responses measured in the full length spectrum. This result indicated that the amount of contamination buildup to this time in the full trace is not severe. This is because an averaging of spectral components takes place to reduce the effects of reflections from the facility boundaries.

A Weibull plot of horizontal forces, is found in Figure 10. The dashed line in the figure represents a Rayleigh distribution and horizontal loading appears to be close to this distribution. Extrapolating to the maximum load shows a maximum load of approximately 1,750 MN, which is a realistic value.

Overturning moments showed similar trends in terms of ranked and Weibull plots as the horizontal loading. This is expected since the overturning moments and horizontal loads are related through the height above the caisson floor at which the resultant load is applied. The ratio of the overturning moments to the horizontal loads, measured in regular waves are shown in Figure 11.

Vertical global forces on the model were considerably smaller than those in the horizontal direction. Non-dimensional vertical loads measured in regular waves are shown in Figure 12. These values are non-dimensionalized

with respect to the wave height and show more scatter at a particular wave period than the horizontal loading results and the overturning moments. This is an indication of the high degree of non-linearity on the vertical loading.

A sample of a ranked plot and a Weibull plot of a vertical load are shown in Figure 13 and 14 respectively. The ranked plot of vertical loads given in Figure 13 indicated the nonlinearities in vertical loading. The results plotted for irregular waves show groups which could provide a possible range of slopes to a fitted line, depending on the range chosen. This plot also illustrates the high sensitivity of vertical loading to slight changes in wave periods. However, fitting a line to the top end of the irregular data will extrapolate to a value of approximately 400 MN at the 30 meter design wave height.

In one series of irregular wave tests, an irregular spectrum was modelled using different phase components such that the mean and significant wave heights for three spectra were within 1% of each other but the resulting time histories of the wave patterns were different in each case. When subjected to these waves a high level of variability was found in the measured vertical loads, whereas the statistics of the horizontal loads and overturning moments were more stationary. This high level of variability in vertical loads is caused by their non-linear nature makes them more sensitive to wave grouping patterns. Horizontal loading and overturning moments have a much more linear response to wave loading and are therefore less sensitive to grouping.

The straight line fit to the Weibull plot of vertical loads given in Figure 14 shows a poorer fit than that for the horizontal loading. Extrapolation using this plot gives a maximum value for vertical loading of 900 MN, which is over twice the measured maximum value of 380 MN measured in that spectrum. The fitted line is influenced by the lower loads measured in the spectrum. An improved fit and estimate of the maximum vertical load may be achieved if only the data at the top end of the plot were used in the fit.

The snapshot of the vertical global load on the GBS given in Figure 15 showed higher percentage differences than those for horizontal loading and overturning moments but are still less than 10%. This discrepancy is attributed to the high sensitivity of the vertical loads to slight changes in wave conditions.

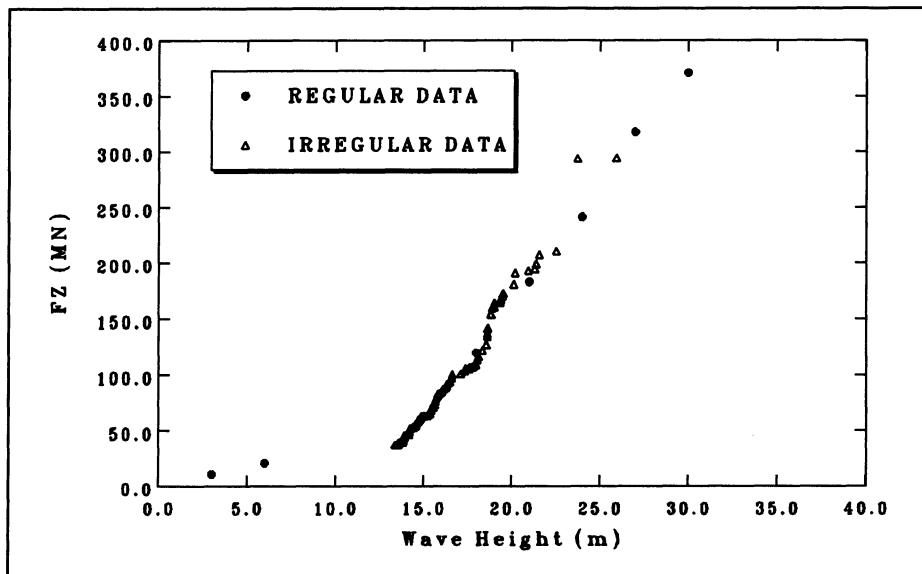


Figure 13. Ranked Plot of Vertical Load

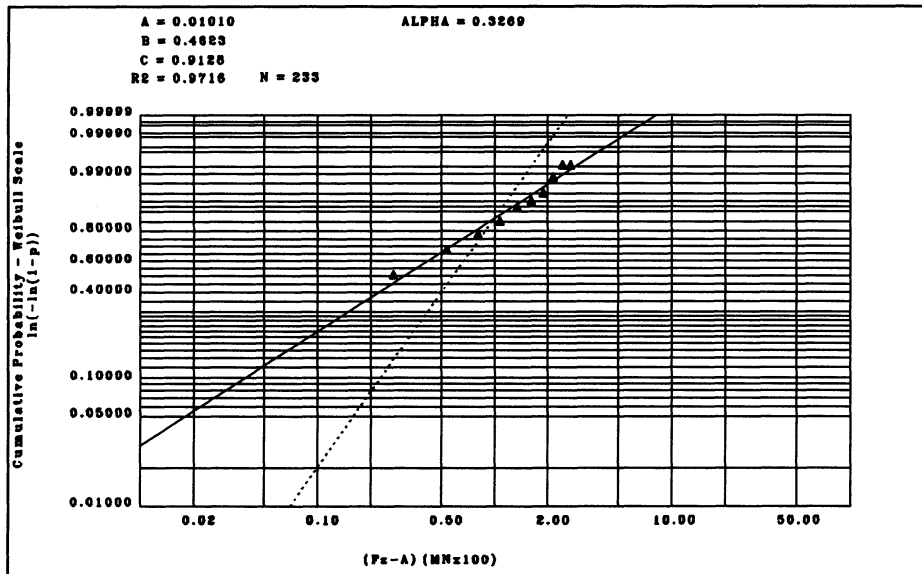


Figure 14. Weibull Plot of Vertical Load

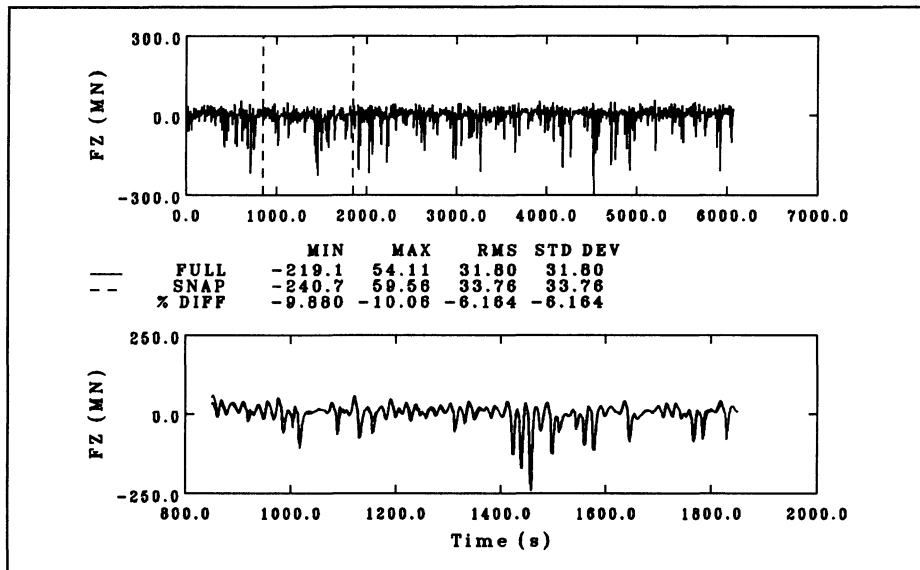


Figure 15. Snapshot of Vertical Load

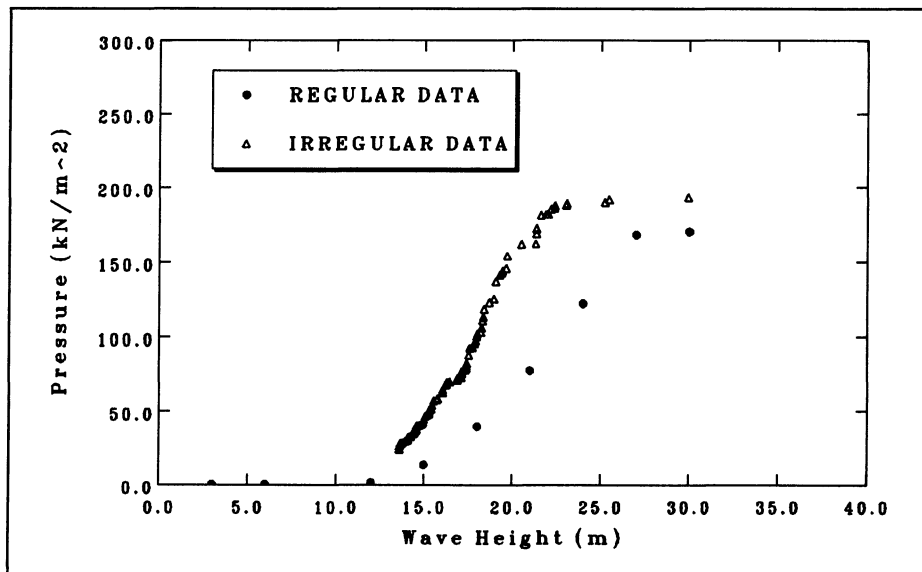


Figure 16. Ranked Plot of Local Pressure vs. Wave Height

Local Pressures

Pressure measurements exhibit a typical impact characteristics with a very fast rise to a maximum pressure followed by a slower decline back to the zero reading. Local pressures measured in both regular and irregular waves were within the same order of magnitude. The method of estimating local pressures using an empirical slamming coefficient of 12, was found to give a reasonable estimate of the local pressures in the columns.

In regular wave runs, there is considerable variation in the peak pressure values at each cycle. These variations may be caused by a number of factors such as instrumentation filtering, temperature variations, or inconsistency in each of the wave cycles. This variability in pressure measurements is evident even locally within a particular transducer matrix. Each pressure transducer represents an area of approximately 5 m^2 which effectively measures pressure over a highly localized area. Depending on structural requirements, a larger measuring area or the average pressure of the transducers in a matrix may be adequate.

In regular waves, the variations in peak pressure measurements were high from cycle to cycle but were averaged over a number of cycles. It was not possible to average local pressures measured in irregular wave spectra since there was only one occurrence of a particular pressure in a wave sequence. One method of obtaining such an average from irregular waves is to repeat a particular group number of times by running it as a number of snapshots in tandem.

A sample of a ranked plot of local pressures against wave height are found in Figure 16. The highly non-linear nature of the local pressures in irregular waves is evident in the ranked plot shown in this figure. Local pressures in irregular waves appear to be very sensitive to surface elevation. Therefore the pressures were ranked against wave crest in Figure 17. Ranking against crests shows only a slight improvement in agreement.

Also, pressures in irregular waves sometimes appear within a group of waves, yielding a single pressure peak, while in other cases, where wave crests are further apart, a number of distinct peak pressures equal to the number of waves in the group are evident. This may explain the large

discrepancies between the maximum pressures measured in irregular waves as compared to the pressure measured for, presumably a regular wave of the same height.

Due to the high sensitivity of local pressures to slight changes in wave conditions, results of snapshot tests on local pressures showed poor agreement. Weibull plots showed very poor straight line fits to the measured data resulting in unrealistic estimates of maximum values. The ranked plot seemed to be the most useful means of extrapolating the data.

Wave Runup and Air Gap

Like the local pressures, wave runup and air gap were found to be very sensitive to surface elevation. A sample of a ranked plots of wave runup against wave height on Column #1 from irregular wave runs are compared to those measured in regular wave runs in Figure 18. In most cases good agreement was found between the regular and irregular wave cases. Both runup and air gap were also ranked against wave crest. Only slight improvement was found from these results.

Snapshots of runup and an air gap showed a high degree of variability in both cases. Weibull plots of runup and air gap were found to give poor fits to straight lines on the log-log scales with extrapolation to the maximum values being unrealistic. The ranked plot technique was found to be the most reliable means of estimating design and extreme values.

General Comments

Data reduction and analysis was focused mainly on comparison of regular waves to irregular wave results. One of the uses of test data relevant to the designer is the estimation of extreme values of the quantities measured. Ranked and Weibull plots were used to provide these estimations. Normalizing data with respect to wave height or wave crest illustrates the degree of non-linearity in the response at a particular wave period. Cases where the degree of non-linearity is not comparatively high, for example in horizontal loads and overturning moments as compared to local pressures, allows measurements made at lower wave heights to be included in extrapolation to realistic extreme values. In cases where the responses are highly non-linear,

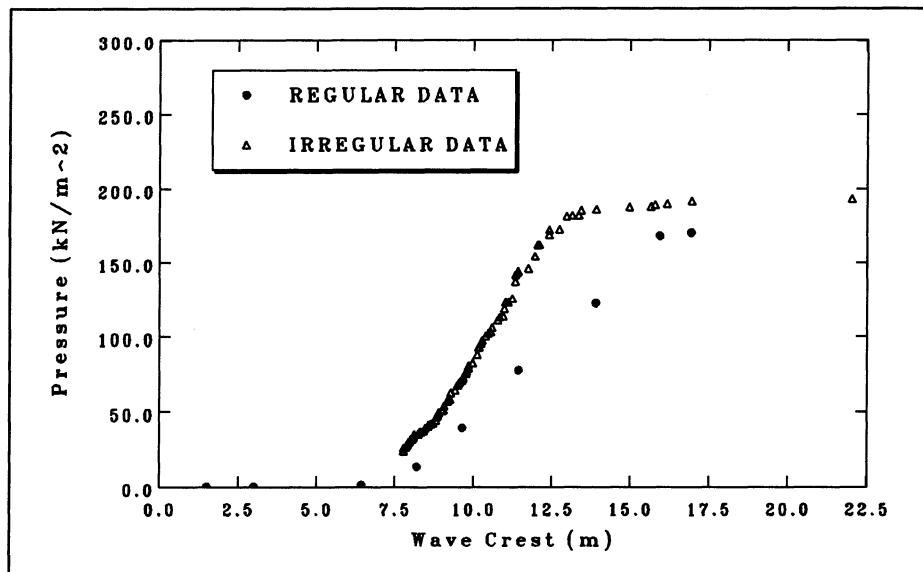


Figure 17. Ranked Plot of Local Pressure vs. Wave Crest

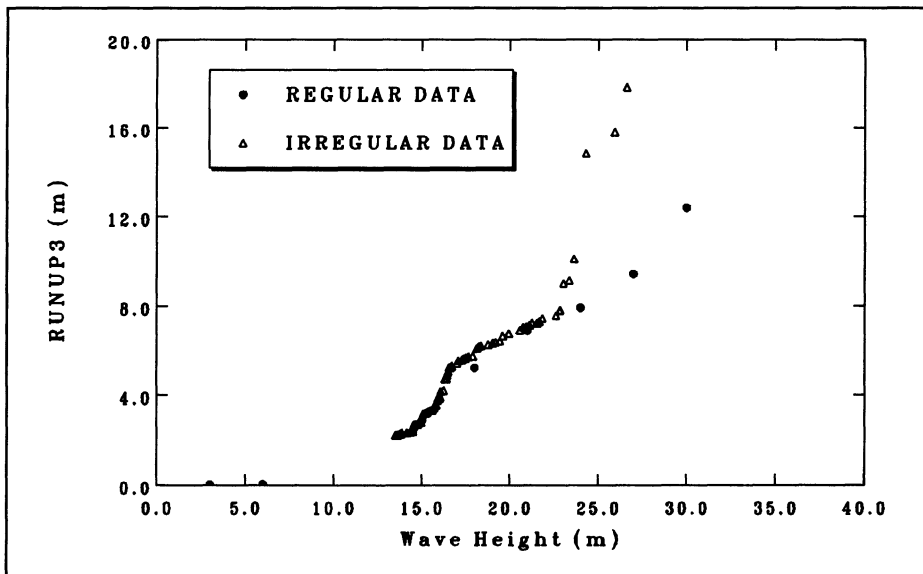


Figure 18. Ranked Plot of Runup

it is necessary to be more selective over the range of data to be used to estimate these extreme quantities.

The assumptions of both the Weibull plots and the ranked plots are basically the same, except that the Weibull approach considers distributions of waves and forces separately, whereas the ranked plotting method considers the two together. The Weibull analysis will yield results that are very close to the ranked plot method when Weibull fitting is done over the upper range of the test results. The choice of appropriate interval is somewhat subjective. However certain judgements are inevitable when dealing with estimates of extreme values.

There are however a number of advantages to be considered with regard to the ranked plots. These may be summarized as follows:

- Ranked plots consider the relationship between the statistics of the wave and the quantity being measured directly, rather than indirectly, immediately illustrating any non-linearities in the relationship.
- The two scales of the ranked plot are linear rather than log or log-log.
- It is easier to consider different intervals of the response range, for different fitting curves. Although this is also possible with the Weibull method, it is more difficult.

Generally model tests involve tests in both regular and irregular waves. One of the objectives of the regular wave tests is to subject the model to a scaled version of the maximum wave that the prototype will experience during its operation. The main concern with the use of the design wave is whether the largest response will occur with the largest wave, and what period is associated with this 'design' wave. Irregular waves provide a more realistic alternative to the design wave since that they allow a statistical means of dealing with this problem.

There is the possibility that the modelled time history in an irregular wave train may not contain a wave having the 'design' wave height. This is a limitation of the finite length of the modelled waves. There will be a distribution of possible maximum wave heights that can be generated from

a particular spectrum. The maximum wave height occurring in any one of these modelled time histories can be larger or smaller than the 'expected' maximum or 'design' value.

In this case the use of the ranked plot technique to estimate extreme values by extrapolation may be difficult if there is no wave height occurring in the wave spectrum equal to or greater than this design wave height. Also the number of data points on the ranked plots can be sparse in this interval and defining a particular point may be difficult. Carrying out a number of additional irregular wave tests with artificially increased wave heights to better define using more points the responses around the highest waves can facilitate the interpolation.

It may also be necessary to investigate the sensitivity of the response to small changes in the waves. In irregular waves the snapshot technique can be used to subject the model to repeated group of waves by running the snapshot in tandem a number of times thus demonstrating the variability in extreme loads. This would provide an indication of the amount of variability in the response to a particular group.

CONCLUSIONS

A 1:40 scaled model of the GBS was successfully designed and constructed to meet the required specifications for global load measurement. The finite-element analysis carried out on the model assembly showed the importance to account for the flexibility of the model when estimating natural frequencies.

Investigations related to the effects of reflections from the basin boundaries on waves incident on the model showed that group velocity is an effective means of identifying the optimum time for data acquisition in regular waves. In irregular waves, snapshots were used to demonstrate that contamination buildup is not severe during irregular wave tests.

Test results showed vertical loading, local pressures, wave runup and air gap to be highly non-linear with respect to both wave heights and crests. All four parameters were highly sensitive to wave grouping and to small changes in wave conditions. Global horizontal loading and overturning moments were found to be more linear and less sensitive to wave grouping patterns.

Ranked plots were found to be more useful in the analysis of the non-linear responses than the Weibull plots since they more readily quantify the degree of non-linearity between waves and responses.

REFERENCES

- [1] Murray, J.J. & Mak, L.M. (1992), "Model Tests on the Preliminary GBS Design for Hibernia", NRC Institute for Marine Dynamics Laboratory Memorandum Number LM-1991-20, St. John's, Canada.
- [2] Faltinsen, O., Kjaerland, O., Nottveit, and Vinje, T., (1977), "Water Impact Loads and Dynamic Responses of Horizontal Circular Cylinders in Offshore Structures", OTC Paper No2741, Houston, Taxes.
- [3] Funke, E.R., (1991), "A Seal For Model Testing of Offshore Structures", National Research Council of Canada, Institute for Mechanical Engineering Hydraulics Laboratory, Lab Memo # IME-CZE-TR-003
- [4] Murray, J.J., Booton, M., Mak, L.M. & Sullivan, M.A. (1992), "Model Design and Testing of a Large Gravity Base Offshore Structure", *Proceedings of 1992 International Congress on Innovative Long Span Structures*, Toronto, Canada. Vol. 1, pp. 826-837
- [5] Murray, J.J. & Mak, L.M. (1992), "An Evaluation of Diffraction Patterns Around a Model Gravity Base Structure in a Wave Basin", *Proceedings of the 11th International Conference on Offshore Mechanics and Arctic Engineering*, Calgary, Canada, Vol. 3, pp.645-652
- [6] Mogridge, G.R., Funke, E.R. and Bryce, P.W. (1989), "Wave Simulation for Run-up and Deck Clearance Tests on a Gravity Base Structure", *Proceedings of the 8th International Conference on Offshore Mechanics and Arctic Engineering*, The Hague, Netherlands, Vol. 2, pp. 563-571
- [7] Broughton, P., Standing, R.G., Vache, M., (1988), "Hydrodynamic Model Testing and Reanalysis of the Ekofisk 2/4 Tank for 6-m Subsidence", 20th Offshore Technology Conference, OTC Paper 5878, Texas.

ADDED HYDRODYNAMIC LOADING DUE TO SACRIFICIAL ANODES.

M.J. DOWNIE, B.A. MURRAY, P. BETTESS and J.V. HASWELL[†]

Department of Marine Technology, University of Newcastle upon Tyne

[†] British Gas Engineering Research Station, Killingworth

There is a scarcity of data relating to the hydrodynamic loading due to sacrificial anodes. A method of calculating factors to apply to circular cylinder force coefficients, using the discrete vortex method is described. The results are presented for uni-directional and oscillatory flows. Equivalent force coefficients are calculated and used in a Morison type analysis of a simple jacket structure in a current and in waves. The overall in-line loading was found to be increased by as much as 9% in modest environmental conditions.

INTRODUCTION

Steel offshore jacket structures are generally protected against corrosion by sacrificial anodes, an impressed current system or a hybrid of the two. Sacrificial anodes are cast from reactive metals (normally zinc or aluminum alloys) which are more electro-negative than the structures they protect, and so corrode in preference to the structural steel of the jacket. Their size is dictated by the desired current and by manufacturing constraints. They are long and slender, of trapezoidal or circular section (perhaps of dimension $2.00 \times 0.25 \times 0.25m$) and weigh in the order of hundreds of kilograms. The optimum stand-off distance between the underside of the anode and the structure to which it is attached has been found to be in the region of 0.25 to 0.35m. Sacrificial anodes are distributed all over the wetted surface of jackets and can number many hundreds even for structures of modest dimensions. It has been estimated that the weight of anodes attached to jackets destined for the North Sea comprises between 4 and 6% of the total weight of the structure when ready for launch⁽¹⁾.

Sacrificial anode systems are usually designed with reference to codes or standards issued by a certifying authority, a government agency, or the owner or operator of the platform. A commonly used code is the DNV Recommended Practice RPB401 'Cathodic Protection Design'⁽²⁾. Whilst codes and guides give detailed information and procedures concerning protection against corrosion, little is specified concerning

the fluid loading relating to individual anodes or their effect on the fluid loading of the structure as a whole.

The in-line force, F , experienced by an element of a jacket structure due to waves is calculated using Morison's equation which, in its simplest form, may be expressed as;

$$F = \frac{1}{2}\rho A C_D U |U| + \rho V C_M \dot{U}, \quad (1)$$

where A and V are the projected area and the volume of the element, U and \dot{U} are the local undisturbed velocity and acceleration of the fluid of density ρ , and C_D and C_M are the drag and inertia coefficients respectively. The terms on the right hand side of the equation represent the drag force and the inertia force experienced by the member in the direction of the ambient flow. Whilst a great deal of research has been carried out to establish values for the force coefficients (see Sarpkaya⁽³⁾, for example) they continue to be a matter of debate. This is because it is difficult to devise appropriate small scale experiments, interpret full scale data (which are in any case scarce) or develop realistic mathematical models for the extremely complex flows involved. Furthermore, the coefficients have been shown to be highly dependent on roughness and protrusions produced by marine growth, or other causes. It is evident that the local forces are likely to be significantly influenced by the presence of sacrificial anodes.

Where the matter is discussed in codes and guidelines it is generally considered that the presence of anodes does not significantly increase volumes and inertia coefficients, but it does increase areas and drag forces. It is therefore normal practice when assessing the drag on structural elements to allow for the increases resulting from the presence of anodes by making adjustments to drag coefficients. This may involve the use of 'equivalent' force coefficients based on the projected areas of the members plus anodes, or it may simply involve the application of a global increase of the drag coefficients of anode bearing members by between 7 and 10%⁽¹⁾. When carrying out fatigue calculations for the anode itself, the fluid particle kinematics may be modified in accordance with simple potential flow theory in which, for example, the velocity at an anode located at the shoulder of a cylinder is taken as approximately twice that of the ambient flow. Estimates of the increase in the net loading on the structure when the force coefficients are modified to account for the presence of the anodes vary from 5%⁽¹⁾ to values several times as much, according to the author of the calculation and the assumptions made.

Such procedures may appear rather vague and simplistic, but the data and the more sophisticated models required for a better informed approach simply do not exist. Although a considerable amount of work has been carried out on interference effects, the configurations considered are usually a small number of cylinders of comparable size, or multi-tube arrangements studied in connection with heat ex-

changers. There has also been some work on risers and multi-tube risers⁽⁶⁾, but for the most part work in this area relates to specific design projects. A modest experimental programme carried out by Singh *et al.*⁽⁷⁾ into the flow past cylinders with various appurtenances in waves at low Keulegan Carpenter number suggested further work on the subject. As far as is known no further work has been done apart from an experimental programme, which is still in progress, and some numerical work, which forms the subject of this paper, carried out by the present authors and associates.

The experimental programme to date comprises an investigation of anode drag in uni-directional flow⁽⁸⁾, and an investigation of the drag of 'blocked anodes', in which the gap between the anode and the member is blocked. Both experiments were carried out on cylinders of diameter D in wind tunnels at Reynolds numbers ($U_m D / \nu$) of approximately 10^5 , where U_m is the magnitude of the velocity of the air of kinematic viscosity ν . A further experiment is planned on anode bearing cylinders using a wave flume capable of generating waves with Reynolds numbers up to 2×10^5 and Keulegan Carpenter numbers up to 50. The objectives of the investigations are to establish the fluid phenomena involved in such flows and to devise a method of estimating the hydrodynamic forces experienced by anode bearing structural members, taking those phenomena into account.

MODELLING THE FLOW

Uni-directional flow about circular cylinders involves boundary layer separation and the formation of a wake downstream from the body composed of regular, organised vortex structures which diffuse with, and are convected by, the ambient flow field. The flow is Reynolds number dependent. At low Reynolds numbers the boundary layers are relatively thick and viscous diffusion is important. As the Reynolds number increases the boundary layers become progressively thinner (giving rise to increasingly high localised velocity gradients) and convection increasingly dominates the flow. A drag crisis, in which the drag coefficient decreases dramatically, occurs at a Reynolds number of around 2×10^5 when the boundary layers undergo transition from laminar to turbulent flow. At still higher Reynolds numbers the flow regains some of the structure observed before transition in the sense that a regular vortex shedding process may once again be detected. The mean location of the time dependent boundary layer separation points vary with Reynolds number and are of great importance in relation to the Reynolds number dependency of the drag.

If uni-directional flow about cylinders is difficult to model, wave flows are even more so. The particle kinematics, which are essentially orbital in nature, can be represented realistically for many applications by planar oscillatory flow. Even so, vorticity generated by the cylinder on one half cycle of the flow may be swept back over the cylinder to interact with the vorticity being generated on the subsequent

half cycle. The complex vortex shedding pattern that ensues is critically dependent not only on the Reynolds number, but also on the Keulegan Carpenter number of the flow, which represents the magnitude of the fluid particle orbits relative to the cylinder diameter. If the Keulegan Carpenter number is sufficiently low the flow, to all intents and purposes, remains attached. If it is sufficiently high, a pseudo Karman vortex street forms on each half cycle of the flow. Regimes of interest offshore tend to be characterised by high Reynolds numbers and high Keulegan Carpenter numbers.

Adding anodes to the configuration has both advantages and disadvantages as far as modelling the flow is concerned. Whilst there is inevitably an interaction between the anode and cylinder flows, in certain arrangements the separation points tend to become fixed. On these grounds, as for flat plates and square cylinders, it can be argued that the Reynolds number dependency of the anode bearing cylinder is likely to be less than that for the bare cylinder. It has in any case become customary, because there is no other choice, to endeavour to predict flow at high Reynolds numbers from small scale experiments and low Reynolds number computations. The same approach has been taken in the work to be described.

Since it is not possible to model the flow rigorously using even the most sophisticated of numerical techniques and the most powerful computers available, and since for various reasons comprehensive large scale experiments are prohibitive, the approach adopted uses as simple a numerical model as possible and available experimental data. The easiest approach is to use force coefficients for cylinders in unbounded flows (which are readily available) and to calculate an equivalent coefficient for the cylinder plus anodes based on the total projected area. The approach could be made more sophisticated by using the force coefficients in conjunction with velocities calculated using simple potential theory. It could be further refined by using instead drag coefficients for cylinders in close proximity to a wall, for which results are also available. However, it has been shown⁽⁹⁾ using experimental results from experiments on anodes in unbounded flows, ground flows and attached to cylinders⁽⁸⁾, that these overly simplistic approaches do not give satisfactory results. This is not surprising. Potential flow theory can only give the crudest approximation to the kinematics of such complex separated flows, and in any case the flow about anode bearing cylinders is quite different from unbounded cylinders or cylinders in a ground flow. For example, although anodes attached transverse to the flow increase the drag considerably, those attached in-line with the flow have been found to decrease it in relation to that of a bare cylinder⁽⁸⁾.

The next simplest class of models available, which have been used with some success with separated flows, are the discrete vortex models and those that have evolved from them. This approach is used to model the flow around a circular cylinder with a protuberance with a view to producing factors which may be applied to circular cylinder force coefficients so as to give an estimate of the forces experienced by cylinders bearing anodes.

THE NUMERICAL MODEL

The flow about a structural member with anodes was modelled by a two-dimensional circular cylinder with protrusions in an incompressible time-dependent flow. This was on the basis that in reality the gap between the anode and the member becomes effectively ‘blocked’ with encrustations and weed. A two-dimensional model was chosen because a three-dimensional one is not viable. Also, in two dimensions, it is possible to treat the flow about the deformed cylinder through calculation of the flow about a circular cylinder, which is relatively simple, using a conformal transformation technique. The transformation which takes a circle of radius a (in the ζ -plane) into a deformed circle (in the z -plane) is based on a Laurent series and is given by;

$$z = e^{i\alpha} \left(\zeta + \sum_{k=1}^{N_t} \frac{a_k}{\zeta^k} \right). \quad (2)$$

All calculation is carried out in the circle plane, although the usual equations for flow about a circular cylinder have to be duly modified to take account of the flow in the real (transformed) plane.

The method used is based on the discrete vortex method which, along with other allied methods, has been thoroughly reviewed by Sarpkaya⁽¹³⁾. The flow is described by the vorticity convection equation,

$$\frac{\partial \omega}{\partial t} + u \cdot \nabla \omega = \nu \nabla^2 \omega, \quad (3)$$

which is solved by an operator splitting technique involving a diffusion step and a convection step over each timestep of a continually evolving flow.

The vorticity in the flow, which is largely confined to subdomains in an otherwise irrotational flow, is modelled by arrays of point singularities, or point vortices. At each timestep discrete vortices are introduced around the cylinder so as to satisfy appropriate boundary conditions. The vortex circulations are then distributed over the nodes of a grid covering the computational domain, where they are allowed to diffuse in accordance with the diffusion equation,

$$\frac{\partial \omega}{\partial t} = \nu \nabla^2 \omega, \quad (4)$$

using a finite difference scheme and properly accounting for the diffusion in the real plane⁽¹⁰⁾.

With the updated distribution of vorticity, the convection step is carried out in accordance with the equation,

$$\frac{\partial \omega}{\partial t} + u \cdot \nabla \omega = 0, \quad (5)$$

using the basic discrete vortex method, a Lagrangian approach in which the vorticity, $\omega = \nabla \times u$, is represented by discrete vortices which are convected with the flow.

The nodal velocities are calculated⁽¹⁰⁾ via the complex potential,

$$W = \phi + i\psi = (\zeta - \frac{a^2}{\zeta})U + \frac{i}{2\pi} \sum_{j=1}^{N_v} \Gamma_j (\ln(\zeta - \zeta_j) - \ln(\zeta - \zeta_j^*)), \quad (6)$$

where ϕ is the velocity potential, ψ is the stream function, U is the free stream velocity, Γ_j is the strength of the j^{th} nodal vortex and ζ_j^* is the location of its image vortex inside the circle required to maintain the boundary condition, $\partial\phi/\partial n = 0$, on the cylinder surface. The velocities of the discrete vortices, located at ζ_p , are calculated by interpolation and moved using a simple time integration scheme;

$$\zeta_p(t + \Delta t) = \zeta_p(t) + \frac{\partial \zeta_p}{\partial t} \Delta t, \quad (7)$$

in which the $\frac{\partial \zeta_p}{\partial t}$ term correctly accounts for the kinematics in the real plane.

The complex force ($Z = X + iY$) on the cylinder plus anode may then be calculated from the generalised Blasius equation which can be shown to reduce to⁽¹⁰⁾;

$$Z = 2\pi\rho a^2 \left(1 - \frac{a_1}{a^2} e^{2i\alpha}\right) \frac{\partial U}{\partial t} - i\rho \sum_{p=1}^{N_v} \left((u_p - u_p^*) \Gamma_p - (a + \zeta_p^*) \frac{\partial \Gamma_p}{\partial t} \right), \quad (8)$$

where u_p and u_p^* are the velocities of the p^{th} vortex and its image respectively. Force coefficients may be obtained by non-dimensionalising the complex force, with respect to $\frac{1}{2}\rho U_m^2 D$, and decomposed into Fourier averaged drag and inertia coefficients for unsteady flows. Further details of the model may be found in reference 10.

NUMERICAL RESULTS

The results for the variation of the drag coefficient with Reynolds number for the bare cylinder in uniform uni-directional flow are shown in Figure 1, and can be seen to be in reasonable agreement with experimental results⁽³⁾ over the sub-critical range. The alternate shedding pattern causes an asymmetric time dependent pressure distribution over the cylinder which leads to a zero mean transverse

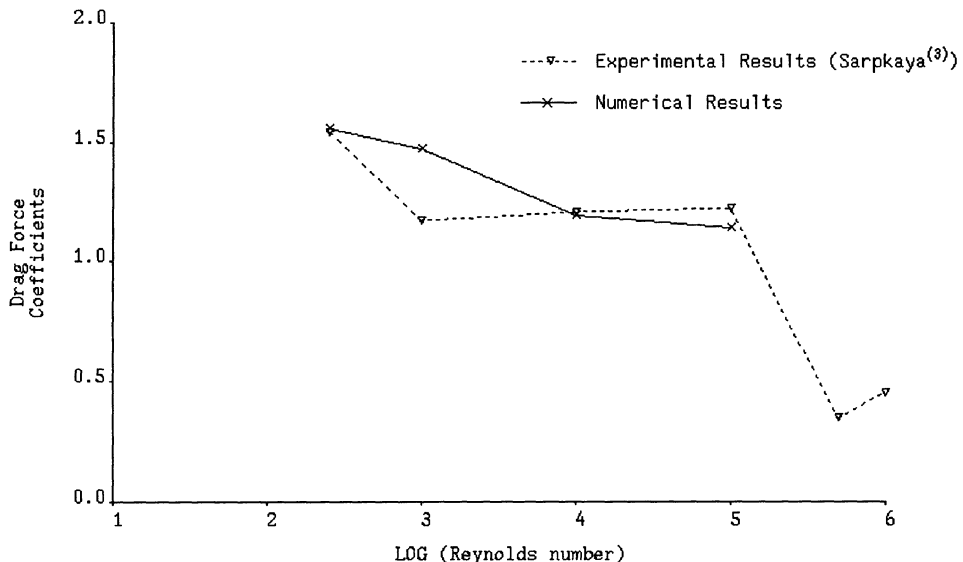


Figure 1 : Drag Force Coefficents for
Uni-directional Flow Around a Circular Cylinder.

(lift) force. The root mean square lift coefficients, $C_{L_{rms}}$, range from 0.57 to 0.73 which, again, are in good agreement with experimental results⁽³⁾.

The addition of a single (blocked) anode has a significant influence on the flow, which depends on the angle of inclination, α , of the anode in relation to the flow direction. The flow patterns for the anode at a variety of angles of incidence at a Reynolds number of 250 are shown in Figure 2. The presence of the anode has at least two fundamental effects on the flow. It allows the possibility of an asymmetric body with respect to the direction of flow, and over a range of angles it fixes the separation point on one side of the body, which also introduces asymmetries into the flow. If the anode is in-line with the flow it behaves rather like a cylinder with a splitter plate ($\alpha = 0^\circ$) or a reversed thick aerofoil ($\alpha = 180^\circ$), leading to a reduction of the drag coefficient in relation to the bare cylinder. If the anode is inclined, whether it is leading or trailing the cylinder, it tends to induce separation in such a manner that the vortices roll up closest to the 'lowest' side of the cylinder, leading to a fluctuating lift force with a steady negative non-zero mean. The drag increases as the location of the anode approaches the shoulder of the cylinder. A typical force trace is shown in Figure 3 and the results for the drag coefficient, expressed as multiples of the bare cylinder drag coefficient, are presented in Table 1. The fluctuations of the transverse force coefficients are of a similar magnitude to those of the bare cylinder, and the magnitude of the steady component of the transverse force coefficients can equal their root mean square value⁽¹⁰⁾. The largest

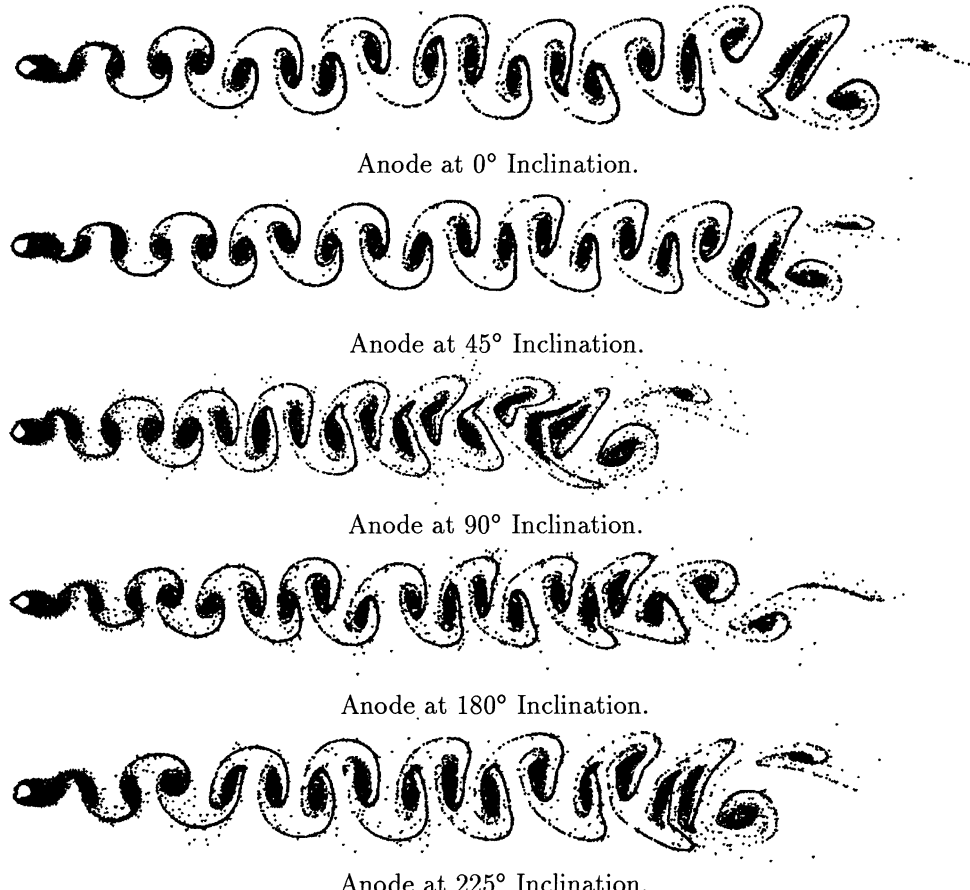


Figure 2 : Flow Visualisations at $R_e = 250$.

lift forces occur when the anode is located on the shoulder of the cylinder ($\alpha = 90^\circ$ or 180°).

The results for a circular cylinder in planar oscillatory flow are dependent upon both the Reynolds number and the Keulegan Carpenter number. The vortex shedding process is very complex, as may be appreciated from Figure 4, which shows the flow pattern when time $t = 75D/U_m$, the Reynolds number is 10^5 and the Keulegan Carpenter number is 15. The figure also shows the variation of the in-line force with time and gives the drag and inertia coefficients. The variation of the root mean square (rms) in-line force coefficient, $C_{F_{rms}}$, with Keulegan Carpenter number is given in Figure 5. It may be seen that the numerical model tends to overpredict the in-line force, and that the coefficients are more appropriate to Reynolds numbers of the order of 10^4 . There is considerable scatter in measured lift coefficients, but the numerical results for the lift coefficient are bounded on ei-

	Re	Angle of Inclination				
		0°	45°	90°	180°	225°
Single Anode (I)	250	1.451	1.137	1.376	0.897	1.158
	10^3	0.898	0.946	1.451	0.928	1.209
	10^4	0.882	0.899	1.621	0.884	1.236
	10^5	0.899	0.884	1.616	0.954	1.263
Single Anode (II)	10^5	0.706	0.998	1.866	0.606	1.421

Table 1 : Drag Coefficient factors for Uni-directional Flow with Anodes Attached.

	Angle of Inclination	Keulegan-Carpenter Number					
		5	10	15	20	25	30
$\frac{\bar{C}_D(\text{body})}{\bar{C}_D(\text{bare cylinder})}$	0°	0.950	0.890	0.957	0.947	0.967	0.809
	45°	1.107	0.972	0.974	1.170	1.219	0.936
	90°	2.186	1.788	1.675	1.520	1.613	1.338
$\frac{\bar{C}_M(\text{body})}{\bar{C}_M(\text{bare cylinder})}$	0°	0.869	0.758	0.904	1.029	0.698	1.007
	45°	1.077	1.054	1.115	0.944	1.117	1.028
	90°	1.075	0.950	1.089	1.496	0.971	1.515
$\frac{C_{F_{rms}}(\text{body})}{C_{F_{rms}}(\text{bare cylinder})}$	0°	0.870	0.813	0.926	0.943	0.896	0.817
	45°	1.076	1.016	1.021	1.116	1.169	0.930
	90°	1.235	1.373	1.467	1.481	1.458	1.337

Table 2 : Force coefficient Factors for Oscillatory Flow with Anodes Attached.

ther side by experimental results for Reynolds numbers of the same order⁽⁷⁾⁽¹¹⁾⁽¹²⁾.

The rms in-line force coefficients for a cylinder bearing a single anode at a number of angles of inclination, α , at different Keulegan Carpenter numbers and at a Reynolds number of 10^5 , are shown in Figure 6. The force coefficients are non-dimensionalised with respect to the cylinder diameter. The configuration is based on working drawings of a real anode of sectional area of $0.17 \times 0.17m$ attached to a cylinder of diameter $0.5m$. The flow mechanisms involved are difficult to decipher,

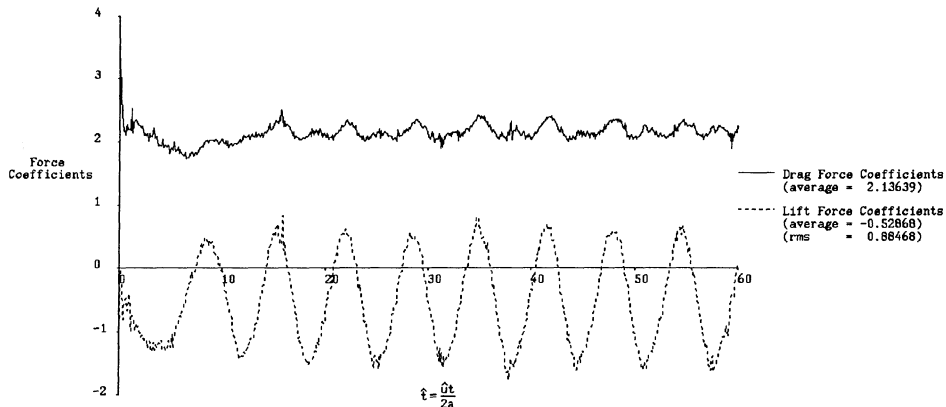


Figure 3 : Force Coefficients for Anode at 90° Inclination ($R_e = 250$).

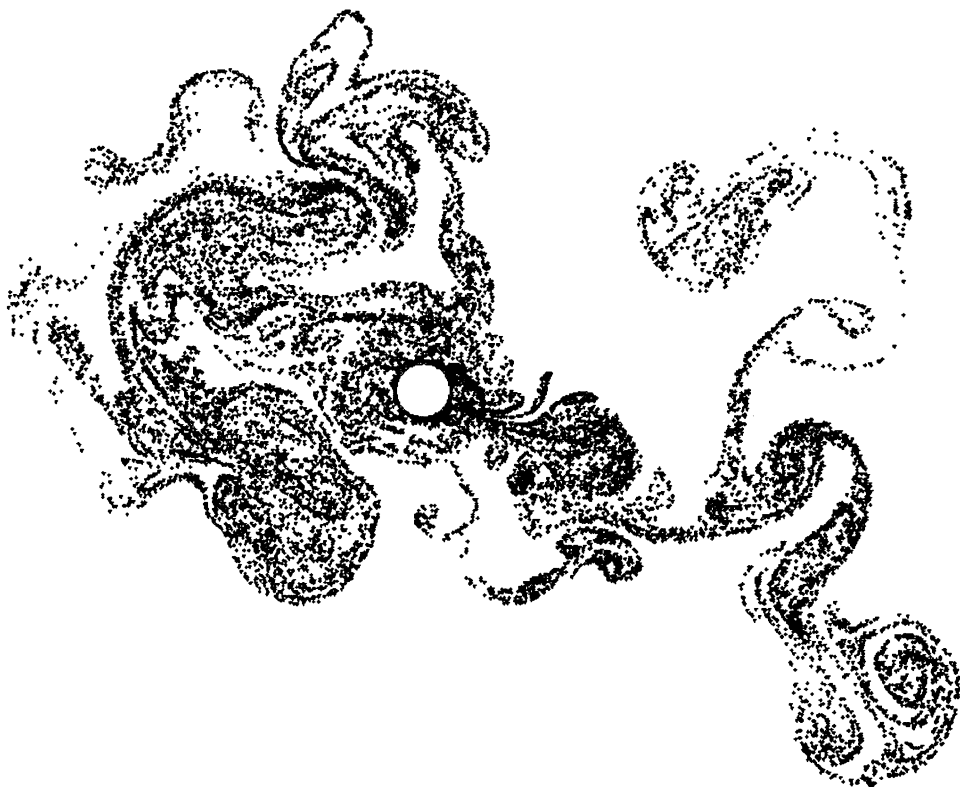
other than that they tend to follow similar trends to those shown by the anode bearing cylinders in uni-directional flows. The largest in-line forces are obtained when the anodes are oriented at right angles to the flow, and the in-line force tends to decrease relative to the bare cylinder when the anodes are in-line with the flow.

The same behaviour was obtained with a cylinder with two anodes attached to it at 180° to one another, as shown in Figure 7. As might be expected, the rms in-line force coefficient increases with the addition of another anode by around 18% when $\alpha = 45^\circ$ to around 50% when $\alpha = 90^\circ$. There are a few exceptions to these general trends but there appears to be no obvious reason for these.

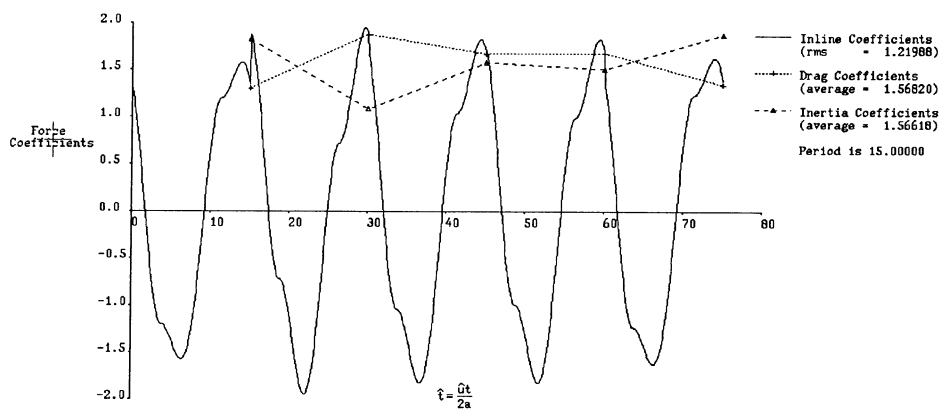
APPLICATION OF RESULTS

As has been mentioned, in assessing the fluid loading on a jacket structure, the Morison equation is used. Global values for the force coefficients may well be taken, but a more refined solution may be obtained by choosing force coefficients associated with a characteristic Reynolds number and Keulegan Carpenter number for each member. When anodes are fixed to the members such a calculation has to be refined still further to account for the flow asymmetries induced by their presence. Each anode will contribute to the in-line force on the member to which it is attached, but it will increase or decrease it depending on whether it is in-line or transverse to the flow.

Whilst an anode bearing member could be further sub-divided for the Morison analysis into elements that contain anodes and those that do not, the simplest approach to modifying the force coefficients is to calculate 'equivalent' force coefficients for each complete member. In the method adopted the input data file to the Morison analysis software was adapted so as to signify whether, or not, members carried anodes, and what the anode orientation was with respect to a local axis



Oscillatory Flow Visualisation.



Oscillatory Flow Force Coefficients.

Figure 4 : Oscillatory Flow at a Keulegan Carpenter number of 15.

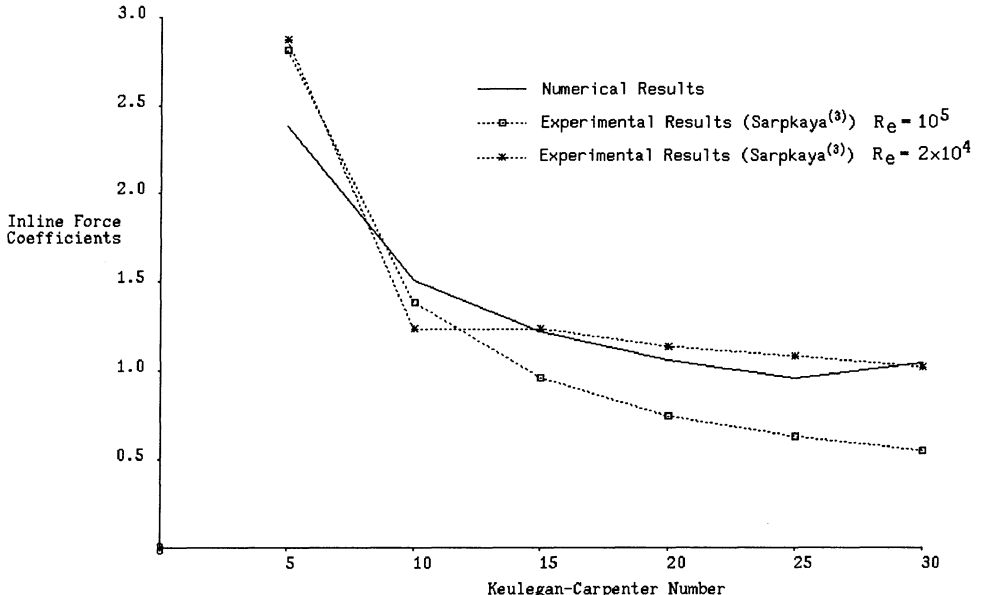


Figure 5 : $C_{F_{rms}}$ against K_c for a Circular Cylinder.

system. The data file was then pre-processed to determine equivalent force coefficients along the two local axes normal to the members using factored force coefficients taken from the numerical study.

The total in-line force on each member was apportioned according to the relative lengths of bare and anode bearing member, and to the anode orientation. The in-line anodes were treated as a generalised geometry with fixed force coefficients taken straight from the numerical results. The numerical transverse drag coefficients were modified so that the relative contributions made by the portion of the cylinder carrying the anode, and the anode itself, were proportioned to their respective projected areas.

The equivalent drag coefficient, for example, of a member of length L_m and diameter D_m bearing N_I different sets of n_j in-line anodes and N_T different sets of n_j transverse anodes is given by⁽¹⁰⁾;

$$C_{D\text{ equiv}} = C_D \left(1 + \frac{1}{L_m D_m} \sum_{j=1}^{N_I+N_T} n_j L_j \beta_j \left(\frac{C_{Dj}^*}{C_D} - 1 \right) \right), \quad (9)$$

where the alignment factor, $\beta_j = D_m$ for an in-line anode, $\beta_j = D_j/\delta_j^*$ for a transverse anode and C_D is the drag coefficient for a bare circular cylinder. The drag coefficient calculated numerically for the j^{th} configuration with the anode to cylinder

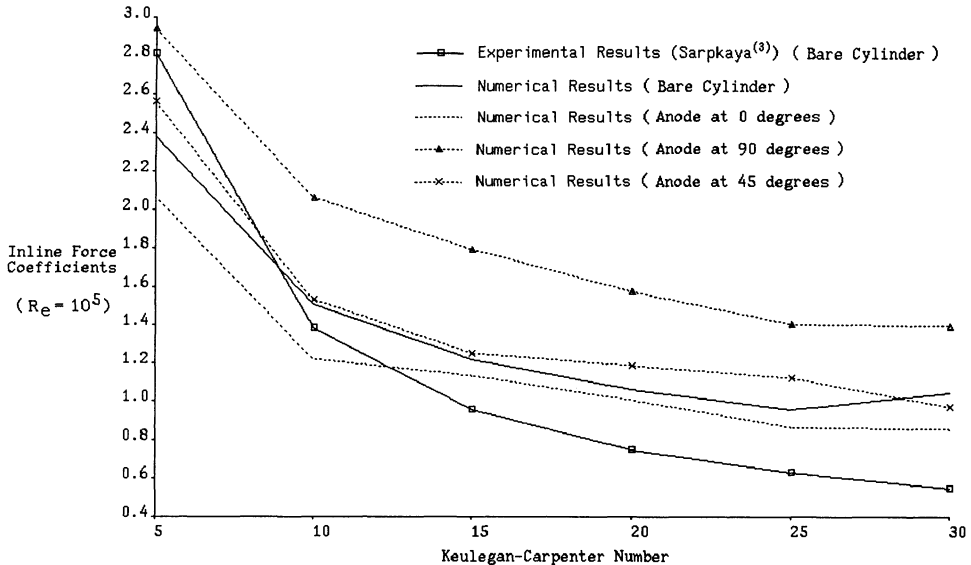


Figure 6 : $C_{F_{rms}}$ against K_c with One Anode Attached.

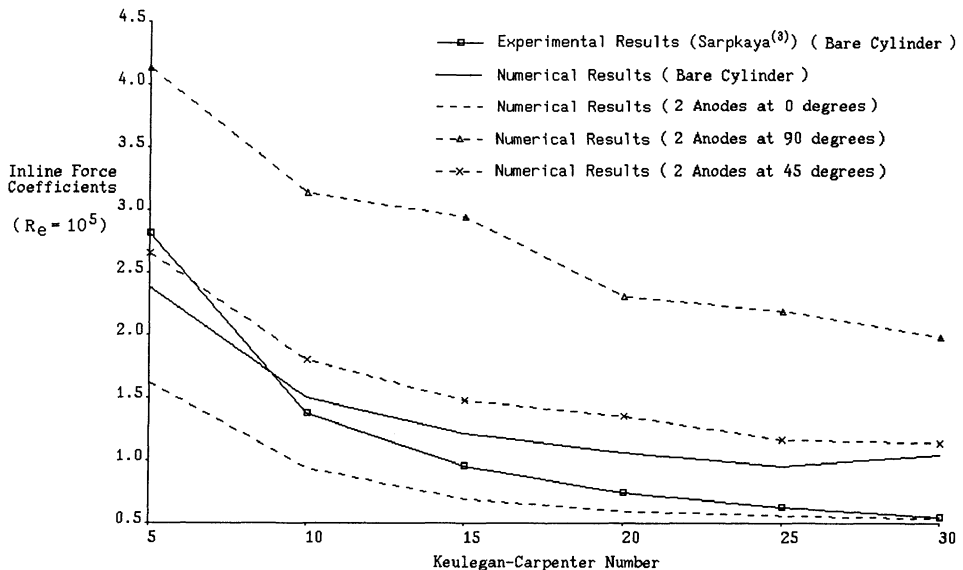


Figure 7 : $C_{F_{rms}}$ against K_c with Two Anodes Attached.

der diameter ratio of δ_j^* is $C_{D_j}^*$. The approach is equally valid with experimental data, and the terms in parentheses could be treated as a multiplication factor to be used with any chosen circular cylinder drag coefficient.

Every member in the data file, having been processed, has associated with it two sets of force coefficients appropriate to its local axes. The calculation of the local forces F then takes the form:

$$\begin{pmatrix} F_2 \\ F_3 \end{pmatrix} = \frac{1}{2}\rho D U_N M_D M \begin{pmatrix} U_1 \\ U_2 \\ U_3 \end{pmatrix} + \frac{1}{4}\rho\pi D^2 M_M M \begin{pmatrix} \dot{U}_1 \\ \dot{U}_2 \\ \dot{U}_3 \end{pmatrix}, \quad (10)$$

where,

$$M_D = \begin{pmatrix} 0 & C_{D_2} & 0 \\ 0 & 0 & C_{D_3} \end{pmatrix}, \quad M_M = \begin{pmatrix} 0 & C_{M_2} & 0 \\ 0 & 0 & C_{M_3} \end{pmatrix}$$

and U_N is the magnitude of the fluid velocity normal to the member and U_i and \dot{U}_i are the local fluid velocities and accelerations in relation to the global axes calculated from linear wave theory. The global fluid loading acting on every node of the jacket can be calculated in a straightforward manner from knowledge of the local fluid loading at any point on the structure.

CASE STUDIES

Four case studies were carried out on the simple jacket structure shown in Figure 8 carrying a realistic distribution of anodes. The structure has 44 nodes, 96 members and 140 anodes and stands approximately 50m above the sea bed. In all the case studies the anodes were single and oriented in the global vertical plane. The case studies were all chosen so that the force coefficients used lay within the data set of the numerical calculations.

In the first case study the structure was subjected to a uniform uni-directional current of $1ms^{-1}$ and in the second, to a uni-directional current varying with water depth with a velocity profile given by $u = 1.06 - 0.24d$, where d varies from 0 at the mean water to 1 at the sea bed. The profile is appropriate for parts of the southern North Sea. The total base shear was calculated for the structure with and without anodes in both cases. For the uniform current, the base shear of the anode bearing structure was 8.8% larger than that of the bare structure. The base shear was increased by 8.5% with the current with a velocity profile.

The calculation of the hydrodynamic forces on the jacket is more complicated for oscillatory flows, since the force coefficients are functions of the Keulegan Carpen-

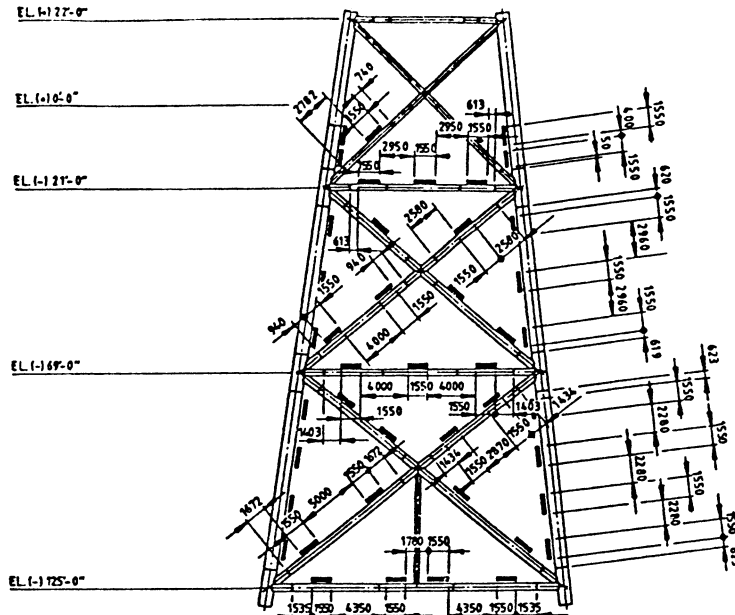


Figure 8 : Jacket Structure.

ter number, which in turn depends on the local fluid velocity amplitude and the diameter of the member. In order to keep the calculations as simple as possible, flow conditions were chosen so that, for a given wave, the Keulegan Carpenter number remained constant for all members of any given diameter. These conditions occur for a shallow water wave of a period of 45s for which the horizontal water particle velocity is independent of elevation and whose amplitude, $\frac{H}{2} \sqrt{\frac{g}{d}}$, depends only on the wave height. By selecting appropriate wave heights, calculations covering the Keulegan Carpenter range from 5 to 30 were carried out. Since a small vertical component of fluid loading is introduced by the wave flow, the comparison between the bare and anode bearing structure was made in terms of the average amplitude of the in-line force over the cycle. The results are given in Table 3.

H (m)	K_c	increase in in-line force
0.5	5 and 10	0.1%
1.0	10 and 20	5.4%
1.5	15 and 30	8.2%

Table 3 : Structure Loading in Shallow Water Waves.

The final case study was carried out for more realistic conditions, namely for a wave period of 10s and wave height 10m. In this case the horizontal water particle velocity amplitude ranges from about $0.32Hm/s$ at mean water level to $0.08Hm/s$ at the sea bed, with an average value of $0.15H$. The Keulegan Carpenter number used for all members was based on the average value of the velocity, which yielded values of 15 and 30, depending on member diameter. The average amplitude of the in-line force over the cycle was found to be 9.2% higher for the anode bearing structure than for the bare structure.

CONCLUSIONS

Experimental data on the hydrodynamic loading due to the presence of sacrificial anodes is scarce, a rigorous method of computing it, for all practical purposes, does not exist, and very simple models, such as potential flow models or the use of drag coefficients in unbounded flows, do not give good results. The objective of the present study was to gain an understanding of the fluid phenomena and to model the flows as simply as possible in order to determine force coefficients for a variety of flow regimes that could be used to estimate the hydrodynamic loading on a jacket structure. The discrete vortex method was used to model the separated flows, which cannot be handled by potential flow models. A number of simplifying assumptions were made which allowed the calculation of factors to be applied to force coefficients for circular cylinders leading to coefficients for cylinders with protrusions in uni-directional flow and oscillatory flow for Keulegan Carpenter numbers from 5 to 30.

The results for the uni-directional flow showed the same trends as obtained by experiment, in that in-line anodes decreased the force coefficients and transverse ones increased them. Similar trends were shown by anodes in oscillatory flow. The results for oscillatory flows also showed that as the Keulegan Carpenter number increases, and the drag increasingly dominates the flow, the influence of the anodes becomes increasingly important as shown in Table 3. Finally, it was shown, for the simple structure chosen, and in the context of assumptions made, even fairly modest environmental conditions can lead to a hydrodynamic loading on the structure with anodes that is 9% greater than the structure without anodes. It may be assumed that this increase will be significantly larger in the harsher environment to which jacket structures are often exposed.

The study indicates that the hydrodynamic loading due to sacrificial anodes is considerably higher than generally estimated from the simple approaches described in the introduction. The method of obtaining a more accurate estimate developed in this study could equally well be used with experimental data rather than the numerical results calculated using the discrete vortex method. The results obtained in this study justify further work of this nature.

ACKNOWLEDGEMENTS

The work carried out for this study was supported by a British Gas Engineering Research Award.

REFERENCES

- (1) Marine Technology Directorate Ltd. (1992) "Design and Operational Guidance on Cathodic Protection of Offshore Structures, Subsea Installations and Pipelines." Publication 90/102.
- (2) Det Norske Veritas (1986) "Cathodic Protection Design." Veritas Recommended Practice RPB 401.
- (3) Sarpkaya T. and Isaacson M. (1981) "Mechanics of Wave Forces on Offshore Structures." Van Nostrand Reinhold and Company.
- (4) Wolfram J. and Theophanatos A. (1989) "The Loading of Heavily Roughened Cylinders in Wakes and Linear Oscillatory Flow." Proc. of 8th Int.Symp. on Offshore Mechanics and Arctic Engineering. The Hague, Holland.
- (5) DOE. (1990) "Guidance Notes for the Design and Construction of Offshore Installations." HMSO.
- (6) Sarpkaya T. (1979) "Hydrodynamic Forces on Various Multiple Tube Riser Configurations." OTC Paper No.3539, Houston, Texas.
- (7) Singh S., Cash R., Harris D. and Boribond L. (1982) "Wave Forces on Circular Cylinders with Large Excrescences at Low Keulegan Carpenter Numbers." NMI Report R133.
- (8) Downie M.J., Shepherd W. and Graham J.M.R. (1991) "A Study of the Geometry and Hydrodynamic Drag of Sacrificial Anodes." Corrosion 1991, Manchester.
- (9) Easton A. (1992) "Fluid Loading on Offshore Jacket Structures due to Sacrificial Anodes." Department of Marine Technology, University of Newcastle upon Tyne.
- (10) Murray B.A. (1992) "Hydrodynamic Loading due to Appurtenances on Jacket Structures." PhD. Thesis, University of Newcastle upon Tyne.
- (11) Bearman P.W. (1984) "Vortex Shedding from Oscillating Bluff Bodies." Ann. Rev. Fluid Mech. 16 (pp.195-222).
- (12) Obasaju E.D., Bearman P.W. and Graham J.M.R. (1988) "A Study of Forces, Circulation and Vortex Patterns Around a Circular." J. Fluid Mech. vol.196 (pp.467-494).
- (13) Sarpkaya T. (1989) "Computational Methods with Vortices - The 1988 Freeman Lecture." J. Fluid Mech. vol.111 (pp.5-52).

THE VORTEX INDUCED VIBRATION OF MARINE RISERS IN SHEARED AND CRITICAL FLOWS

G.Jones (Stena Offshore Ltd) & W.S.Lamb (Flowmaster UK Ltd)

Marine risers are commonly exposed to sheared flows, and the Reynolds number is often high enough to ensure that the flow lies in the critical regime. Despite this, the analysis of vortex induced vibration in marine risers is largely based on physical data obtained from model tests where the flow was subcritical and had a uniform profile.

This paper begins with a brief review of current knowledge pertaining to the effects of shear and critical flow on levels of vortex induced vibration. Details are then presented of a new analytical model which can be used to predict amplitudes of vibration in sheared (and uniform) flows.

In order to gain new information on the behaviour of marine risers in sheared and critical flows, and to validate the analytical prediction method, a large scale model test programme was carried out using a 6 m deep water flume.

The presence of shear in the incident flow was found to reduce the peak levels of vibration, but the shear extended the range of velocity over which the vibration occurred. These effects were, in general, predicted quite accurately by the analytical model.

Critical flow was also found to reduce levels of vibration (by about 40%) and shifted the amplitude response curve to lower Reduced Velocities.

KEY WORDS: Vortex, Vibration, Sheared Flow, Marine Riser.

NOTATION

Symbol	Description	Unit
ARM	Amplitude response model.	-
C_d	Drag coefficient.	-
$C_l(z)$	Local coefficient of fluctuating lift force.	-
D	Diameter.	m
DWF	Deep water flume.	-
EHD_l	Energy lost by cylinder per cycle due to linear hydrodynamic damping.	J
EHD_q	Energy lost by cylinder per cycle due to quadratic hydrodynamic damping.	J
EHE	Energy transferred to cylinder per cycle due to hydrodynamic excitation.	J
ESD	Energy lost by cylinder per cycle due to structural damping.	J
K_s	Stability Parameter.	-
L	Length of cylinder.	m
LSP	Linear shear velocity profile.	-
$m(z)$	Local mass per unit length.	kg/m
Re	Reynolds number.	-
RVM	Reduced Velocity multiplier.	-
RVRR	Reduced Velocity response range.	-
SSP	Stepped shear velocity profile.	-
t	Time.	s
$U(z)$	Local free stream velocity.	m/s
U_{ref}	Reference free stream velocity depending on flow profile.	m/s
V_r	Reduced Velocity.	-
$V_r(z)$	Local Reduced Velocity.	-
Y	Maximum cross-flow displacement.	m
$Y_l(z)$	Local maximum cross-flow displacement.	m
Y/D	Reduced Amplitude.	-
Y_β/Y_o	Normalised shear amplitude.	-
y	Cross-flow cylinder displacement.	m
z	Distance along cylinder's longitudinal axis.	m

Greek symbols

β	Steepness Parameter.	-
γ	Ratio of excitation length to cylinder length.	-

δ_s	Logarithmic decrement of structural damping.	-
δ_h	Logarithmic decrement of hydrodynamic damping.	-
ρ	Density.	kg/m^3
$\psi(z)$	Mode shape.	-
ω	Frequency of structural vibration.	r/s

1 INTRODUCTION

The exploitation of offshore oil reserves involves the extensive use of slender cylindrical structures, such as drilling and production risers, which are often exposed to strong ocean currents. Marine risers are compliant structures and their natural frequencies are, in many cases, similar to the natural frequency of vortex shedding caused by the local currents; they are, therefore, susceptible to vortex induced vibration.

Marine risers are commonly exposed to sheared flows, and the Reynolds number is often high enough to ensure that the flow lies in the critical regime. Despite this, the analysis of vortex induced vibration in marine risers is largely based on physical data obtained from model tests where the flow was sub-critical and had a uniform profile. The main reason for this over-simplified approach is simply a lack of knowledge; the effect of critical flow on vibration levels is unknown and, although shear is known to reduce peak vibration levels, it is generally not possible to predict the magnitude of the reduction.

The work reported in this paper was carried out to enable the effects of shear and critical flow to be quantified so that they can be included in the vortex induced vibration analysis of marine risers.

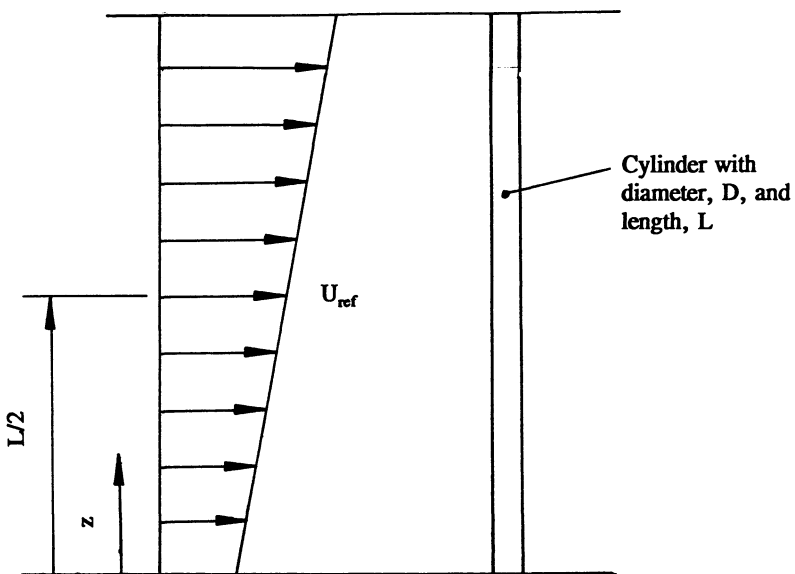


Fig. 2.1 Circular cylinder in a linearly sheared flow profile.

2 BACKGROUND

Consider a circular cylinder of length L and diameter D which is subjected to a linearly sheared flow profile, as illustrated in Fig 2.1. The degree of shear is characterised by the Shear Parameter, β as defined in the following equation:-

$$\beta = \frac{D}{U_{ref}} \times \frac{dU}{dz} \quad (1)$$

Where: U_{ref} = Reference velocity, usually defined as the mid-span or mean value.
 dU/dz = Velocity gradient.

The cylinder's amplitude of vibration can, in theory, be described as a function of the following dimensionless parameters :-

$$\frac{Y}{D} = f \left\{ V_x, K_s, \beta, \psi(z), Re, \frac{L}{D} \right\} \quad (2)$$

In uniform sub-critical flow (i.e. $\beta=0$ $Re < 3 \times 10^5$), the influence of the dimensionless groups in equation 2 on Reduced Amplitude is quite well understood. Cross-flow vortex induced vibration is known to occur when the Reduced Velocity lies in the range 4.5 to 10, and maximum vibration levels usually occur in the range 6.5 to 8.0¹ (Sarpkaya, 1979, King, 1977). The Stability Parameter (K_s) and mode shape ($\psi(z)$) determine the magnitude of the peak vibration amplitude, which can be as high as two diameters (Fig. 2.2).

When the flow becomes non-uniform or the Reynolds number is increased beyond 3×10^5 into the critical regime, however, the relationship between Reduced Amplitude and the governing dimensionless parameters (equation 2) is unknown.

Recent reviews by Humphries (1987) and Griffin (1985) highlight the lack of work which has been carried out to investigate the effect of shear on the vortex induced vibration of flexible cylinders, and the consequent incomplete understanding of the phenomenon. The majority of investigations have been

¹ These ranges are for vibration in water; the ranges are shifted slightly for vibrations in air (Sarpkaya, 1979)

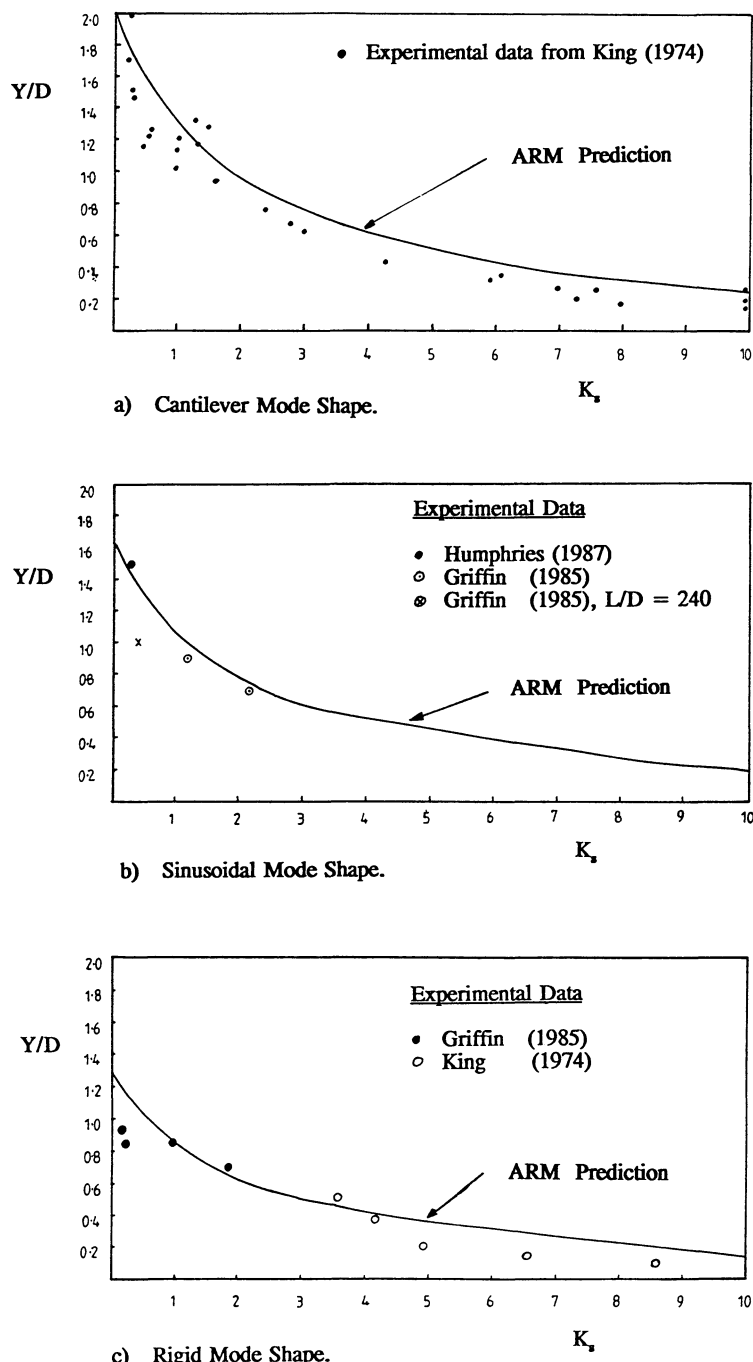


Fig. 2.2 Predicted and measured Reduced Amplitude versus Stability Parameter for a variety of mode shapes.

concerned with very slender cables, where the lock-on phenomenon can, under certain circumstances, be ignored (see Vandiver and Chung 1988, for example). Such studies are, therefore, not directly relevant to this paper, except, perhaps, for the case of very deep water risers which may behave more like cables than flexible cylinders.

The most recent comprehensive study of the effects of sheared flow under lock-on conditions was carried out by Humphries (1987), who found that shear flow decreased the maximum amplitude of vibration, but slightly increased the range of Reduced Velocity over which the vibrations occurred (This range is known as the Reduced Velocity Response Range (RVRR)).

Humphries (1987) has shown that, provided the Reduced Velocity (V_r) is based on the free stream velocity at the structural antinode, the RVRR and position of the peak vibration is unaffected by shear.

In an attempt to develop a method of predicting vibration amplitudes in sheared flow, Humphries used his own experimental results to test Vandiver's 'Equivalent Stability Parameter' prediction method (Vandiver, 1985). He concluded that there were too many fundamental uncertainties pertaining to the method to enable it to be used in practice and, instead, proposed an empirical method of predicting the peak Reduced Amplitude which was based on the shear parameter, β (equation 1).

The prediction curve, shown in Fig. 2.3, is extremely conservative as it embraces all the data points, some of which are highly scattered. At low values of shear parameter the method over-predicts by as much as 50%.

Very little information is available on vortex induced vibration in critical flow. Lamb & Walker (1987) found that critical flow reduced the peak level of vortex induced vibration on an artificially roughened model cylinder, but the extent to which this was due to the critical flow (rather than the surface roughness) was unclear. Humphries & Walker (1988) reported the results of experiments on a large scale model cylinder which was thought to be subjected to critical flow. The cylinder underwent large amplitude vortex induced vibration and Humphries concluded that critical flow had little effect on vibration levels. On closer inspection, however, it became apparent that the peak vibration had occurred in the upper sub-critical region and not in fully critical flow. The large measured amplitudes were, therefore, to be expected, and the effect of fully critical flow remained unknown.

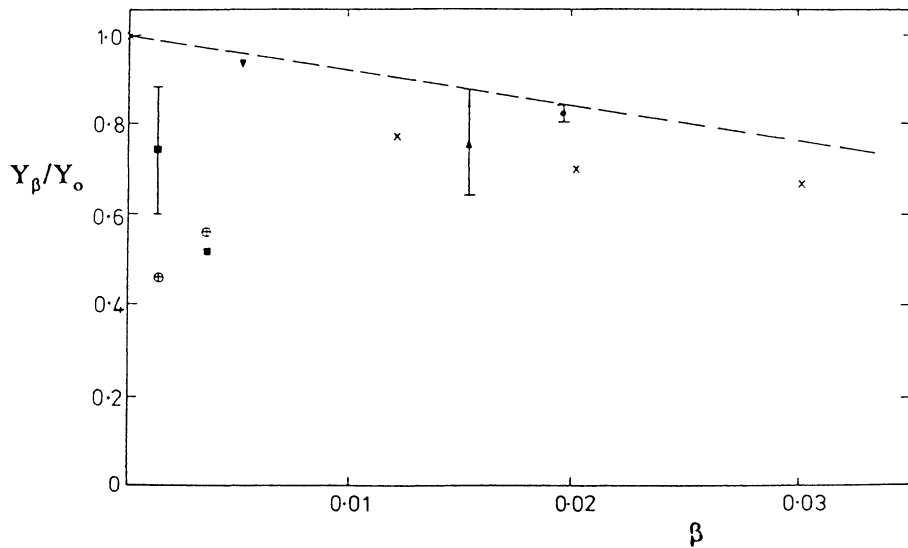


Fig. 2.3 Normalised shear amplitude versus Shear Parameter (Humphries, 1987).

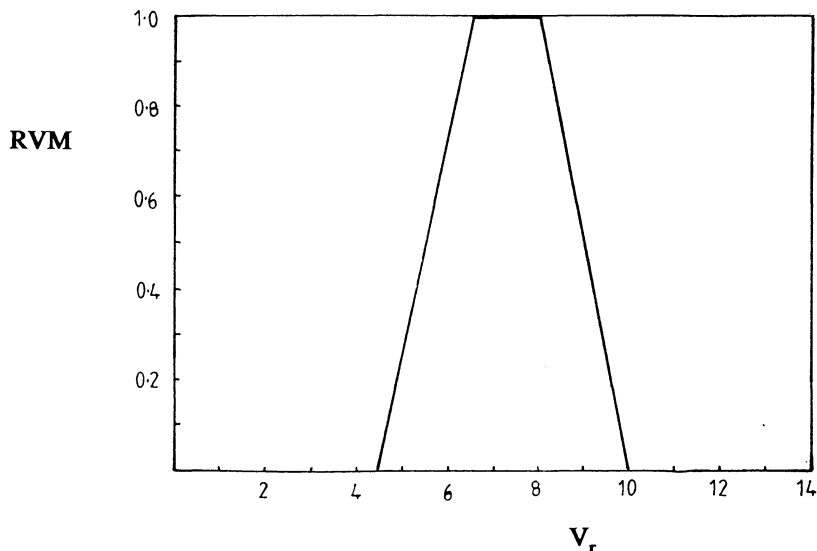


Fig. 3.1 Reduced Velocity multiplier (RVM) versus Reduced Velocity.

3 ANALYTICAL MODEL

By considering relatively simple riser configurations it is possible to show that the effect of shear on amplitude levels will depend on riser length and mode shape. It follows that the Shear Parameter alone cannot be used to predict the effect of shear on vibration levels, and attempts to produce a simple empirical relationship by plotting amplitude reduction versus Shear Parameter will, in general, result in scattered data, as illustrated by Fig. 2.3.

Given the complex nature of the phenomenon, it was decided that the best way of predicting Reduced Amplitude in sheared flows was to develop a computer based mathematical model which would be flexible enough to model a wide variety of riser configurations and which would automatically account for the effects of mode shape, riser length and Stability Parameter.

Before any development work was undertaken, a review of the many existing vortex induced vibration models was carried out (Lamb, 1991). The objective of this work was centred around the prediction of the maximum steady state amplitude of vibration, and it was concluded that this would be most efficiently accomplished by considering an energy balance, such as used by Brooks (1987). The method is generally applicable to a wide variety of physical situations and, in particular, is ideal for the inclusion of axial variations in the input parameters such as those produced by sheared incident current and the application of certain types of suppression device.

3.1 Outline of the Model

The amplitude response model (ARM) consists of the following principal elements:-

Structural motion

The cylinder is assumed to oscillate in one of its normal modes, such that the local maximum amplitude ($Y_l(z)$) is related to the global maximum amplitude (Y) by a mode shape parameter ($\psi(z)$):-

$$Y_l(z) = Y \cdot \psi(z) \quad (3)$$

The cylinder is modelled as a one dimensional body which oscillates with

simple harmonic motion. Since the in-line motion, which inevitably accompanies cross-flow vortex induced vibration, is relatively small it is ignored, and the equation of motion for the cylinder is:-

$$y(z, t) = Y_1(z) \cdot \sin(\omega \cdot t) \quad (4)$$

Energy formulae

It is assumed that, in general, there are three principal forces acting on the structure:-

- Hydrodynamic excitation caused by the vortex shedding in regions of lock-on.
- Hydrodynamic damping caused by the relative motion between the structure and the fluid in regions outside the lock-on range.
- Structural damping caused by internal friction.

The criterion for establishing the presence of lock-on is based on the local Reduced Velocity ($V_r(z)$). All regions along the length of the cylinder where $V_r(z)$ lies in the range 4.5 to 10 are defined as regions of lock on. All other regions are assumed to be subjected to hydrodynamic damping rather than excitation.

The following formulae can be derived for the work done by each of these forces during one complete cycle of the cylinder's vibration ¹:-

The energy transferred to the cylinder due to hydrodynamic excitation (EHE) is given by:-

$$EHE = \pi \cdot D \cdot \frac{\rho}{2} \cdot Y \cdot \int_0^L C_1(z) \cdot U^2(z) \cdot \psi(z) \cdot dz \quad (5)$$

The energy dissipated by the cylinder as a result of structural damping (ESD) is:-

¹ The meaning of the symbols in the following equations is defined in the Notation at the beginning of the paper.

$$ESD = \delta_s \cdot \omega^2 \cdot Y^2 \cdot \int_0^L m(z) \cdot \psi^2(z) \cdot dz \quad (6)$$

And the energy dissipated as a result of hydrodynamic damping (EHD) can be expressed by two equations, depending on the type of damping assumed; quadratic damping (equation 7) or linear damping (equation 8).

$$\begin{aligned} EHD_q &= \frac{4}{3} \cdot \rho \cdot C_d \cdot D \cdot (Y \cdot \omega)^2 \\ &\times \int_0^L \frac{8}{3} \cdot \left\{ \frac{1}{2} \left(\frac{5 \cdot U(z)}{3\omega} \right)^2 + (Y \cdot \psi(z))^2 \right\}^{1/2} \cdot \psi^2(z) \cdot dz \end{aligned} \quad (7)$$

$$EHD_l = \delta_h \cdot \omega^2 \cdot Y^2 \cdot \int_0^L m(z) \cdot \psi^2(z) \cdot dz \quad (8)$$

Note that, because equations 5 to 8 are written in terms of local parameters (e.g. $U(z)$, $\psi(z)$) they are applicable to any current profile, uniform or sheared.

Energy balance solution

The law of conservation of energy is used to form an energy balance which results in an expression of the form:-

$$\frac{Y}{D} = f \{ K_s, V_r, \psi(z), C_l(z) \} \quad (9)$$

Experimental results are used to derive an expression for $C_l(z)$ ¹ and, since K_s , V_r and $\psi(z)$ are known, or can be estimated, equation 9 can be used to determine the Reduced Amplitude. A computer program has been written to implement the method. An iterative technique is used because of the dependence of the lift coefficient on the amplitude of vibration.

¹ Equations are derived which allow the lift coefficient to be calculated as a function of local Reduced Amplitude and Reduced Velocity. For full details see Lamb (1991).

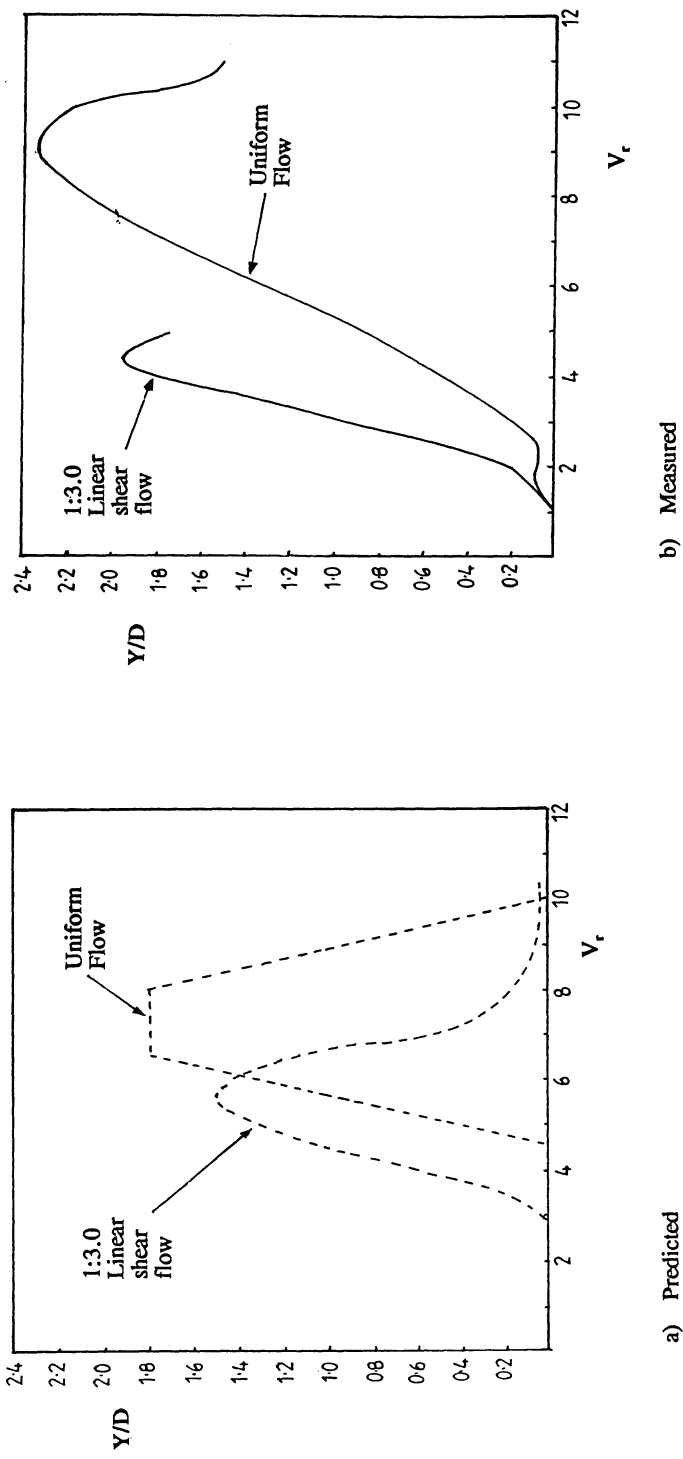


Fig. 3.2 A comparison between predicted and measured Reduced Amplitude in uniform and sheared flows: $K_s = 0.22$.

3.2 Model Predictions

Uniform Flow

The peak Reduced Amplitude predicted by the ARM depends on Stability Parameter and mode shape, as shown in Fig. 2.2. Experimental results from a variety of sources have also been included in this figure and, in general, there is good agreement with the predicted curves.

Peak values are predicted to occur when the Reduced Velocity lies in the range 6.5 to 8.0, outside this range, the response is reduced by a factor (the Reduced Velocity multiplier (RVM)) as shown in Fig. 3.1.

Sheared Flow

The method of treating shear which is used by the ARM program is akin to representing the cylinder as a collection of small (rigid) cylinders, each of which behaves as if it were exposed to its own, local, uniform Reduced Velocity. The lift force and energy input per unit length due to hydrodynamic excitation for each element is exactly the same as for an equivalent rigid cylinder in a uniform flow (i.e one with identical Reduced Amplitude and Reduced Velocity).

Before carrying out the large scale experimental work described in section 4, it was possible to test the ARM's predictions by direct comparison with experimental results from small scale tests on a series of cantilevered cylinders carried out by Humphries (1987).

Humphries tests were designed to determine the effect of a linearly sheared flow profile ($\beta = 0.02$) on the Reduced Amplitude of the cantilevers over a range of Stability Parameter. His results, some of which are reproduced here as Figs. 3.2b, 3.3b and 3.4b, demonstrated that the shear profile reduced the peak response (when compared to the uniform flow case) by a factor of about 0.82, and that this factor appeared to be independent of Stability Parameter.

The ARM was run using the input parameters appropriate to three of the cylinders used by Humphries and used to predict the response to a uniform and linearly sheared flow profile, over a range of Reduced Velocity¹. The results are shown in figures 3.2a, 3.3a and 3.4a, and a summary of the predicted and measured peak amplitudes is given in table 1, below.

¹ The predictions shown in Figs. 3.2a, 3.3a and 3.4a were obtained by assuming quadratic damping. Both quadratic and linear hydrodynamic damping models were tried; the difference in the results was small in this case.

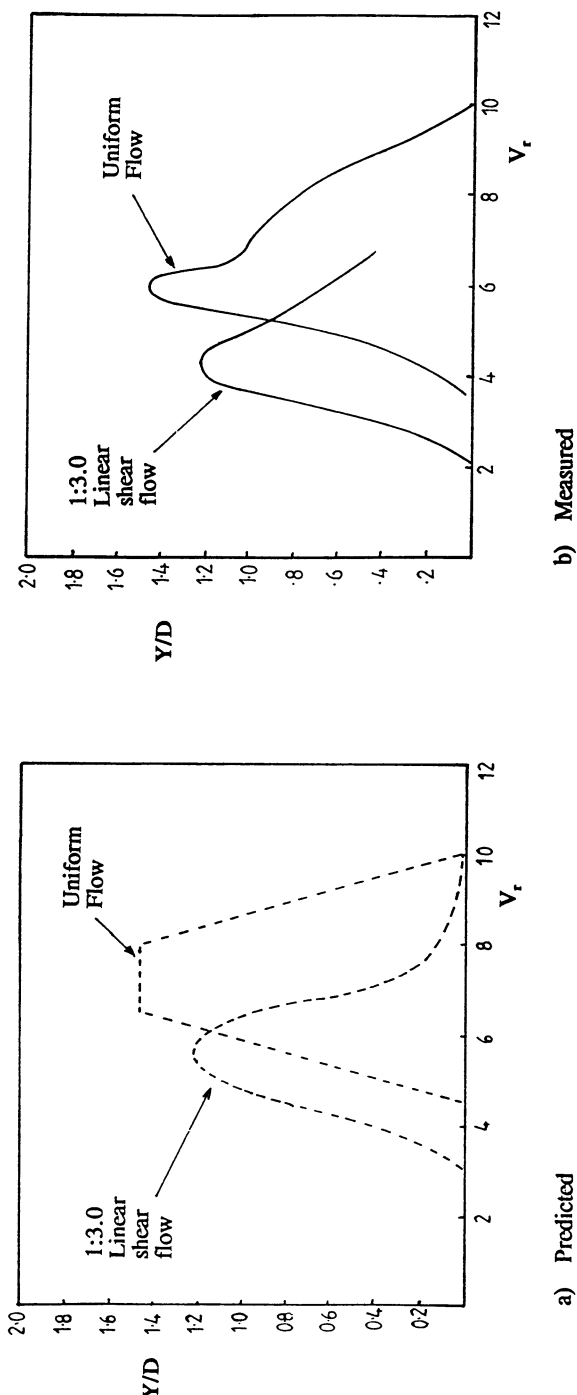


Fig. 3.3 A comparison between predicted and measured Reduced Amplitude in uniform and sheared flows: $K_s = 0.68$.

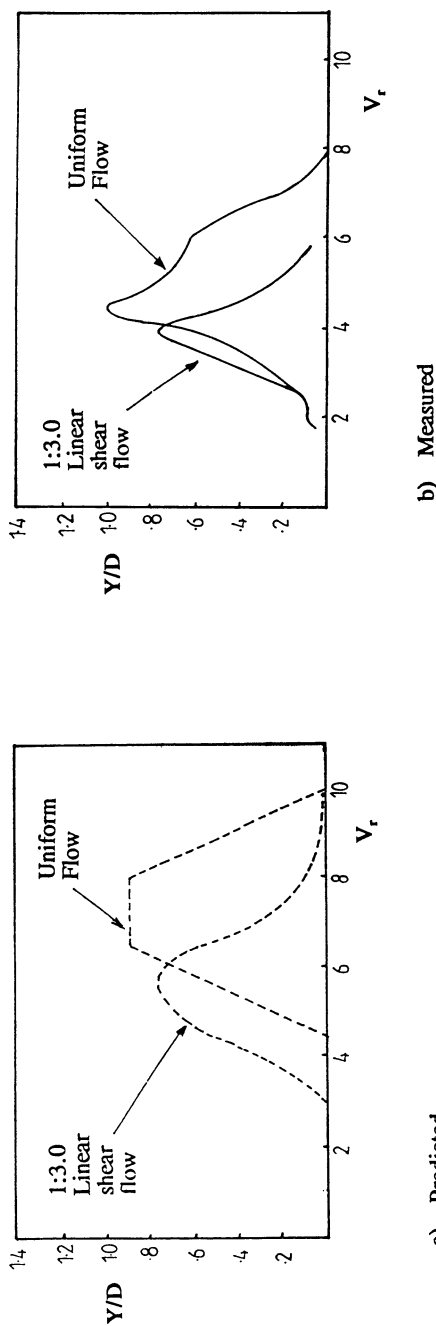


Fig. 3.4 A comparison between predicted and measured Reduced Amplitude in uniform and sheared flows: $K_s = 2.3$.

Table 1 The effect of linear shear on peak amplitude response

Stability Parameter	Peak amplitude ($\beta = 0.02$)	
	Peak amplitude ($\beta = 0$)	
	ARM prediction	Measured
0.22	0.84	0.83
0.68	0.84	0.84
2.30	0.85	0.80

Considering the complexity of the physics involved in the cantilevers vibration and the relative simplicity of the ARM model, the agreement between the predicted and measured results was judged to be good.

The relative ¹ reduction in peak amplitude and shift in response toward lower Reduced Velocities which occurred as a result of the sheared flow was modelled well by the ARM, although the absolute value of amplitude and RVRR was less well predicted.

Perhaps the most important aspect of the cylinder's response, from an engineering design viewpoint, is the maximum Reduced Amplitude (Y/D_{\max}). For the cylinders having a Stability Parameter of 0.68 and 2.3 the ARM accurately predicted the value of Y/D_{\max} in the uniform and sheared flow cases. The response of the cylinder with the lowest Stability Parameter (0.22) was under-predicted, although the relative effect of the shear was well modelled. For this cylinder, Humphries measured a peak Reduced Amplitude of 2.4 which is well above the accepted maximum value for cantilevers of 2.0. The under-prediction was, therefore, to be expected.

The ARM predicted that the effect of the linear shear on peak amplitudes would be independent of Stability Parameter, as stated by Humphries (see table 1 above).

¹ Relative to the uniform current case.

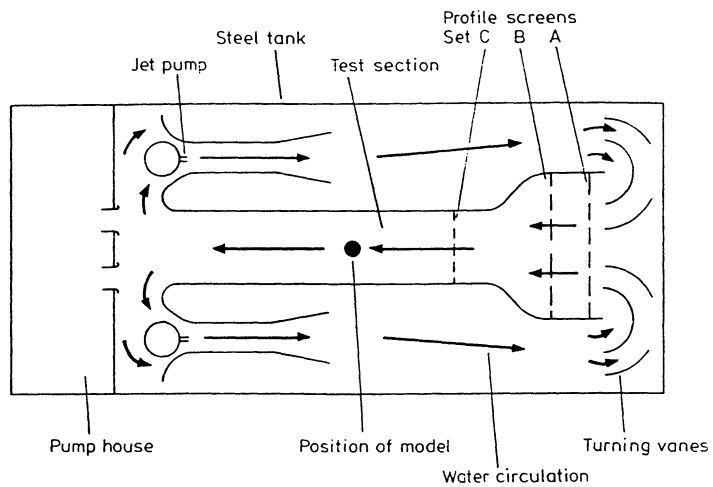


Fig. 4.1 Plan view of the Deep Water Flume.

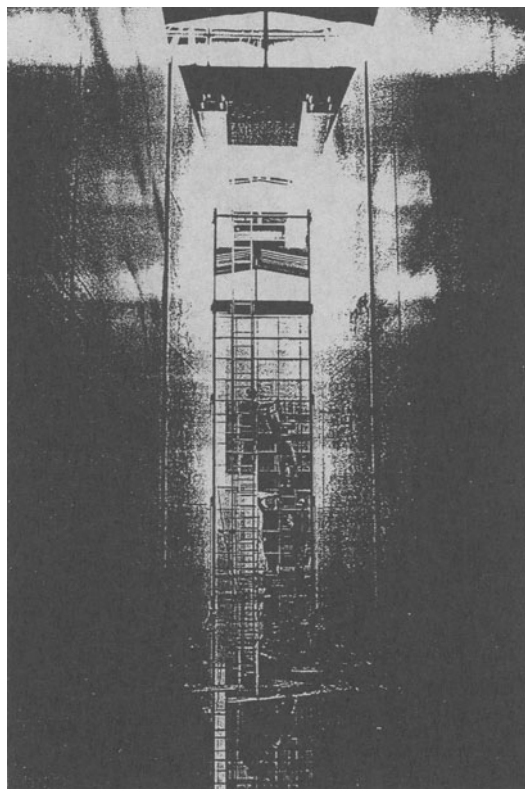


Fig. 4.2 The 6 m deep test section of the Deep Water Flume.

4 EXPERIMENTAL TEST PROGRAMME

4.1 Test Facility and Models

Experimental work was required to meet two objectives:-

- 1 Validate the ARM predictions at large scale.
- 2 Determine the effects of critical flow on vortex induced vibration.

Testing was carried out in BHR Group's Deep Water Flume (DWF) test facility. The DWF consists of a large steel tank with internal plate steel fabrications in which water is made to circulate as shown in Fig. 4.1. The circulating flow is generated by two 275 kW pump sets, each of which discharges through a narrow, vertically positioned slit which acts as a jet pump.

The test section is 6 m deep, 1.5 m wide and 8 m long. A photograph of the test section is shown in Fig. 4.2. Velocity through the test section can be controlled in the range 0.5 m/s to 2.1 m/s (uniform profile) using gate valves which are positioned immediately downstream of the centrifugal pumps.

Three sets of perforated metal screens can be positioned upstream of the test section so as to generate non-uniform flow profiles (4.1). Set A straightens the flow and reduces any large scale turbulence. Set B is used to generate sheared current profiles which vary linearly over the vertical extent of the test section (known as linear shear profiles or LSPs). Set C is used in conjunction with Set B in order to generate steep LSPs. In order to produce stepped shear profiles (SSPs), blockage screens are placed in position C only.

Ocean current profiles can be complex, and may include both linear and stepped shear regions. Consequently, a range of profiles has been used during this project which includes stepped and linearly sheared examples (Figs. 4.3 and 4.4). LSPs are characterised by the Shear Parameter (β), as discussed in section 2. In order characterise the SSPs the excitation ratio is defined as follows:-

$$\gamma = \frac{\text{Excitation length}}{\text{Cylinder length}} \quad (10)$$

In this project, the excitation length was the length of the cylinder which was exposed to the high velocity flow (Fig. 4.4).

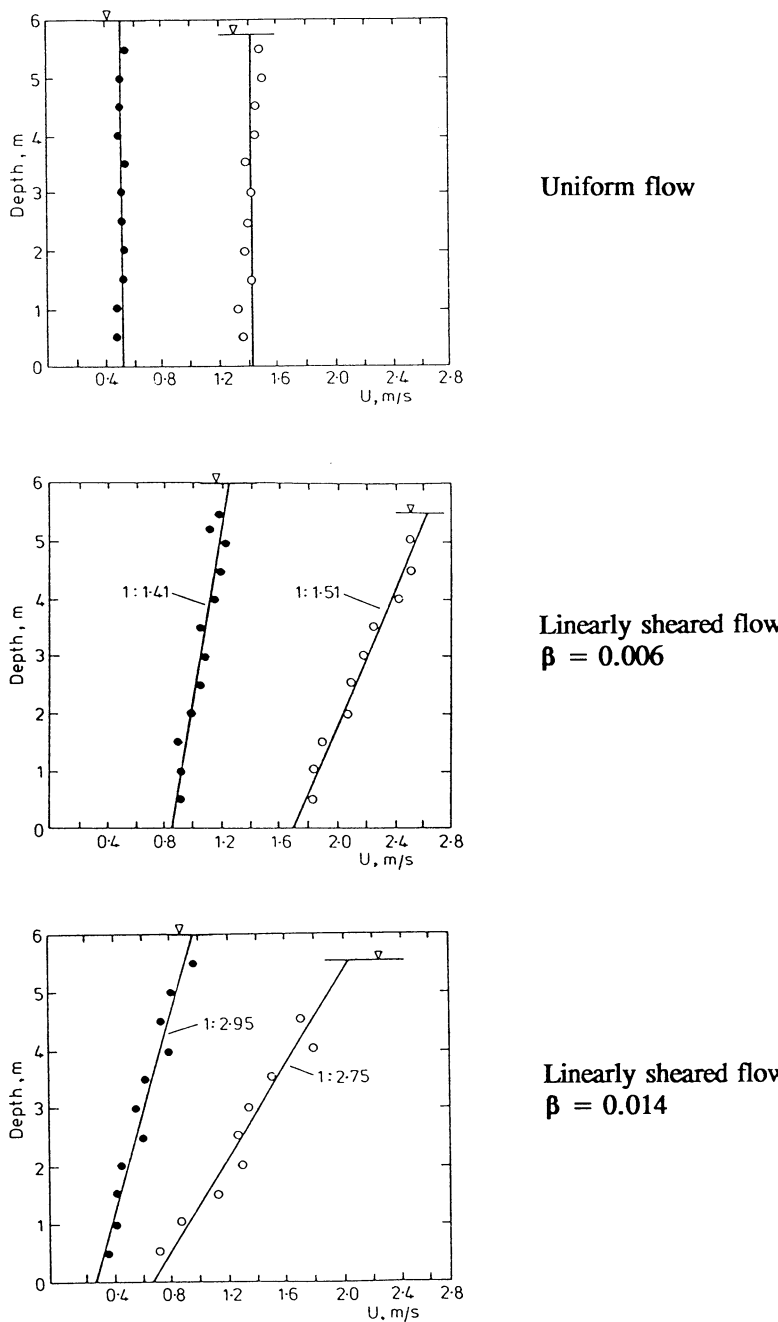


Fig. 4.3 Uniform a linearly sheared flow profiles.

Two models were used in the test programme, as described below:-

Model 1

This cylindrical plastic model was designed to meet objective No. 1; it was 5.6 m long and had a diameter of 0.076 m. The model was extremely flexible and had a low Stability Parameter, typical of a marine riser ($K_s < 1$). Axial tension was applied to the top of the model to produce the required first mode natural frequency (1.5 Hz).

Model 2

To meet objective No. 2 it was necessary to construct a second model, similar in design to Model 1, but with a larger diameter (0.15 m). This allowed testing to be carried out in the fully critical regime¹. Model 2 was designed to vibrate with a frequency of 1.7 Hz in first mode.

4.2 Instrumentation

Flow velocity was measured at three different depths in the test section using A.OTT propeller meters with a quoted accuracy of +/- 2%. The vibration of both models was measured using Sensotec type RM waterproof accelerometers which were positioned inside the models at the modal antinodes. A frequency analyzer was used to record the signals from the accelerometers. These signals were later integrated twice to obtain the amplitude of vibration.

Note that hydrodynamic drag was also measured using load cells positioned within the model supporting framework, but drag is not discussed in this paper because of space limitations.

4.3 Test Programme

A summary of the tests carried out on the two models is given in the table below. All tests were carried out twice as a check on the repeatability of the experiment. For linearly sheared flows, the reference velocity (U_{ref}) was the mid-span (i.e. average) velocity. For the stepped shear profiles, the reference velocity was the flow velocity in the region of vibration excitation (i.e. the higher velocity region over the upper portion of the model (Fig. 4.4)).

¹ Reynolds numbers were of the order of 2×10^5 which, because of the high turbulence level in the flume (3%) resulted in critical flow around the model.

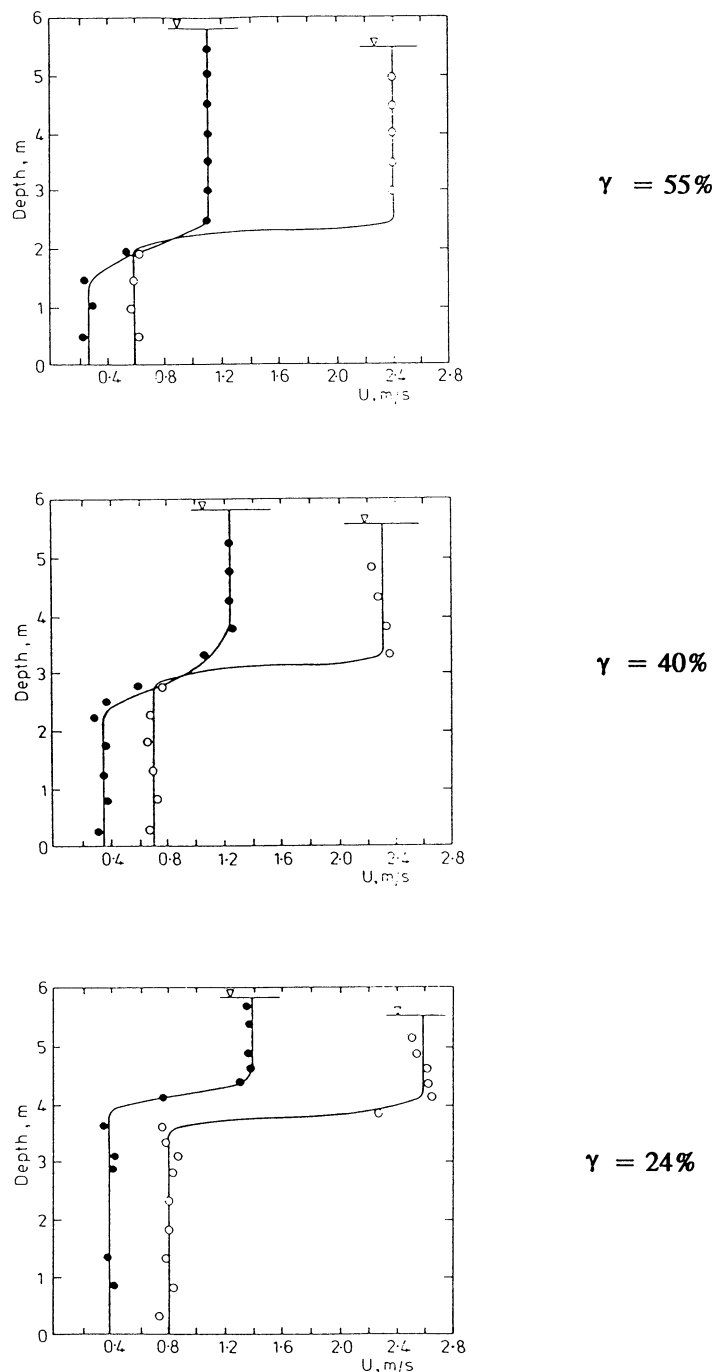


Fig. 4.4 Stepped shear velocity profiles.

Table 2 Test programme

Model	Flow Profile	Degree of Shear	Velocity Range (U_{ref} , m/s)	Velocity Increment (m/s)
Model 1	Uniform	$\beta = 0$	0.5 to 2.0	0.1
"	Linearly sheared	$\beta = 0.006$	0.5 to 1.9	0.1
"	"	$\beta = 0.014$	0.3 to 1.5	0.1
"	Stepped shear	$\gamma = 55\%$	0.6 to 2.0	0.1
	"	$\gamma = 40\%$	0.6 to 2.0	0.1
	"	$\gamma = 24\%$	0.6 to 2.0	0.1
Model 2		$\beta = 0$	1.3 to 2.0	0.1

4.4 Results and Discussion

Effects of Current Shear (Model 1 Tests)

The experimental results for the uniform and linearly sheared profiles are shown in Fig. 4.5. In uniform flow, the model's vibration response was classical in that significant amplitudes occurred within the Reduced Velocity range 4.5 to 10 and the peak response occurred at a Reduced Velocity of about 7. The maximum Reduced Amplitude recorded was 1.52 and this is typical of a cylinder which has a sinusoidal mode shape and a low Stability Parameter (Fig. 2.2).

It is evident from Fig. 4.5 that linear shear affected the amplitude response in three ways:-

- The peak was reduced.
- The RVRR was widened, particularly at the upper end.
- The Reduced Velocity at which the peak response occurred was shifted, however, this shift was small and did not take the peak outside the Reduced Velocity range 6.5 to 8.0 which is the accepted band for uniform flow.

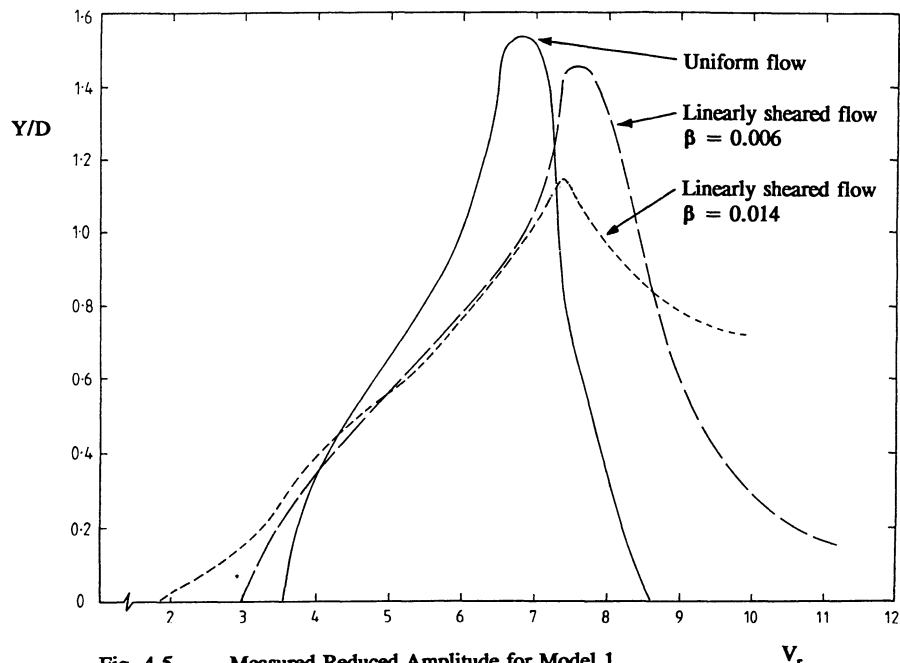


Fig. 4.5 Measured Reduced Amplitude for Model 1
in uniform and linearly sheared flow.

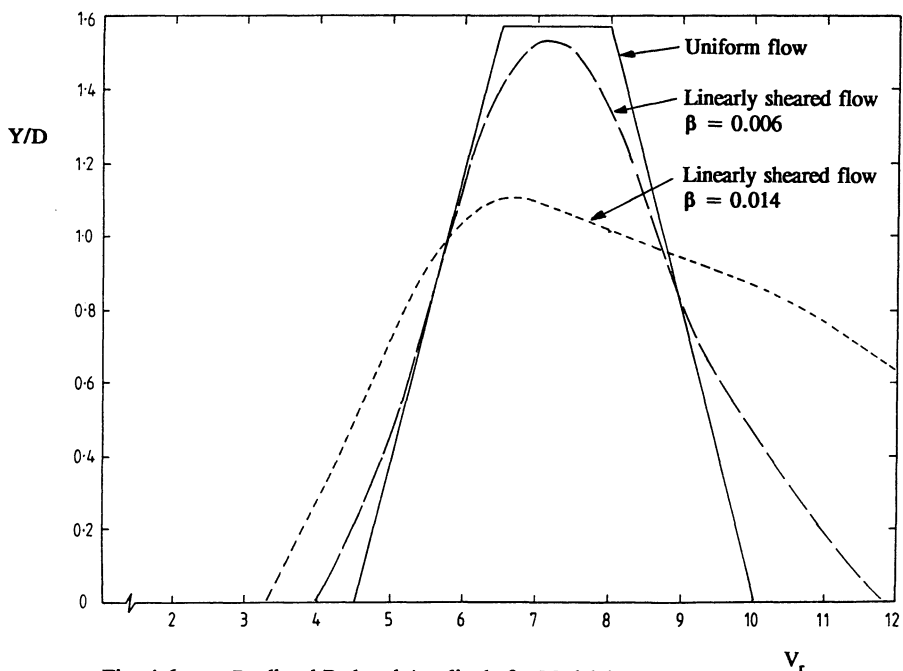


Fig. 4.6 Predicted Reduced Amplitude for Model 1
in uniform and linearly sheared flow.

Details of Model 1 and the experimental conditions described above were used as input to the ARM computer model. The resulting ARM predictions for the uniform and linearly sheared flows are shown in Fig. 4.6. Linear hydrodynamic damping was assumed because of the relatively low velocity of the ambient fluid in the damping regions (Appendix 1).

By comparing Figs. 4.5 and 4.6, it can be seen that, in general, the ARM's predictions are good; the reduction in peak amplitude due to shear was modelled (see table 3 below) as was the widening of the RVRR.

Table 3 Model 1's predicted and measured Reduced Amplitude in uniform and linearly sheared flow.

Flow profile	Reduced Amplitude		
	Predicted	Measured	Degree of over-pred. (%)
Uniform	1.57	1.52	3.3
$\beta=0.006$	1.52	1.45	4.8
$\beta=0.014$	1.10	1.13	-2.7

The experimental results for the stepped shear tests are shown in Fig. 4.7. Not surprisingly, the main effect of the shear was to reduce the amplitude response but, in addition, the RVRR was extended at the upper end for some of the profiles. This second effect was not expected because, even at the highest test velocities, the flow over the lower regions of the riser was not fast enough to cause cross-flow vortex induced vibration (i.e the Reduced Velocity was less than 4.5).

The most likely explanation for the widened first mode RVRR concerns the model's vibration in higher modes. At the higher test velocities the model's vibration became multi-modal (first and second modes were observed) and the hitherto narrow band frequency spectrum changed to a broader band. It is thought that the model's vibration in first mode at the higher test velocities was due to sub-harmonic excitation from mode 2 (i.e. energy was transferred from mode 2 to mode 1).

Again, the ARM was used (with linear hydrodynamic damping) to predict the amplitude response, and the results are shown in Fig. 4.8. The increase in RVRR was not predicted by the ARM, but this is not surprising given the physical explanation for the phenomenon and the relative simplicity of the

mathematical model. For the $\gamma=55\%$ and 40% flow profiles, the predicted peak Reduced Amplitude was close to the experimentally measured values (table 4 below), although for the $\gamma=24\%$ case, the ARM under-predicted by 22%. This discrepancy was probably caused by a distortion of the model's mode shape which was not included in the ARM program ¹.

Table 4 Model 1's predicted and measured Reduced Amplitude in stepped shear flow.

Flow profile	Reduced Amplitude		
	Predicted	Measured	Degree of over-pred. (%)
$\gamma = 55\%$	1.32	1.20	10
$\gamma = 40\%$	1.20	1.07	12
$\gamma = 24\%$	0.61	0.78	-22

Effects of Critical Flow (Model 2 Tests)

The amplitude response of Model 2 in fully critical flow is shown in Fig. 4.9. The most striking feature of the curve is its low peak value which only reached 0.87, significantly less than that which would normally be expected from the model's Stability Parameter ².

In the critical flow regime, the fluid separates from points nearer to the cylinder's base and the wake width is significantly reduced. Under these conditions it is reasonable to expect that the vortices which are shed would be of reduced size (compared to their sub-critical counterparts). In addition, because the vortices are shed closer to the base of the cylinder, the fluctuating lift force which is associated with them would be reduced. Both these effects would tend to reduce the amplitude of vortex induced vibration.

¹ Where the region of excitation is small relative to the region of damping, the mode shape will not remain a perfect sinusoid; that part of the cylinder which is subjected to hydrodynamic damping will, of course, tend to vibrate with a smaller amplitude than that part in the region of excitation. Thus, the assumption of a sinusoidal mode shape will lead to under-prediction of the vibration amplitude.

² Model 2's Stability Parameter was 0.15. In sub-critical flow this would result in a peak Reduced Amplitude of about 1.5.

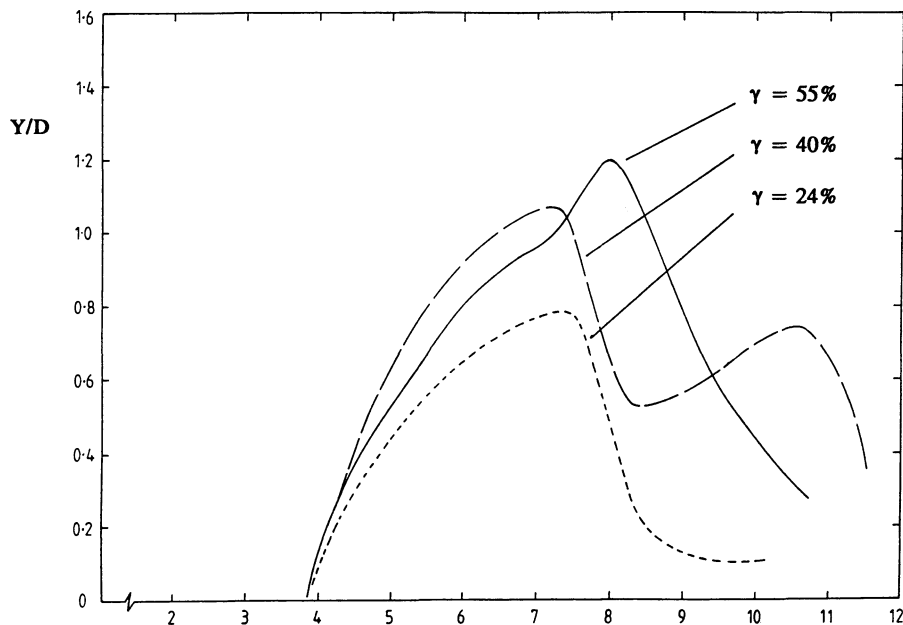


Fig. 4.7 Measured Reduced Amplitude for Model 1
in stepped shear flow.

V_r

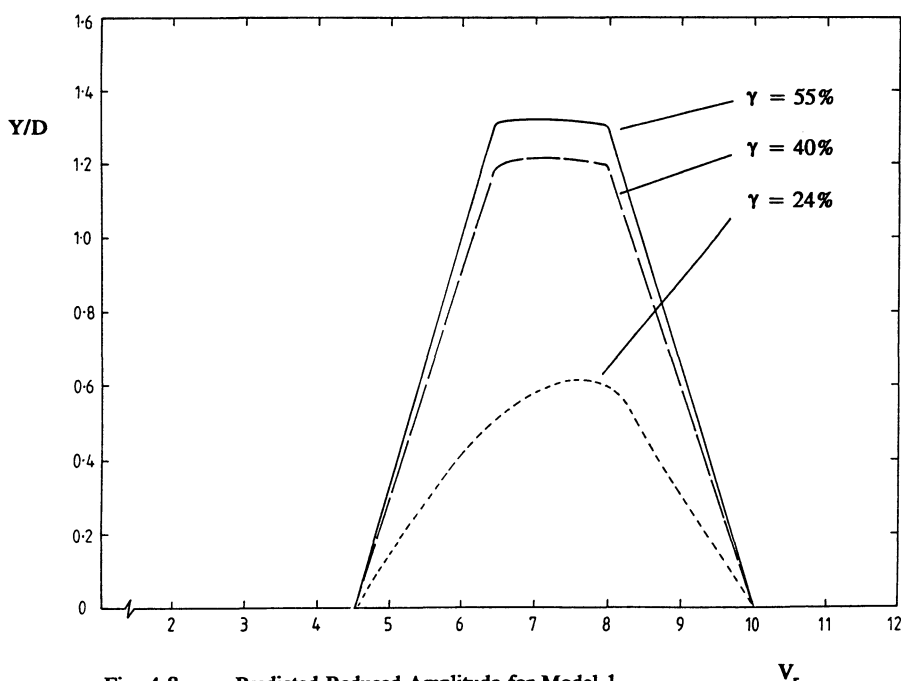


Fig. 4.8 Predicted Reduced Amplitude for Model 1
in stepped shear flow.

V_r

At a Reduced Velocity of about 7, the model stopped vibrating in first mode and began to vibrate cross-flow in second mode. This is a remarkable event because the Reduced Velocity at this point, based on the second mode natural frequency of 5.5 Hz, was only 2.2, much lower than the established value for the onset of vortex induced vibration of about 4.5.

An explanation for this is that, because of the narrow wake which accompanies the critical flow, the model was behaving as if it had a smaller diameter. If this were the case the effective Reduced Velocity would be raised, and would fall closer to the established value of about 4.5.

This argument can also be used to explain why the Model's first mode amplitude response peaked over a relatively low band of Reduced Velocity (5.0 to 6.5, rather than the established 6.5 to 8.0.

In its present state, the ARM is not capable of accounting for critical flow, however, a simple modification involving a change in the cylinder's effective diameter is proposed which would allow critical flows to be modelled over part or all of a riser's length.

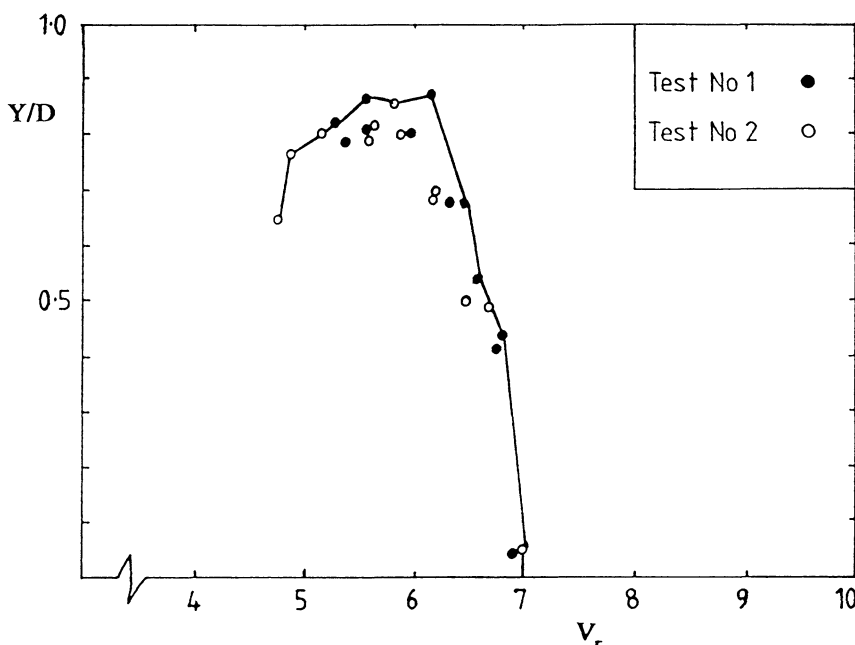


Fig. 4.9 Measured Reduced Amplitude for Model 2 in critical flow.

5 CONCLUSIONS

- 1 The introduction of shear in the current profile reduces the peak amplitude of vortex induced vibration of a cylinder, but tends to broaden the RVRR. This is true of both linear and stepped shear profiles.
- 2 Vortex induced vibration does occur in critical flow, but at reduced levels. For a cylinder with a sinusoidal mode shape, the peak amplitude appears to be reduced by about 40% as a result of fully critical flow.
- 3 The main effects of current shear on amplitude response (i.e. the relative reduction in $Y/D_{(max)}$ and shift in the RVRR) can be predicted using the ARM computer model.
- 4 ARM predictions are improved by using a linear hydrodynamic damping model in place of a quadratic model.

6 ACKNOWLEDGEMENT

The authors gratefully acknowledge the help of Bryan Bruce, of BHR Group, for his help with the experimental test programme.

REFERENCES

- Brooks I.H. "A pragmatic approach to the vortex induced vibration of a drilling riser", OTC 5522, Houston, Tx., April 1987.
- Griffin O.M. "Vortex Shedding from Bluff Bodies in a Shear Flow. - A Review." Trans. ASME. Jnl. Fluid Eng. Vol 107, Sept. 1985.
- Humphries J.A. "Vortex induced vibrations of slender cylinders in sheared flow", Ph.D. thesis, DFEI, C.I.T., Cranfield, England. 1987.

- Humphries J.A.
& Walker D.W. "Vortex Excited Response of Large Scale Cylinders in Sheared Flow". Proc, ASME, OMAE, 6th Int. Conf. VII, Houston Tx., 1988.
- King R. "Vortex excited structural oscillations of a circular cylinder in flowing water". Ph.D. Thesis, Loughborough Univ. July, 1974.
- King R. "A Review of Vortex Shedding Research and its Application". Ocean Eng. vol. 4, pp 141-171. Pergamon Press 1977.
- Lamb W.S. "Suppression of the vortex induced vibration of slender cylindrical structures" Ph.D. Thesis, Cranfield Institute of Technology, August 1991.
- Lamb W.S.
& Walker D.H. "Collaborative Research Programme for Vortex Induced Vibration in Sheared Velocity Profiles". BHRA Report CR275€, Vol 1, March 1987.
- Sarpkaya T. "Vortex Induced Oscillations - A Selective Review". Jn. App. Mech. ASME, Vol 46, No. 2, June 1979.
- Vandiver J.K. "The prediction of lock-in vibration on flexible cylinders in a sheared flow", OTC 5006, Houston Tx. May 1985.
- Vandiver J.K.
& Chung "Predicted and measured response of flexible cylinders in sheared flow", Pre-print for OTC, Houston, Tx., 1988.

APPENDIX 1 HYDRODYNAMIC DAMPING

King (1974) has demonstrated that vibrations of a circular cylinder in a quiescent fluid are subject to linear, rather than quadratic damping. Where the free stream flow velocity is small (relative to that of the vibrating cylinder) it is likely that the hydrodynamic damping will approximate to the quiescent case. In other cases, where the free stream velocity is relatively high, it is likely that the hydrodynamic damping would be quadratic.

Note that quadratic damping was tried during the modelling of Model 1's amplitude response in sheared flows. In stepped shear flows, this resulted in significant under-prediction of the peak amplitudes, and in linear shear flows the broadening of the RVRR which was clearly observed in the experimental results was not modelled. Changing to the linear damping model greatly improved the ARM's predictions, both in terms of the general form of the response and the peak amplitudes.

King R.

"Vortex excited structural oscillations of a circular cylinder in flowing water". Ph.D. Thesis, Loughborough Univ. July, 1974.

SUPPRESSION OF VORTEX SHEDDING FROM SATELLITE RISERS IN A CURRENT

M M ZDRAVKOVICH and J L BALDARO*

Department of Aeronautical and Mechanical Engineering
University of Salford
Salford M5 4WT
England

Wave and current-induced oscillations have plagued marine risers. An enormous experimental research and computational effort are expended in measuring and predicting the response of risers due to the vortex shedding excitation. Another promising avenue of research is the effect of spacing of risers in a satellite cluster on the suppression of vortex shedding. The present paper describes and gives a video illustration of a successful suppression of vortex shedding behind 8+1 cluster in an optimal arrangement. Another important parameter, central to satellite riser diameter ratio, is also investigated.

INTRODUCTION

Multiple marine risers have been designed and constructed in vast numbers in order to meet the ever increasing demand for offshore oil. Many parameters guided the design and determined the size and number of riser tubes. A low priority seems to be given to the grouping of riser tubes despite its strong effect on vortex shedding and hydrodynamic loading in current and/or waves.

The hydrodynamic loading of satellite risers strongly depends on the arrangement of tubes in a cluster. For example, when two riser tubes are arranged in tandem and touch each other the overall drag may be only 40% of the drag of a single riser. The proximity and wake interference produce a negative drag (thrust) on the downstream riser in tandem (see review by Zdravkovich (1977)). When the riser tubes are in the cluster, the effect of interference may reduce the mean drag on, and suppress vortex shedding from some of them. The classification of the interference effects in various clusters, arrangements, and orientations are reviewed by Zdravkovich (1987).

An attempt to use beneficial interference effects by optimally arranging risers in the cluster seems to be ignored by the designers. Instead, they directed research towards the dynamic behaviour of arbitrarily arranged satellite risers in currents and/or waves (see Ottesen et al (1979), Moe and Overvik (1982), Hartnup et al (1987), etc. The excitation of marine risers was assumed to be due to vortex shedding only. Price et al (1989) and Zdravkovich (1990) pointed out that marine risers might undergo the interference kind of excitation, like transmission lines and heat exchangers, respectively.

*Now with RAF

REVIEW OF PREVIOUS RESEARCH

Demirbilek and Halvorsen (1985) reported measurements of forces carried out in NMI and DHI on eighteen different satellite risers submerged in a steady current or subjected to forced oscillation. A wide variation in drag coefficient was found, not only from riser to riser in the same cluster, but also on different clusters themselves. For example, the drag coefficient of tubes in the cluster varies from $0.30 < C_d < 1.15$ while the overall drag coefficient of satellite risers was in the range $0.44 < C_D < 0.70$. The authors did not attempt to correlate the grouping of the riser tubes to the measured drag coefficient.

The optimisation of tube-grouping in a satellite cluster consisting of 6+1 risers was carried out by Johnson and Zdravkovich (1991). The optimal arrangement was found having the minimum overall drag and vortex shedding suppressed behind most risers. The close proximity of risers in the optimal arrangement differed considerably from the conventional satellite riser arrangement.

The aim of the present paper is to describe new tests on 8+1 cluster and to examine the effect of the increase of the central tube. The ratio of the latter and satellite tube was $D/d = 3$.

FORMULATION OF INTERFERENCE PARAMETERS

The interference effects on flow past two parallel tubes of the same diameter depend on their orientation to the free stream velocity, α , and the spacing between the tubes, L/D . When the two tubes have different diameters the ratio D/d becomes an additional interference parameter.

Satellite risers usually consist of a large diameter central tube, D , and small diameter, d , satellite tubes arranged circumferentially at a radius, R , around the central tube, see Figure 1. The interference effects may be due to:

- (i) Satellite tube positioned upstream of the central tube.
- (ii) Satellite tube positioned downstream of the central tube.
- (iii) Mutual interference of equidistantly spaced satellite tubes.
- (iv) Shielding of the central tube by the satellite tubes acting as a circumferential shroud.

The first and second effect may be described by R/d and R/D , respectively. The distance between the satellite tubes is $2\pi R/n$, where n is the number of satellite tubes. The distance decreases by reducing the radius of the satellite ring or by increasing the number of satellite tubes. The latter does not affect R/d and R/D but the former changes both of them. The fourth can be quantified as the porosity ratio, $nd/2R\pi$ which varies from 0 to 1. The porosity ratio appears to be the reciprocal value of the dimensionless spacing ratio of satellite tubes.

The drag coefficient of satellite risers may be expressed in terms of:

$$C_D = f(\alpha, D/d, n, R/d, R/D, 2\pi R/nd, Re) \quad (1)$$

where

$$C_D = D^{1/2} \rho V_0^2 L (D+8d) \quad (2)$$

In this paper, $n = 8$, $D/d = 3$, and three characteristic orientations are chosen, $\alpha = 0 \text{ deg}$ (Figure 1a), $\alpha = 22.5 \text{ deg}$ (Figure 1b), and $\alpha = 11 \text{ deg}$ (asymmetric stagger). The optimal arrangement for an 8+1 riser is assumed to be similar to that for the 6+1 riser. Hence, only three values of R are used being higher, the same, and smaller than optimal for the 6+1 riser.

EXPERIMENTAL FACILITIES

The closed circuit wind tunnel has a working section of $1.22 \text{ m} \times 0.91 \text{ m}$. It is capable of continuous variation of velocity from 15 m/s to 36 m/s , and the intensity of free stream turbulence is 0.3% . A six-component balance is located above the working section. The model is supported by two fixed vertical struts which protrude into the working section and are shielded from the flow by streamlined shrouds.

The model consists of a central tube, $D = 60 \text{ mm}$, and eight satellite tubes, $d = 20 \text{ mm}$ placed between two end plates 1.092 m apart (see Figure 2). The blockage ratio of the cluster is 0.1. (not corrected). The end plates, $5D$ in diameter contribute to the measured drag by less than 0.5% . Two spacer plates, $6.25D$ in diameter, 0.6 m apart are fastened to the balance struts, Figure 2.

The flow visualisation is carried out in an open water channel $0.3 \text{ m} \times 0.3 \text{ m}$ in cross section with aluminium powder sprinkled over water. The model, videocamera and reflectors, are attached to a trolley, Figure 3. The riser model for the water tests consists of tubes, $D = 45 \text{ mm}$, and $d = 15 \text{ mm}$, 385 mm long. The blockage ratio is 0.22, and the speed of the trolley is restricted to 0.15 m/s ($Re = 1.1 \times 10^3$) due to wave formation. The mechanism of vortex shedding is unchanged in the range $300 < Re < 3 \times 10^5$ and the Strouhal number is constant. Hence, it is expected that the flow visualisation at $Re = 10^3$ is compatible with force measurements at $Re = 1.4 \times 10^5$. Neither of them should be extrapolated to the supercritical flow regime.

FORCE MEASUREMENTS

Johnson and Zdravkovich (1991) measured the overall force on the 6+1 satellite riser for six cluster arrangements within $0.73 \leq R/D \leq 1.87$ for $D/d = 2.4$. The small drag is found in the range $0.73 \leq R/D < 1.19$. When the central tube diameter is increased so that $D/d = 3$, the three relevant arrangements are as given in Table 1.

<i>Arr</i>	<i>D/d</i>	<i>R/D</i>	<i>R/d</i>	<i>s/d</i>	<i>nd/2πR</i>
<i>A</i>	3	1.13	3.40	2.60	0.38
<i>B</i>	3	0.95	2.85	2.20	0.45
<i>C</i>	3	0.77	2.30	1.87	0.53

Table 1: Geometry of 6+1 and 8+1 riser models

Figures 4 and 5 show the variation of the overall drag coefficient for three orientations of the arrangement A for 6+1 and 8+1 cluster, respectively. There is a small variation in terms of Reynolds number as expected. The effect of orientation is reversed in Figure 5, i.e., minimum C_D is at $\alpha = 22.5$. The reason for this is that at $\alpha = 0$, the 6+1 cluster has

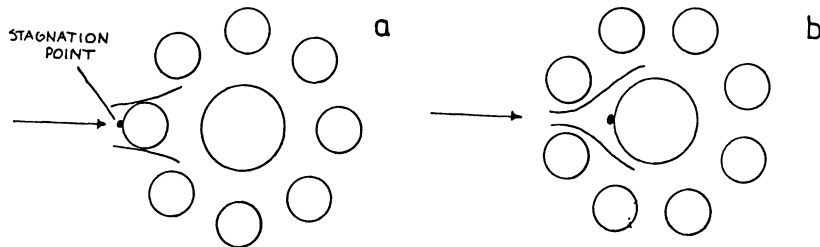


Figure 1: 8+1 satellite riser, (a) $\alpha = 0 \text{ deg}$ orientation (b) $\alpha = 22.5 \text{ deg}$ orientation.

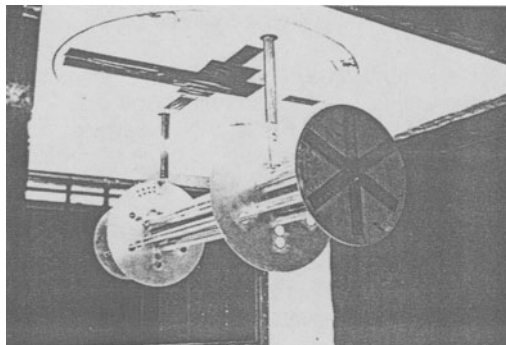


Figure 2: 8+1 riser model in test section of a wind tunnel.

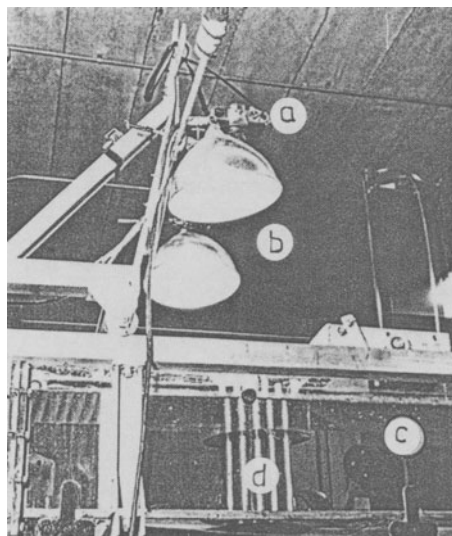


Figure 3: 8+1 riser model in open channel (a) video camera, (b) trolley, (c) water channel, (d) riser model.

five tubes in-line (beneficial interference) while at $\alpha = 30 \text{ deg}$ the satellite tubes are in a symmetric staggered arrangement. The asymmetric staggered arrangement at $\alpha = 12 \text{ deg}$ produces the highest drag as expected.

The arrangement *B* shows similar drag variation in terms of Reynolds number and orientation, as seen in Figures 6 and 7. However, the values of the drag coefficient are reduced in comparison to the arrangement *A*. Table 2 shows the mean drag coefficients for the 6+1 and the 8+1 clusters in three orientations.

<i>Arr</i>	6+1			8+1		
	0	15	30	0	12	22.5
<i>A</i>	.69	.76	.82	.65	.67	.59
<i>B</i>	.67	.68	.77	.62	.60	.53
<i>C</i>	.66	.70	.76	.53	.58	.63

Table 2: Mean drag coefficients of 6+1 and 8+1 models

The arrangement *C* does not reduce the drag coefficient further, as seen in Table 2 and Figures 8 and 9. The measured mean lift coefficient is two order of magnitudes smaller than the drag coefficient and as such can be ignored.

FLOW VISUALISATION

In the previous paper (Johnson and Zdravkovich (1991)), the flow visualisation has shown that the decrease in drag was related to the suppression of vortex shedding behind some tubes in the 6+1 cluster. The same visualisation technique is used for an 8+1 cluster in three orientations and arrangements. The prohibitive cost of video prints forced us to sketch the vortex patterns by using slow playback and still frame facility on the video recorder. The observed dimples on the water surface were drawn as circles and free shear layers were represented by curled lines.

As an example of how the interference suppresses vortex shedding, Figure 10 shows the flow patterns for arrangement *A* in three orientations. Only tube 1 does not shed vortices and it is reflected in the measured drag coefficient in Figure 4. There is a considerable change in flow pattern in Figure 11 for arrangement *B*. 1, 2, and central tube suppress vortex shedding in all three arrangements.

The effect of increasing the diameter of the central tube from $D/d = 2.4$ to $D/d = 3.0$ on the flow pattern is illustrated in Figure 12. For $\alpha = 0 \text{ deg}$, the vortex shedding is suppressed behind tubes 1, 2, 5, 8, and central for $D/d = 2.4$ and behind all tubes except 3 and 7 for $D/d = 3.0$. Note that the latter produced the least drag coefficient for all arrangements and orientations.

Figure 13 shows that for $\alpha = 22.5 \text{ deg}$ vortex shedding occurs only behind tubes 3, 6 and the cluster. The ratio $D/d = 3$ shows vortex shedding behind tubes 2, 3, 6, and 7 but not behind the cluster as a whole.

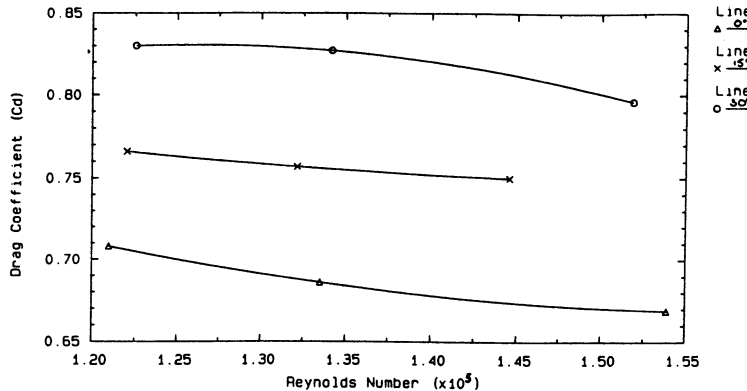


Figure 4: Drag coefficient for three orientations, arrangement *A*, 6+1 cluster.

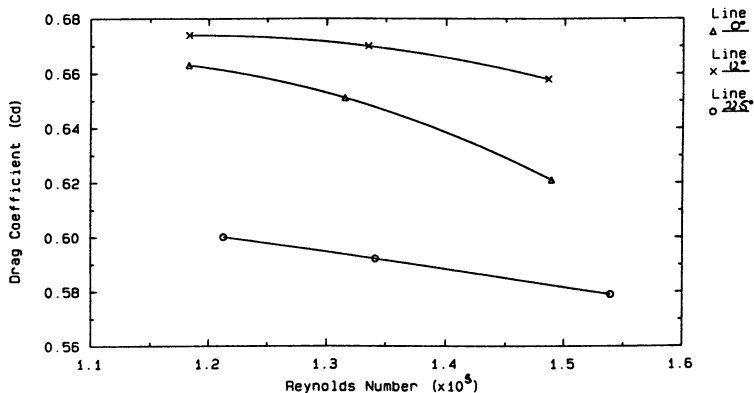


Figure 5: Drag coefficient for three orientations, arrangement *A*, 8+1 cluster.

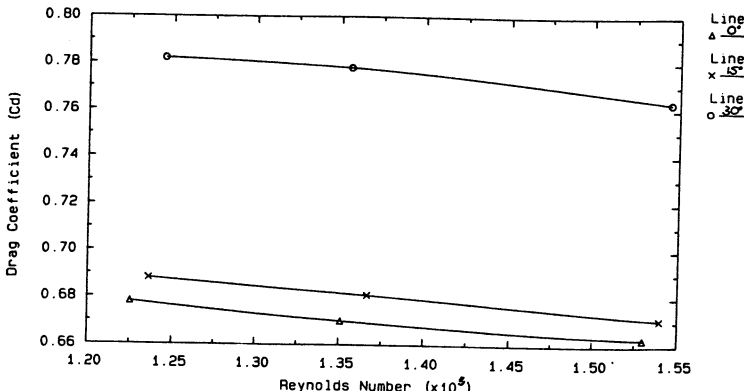


Figure 6: Drag coefficient for three orientations, arrangement *B*, 6+1 cluster.

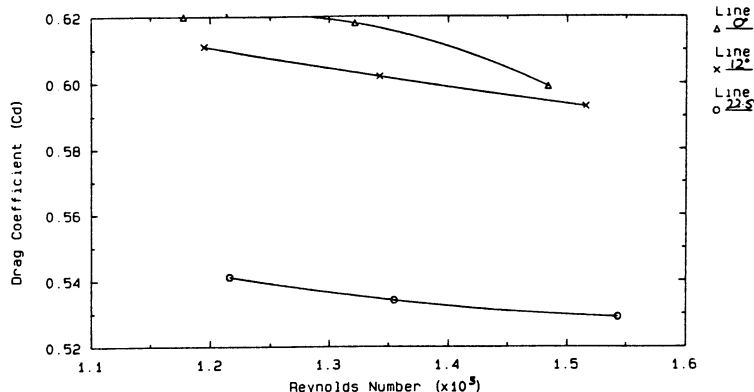


Figure 7: Drag coefficient for three orientations, arrangement B, 8+1 cluster.

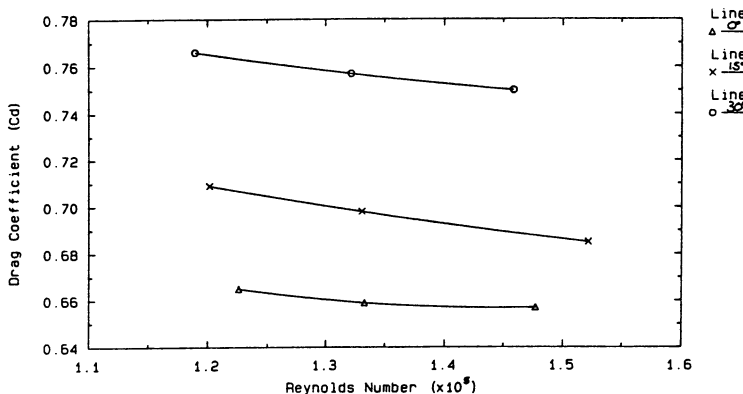


Figure 8: Drag coefficient for three orientations, arrangement C, 6+1 cluster.

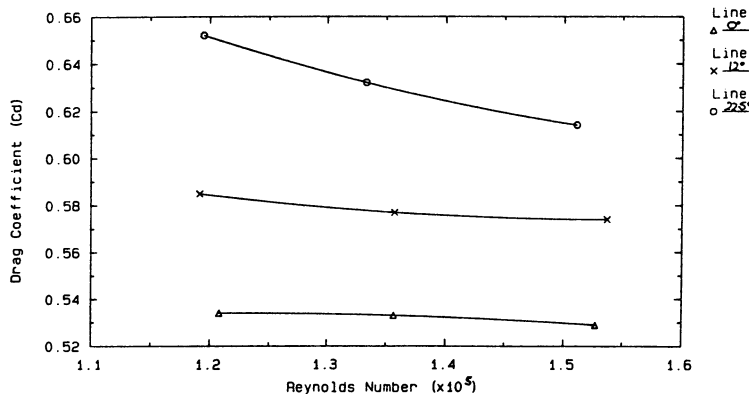


Figure 9: Drag coefficient for three orientations, arrangement C, 8+1 cluster.

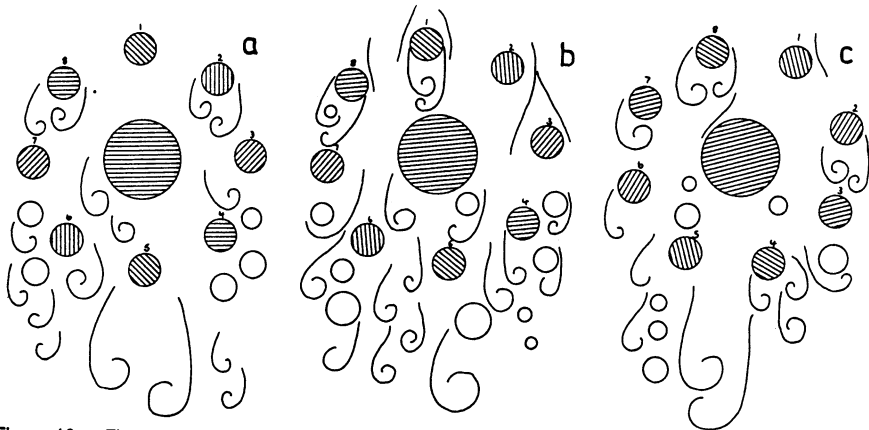


Figure 10: Flow patterns around 8+1 cluster, arrangement A, (a) $\alpha = 0 \text{ deg}$,
(b) $\alpha = 12 \text{ deg}$, (c) $\alpha = 22.5 \text{ deg}$.

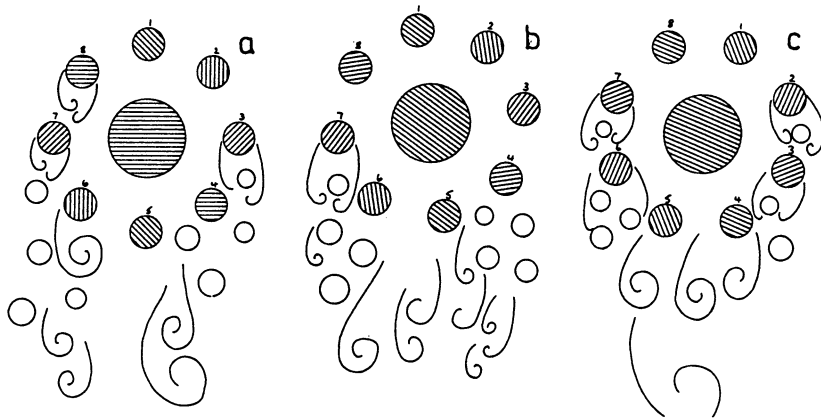


Figure 11: Flow patterns around 8+1 cluster, arrangement B,
(a) $\alpha = 0 \text{ deg}$, (b) $\alpha = 12 \text{ deg}$, (c) $\alpha = 22.5 \text{ deg}$.

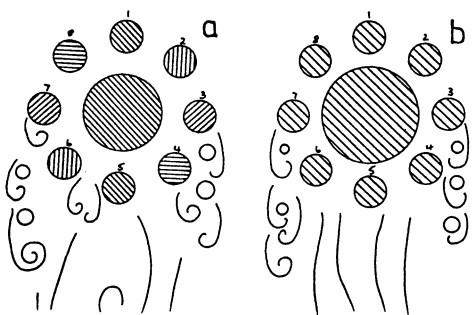


Figure 12: Flow patterns around 8+1 cluster,
arrangement C, $\alpha = 0 \text{ deg}$, (a) $D/d = 2.4$,
(b) $D/d = 3$.

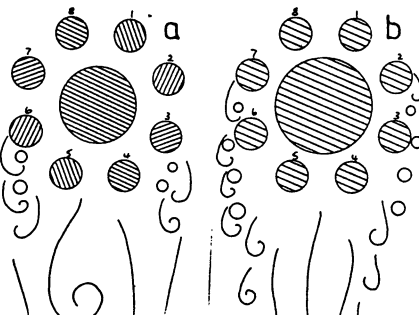


Figure 13: Flow patterns around 8+1 cluster,
arrangement C, $\alpha = 22.5 \text{ deg}$, (a) $D/d = 2.4$
(b) $D/d = 3$.

CONCLUSIONS

Force measurements and flow visualisation (at 100 times smaller Reynolds number) show that a further reduction of drag force and suppression of vortex shedding can be achieved by increasing the number of risers to 8 and ratio of central to satellite tube to 3. It is shown that the drag force in satellite risers depends on seven parameters. All these parameters are varied in the tests: orientation, central to satellite tube diameter ratio, number of tubes in a cluster, radius of satellite ring, porosity, and Reynolds number. The latter is varied in a very narrow range and the value is one order of magnitude lower than that in real riser applications. The current research is planned towards higher Reynolds numbers.

REFERENCES

- Demirbilek, Z. and Halvorsen, T. (1985) "Hydrodynamic forces of multtube production risers exposed to current and waves", *J. Energy Resources Techn.*, 107, 226-234.
- Hartnup, G. C., Airey, R. G., and Shiells, D. F. (1987) "Model basin tests on multtube production risers", In Proc. 6th Int. O.M.A.E Symposium, ed. J. S. Chung et al, Houston, Texas, 1, 109-117.
- Johnson, S. P. and Zdravkovich, M. M. (1991) "Optimal arrangement of 6+1 satellite riser in a current", Proc. 1st Int. ISOPE Conference, eds. M. S. Triantafyllou et al, Edinburgh, UK, II, 164-169.
- Moe, G. and Overvik, T. (1982) "Current-induced motion of multiple riser", Proc. 3rd Int. Conference B.O.S.S., M.I.T., Cambridge, Mass., U.S.A., 618-659.
- Ottesen-Hansen, N. E., Jacobsen, V., and Lundgren, M. (1979) "Hydrodynamic forces on composite risers and individual cylinders", Proc. Offshore Techn. Conference, Houston, Texas, 1607-1621.
- Price, S. J., Paldoussis, M. P., Mark, P., and Marelli, W. N. (1989) "Current-induced oscillations and instabilities of a multtube flexible riser: water tunnel experiments", Proc. 8th Int. O.M.A.E. Conference, Hague, 1, 447-454.
- Zdravkovich, M. M. (1977) "Review of flow interference between two circular cylinders at various arrangements", *J. Fluids Eng.*, 99, 618-633.
- Zdravkovich, M. M. (1987) "Effect of interference between circular cylinders in cross flow", *J. Fluids and Structures*, 1, 239-261.
- Zdravkovich, M. M. (1991) "Comparative overview of marine risers and heat exchanger tube banks", *J. O.M.A.E.*, 113, 30-36.

Session 3

Coastal Conditions

REVIEW OF WAVE BREAKING IN SHALLOW WATER

H N SOUTHGATE
HR Wallingford Ltd
Wallingford, Oxon, OX10 8BA
UK

This paper contains a critical review of methods of prediction of wave heights during and after breaking in shallow water. It is concluded that the choice of the most appropriate methods is crucial both for initial design calculations and for computational modelling of the surf zone.

INTRODUCTION

Wave breaking is the most obvious and spectacular of all the physical processes that affect surface water waves. It is also the most complex, and any thorough attempt to understand the physical processes involved needs to address many different aspects of the phenomenon. Amongst the most important are:

a) Transformation of Waves during Breaking

- Flow field under nearly-breaking and broken waves
- Factors influencing the initiation of breaking
- Formation and propagation of a roller and broken wave
- Reformation of unbroken waves after breaking over banks or bars
- Energy exchange between spectral components

b) Generation of Surf Zone Phenomena

- Production and dissipation of turbulence
- Water level set-up
- Longshore currents
- Cross-shore currents (undertow)
- Nearshore current circulation patterns
- Low-frequency waves

c) Effects on Solid Material

- Erosion and deposition of seabed sediment

- Erosion of dunes and cliffs
- Forces on breakwaters and seawalls

Wave breaking is an essential consideration in most coastal engineering design studies. This paper contains a critical review of two aspects of wave breaking necessary for such studies: the prediction of wave height and water depth at which waves start to break, and the rate of energy losses from waves once they have broken. This review contains both simple methods suitable for hand calculations and more detailed methods for inclusion in computational models of wave propagation in shallow water.

PHENOMENOLOGICAL DESCRIPTION OF WAVE BREAKING

Before breaking, waves have a relatively smooth water surface. After breaking the wave fronts are usually white and foamy often with a lot of spray and bubbles. Complex processes take place during breaking, involving a rapid change of wave shape and the conversion of wave energy to turbulence and subsequently heat. After a short distance, roughly several times the depth at breaking, the breaking-induced turbulence becomes fully developed and the wave adopts a steady, well-organised profile which is more-or-less independent of the initial breaking behaviour, but still often with white water at the crest face. In this paper the term "broken wave" will be used to describe this steady phase, and "breaking wave" to describe the initial breaking process. The term "transition zone" is often applied to the region where the initial breaking phase occurs. Svendsen et al (1978) also use the terms "inner region" and "outer region" respectively for the regions of steady broken and initial breaking behaviour.

The most visually apparent phase occurs when waves initially break and the wave crest overturns, or comes as close as possible to overturning, and generates white water. The different visual characteristics of breaking waves provide a classification of breaker types (Galvin (1968)), described below:

- (a) Spilling Breakers. Spilling breakers occur when white water initially appears at the wave crest and spreads down the front face. An overturning jet of water is either very small or absent altogether. Spilling breakers usually occur on flat or gently sloping beaches.
- (b) Plunging Breakers. Plunging breakers occur when the top of the wave crest forms a jet which overturns and plunges into the

water in front of the face of the wave. A body of air is initially enclosed between the jet and the wave face, causing a lot of spray and white water. Plunging breakers are most common on moderately steep beaches.

- (c) Surging Breakers. Surging breakers occur when a relatively small wave close to the shoreline builds up a crest as in a plunging breaker, but before the jet can form, the bottom of the wave surges forward up to the water line. Surging breakers occur on steep beaches close to the water line.

These are the three main breaker types, but since there are smooth transitions between them, various sub-classifications have been proposed. The term "collapsing breaker" is sometimes used for breakers between plunging and surging, but further sub-classifications are not standardly used.

Attempts have been made to relate breaker type to some quantifiable property of the wave. The earliest criterion was that of Irribarren and Nogales (1949), who used the beach slope and deep-water wave steepness,

$$I_o = \frac{m}{(H_o/L_o)^{\frac{1}{2}}} \quad (1)$$

where m is the beach slope, H_o is the wave height at an offshore point and L_o is the wavelength at that point. The subscript 'o' indicates offshore conditions in these variables and later ones in the paper. I is generally known as the Irribarren number or the Surf Similarity parameter. Galvin (1968) carried out a series of experiments of breaking waves on various bottom slopes and proposed a new parameter,

$$I' = \frac{m}{(H_b/L_o)^{\frac{1}{2}}} \quad (2)$$

in which H_b is the wave height at breaking. It is probable that Galvin still used the offshore wavelength, L_o , because of the difficulty in measuring or estimating the wavelength in the surf zone. Nowadays, however, numerical models can calculate local values of H and L even for irregular beaches, and it is logical to define I completely in terms of local variables,

$$I = \frac{m}{(H/L)^{\frac{1}{k}}} \quad (3)$$

Yoo (1986) compared both I and I' against Galvin's experimental data and found, rather paradoxically, that I' gave a clearer classification of breaker type than I , despite the obvious weakness of using an offshore parameter, L_o , to define an inshore process. This prompted Yoo to devise a new surf zone parameter, entirely in terms of local variables but which would give a more reliable breaker classification than I . Yoo's new surf zone parameter, β , is based on the fact that steeper bed slopes retard the speed at which the wave energy travels more strongly than shallower slopes. Using this idea Yoo derived the following surf zone parameter,

$$\beta = \frac{2m^2}{k^2 h H} \quad (4)$$

in which k is the local wavenumber and h the local depth. β is related to I by

$$\beta = \frac{I^2}{\pi k h} \quad (5)$$

Comparisons with Galvin's experimental data indicate that β gives a clearer classification of breaker type than I , although further experimental measurements are desirable. On the basis of present measurements the breaker types can be classified according to

Spilling	$\beta < 0.2$	$I' < 0.6$	$I_o < 0.45$	
Plunging	$0.2 \leq \beta \leq 2.1$	$0.6 \leq I' \leq 2.0$	$0.45 \leq I_o \leq 3.2$	(6)
Surging	$\beta > 2.1$	$I' > 2.0$	$I_o > 3.2$	

These values are based on data analyses from respectively Yoo (1986), Battjes (1974) and Van Dorn (1978), and Galvin (1968 and 1972).

THE BREAKER HEIGHT CRITERION

Wave breaking in deep and shallow water

In deep water the breaker height is governed by the wavelength whereas in shallow water it is determined by the water depth. It is usual therefore to express the breaker height as a dimensionless ratio of wave height to wavelength or depth at breaking, depending on whether the water is shallow or deep. The symbols γ_s (shallow) and γ_d (deep) will be used for these ratios,

$$\gamma_s = \left(\frac{H}{L} \right)_{b, \text{ shal}} \quad (7)$$

$$\gamma_d = \left(\frac{H}{L} \right)_{b, \text{ deep}} \quad (8)$$

where the subscript b denotes conditions at the onset of breaking. Before describing the various methods for determining γ_s , it is useful to show that once expressions for γ_s and γ_d have been found, it is possible to combine both expressions in a single formula that is valid at all depths,

$$\left(\frac{H}{L} \right)_b = \gamma_d \tanh \left[\left(\frac{h}{L} \right)_b \frac{\gamma_s}{\gamma_d} \right] \quad (9)$$

This expression gives the appropriate forms in shallow water ($\tanh x \approx x$) and deep water ($\tanh x \approx 1$). This method of linking shallow and deep water breaking criteria was first suggested by Miche (1944) who adopted the following value for γ_d , based on the analysis by Michell (1893) of deep-water waves using Stokes theory,

$$\gamma_d = 0.142 \quad (10)$$

Recent work by Williams (1981) using more detailed non-linear wave theory has confirmed this value. Methods of determining γ_s will now be considered, noting that any of these methods can be extended to cater for breaking in intermediate or deep water via Eqs 9 and 10.

Regular waves on nearly flat beds

The earliest shallow-water breaking criteria considered waves breaking on flat or very nearly flat seabeds. Analysis by McCowan (1891) of the solitary wave in shallow water showed that breaking starts to occur when

$$\gamma_s = 0.78 \quad (11)$$

This "0.78" criterion is still the most widely used breaker criterion for shallow water in present-day coastal engineering practice. Recent work using more detailed non-linear wave theory suggests a slightly higher theoretical value (Hunter and Vanden-Broeck, 1983; Fenton 1990).

$$\gamma_s = 0.83 \quad (12)$$

Laitone (1960) and Wiegel and Mash (1961) attempted to derive theoretically a simple expression explicitly including the effects of offshore wave steepness

$$\gamma_s = 0.73 - 1.12 \left(\frac{H_o}{gT^2} \right)^{\frac{1}{2}} \left(\frac{h_b}{H_o} \right)^{\frac{1}{2}} \quad (13)$$

in which g is the acceleration due to gravity and T the wave period. It should be mentioned that some experiments on shallow water breaking on nearly-flat beds indicate substantially lower values of γ_s , around 0.55 (LeMehaute et al, 1968; Nelson, 1987; reported in Fenton 1990), indicating that waves can become unstable before the theoretical limit is reached. In apparent contradiction to this, the considerably larger number of experiments that have been conducted on sloping beds (see below) indicate that, when results are extrapolated to the zero-slope condition, values of γ_s closer to the theoretical ones (Eqs 11 and 12) are obtained. However, in all these experiments there is considerable scatter in the measured values of γ_s .

Regular waves on a slope

The previous section has considered shallow-water breaking on a nearly-flat seabed. However, in most cases, breaking will take place on a seabed with a substantial slope ($> 1:100$). The experimental evidence indicates a distinct trend of increasing γ_s with increasing slope, with values as high as 1.5 being obtained on the steepest slopes ($\sim 1:5$). The physical reason for this trend appears to be that the wave form has not sufficient time to adjust to the

equilibrium profile pertaining to the local water depth, and therefore a higher unbroken wave height can be achieved than would be indicated by an equilibrium-profile theory. Because of the difficulties in a thorough theoretical treatment of shallow-water wave breaking on a bed slope, the breaking criteria that have been put forward have been empirical relationships based on laboratory measurements. A considerable amount of experimental work was carried out in the late sixties and early seventies and a wide range of simple empirical expressions devised, taking account of the bed slope. The following are three such attempts (m is the bed slope),

Galvin (1969)

$$\begin{aligned}\gamma_s &= 1.09 & m \geq 0.07 \\ &= (1.4 - 6.85m)^{-1} & m < 0.07\end{aligned}\tag{14}$$

Collins and Weir (1969)

$$\begin{aligned}\gamma_s &= 1.28 & m \geq 0.1 \\ &= 0.72 + 5.6m & m < 0.1\end{aligned}\tag{15}$$

Madsen (1976)

$$\begin{aligned}\gamma_s &= 1.18 & m \geq 0.1 \\ &= 0.72 + 4.6m & m < 0.1\end{aligned}\tag{16}$$

There are some differences between these expressions but they all show that γ_s increases with slope up to a maximum value reached when the slope is about 0.1. For a flat seabed the expressions are slightly less than the theoretical values (Eqs 11 and 12).

The most widely used of these empirical formulas, and the one currently recommended in the American Shore Protection Manual, was derived by Weggel (1972) using data from ten separate experiments,

$$\gamma_s = \frac{b}{1 + \frac{ah_b}{gT^2}}\tag{17}$$

in which a and b are functions of the seabed slope, m ,

$$a = 43.75 (1 - \exp(-19m))\tag{18}$$

$$b = 1.56 (1 + \exp (-19.5m))^{-1} \quad (19)$$

This expression takes account of the offshore wave steepness as well as the bed slope.

Later authors have attempted to refine Weggel's formula, some of whom use additional experimental data. Scarsi and Stura (1980) suggested using Eq 17 for slopes greater than 0.05. For smaller slopes they proposed the formula,

$$\gamma_s = (0.73 + (13m)^2) - (1.12 + (30m)^2) \left(\frac{h_b}{gT^2} \right) \quad m < 0.05 \quad (20)$$

This gives a better fit to the experimental data in this range of m , although Eq 17 and Eq 20 do not match at $m = 0.05$. Eq 20 reduces to the formula of Collins and Weir (Eq 15) and Madsen (Eq 16) for zero slope and to that of Laitone (Eq 13) for low steepness waves ($T \rightarrow \infty$). A different modification of Weggel's formula was suggested by Moore (1982), incorporating the breaking criterion of Komar and Gaughan (1972),

$$\gamma_s = b - 0.083 a \left(\frac{H_o}{L_o} \right)^{0.8} \quad (21)$$

with b and a defined in Eqs 18 and 19, and L_o is the deepwater wavelength ($L_o = gT^2/2\pi$).

Two more recent expressions have been put forward by Singamsetti and Wind (1981),

$$\gamma_s = 1.16 [m (H_o/L_o)^{-1/2}]^{0.22} \quad (22)$$

and Sunamura (1981),

$$\gamma_s = 1.1m^{1/6} (H_o/L_o)^{-1/12} \quad (23)$$

Nairn (1990) compared the expressions of Moore (Eq 21) and Singamsetti and Wind (Eq 22) with experimental data from Hansen and Svendsen (1979)

and concluded that the Moore criterion was more satisfactory, especially at low wave steepnesses.

In all these expressions, the wave steepness has appeared as an offshore value. Yoo (1986) reasoned that local wave steepness values should be used, and should be introduced together with the bed slope via a surf zone parameter. Accordingly, Yoo re-analysed the experimental data used by Weggel and introduced more recent data from Iwagaki et al (1974) and Van Dorn (1978). A regression analysis to a hyperbolic tangent function yielded the following best-fit curves,

$$\gamma_s = \frac{2\pi}{7} [0.8 + \tanh (1.06 l)] \quad (24)$$

where l is the local Irribarren number, Eq 3, and

$$\gamma_s = \frac{2\pi}{7} [0.8 + \tanh (3.0 \beta)] \quad (25)$$

where β is Yoo's surf zone parameter, Eq 5. There is little to choose between Eq 24 and Eq 25 in terms of agreement with experimental data.

Finally, it is possible to render these expressions for γ_s applicable to all water depths using Eq 9. Ostendorf and Madsen (1979) have suggested this approach for Eq 16, and Battjes and Janssen (1978) have used a constant γ_s , but any of the above-mentioned expressions can be treated in this way. One of the data sets considered by Weggel contains breaker height measurements in this intermediate region between deep and shallow water breaking, and agreement with predictions from an expression of the type in Eq 9 is good.

Random waves

The foregoing sections have been concerned with the breaking of regular waves in shallow water. In this section methods of determining the breaker height for random waves are considered. At first sight it might be expected that, since waves in shallow water are largely non-dispersive, individual waves within a random wave train would behave like regular waves. Although for moderate bed slopes and wave steepnesses breaker height measurements with random waves are roughly similar to those with regular

waves, the trends relative to these two parameters are quite different, especially at low wave steepnesses.

The most comprehensive analysis of random wave breaker height data has been carried out by Battjes and Stive (1985). They analysed twenty results from three separate laboratory exercises and two field exercises. The nearshore bathymetries consisted of plane, concave and bar-trough forms. Their analysis of results indicated no systematic dependence of the breaker height (of the root-mean-square wave height) on bed slope, but a dependence on offshore wave steepness. A best-fit to a hyperbolic tangent function gave the following expression,

$$\gamma_s = 0.5 + 0.4 \tanh(33 H_o/L_o) \quad (26)$$

In this equation γ_s was determined by comparing predicted H_{rms} values from a surf zone wave transformation model with the measured H_{rms} values for each of the twenty test cases. For each case several model runs were performed, varying the γ_s value, until the best fit between the predicted and measured H_{rms} values was obtained. H_o is the offshore rms wave height and L_o the offshore wavelength corresponding to the peak spectral period. In each case the measured H_{rms} values were derived from spectral analysis.

The dependence of Eq 26 on bed slope and offshore wave steepness is in marked contrast to the regular wave experiments which indicate γ_s increasing with larger bed slopes and decreasing with steeper offshore waves. The deviation of random wave γ_s values from their regular wave counterparts is particularly apparent at low wave steepnesses. To test the steepness trend indicated by Eq 26, Nairn (1990) introduced an additional set of low steepness field data measured at Leadbetter Beach, California, USA. The additional data confirmed the trend, and even suggested the trend becomes more marked at low steepnesses. A regression analysis including the Leadbetter Beach data (an additional six results) yielded the following new expression,

$$\gamma_s = 0.39 + 0.57 \tanh(33 H_o/L_o) \quad (27)$$

The physical explanation for the discrepancy in trends between regular and random wave γ_s values is not clear. The non-dispersive character of shallow-water waves suggests that individual waves within a random wave sequence should not behave in a radically different manner from regular waves. The most likely explanation probably lies with some property of random waves unrelated to the onset of breaking. Nairn (1990) has

suggested the trend of γ_s with wave steepness could be the result of energy transfer from the primary waves to infragravity wave periods (energy at these periods would normally be excluded from spectral analyses of wave measurements, where primary wave properties are sought). It is known that such wave energy transfer is stronger for low steepness random waves, which is consistent with the observed trends.

Wave breaking on irregular nearshore bathymetry

Most experimental measurements of breaker height have been made on plane slopes. However, about half the data sets considered in the Battjes and Stive (1985) analysis were on concave or barred profiles. The resulting values of γ_s have subsequently been used in numerical model comparisons of wave height against laboratory data, generally with good agreement.

ENERGY DISSIPATION IN BROKEN WAVES

The previous sections have considered the methods of predicting the wave height at which waves start to break at a given location. Once waves have broken they will continue to travel forwards, but in a manner quite different from unbroken waves. The following sections are therefore concerned with the prediction of the spatial rate at which wave energy is dissipated from a broken wave as it travels shorewards.

Regular waves - empirical methods

There are two basic approaches to the modelling of energy decay of regular waves after breaking, an empirical approach and one based on solving the wave energy equation. Empirical methods are applicable only to wave breaking on monotonic depth profiles and are based on experimentally-derived relationships between the broken wave height, H , and the water depth, h . The simplest, and most commonly used, relationship is the linear one,

$$H = \gamma_s h \quad (28)$$

The various formulas described earlier for γ_s can be used in Eq 28. However, several investigators have established that the energy decay of broken waves in the surf zone deviates significantly from this linear relationship. Experimental measurements typically show a concave curve in graphs of H versus h , indicating a relatively large dissipation of energy

immediately after breaking, and a progressively smaller rate of dissipation further shorewards.

To better represent this concave profile, Smith and Kraus (1987) have proposed a power law for the wave height decay,

$$H = \gamma_s h_b \left(\frac{h}{h_b} \right)^n \quad (29)$$

where the subscript b denotes the breaking condition, and the exponent n, to be empirically determined, is dependent on the beach slope and breaking wave conditions. A comparison of predictions using Eq 29 with experimental data, principally from Horikawa and Kuo (1966), showed that n depended on γ_s and the bed slope, m. A multiple regression against the experimental data gave the following formula for n,

$$n = 0.657\gamma_s + \frac{0.0438\gamma_s}{m} - 0.0096m + 0.032 \quad (30)$$

γ_s was obtained from a suitable formula such as those outlined earlier. Smith and Kraus were able to obtain a better fit to the experimental data using this method than the simple linear relationship, although an additional empirical factor has had to be introduced. Further tests are necessary to provide greater validation evidence for this type of approach and to test the universality of the constants n and γ_s .

These empirically-based methods have the advantage of simplicity but ideally require site-specific calibration. They are limited to the surf zone in front of a beach, and cannot be used seawards of the breaker line or for depth profiles which do not vary monotonically, such as a bar-trough formation.

Regular waves - wave energy equation

The second type of approach to modelling the energy decay of broken waves is based on the solving the equation for wave energy balance through the surfzone,

$$\nabla \cdot (E c_g) = - D_b \quad (31)$$

In this equation, E is the mean wave energy density, c_g is the group velocity of the waves, D_b is the spatial rate of dissipation of wave energy flux by breaking, and ∇ is the 2-D horizontal gradient operator. For small amplitude linear waves, E is given by,

$$E = \frac{1}{8} \rho g H^2 \quad (32)$$

where ρ is the water density.

The most commonly used expression for D_b is based on the analogy with a tidal bore, a phenomenon similar in appearance to a broken wave,

$$D_b = \frac{\lambda \rho g^{3/2} k H^3}{8\pi h^{1/2}} \quad (33)$$

in which λ is an empirical constant, of the order one, to account for the differences between the breaking wave and tidal bore processes. Le Mehaute (1963) was the first to use this form for the dissipation of broken wave energy, and was followed by Divoky et al (1970), Hwang and Divoky (1979) and Stive (1984), all of whom compared breaking wave models based on the tidal bore analogy with experimental data using regular waves. Svendsen (1984) also used Eq 33 but attempted also to take account of the wave non-linearity at breaking by altering the "1/8" factor in Eq 32 to a value more appropriate to the non-linear wave form and he explicitly introduced a contribution to the wave energy flux from the wave roller. He also derived an expression for λ in terms of the wave crest elevation and the wave height-to-water depth ratio, H/h .

There exist other approaches to the problem of the decay of broken wave energy. Mizuguchi (1981) used the formula for energy dissipation due to internal viscosity, but replaced the kinematic viscosity by an eddy viscosity term,

$$D_b = 0.5 \rho g v_e (k H)^2 \quad (34)$$

in which v_e is the eddy viscosity coefficient. This method has the practical difficulty of obtaining a reliable prediction of v_e . Dally et al (1985) assumed that the rate of dissipation of broken wave energy is proportional to the difference between the actual energy flux and a lower stable flux level,

$$D_b = \frac{K}{h} [E c_g - (E c_g)_s] \quad (35)$$

where K is a factor to be empirically determined and the subscript s denotes the stable energy flux. In their analysis Dally et al assume that, when the stable flux level is reached, the wave height is proportional to the water depth ($H = \Gamma h$, Γ constant) thereby giving,

$$(E c_g)_s = \frac{\rho g c_g \Gamma^2 h^2}{8} \quad (36)$$

There are two empirical parameters to be determined, K and Γ . Based on laboratory data from Horikawa and Kuo (1966), Dally et al recommend values of $K = 0.15$ and $\Gamma = 0.4$.

The best means of solving Eq 31, using the various expressions for D_b , is by means of a computational model using a space-stepping procedure starting at some location seawards of the surf zone, and following a wave up to the point of breaking and then through the surf zone to the water-line. Grid points should be sufficiently closely spaced to provide a good resolution of the breaking process and transformation of the wave in the surf zone. One of the main benefits of a modelling approach is that wave set-up can be accounted for; this is especially important close to the water-line where substantially higher waves can be obtained than would be predicted if set-up were ignored. Nevertheless it is possible to solve Eq 31 in a closed analytical form given certain simplifying assumptions (beach of constant slope, set-up ignored etc). Thornton and Guza (1983) present such a solution using their modification of Eq 33 for D_b , while Dally (1990) provides a solution using Eq 35 for D_b . Both solutions are also applicable to random waves, given certain assumptions about the wave height distribution.

Random waves - empirical methods

The starting point for random wave breaking analyses is the specification of a wave height distribution immediately outside the surf zone. Most authors assume a simple Rayleigh distribution which has been demonstrated in field measurements to be a good approximation in shallow water (Thornton and Guza, 1986), although theoretically valid for narrow-banded spectra in deep water. In the surf zone, however, the Rayleigh distribution needs to be substantially modified. The simplest approach is to use the linear relation Eq

28 and to truncate the distribution at the breaker height so that no wave energy exists at larger wave height values than the breaker height. The truncated wave energy then has to be redistributed in some way at wave heights equal to or lower than H_b . In Collins (1970) and Battjes (1972) the broken wave energy is assumed to all exist at H_b , and therefore the truncated Rayleigh distribution has a delta function at H_b . Kuo and Kuo (1974) and Goda (1975) redistribute the broken wave energy to wave heights lower than H_b , but this loses the distinction between broken and unbroken waves.

The main virtue of the empirical approach for regular waves is its simplicity, but this simplicity tends to disappear when the approach is used for random waves. As computer models become more commonplace it is logical to adopt methods which solve the wave energy equation. For random waves, these methods fall into two types, those which follow the transformation of a single wave height value representative of the full distribution, and those which divide the distribution into a number of wave height bands and follow each band through the surf zone. The latter is known as the probability density function (or pdf) method.

Random waves - wave energy equation, single representative wave height method

The first authors to apply the wave energy equation Eq 31 to the dissipation of random breaking waves were Battjes and Janssen (1978). In their method, the wave height distribution was taken to be a Rayleigh distribution truncated at the breaker height and with all the broken wave energy existing at that height. A single representative wave height value, the rms wave height, is transformed through the surf zone. It is assumed that the same truncated Rayleigh shape is maintained throughout, but the overall size of the distribution is determined by the changing H_{rms} values. In this method H_{rms} is the root-mean-square of all wave heights, broken and unbroken. An essential element of Battjes and Janssen's model is the prediction of the fraction of broken waves (Q_b) at any point. Their analysis shows that Q_b is related to H_{rms} and H_b by,

$$\frac{1 - Q_b}{-\ln Q_b} = \left(\frac{H_{rms}}{H_b}\right)^2 \quad (37)$$

The final part of their model involves the integration of Eq 31 across the surf zone using Eq 33 for D_b , interpreting H as H_{rms} and applying this calculation

only to the fraction of broken waves at each point. Similar treatments with different expressions for D_b are given by Thornton and Guza (1983), Stive (1984), Svendsen (1984) and Dally and Dean (1986). A number of coastal profile models have been developed using the Battjes and Janssen method (Southgate 1989; Southgate and Nairn, 1993; Roelvink and Stive, 1989) and quite extensively verified against laboratory and field data sets, generally with good predictions for H_{rms} . Ebersole (1987) has compared the methods of Dally et al (1985) and Svendsen (1984) against field data, both models giving an rms error of about 10%. The scatter of field data tended to mask any genuine comparison of the models.

Random waves - wave energy equation, pdf method

In the probability density function (pdf) method, the incident wave height distribution, located seawards of the surf zone, is divided up into a series of wave height bands each with a probability of occurrence. Each band is separately transformed through the surf zone, and statistical wave parameters can be reassembled at any point from knowledge of the transformed wave height for each band and its probability of occurrence. This method relies on no (or only weak) interaction between individual waves in a random wave train, a condition which is approximately satisfied in shallow water. It has the advantage over the "single representative wave height" method of not imposing a particular type of wave height distribution as the waves propagate. A further possibility is to use a non-linear shallow-water theory which can be justified on account of the (approximately) non-dispersive character of the waves. The main drawbacks are the considerably larger amount of computational effort required, and that inshore wave parameters will have a statistical rather than an energy-based definition, which may not be suitable for further applications to wave-driven phenomena in the surf zone (the distinction between statistical and energy-based definitions of shallow-water wave parameters is discussed in Nairn, 1988).

Authors who have used this approach include Mase and Iwagaki (1982), Dally and Dean (1986) and Nairn (1990). Wave height computations are comparable to those using the single representative wave method, although somewhat higher values are usually obtained around the breaker zone, a feature which becomes more prominent with the use of non-linear wave transformation theories. Care has to be taken in making comparisons with laboratory or field data, since most modern data sets are based on spectral rather than statistical analysis.

CONCLUSIONS AND RECOMMENDATIONS

Wave breaking is the most physically complex process that surface water waves undergo. In order to render any theory of breaking amenable to hand calculations or computational models of wave transformation, the representation of breaking has to be considerably simplified. Furthermore, there is an inherent variability in the process, demonstrated by the scatter of experimental data. In view of this, predictions of breaking wave heights and energy losses cannot be considered reliable for individual waves, although they can represent average values over a series of waves which are sufficiently accurate for engineering applications. Bearing these points in mind, the following conclusions and recommendations can be made.

- a) Breaker Height. Experimental measurements show different trends in breaker height for regular and random waves. For regular waves there is a distinct dependence of breaker height on bed slope and wave steepness, and therefore formulas that neglect either of these parameters are not recommended. Of the expressions that do include both parameters, the Weggel formula (Eq 17) has been compared with a large quantity of experimental data and has been widely used in coastal engineering practice. However, the use of an offshore steepness rather than a local value is a weakness. The expressions of Yoo (Eq 24 and 25) are entirely defined in terms of local parameters and have been compared against many separate sets of experimental data. This type of expression should be increasingly used where knowledge of local values of slope and wave steepness at the breaker line is known, as is usually the case in present-day computational models.

For random waves, the expression obtained by Battjes and Stive (Eq 26), or its modification by Nairn (Eq 27), is recommended. These formulas have been derived from a large number of, and varied types of, laboratory and field data. The modification by Nairn is likely to be more accurate at low wave steepnesses without affecting accuracy at other steepness values. However, further good-quality data is required to provide additional validation and to shed light on the reasons for the different trends in breaker height of regular and random waves.

- b) Dissipation of Broken Wave Energy. For regular waves in the surf zone a power law relationship between broken wave height and water depth such as that of Smith and Kraus (Eqs 29 and 30) is preferred to

the simple linear relationship (Eq 28). Alternatively, for both regular and random waves, the analytical solutions to the wave energy equation (Eq 31) for simplified bathymetries can be used. However, these methods are limited to plane nearshore profiles, and care must be taken concerning wave height predictions close to the water-line, which can be substantially under-predicted if wave-induced set-up is not considered. The main alternative approach, based on a computer model solution of the wave energy equation through the surf zone, is physically better founded and can be used for any type of depth profile and be readily combined with other dissipative or generative processes (such as bottom friction and wind growth). The method is applicable to both regular and random waves, and wave set-up is usually calculated in such models. The most commonly used expressions for the rate of dissipation of broken wave energy are those of Battjes and Janssen (Eq 33) and Dally et al (Eq 35). For random waves, a "single representative wave" method or a probability density function method can be used. The former is computationally quick, provides good accuracy in wave height predictions, and provides a good framework for subsequent calculations of large-scale wave-driven processes. The latter can provide more detail on the statistical wave height distribution at any point in the surf zone.

ACKNOWLEDGEMENTS

This work was undertaken as part of the MAST G6M Coastal Morphodynamics research programme. It was funded in part by the UK Ministry of Agriculture, Fisheries and Food, and in part by the Commission of the European Communities Directorate General for Science, Research and Development under Contract No MAST 0035-C.

REFERENCES

- 1 BATTJES J A. (1972). "Set-up due to irregular waves", Proc. 13th Int. Conf. on Coastal Eng., ASCE, pp 1993-2004.
- 2 BATTJES J A. (1974). "Computation of set-up, longshore currents, run-up and overtopping due to wind-generated waves", Delft Univ. of Tech., Report No 74-2.
- 3 BATTJES J A and JANSSEN J P F M. (1978). "Energy loss and set-up due to breaking of random waves", Proc. 16th Int. Conf. on Coastal Eng., ASCE, pp 569-587.

- 4 BATTJES J A and STIVE M J F. (1985). "Calibration and verification of a dissipation model of random breaking waves", *J Geophys Res.* Vol 90, No C5, pp 9159-9167.
- 5 COLLINS J I. (1970). "Probabilities of breaking wave characteristics", Proc. 12th Int. Conf. on Coastal Eng., ASCE, pp 399-412.
- 6 COLLINS J I and WEIR W. (1969). "Probabilities of wave characteristics in the surf zone", Tetra Tech Report TC-149.
- 7 DALLY W R. (1990). "Random breaking waves: a closed-form solution for planar beaches", *Coastal Engineering*, Vol 14.
- 8 DALLY W R and DEAN R G. (1986). "Transformation of random breaking waves on surf beat", Proc. 20th Int. Conf. on Coastal Eng., ASCE, Vol 1.
- 9 DALLY W R, DEAN R G and DALRYMPLE R A. (1985). "Wave height variation across beaches of arbitrary profile", *J Geophys Res.*, Vol 90, No C6, pp 11917-11927.
- 10 DIVOKY D, LE MEHAUTE B and LIN A. (1970). "Breaking waves on gentle slopes", *J Geophys Res.*, Vol 75, pp 1681-1692.
- 11 EBERSOLE B A. (1987). "Measurement and prediction of wave height decay in the surf zone", ASCE Speciality Conf. on Coastal Hydrodynamics, Univ. of Delaware, USA.
- 12 FENTON J D. (1990). "Non-linear wave theories", In *The Sea, Ocean Engineering Science*, Vol 9, Part A, Eds. B Le Mehaute and D M Hanes, Pub. Wiley Interscience.
- 13 GALVIN C J. (1968). "Breaker type classification on three laboratory beaches", *J Geophys Res.* Vol 73, pp 3651-3659.
- 14 GALVIN C J. (1969). "Breaker travel and choice of design wave height", *J Waterways and Harbours Div*, ASCE, Vol 95, pp 175-200.
- 15 GALVIN C J. (1972). "Wave breaking in shallow water", In *Waves on Beaches*, Ed. R E Meyer, Pub. Academic Press, New York.

- 16 GODA Y. (1975). "Irregular wave deformation in the surf zone", Coastal Eng. Japan, Vol 18, pp 13-26.
- 17 HANSEN J B and SVENDSEN I A. (1979). "Regular waves in shoaling water -Experimental data", Series Paper No 21, Technical University of Denmark.
- 18 HORIKAWA K and KUO C T. (1966). "A study of wave transformation inside the surf zone", Proc. 10th Int. Conf. on Coastal Eng., ASCE, Vol 1, pp 217-233.
- 19 HUNTER J K and VANDEN-BROECK J M. (1983). "Accurate computations for steep solitary waves", J Fluid Mech., Vol 136.
- 20 HWANG L S and DIVOKY D. (1970). "Breaking wave set-up and decay on gentle slopes", Proc. 12th Int. Conf. on Coastal Eng., ASCE, Vol 1, pp 377-389.
- 21 IRRIBARREN C R and NOGALES C. (1949). "Protection des Ports II", 17th Int. Navig. Congress, Lisbon, pp 31-80.
- 22 IWAGAKI Y, SAKAI T, TSUKIOKA K and SAWAI N. (1974). "Relationship between vertical distribution of water particle velocity and types of breakers on beaches", Coastal Eng. Japan, Vol 17, pp 51-58.
- 23 KOMAR P D and GAUGHAN M K. (1972). "Airy wave theory and breaker height prediction", Proc. 13th Int. Conf. on Coastal Eng., ASCE.
- 24 KUO C T and KUO S T. (1974). "Effect of wave breaking on statistical distribution of wave heights", Proc. Civil Eng. Oceans/3, ASCE, Vol 2.
- 25 LAITONE E V. (1960). "The second approximation to cnoidal and solitary waves", J Fluid Mech, Vol 9, No 3.
- 26 LE MEHAUTE B. (1962). "On non-saturated breakers and the wave run-up", Proc. 8th Int. Conf. on Coastal Eng., ASCE, pp 77-92.

- 27 LE MEHAUTE B, DIVOKY D and LIN A. (1968). "Shallow water waves: A comparison of theories and experiments", Proc. 11th Int. Conf. on Coastal Eng., ASCE, Vol 1.
- 28 MADSEN O S. (1976). "Wave climate of the continental margin; elements of its mathematical description", Marine Sed. Trans. and Environ. Manag., pp 65-90.
- 29 MASE H and IWAGAKI M. (1982). "Wave height distributions and wave grouping in the surf zone", Proc. 18th Int. Conf. on Coastal Eng., ASCE, Vol 1.
- 30 McCOWAN J. (1891). "On the solitary wave", Phil Mag J Science, Vol 32, 5th series.
- 31 MICHE M. (1944). "Mouvements ondulatoires de la mer en profondeur constante ou décroissante", Annales des Ponts et Chaussees.
- 32 MICHELL J H. (1893). "On the highest waves in water", Phil Mag J Science, Vol 36, 5th series, pp 430-437.
- 33 MIZUGUCHI M. (1981). "An heuristic model of wave height distribution in surf zone", Proc. 17th Int. Conf. on Coastal Eng., ASCE, Vol 1, pp 278-289.
- 34 MOORE B D. (1982). "Beach profile evolution in response to changes in water level and wave height", MSc thesis, Dept. Civil Eng., Univ. of Delaware, USA.
- 35 NAIRN R B. (1988). "Statistical vs variance definitions of wave parameters in the surf zone", postscript to *Prediction of wave height and mean return flow in cross-shore sediment transport modelling*, IAHR symposium on math. modelling of sed. trans. in the coastal zone, Copenhagen, Denmark.
- 36 NAIRN R B, (1990). "Prediction of cross-shore sediment transport and beach profile evolution", PhD thesis, Dept. Civil Eng., Imperial College, Univ. of London.

- 37 NELSON R C. (1987). "Design wave heights on very mild slopes - An experimental study", Civil Eng. Trans. Inst. Engs. Australia, Vol CE29.
- 38 OSTENDORF D W and MADSEN O S. (1979). "An analysis of longshore currents and associated sediment transport in the surf zone", Dept. Civ. Eng., MIT, Report 241.
- 39 ROELVINK J A and STIVE M J F. (1989). "Bar-generating cross-shore flow mechanisms on a beach", J Geophys Res., Vol 94, No C4.
- 40 SCARSI G and STURA S. (1980). "Il frangimento delle onde su profondità molto basse", Istituto Lombardo, Rend Sc B, Vol 114, pp 52-60.
- 41 SINGAMSETTI S R and WIND H G. (1980). "Characteristics of shoaling and breaking periodic waves normally incident to plane beaches of constant slope", Delft Hydr Lab, Report M1371.
- 42 SMITH J M and KRAUS N C. (1987). "Longshore current based on power law wave decay", ASCE Speciality Conf. on Coastal Hydrodynamics, Univ. of Delaware, USA.
- 43 SOUTHGATE H N. (1989). "A nearshore profile model of wave and tidal current interaction", Coastal Engineering, Vol 13, pp 219-245.
- 44 SOUTHGATE H N and NAIRN R B. (1993). "Deterministic profile modelling of nearshore processes. Part 1. Waves and Currents", Coastal Engineering (to appear).
- 45 STIVE M J F. (1984). "Energy dissipation in waves breaking on gentle slopes", Coastal Engineering, Vol 8.
- 46 SUNAMURA T. (1981). "A laboratory study of offshore transport of sediment and a model for eroding beaches", Proc. 17th Int. Conf. on Coastal Eng., ASCE, pp 1051-1070.
- 47 SVENSEN I A, MADSEN P A and HANSEN J B. (1978). "Wave characteristics in the surf zone", Proc 16th Int. Conf. on Coastal Eng., ASCE, pp 520-539.

- 48 SVENSEN I A. (1984). "Wave heights and set-up in a surf zone", Coastal Engineering, Vol 8, pp 303-329.
- 49 THORNTON E B and GUZA R T. (1983). "Transformation of wave height distribution", J Geophys Res, Vol 88, pp 5925-5938.
- 50 THORNTON E B and GUZA R T. (1986). "Surf zone longshore currents and random waves: Field data and models", J Phys Oceanography, Vol 16, No 7.
- 51 VAN DORN W G. (1978). "Set-up and run-up in shoaling breakers", Proc. 16th Int. Conf. on Coastal Eng., ASCE, pp 738-751.
- 52 WEGGEL J R. (1972). "Maximum breaker height", J Waterways, Harbours and Coastal Div ASCE, Vol 98, No WW4, pp 529-548.
- 53 WIEGEL R L and MASH F D. (1961). "Cnoidal wave tables of functions", Council of Wave Res., Univ. of California.
- 54 WILLIAMS J M. (1981). "Limiting gravity waves in water of finite depth", Phil. Trans. Roy. Soc. London A, Vol 302.
- 55 YOO D. (1986). "Mathematical modelling of wave-current interacted flow in shallow waters", PhD thesis, Univ. of Manchester.

THREE-DIMENSIONAL BREAKING WAVE KINEMATICS

K. SHE*, C.A. GREATED[†], and W.J. EASSON[‡]

* Department of Civil Engineering

† Department of Physics

‡ Department of Mechanical Engineering

University of Edinburgh, Edinburgh, EH9 3JZ

U.K.

An investigation into three-dimensional waves has been carried out using Particle image velocimetry. The wave field contains a single frequency with a uniform angular spreading within a given range $\{-\alpha, \alpha\}$. The waves are designed such that the wave energy is focused at a given point. Several α values between 30 and 60 degrees were tested. Angular spreading was found to have great effects on the breaking characteristics and kinematics. Two types of breakers were observed, with the first being plunging breaking and the second being spilling breaking. The extreme wave kinematics were enhanced by the increased spreading. The maximum velocity to deep water celerity ratio of unity seemed to be the upper limit for spilling breakers and the lower limit for the plungers. The maximum velocity did not, in general, appear at the crest. The limiting crest velocity was found to be the value of the deep water celerity, which is in line with the observation of Griffiths (1989).

INTRODUCTION

Wave breaking has been a subject under vigorous investigations in recent years. As more and more advanced measuring techniques such as LDA (Laser-Doppler Anemometry), PIV (Particle Image Velocimetry) and FOS (Fibre Optical Sensors) become available for scientific researches, much wider scope of wave-associated problems are being examined. Using LDA, Griffiths¹ made a detailed parametric study of shoaling of two-dimensional mono-chromatic waves on a beach of various slopes. The deep water celerity was found to be the limiting crest velocity. In pursuing an understanding of the intricate nature of breaking waves, many researchers developed various numerical methods which allowed them to examine breaking wave properties in detail. A good example of this is that of Cokelet (1979). These numerical methods can, however, only be used to simulate two-dimensional breaking waves, although some of them can in principle be

expanded to deal with three-dimensional cases. The existing experimental works are also largely limited to two-dimensional conditions. Studies of three-dimensional wave breaking in laboratories and open seas are difficult and rare. Su (1982) reports an interesting phenomenon where a two-dimensional Stokes wave develops into fully three-dimensional breakers as a result of three-dimensional instability. Kjeldsen et al (1981) reported some field measurements of breaking waves where surface elevations were utilised to derive a description of surface properties.

To take the large step from two-dimensional measurements to fully three-dimensional measurements would involve the introduction of a large number of parameters and would require a research programme on a very large scale. Choice of spectrum (P-M, JONSWAP), spreading angle, water depth, currents; selection of measuring point and definition of breaking all influence the final form of the breaking wave. For this reason it is first necessary to isolate the individual parameters and measure their effects. She et al (1991) looked at the addition of two angled wave crests and concluded that the velocity field of two crossing wave trains was more severe than that of a sinusoidal two-dimensional wave. The effects of angular spreading on wave breaking was further examined by She et al (1992) and the surface parameters, such as breaking wave height and steepness, were found to be strongly influenced by angular spreading, underlying the importance of three-dimensional effects.

The present work is an attempt to investigate the effects of angular spreading on breaking wave kinematics. Particle image velocimetry has been employed to obtain the under-crest velocity field.

EXPERIMENTAL ARRANGEMENTS

The experiments were conducted in the wave basin of Edinburgh University. The basin is 27 m wide and 12 m long with a water depth of 1.2 m. A sketch of the wave basin is shown in Figure 1. The wave generation system has 75 paddles, each being connected to an electronic board, which acts not only as a messenger between the control centre and the driving motor but also as a controller of wave absorption. This means that the wave makers not only generate waves but also absorb the reflected waves. In general, the wave reflection is under 5%. The wave signal generation is based on wave component superpositions and up to 1024 wave fronts of different frequencies and directions can be generated simultaneously.

To minimise the number of parameters involved, we have chosen a simple and yet very important case in our investigation. The wave field consists of a single frequency focusing wave. This wave is generated by using 360 wave fronts of the same height and frequency equally spaced within the angular range $-\alpha$ to α degrees. The phases of all fronts are calculated in terms of linear wave theory such that the

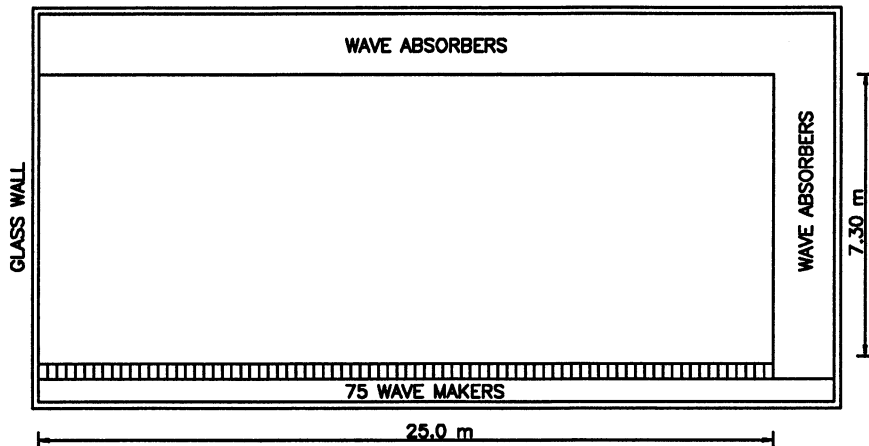


Figure 1: A sketch of the Edinburgh wave basin.

energy becomes focused at a pre-determined point. The crest-trough patterns of such wave fields are shown in Figure 2.

PARTICLE IMAGE VELOCIMETRY (PIV)

Particle image velocimetry has become an established measuring technique for 2D wave studies at Edinburgh University (see Gray et al, 1988, Skyner et al, 1990, and Sutherland et al, 1990). The use of this technique in Edinburgh involves the following procedures:

- i) to guide a laser beam to scan through a vertical plane of fluid in which the velocity field is to be measured;
- ii) to seed the water with particles such as Pollen powder, which are illuminated by the laser beam at a certain scanning rate;
- iii) to take a photograph of the illuminated fluid area at a certain shutter speed such that the negative records 2 or more images of the same particles as they move with the fluid to new positions;
- iv) to find the image separations;
- v) to find the velocities by relating the image separation, scanning rate and camera magnification.

More details may be found in Gray et al (1988).

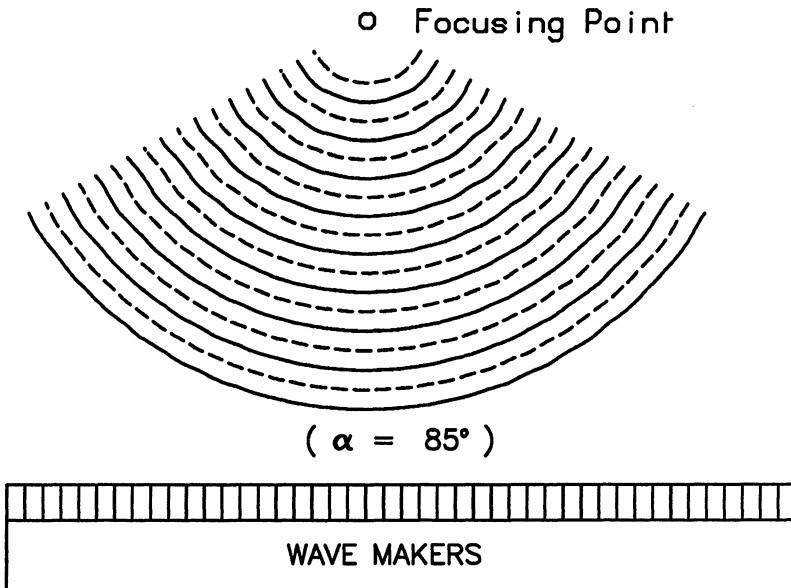


Figure 2: Crest-trough pattern of a focusing wave.

In 2D applications, the scanning system is underneath the wave flume and the laser beam is directly guided through the glass bottom of the flume into the water. In a 3D wave basin, the setup becomes more complicated, as shown in the next section.

PIV SETUP

The technology of particle image velocimetry has made enormous improvement in our effort of pursuing an understanding of 2D waves. But it is yet to find its use in the studies of 3D waves. To set up a PIV system in the middle of the wave basin would be ideal for our 3D wave measurements. To do this requires the development of a new PIV system. It has to be waterproof. It must not introduce too much interference with the waves. This task may take a few years to accomplish. To avoid such a huge task, it was decided that a PIV system was set up at the glass wall of the wave basin. This required an underwater system which would guide the scanning beam to an upward direction.

The optical layout of the modified PIV system is shown in Figure 3. A 15 watt Argon Ion laser was used. The PIV box consists of a rotating mirror and parabolic mirror, converting a laser beam of about 2mm diameter into a 500mm wide laser

sheet. Through the glass wall of the tank, the laser sheet is guided to an upright direction via an underwater mirror. The mirror was glued onto a 25mm diameter solid aluminium bar of a semi-circular cross section. The problem was how to support the underwater mirror from above the glass wall without causing too much interference, while preventing vibration. Four different designs were tested. The first two had the aluminium bar mounted onto two aluminium plates. The thickness of 12mm was seen to cause large interference with the incoming waves. The third one used a perspex plate as a dummy wall which significantly reduced the interference level. This design, however, had two other problems. One was that air bubbles and solid particles were found trapped between the perspex plate and the glass wall of the tank, which significantly reduced the quality of PIV images. The other problem was the reduction of the laser beam intensity. The laser sheet from the parabolic mirror first enters the glass wall with some loss due to reflection, and then through a very thin layer of water it meets the perspex plate where the laser intensity was further reduced as a result of reflection. The reduced laser intensity also means lower PIV image quality. Because of these problems, a fourth version of the under water system was designed. The underwater mirror was supported by four 2mm stainless steel plates being reinforced by four weights via four 1mm stainless steel wires, as shown in Figure 4. This system causes little interference with waves and provides sufficient rigidity for mounting the mirror.

SEEDING

Having set up the PIV system, another problem arose, that of how to seed the water. To some extend, this has always been a problem in applying PIV to wave studies only that in the present circumstances it was more difficult to tackle. The seeding has to sink eventually, otherwise one has to spend days to fish out the floating particles. The seeding needs to be continuously added into the measurement region to make up the rapidly dispersed particles. This requires a large quantity of seeding and the seeding used has to be cheap. After some preliminary tests, talcum powder was found to be a reasonable choice. Talcum powder has previously been used with LDA measurements in 2D wave flumes (Griffiths, 1990). Although the image quality is not as good as Pollen powder it is in cheap supply. Unlike Pollen powder, it sinks after a while, saving all the trouble of cleaning up the surface.

To take good PIV pictures, the seeding density has to be appropriate and the particles have to be fairly evenly distributed across the measurement region. Sufficient, but not too much perturbation must be given to the newly seeded particles to make them evenly distributed. Enough, but not too much time must be allowed between seeding the water and starting the wave so that the perturbed water is settled while the particles have not begun to sink. There also has to be a precise control of time between starting the wave and opening the camera shutter so that a steady breaking wave pattern has been established while the seeding is not

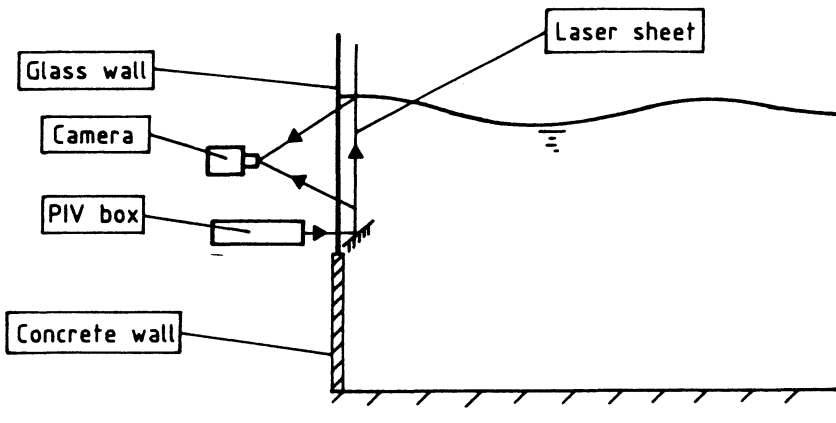


Figure 3: Optical layout of the modified PIV system.

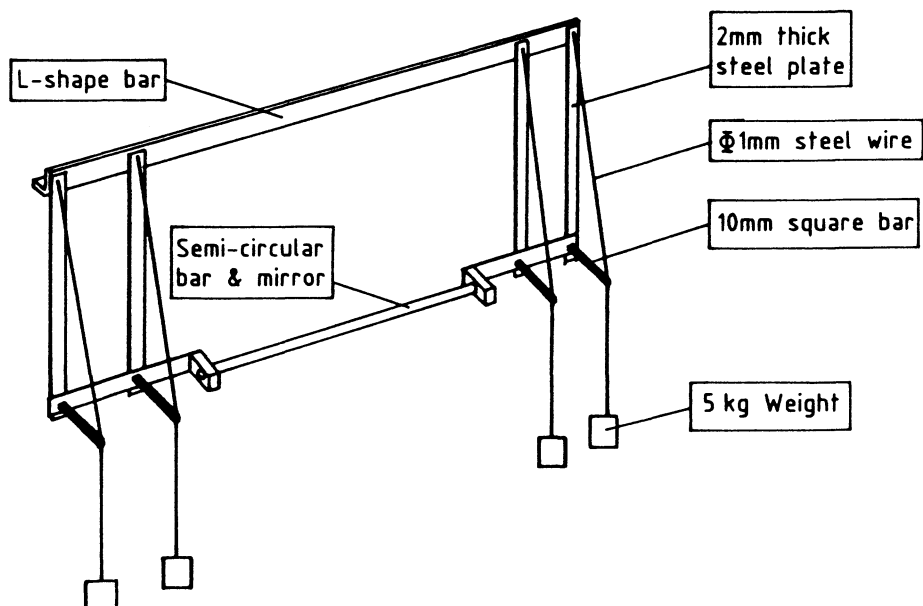


Figure 4: Sketch of the underwater mirror system.

yet fully dispersed. For all these reasons, PIV measurements in the 3D basin are many times more time consuming and more difficult to control than in a 2D flume.

PRELIMINARY REMARKS

Although PIV has become an established measuring system in the study of two-dimensional wave kinematics, this is the first attempt to use it in a three-dimensional wave environment. The accuracy in applying PIV to wave studies may be referred to Gray et al (1988) and Skyner et al (1990). To achieve good PIV measurements, it is of vital importance to obtain high quality fringes. This depends on many factors, the most important of which are:

- a) laser sheet intensity;
- b) beam scanning rate;
- c) camera shutter speed and magnification;
- d) evenness and density of particle distribution;
- e) uniformity of particle sizes.

In the present application, d) has been seen to be the most crucial factor of all. For different types of waves, namely, single frequency focusing waves, multiple frequency focusing waves and two-component crossing waves, the optimum quantity of seeding varied. The amount of seeding for crossing waves was about one-sixth of that needed for multiple frequency focusing waves.

One particular problem associated with three-dimensional wave measurements is the surface reflection. This can be very serious if the free surface reflects the scattered light and laser sheet towards the camera direction and this would significantly reduce the negative contrast or even destroy the wanted particle images. This was found to be the very case in the present application. This problem was solved by mounting the camera at about the same height as the wave crest to be measured. The defect of this was that the measuring area was reduced. This was not much of a concern in this study since the main interest was the kinematics in the crest region.

It should be mentioned at this point that the use of PIV in three-dimensional waves has been assumed to be of the same order of accuracy as in two-dimensional waves. This should be the case in the present study so long as the fringe quality is high. This is because the waves under investigation are geometrically symmetrical in relation to the measurement plane, that of the laser sheet, and the velocity component crossing this plane has to be very small if at all.

It is worth noting that in the case of breaking waves, very careful consideration should be given to the selection of scanning speed of the laser beam. It has to be a compromise between capturing the maximum velocity vector and obtaining the minimum velocity vector if the whole flow field measurement is to be achieved.

In general, the fringe quality has been high for all cases studied. Good control of seeding and scanning speed is of vital importance.

Finally, to obtain velocity vectors from the fringe analysis of negatives, one needs to find the correspondence between the image distance and that of the actual particle movement. The conventional way of doing this PIV calibration is to use a perspex plate with large square grids of a known size. By measuring the grid size on the negative, one can then work out the calibration factor. This involves manual operations which has to be very carefully performed to avoid any unnecessary errors. Instead of following this convention, pairs of dots of 2 mm separations were randomly plotted on an A3 paper which was then sealed in between two thin sheets of perspex. These computer generated dots were photographed at the position of the laser sheet. The negative was then analysed to give the ratio between the actual particle separations and fringe wave numbers. Relating this to the scanning rate of the laser beam, the particle velocities were easily calculated.

A 35 mm Nikon camera was used with a measurement area to negative ratio of about 15 throughout all the experiments. A calibration was carried out at every new set of tests.

RESULTS AND DISCUSSIONS

With the focal point close to the glass surface (about 20 mm), the wave makers only generated wave fronts at angles between 0° and α . The glass wall was assumed to be completely solid and therefore to reflect all waves at a 100% efficiency. As a result, the wave field was as if it had been half of a wave field generated in the middle of the basin with wave fronts uniformly varying from $-\alpha$ to α . Breaking started to happen at the focal point when the wave height at the wave makers (the total wave height of all wave fronts, which is hereafter referred to as nominal initial wave height) reached certain values which depended on α and the distance between the focal point and the wave makers. Further increase of nominal initial wave height did not have much effect on the breaking wave height. It, however, resulted in the breaking point moving farther away from the focal point. For more details of this, refer to Greated et al (1992). A range of nominal initial wave height has tested.

For a given set of input wave parameters (α values and initial wave heights), the wave field was repeated a number of times. A photograph was taken at each run of the same sea condition. The time interval between starting the wavemakers and opening the camera shutter varied from one run to the next such that the difference between the time intervals of two consecutive runs was one-fortieth of a second. Assuming 100% repeatability between different runs, the above procedure was as if consecutive frames of photographs were taken at an interval of one-fortieth of a second as a wave was passing through the measurement region. This made it

possible to capture the velocity field at a point when the front face of the wave became vertical. In general, seven to nine frames were needed to achieve this.

Before proceeding with the presentation of results, possible errors in the experiment and PIV analysis needs to be addressed. Experimental errors come from three major sources:

- a) wave reflection from the beach, causing an error of up to 5%;
- b) turbulence when seeding the water;
- c) photographic distortion.

b) and c) are very small error sources compared with a). Errors in PIV analysis may be attributed to

- a) averaging over a small area to obtain the velocity at the centre of the area;
- b) uncertainty in the scanning rate of the laser beam, which determines the particle image separations at any given velocity;
- c) velocity gradients;
- d) numerical error in the Fourier analysis.

Any difference between the actual scanning rate and assumed rate would bring about an error. As a whole, the errors in the PIV analysis are very small. The overall error is estimated to be of an order of 7%.

An earlier study by the authors (Greated et al, 1992) investigated the effects of spreading effects on the surface parameters of breaking waves. Exactly the same type breakers were generated at the centre of the wave basin. In the present experiment, the measurement area was farther away from the wavemakers than in the surface tests. This means that the distance between the focal point and wavemakers is greater than that in the surface experiment. As a result, a strong nonlinear effect was observed. The change of the measurement region required the phases of all wave fronts to be re-calculated, which was based on the linear wave theory. The phases were such that all fronts were in phase at the focal point. If there was no nonlinear interactions, the focal distance from the wavemakers should not have any effect on the breaking wave height. This was not the case. The crest elevation when breaking first occurred showed a clear increase of up to 40 mm compared with that in the surface measurements. This increase was accompanied by an increase in the initial wave height at the wavemakers. Because of nonlinearity, the phase differences between wave fronts at the focal point were different from the expected values. The greater the distance between the measuring location and the wavemakers, the larger the discrepancy between the actual phase differences and anticipated values. The observed increase in the wave height before breaking began to happen indicated that wave height alone could not dictate breaking events.

As happened in our earlier surface tests, the crest elevation at breaking showed little change with the increase in the initial wave height at the wavemakers. To keep the breakers in the measurement region, the focal point moved farther away from

the wavemakers as the initial wave height increased. This meant a greater discrepancy in the phase differences between the actual and expected values at the focal point. This, however, did not seem to bring about a larger discrepancy in the measurement region, which was at a fixed distance from the wavemakers.

Spreading angles of 30° , 40° , 50° and 60° were tested. A frequency of $1.41\ Hz$ was used throughout these tests. The camera aperture was set to f2.8 with a film speed of ASA 400. The particle illumination was at a rate of 688 times per second while the camera shutter was set to one 125th of a second.

A typical example of velocity vector plots is shown in Figure 5. In engineering practice, what is of the most concern is the extreme wave kinematics. Figure 6 shows the maximum velocities for various angles with each being tested for a range of initial wave heights. For a given spreading angle, the maximum velocity was seen to be the smallest when the initial wave height was just big enough for breakings to occur. Although only a limited number of tests were carried out, a distinctive pattern can be seen from the measurements. For spreading angles above 40° , the maximum velocity are all above the wave celerity estimated according to the linear wave theory. The ratios of the smallest values at different angles to the linear celerity is about 1.04. For a smaller spreading angle of 30° , the maximum velocity keeps below the wave celerity, with the largest value to celerity ratio being 0.96. Taking into account the experimental errors of around 6%, it seems that with large spreading angles breaking occurs when the crest velocity exceeds the wave celerity. With smaller angles, breaking can happen at a much lower crest velocity with a limiting maximum value of celerity.

The above described phenomenon seems to have a close link with the breaking types which the tested breakers fall into. As observed in the surface measurements, two distinct types of breakers were recorded in the PIV tests. At large spreading angles, the breakers were the plunging type. As spreading angle decreased, the plunging characteristics gradually decayed. At $\alpha=30^\circ$ the breaking became spilling. If we associate the measured kinematics with the breaking characteristics, it seems that the plunging breakers have maximum velocities of at least the value of celerity while the spilling breakers have a limiting maximum velocity of celerity.

Griffiths (1989) looked into the breaking wave kinematics due to shoaling on various sloping beaches and found a limiting crest velocity equal to the deep water celerity. In the case of spilling breakers, this finding is well supported by other previous experimental results, that of Van Dorn and Pazan (1975), Hedges and Kirkgoz (1981), and Skielbreia (1987). For plunging breakers, Griffiths also found a ratio of 1. Others, including Mizuguchi (1986), seemed to indicate a greater value than that for spilling breakers.

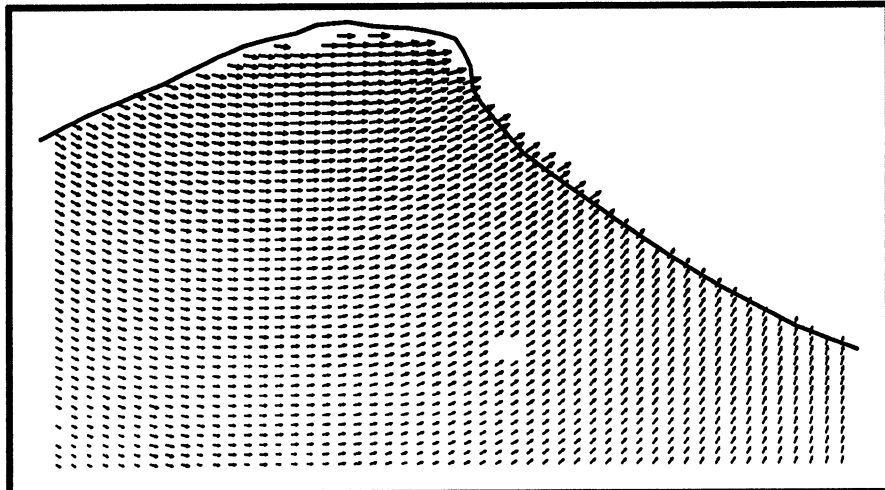


Figure 5: Velocity field of a single frequency focusing wave ($\alpha = 60^\circ$).

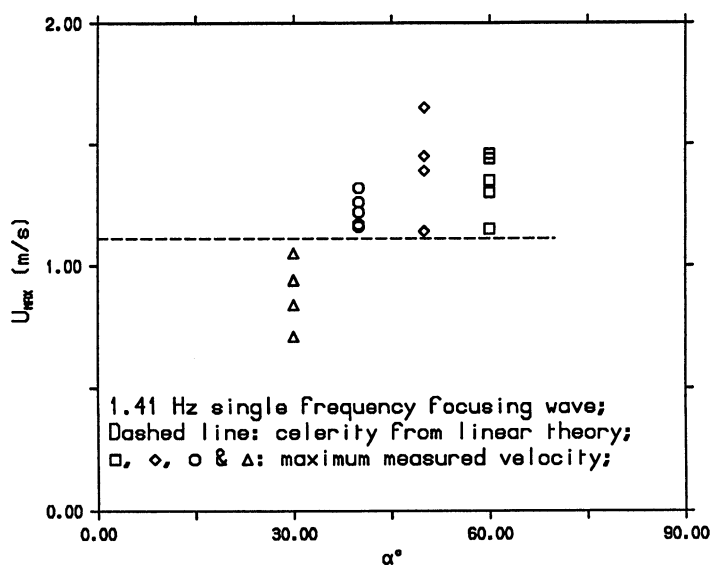


Figure 6: Maximum velocity versus spreading angle (single frequency).

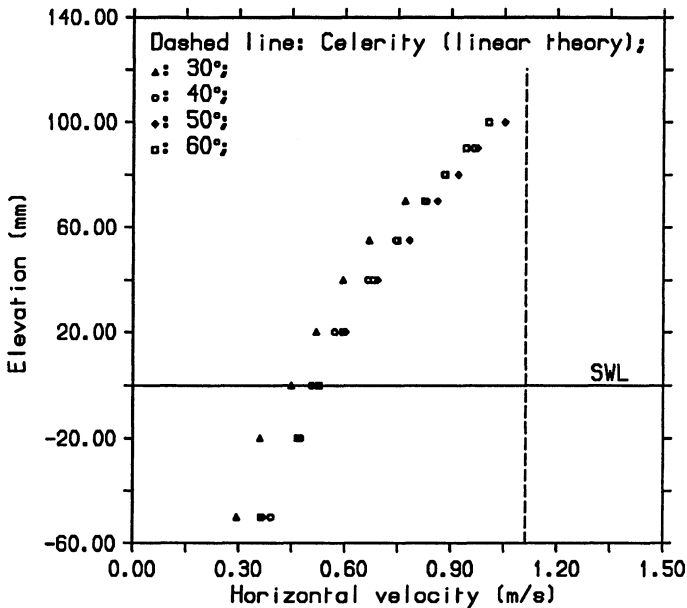


Figure 7: Under-crest velocity versus elevation (single frequency).

Up to this point, special attention has to be drawn to the difference between the crest velocity and maximum velocity. In the experiments of Griffiths, velocities were measured at positions directly underneath the wave crest, using a LDA system. But the crest velocity is not the maximum velocity in a breaking wave. The whole field measurements in the present study have shown that the maximum velocity occurs close to the front face of a breaker rather than at the wave crest. If we extract the under-crest velocities from the present measurements, as shown in Figure 7, a limiting crest velocity equal to celerity can be clearly observed. RMS values are used in Figure 7. For $\alpha = 40^\circ, 50^\circ \& 60^\circ$, the under-crest velocities showed only a small scattering, with an error margin of around 5%. For $\alpha = 30^\circ$, however, larger scattering occurred, with an error margin of around 10%. This could be caused by the greater unsteadiness of the spilling breakers which was observed during the experiment. It made it more difficult to determine the breaking point.

By now, it seems clear that single frequency breakers due to 2D shoaling or 3D focusing have a limiting crest velocity equal to the deep water celerity. But the maximum velocity to celerity ratio has an upper limit or lower limit of unity, depending on the breaking types.

CONCLUSIONS

The results from the PIV measurements confirm the findings of the surface tests. Spreading affects the characteristics of the breaking waves, which in turn influence the magnitude of wave kinematics. In the event of single frequency breaking due to 2D shoaling or 3D focusing, the crest velocity has a limiting value of deep water celerity. The crest velocity does not, however, represent the extreme wave kinematics of a breaking wave. The maximum velocity is in general higher than the crest velocity. A maximum velocity to celerity ratio of unity appears to be the upper limit for spilling breakers and the lower limit for plunging breakers.

ACKNOWLEDGEMENT

This research is funded by SERC. The authors also wish to thank Mr P. Woodhead of the Edinburgh Wave Power Project for his technical assistance during the course of this research and Professor S. Salter for the use of the wave basin.

REFERENCES

- Cokelet E.D. (1979) "Breaking waves - the plunging jet and interior flow field", Mechanics of Wave-Induced Forces on Cylinders, ed., T.L Shaw, Pitman, 287-301.
- Dold J.W. and Peregrine D.H. (1985) "An efficient boundary integral method for steep unsteady water waves", Numerical Methods for Fluid Mechanics II, Clarendon Press.
- Created C.A., J. Martin and K. She (1989) "Loading in three dimensional seas", Project A06 final report, Fluid Dynamics Unit, Edinburgh University.
- Created C.A., W.J. Easson and K. She (1992) "3D wave breaking" Project AFF02 final report, Fluid Dynamics Unit, Edinburgh University.
- Griffiths M.W.P. (1989) "Breaking waves", PhD thesis, Edinburgh University.
- Kjeldsen S.P., Lystad M. and Myrhaug D. (1981) "Forecast of breaking waves on the Norwegian Continental Shelf", Project Report, The Norwegian Meteorological Institute and Norwegian Hydrodynamic Laboratories, Division Ship and Ocean Laboratory.
- She K., Created C.A. and Easson W.J. (1991) "Effects of three-dimensionality on wave kinematics and loading", Proc. of The First International Offshore and Polar Engineering Conference, Edinburgh, U.K., III, 1-5.
- Skyner D.J., Gray C. and Created C.A. (1990) "A comparison of time stepping numerical predictions with whole field flow measurement in breaking waves", Water Wave Kinematics, Kluwer Academic Publishers, 491-508.
- Su M.Y., 1982, "Three dimensional deep water waves", J. Fluid Mechanics 124, 73-108.

ENVIRONMENTAL FORCES AT THE COASTLINE AND IMPLICATIONS FOR COASTAL DEFENCE

N.W. Beech and J.L. Andrews
Posford Duvivier
Rightwell House
Bretton Centre
Peterborough PE3 8DW
United Kingdom

ABSTRACT

Waves tides and currents exert continuous, and sometimes formidable, forces on the shoreline. The response of the shoreline is a function of these forces together with the geological make-up of the seabed and the coast. The nature of this response is a major factor in the process of determining the correct measures to defend the coast from erosion or from flooding. This paper reviews the significance of these coastal forces and outlines some methods for determining them. Three example cases are presented in the second part of the paper.

INTRODUCTION

Severe storms during the winters of 1989/90 and 1991 caused extensive damage to the coasts of England and Wales. The failure of the sea defences at Towyn in North Wales, and the flooding which resulted, probably received the most media coverage. Damage to coastal defences was however widespread; at some locations, such as Eastbourne and Sidmouth, storms resulted in a significant loss of beach sediment. This is a major concern as it lowers the beach and thus exposes the man-made defences behind to increased attack from the sea.

These recent events have heightened public awareness to coastal and sea defence issues; an awareness made more acute by the topical debate over global warming and sea level rise.

It is the business of coastal engineers, both in the public and private sectors, to devise solutions to these problems. Such solutions must recognise not only the need to carry out works to remedy immediate problems, but also to facilitate management of the coastline or more specifically the shoreline, over an economic scheme life. In this context the scheme life is usually between 25 and 50 years.

The appraisal and development of schemes entails consideration of several facets. In

broad terms these can be summarised by the following:

- **Technical issues** - the proposed scheme must:
 - satisfy its primary functional requirements, eg. avoidance of coast erosion and/or flooding
 - be sustainable for the targeted scheme life
 - not create problems elsewhere or for the future
- **Environmental Issues** - The coast is both immensely valuable and extremely sensitive in environmental terms. All major schemes require appraisal of the environmental impacts of all relevant parameters which might include ecological, conservation, fishery, water quality, archaeological, visual and other human sensory impacts. This requires as a prerequisite a sound environmental database. Extensive consultation is invaluable.
- **Economics** - Engineering works for coast erosion and flooding are grant aided by MAFF in England, the Secretary of State for Wales or the Scottish Development Department. To qualify for grant aid, the scheme must be demonstrated to be economically worthwhile. This is determined by comparing the costs of a scheme with the benefits afforded by it. The benefits are determined by assessing the value of damages avoided by the scheme. The analysis must also take into account the reduced losses which may continue to occur after the scheme is in place, as it is not usually practical and not necessarily economic to eliminate all possibilities of damage.

To satisfy each of the above criteria entails a thorough understanding of the problem. This in turn requires that the coastal processes, ie. the interaction between the sea, the shore and coastal defences, are properly investigated. Only when these processes are understood and the problem is identified can the right solution be put forward.

There are various measures which can be applied to defend the coast, including seawalls, beach replenishment, groynes and shore parallel (offshore) breakwaters. In some situations it might be appropriate to "do-nothing", either because works are not warranted, or because interference might be detrimental. All these options however, affect the shoreline differently. The performance of each and hence its suitability for any given problem depends on the interaction with the coastal processes.

COASTAL PROCESSES

The principal objective in studying coastal processes is to gain an understanding of the behaviour of the shoreline in response to the action of the sea. This requires the following areas to be explored:

- topography, bathymetry and geology

- sea level
- wave climate
- currents
- sediment transport (longshore, onshore-offshore)
- sediment balance

Topography, Bathymetry and Geology

It is usually necessary to extend the study area beyond the boundaries of the area of immediate concern - the problem area. This is because the coastal processes within the problem area will almost certainly be influenced by factors which are further afield, eg. sediment supply or the shielding effect of a headland or of offshore sandbanks. By the same token, works undertaken to protect a length of coast can have an influence elsewhere. When practicable the study should be extended to the limits of the "coastal cell" in which the problem lies. The coastal cell is a natural demarcation bounded by coastal features which sever or intrude into the coastal regime such as major headlands or river estuaries, as distinct from statutory boundaries.

A detailed knowledge of the offshore bathymetry is essential for the computation of wave transformations from deep to shallow water. In some cases sufficient information can be derived from Admiralty Navigation Charts but for some applications these are too coarse. More detailed survey data can be obtained by procuring the relevant collector charts from the Admiralty.

At sites with offshore sandbanks it is important to consider whether the banks are stable or whether, in fact, they tend to migrate. Such movements may not be perceptible in the short-term but over periods of tens of years can result in significant changes in the exposure of the shoreline to offshore wave attack. Such changes are clearly of importance to projects with scheme lives of up to 50 years.

Inter-tidal bed levels are obtained by surveying beach profiles at low water. Again it is likely that these will have changed with time being subject to storm and seasonal variations, and long-term trends. Where beach profiles have previously been routinely measured then it may be possible to ascertain trends but monitoring must generally have been undertaken for at least 10 years say for trends to be meaningful.

In addition to knowing the bathymetry and beach levels, the geology of the site must be understood. This will include the extent, and grain size, of mobile sediments - shingle, sand, silt. In the "active" part of the seabed, (ie. the beach, the foreshore and shallower waters) the depth and hence the volume of mobile deposits is important as this sediment represents the "building material" from which the natural coastal defence can be forged by the action of the sea. The character of the stratum below the mobile sediment also must be known; in particular, whether it is a hard rock or is erodible when exposed, eg. clay, chalk. Landward of the beach the geology of cliff forms is important as these provide, through erosion, sediment input to the coastal zone.

Sea Level

A thorough understanding of normal and extreme sea levels is essential. Sea level is, of course, a main parameter in determining flooding risk at the coast. It also has a major influence on waves at the shore. Extreme waves at coastal structures are often dictated by the depth limitation imposed by the sea level rather than by the extreme offshore waves.

Sea level comprises the astronomical tide and meteorological effects (surge). Bad weather normally accompanies meteorological surges, so depending on the occurrence of high astronomical tides, storm waves can accompany high seas. The likelihood of extreme waves and water levels at the shore thus depends on a number of factors that vary around the coasts. This can be examined using joint-probability techniques.

Data on tide levels may be obtained from the Admiralty and Proudman Oceanographic Laboratory (POL), and sometimes local sources such as harbour authorities. Extreme levels may be derived where records of sufficient duration to enable extrapolation exist.

In addition to the factors mentioned above, sea level rise must also be considered. Over a scheme life of say 50 years this can have a significant impact on coastal schemes where a rise of only a fraction of a metre can represent a large relative increase in the depth of water.

Wave Climate

The initial step in the derivation of sediment transport is the development of directional wave climate at the shore. There are two stages in the development of nearshore wave data. These are:

- (i) derivation of offshore wave climate
- (ii) transformation of waves to nearshore

There are two main options available for gaining long term **offshore wave data**, as described below:

- Visually observed wave data - Such data, obtained from ships records, is available from the Meteorological Office and elsewhere. The advantages of this data source are its relatively low cost, plus the fact that swell waves are identifiable. The disadvantages are: that wave data are usually drawn from a rather large sea area and consequently waves originating from directions with confined fetches may not be accurately resolved. It is not normally possible or practical to abstract waves pertaining to specific storm events.

- Hindcast wave data - Numerical models exist for the computation of waves from hourly wind data, the latter being available from the Meteorological Office. Hindcasting does not identify swell waves.

Further to the above, the Meteorological Office also operate, on a routine basis, a deep water wave hindcast model covering the sea areas around the UK coast. The data is computed at grid points spaced 0.4° longitude by 0.25° latitude. Hindcast data from the model are available from 1986.

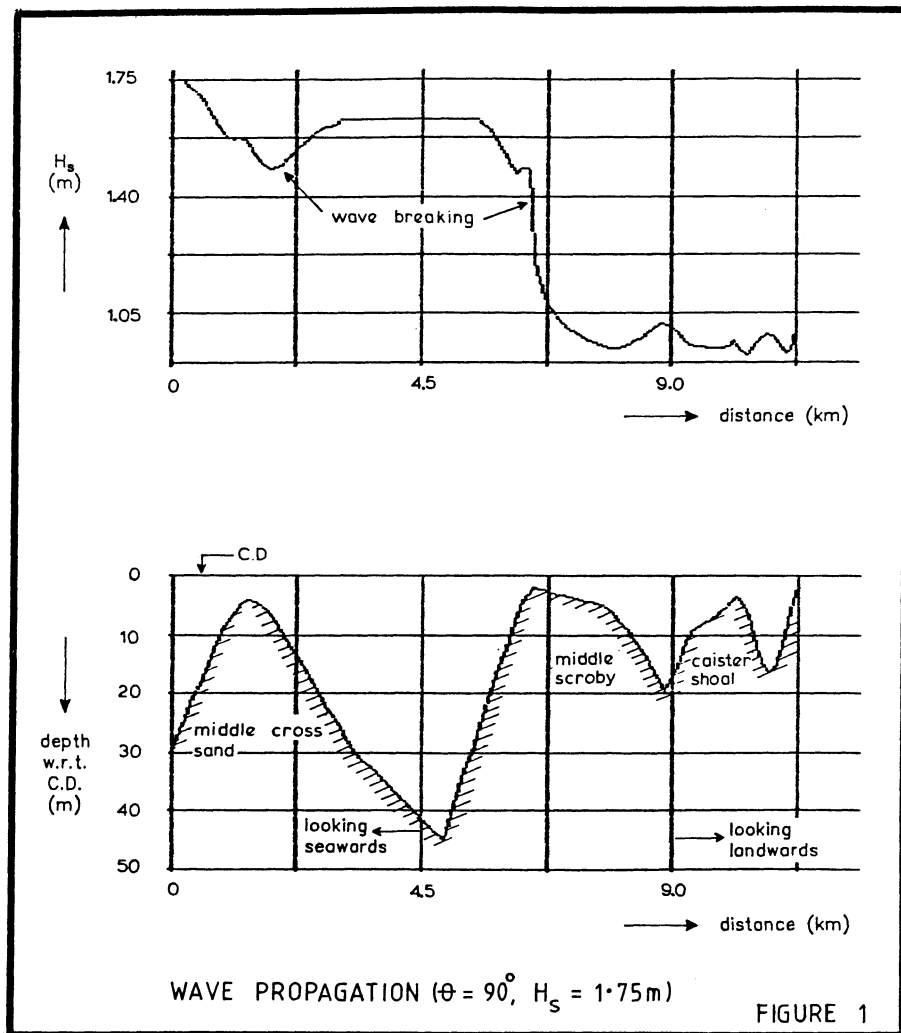
Depending upon the nature and value of the project, a wave measurement campaign may be commissioned. Such measurements are usually undertaken in conjunction with long-term data from hindcasting or visually observed waves, in order to derive reliable average annual wave conditions.

Nearshore waves are determined by transforming the offshore wave climate with respect to the shallow water processes of refraction, shoaling, friction at the seabed and wave breaking. In situations where waves are reduced in height by offshore sandbanks or reefs, wave growth between the obstruction and the shore can be important. These processes are now evaluated with the aid of mathematical models. One-dimensional modelling, that is, the modelling of wave processes along given wave rays, can suffice at locations with sensibly straight parallel seabed contours, or where data are only required at a limited number of shoreline stations. For locations with complex bathymetry or where a large number of shoreline stations are to be examined, the modelling effort can be reduced by using a 2-dimensional model.

Figure 1 shows an example of a one-dimensional computation of a wave approaching the Caister (Great Yarmouth) shoreline (Ref. 1). In this case wave energy gain due to wind was included - note the gain in wave height on the landward side of the offshore banks.

Currents

Currents due to tidal forces can also be important in mobilising sediment though their significance is generally greater away from the shore. Inequalities in the net direction of the tide can result in an overall drift; residual currents, as they are called, can arise because of flow separation from a headland which affects flow in one direction but not the other. Seabed features can also give rise to residual currents. Existing data on currents should be examined in order to make an initial assessment of the significance of currents relative to wave effects. If they are found to be significant, then it may be necessary to carry out measurements using current meters.



Longshore Transport

Longshore transport is the name given to the movement of sediment along and parallel to the shore, by the action of waves and currents.

The CERC formula (Ref. 2) relates the rate of sediment transport to the component of wave energy flux parallel to the shore at breaking thus:

$$I_s = kP_s$$

where:

- I_s = immersed weight longshore transport rate
- P_s = longshore component of wave energy flux at breaking
- k = constant of proportionality

P_s is a function of the breaking wave height and celerity, and the angle that the wave crest makes to the shoreline, together with water density and gravity. Hence, in order to determine the net annual longshore transport rate it is necessary to know the annual distribution of wave heights, periods and directions of the shoreline.

Values of k for sand have been put forward varying between 0.1 and 2.0 (Ref. 3); a value of 0.39 is quoted in the Shore Protection Manual (Ref.2). A version of the formula applicable to shingle transport was developed by Scripps and Komar (Ref. 4). Shingle is, of course, much less mobile than sand and this reflects in a lower k value.

More recent work by Van Hijum and Pilarczyk (Ref. 5) introduces shingle size into the longshore shingle transport formulae. Grain size also affects sand transport and is important in distinguishing bed transport from suspended transport; as given, for example, by the formulations according to Bijker (Ref. 6)

Whereas the CERC formula gives the total transport (integrated over the shore cross-section) for a given breaking wave condition, numerical models using more recent formulations now enable the distribution of longshore transport over the shore cross-section to be computed, including the shear stress due to currents, and the influence of particle size.

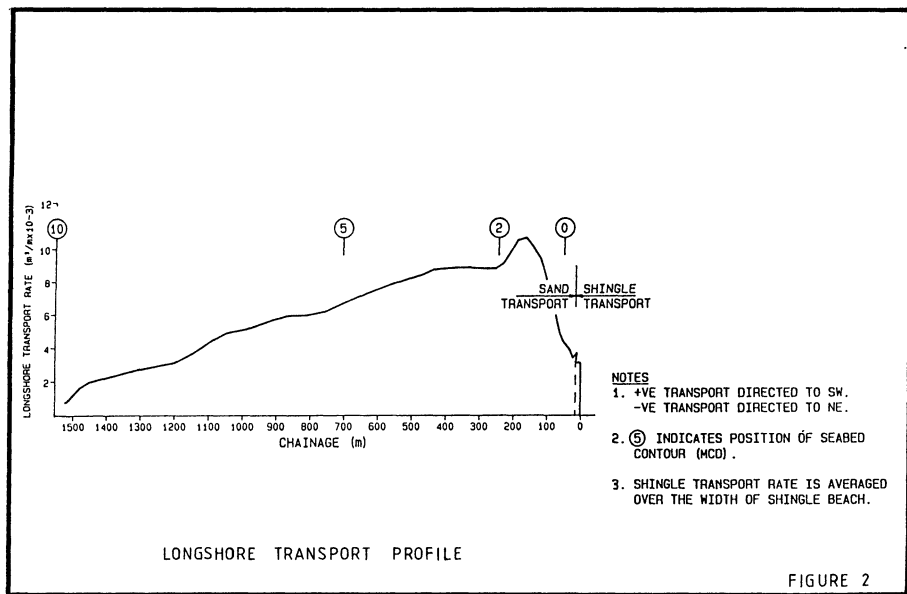


FIGURE 2

Figure 2 shows an example (Ref. 7) of a computed longshore transport distribution on a predominantly sandy foreshore with a shingle upper beach. In this particular case the effect of tide height variation of transport was taken into account by computing the transport at several tide levels.

Onshore-Offshore Transport

As its name suggests, onshore-offshore transport is the movement of sediment normal to the shoreline. This movement is closely related to the shore profile (cross-section) as changes to the profile are likely to be associated with sediment transport within it.

The analytical treatment of onshore-offshore transport is less developed than that of longshore transport. There are two complicating factors to consider, viz: (i) the process is time dependent; ie. given wave conditions will change the bed profile, which in turn modifies the nearshore wave field (note that the active shore profile extends several metres below the visible shoreline); (ii) non-linear wave effects, ie. asymmetry in the orbital bed velocities are important. There are few numerical models available to compute onshore-offshore transport of sand. Figure 3 shows the output of one model (Ref. 1) in which the profile development is calculated according to the sediment transport formulations of Baillard (Ref. 8).

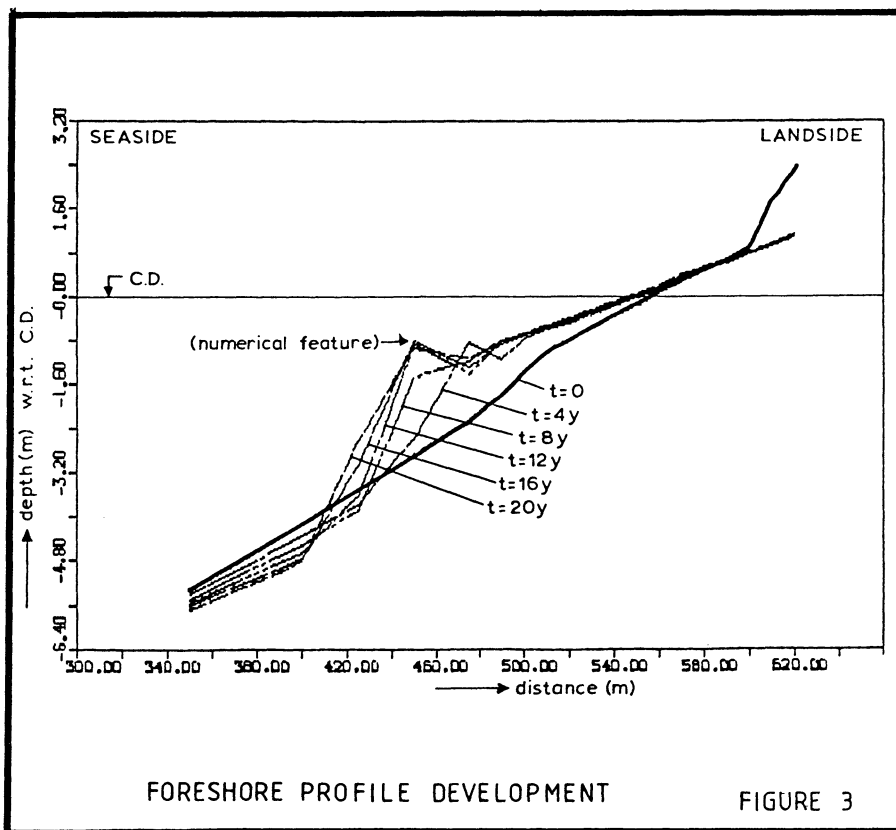


FIGURE 3

Numerical models of shingle transport are based on flume studies supported by field observation. Shingle beaches tend to respond quite rapidly to incident wave conditions. A common coastal defence problem is that there is an inadequate initial volume of shingle to form a new profile during a storm. The result is that the available shingle is forced back by the waves, overtopping the seawall behind. Once the shingle is removed then waves can reach the seawall and interact with it by way of reflection.

Some advances have been made in the mathematical representation of scour at seawalls but it remains a highly complex phenomenon depending on several inter-related processes. In many cases physical modelling will be necessary.

Sediment Balance and Shoreline Development

By summing the various input to and outputs from the shore, the likelihood of sediment erosion or accretion can be assessed.

Inputs included:

- longshore gain
- land erosion supplying sediment
- onshore transport

The outputs include:

- longshore loss
- offshore transport

The sediment balance calculated according to annual average conditions of waves and currents indicates whether the shore is, in the long term, eroding or accreting. However, consideration must also be given to storm events as these can have serious implications for coastal defences, including the following:

- abnormal loss of sediment due to longshore drift arising from prolonged weather from one direction
- offshore loss of fine sediment (sand)
- onshore migration of shingle on the upper beach possibly leading to breaching of the shingle ridge, or exposure of a seawall behind

Numerical models can be used to aid the assessment of shoreline evolution. The most common form of this is the "one-line" model, so called because it models the changing position of a single contour (usually the high water line).

Physical Models

In some situations, and particularly during the refinement of specific schemes, it may be desirable to build a physical model. Physical models can be advantageous over numerical models when the shoreline regime is highly complex, for example due to interaction between the environmental forces, the structure and the sediment.

Essentially, there are two kinds of physical model, viz: three dimensional models, used to examine the plan configurations of schemes - these can represent typically up to 1km of coastline; and two dimensional flume models, used to examine in greater detail (and at greater scale) the integrity and performance of the cross-section.

Physical models also have limitations though. The scaling of beach sediment so that it behaves "realistically" can be difficult and it is often problematic to simulate waves and tidal currents in the same model.

Supporting Studies

The previous sections deal with coastal processes and the various methods that are used to determine them. The methods, primarily entail the analytical treatment of data and the application of modelling techniques, in order to identify and quantify the action of waves and currents at the shore.

Major studies also require various other historic information to be examined in order to develop a comprehensive understanding of the shoreline. This can include the following supporting studies:

- review of historic maps, charts and aerial photographs
- records of man's intervention at the coast, ie. when things were built
- records of any offshore activities, eg. dredging
- analysis of past beach profiles, if these have been surveyed routinely

INTERPRETATION OF THE PROBLEM

From the examination of the coastal processes and the supporting information, the nature of the coastal problem is identified. The problem may be due to the shoreline processes or may for example be due to the presence of a hard structure (eg. seawall or breakwater). In the extreme case the problem may be directly attributable to man's activities such as sand extraction. The problem may be new (due to a change in circumstances), long term, or due to an isolated severe event. Only when the problem is understood can the right solution be formulated.

Types of Solution

This section briefly reviews the principal types of solution. The distinction is made between those solutions which are aimed at holding the beach, ie. shoreline protection measures; and those which are aimed at securing the hard line of defence, ie. the seawall. A further distinction is made between direct measures and indirect measures. Direct measures deal with the cause of the problem, eg. removing an obstruction to longshore drift. Indirect measures are aimed at mitigating the problem by some alternative means.

Shoreline Protection

The principal methods are as follows:

Groynes. Constructed normal to the shore in a variety of materials (timber, concrete, rock, steel), groynes trap a proportion of the sediment which is moved along the shore. In so doing, the orientation of the shoreline is changed and this has the effect of locally reducing the longshore transport rate. By trapping some of the sediment in transit, groynes tend to cause erosion on the downdrift side. In some situations this can be tolerated, or the groyne field can be extended to a place where downdrift erosion is not important, eg. at a natural intrusion such as an estuary.

Groynes can also be used to deflect currents away from the shore and to reduce the effects of longshore drift reversal.

Groynes are not effective in preventing offshore loss because, in this case, the sediment is literally drawn out from between the groynes.

Offshore Breakwaters. These are breakwaters built parallel to the shore (though angled groynes may be used to deliberately encourage a bias with respect to a particular wave direction) and constructed usually in rock, with rock or concrete armour. They work by reducing wave energy between the breakwater and the shore. This has the effect of reducing longshore transport and offshore transport. The beach tends to grow in the shadow of the breakwaters, usually at the expense (to some degree) of the exposed beach on either side. It is therefore usually necessary to consider offshore breakwaters in conjunction with beach recharge.

Beach Nourishment. Beach nourishment with sand or shingle may be required in conjunction with an offshore breakwater scheme as noted above, or with a groyne scheme, or in its own right. Shingle recharge can be used to provide a sufficient volume of beach to accommodate storm changes - commonly there is an insufficiency of existing material fronting hard defences. Similarly sand recharge can be used to effectively move the shoreline seawards and hence create a buffer to the hard defences (if such exists).

Seawall

In some cases the solution lies in the construction of, or modification to a seawall. The remedy must be a response to the specific problem. This may include for example; strengthening of an existing seawall or construction of a new one for structural reasons; improvements to the hydraulic performance; changes to the alignment (and hence reconstruction) of a seawall.

EXAMPLES OF COAST DEFENCE SCHEMES

The following three examples have been chosen to demonstrate how the coastal processes have interacted with other issues such as constructability, environment and economics.

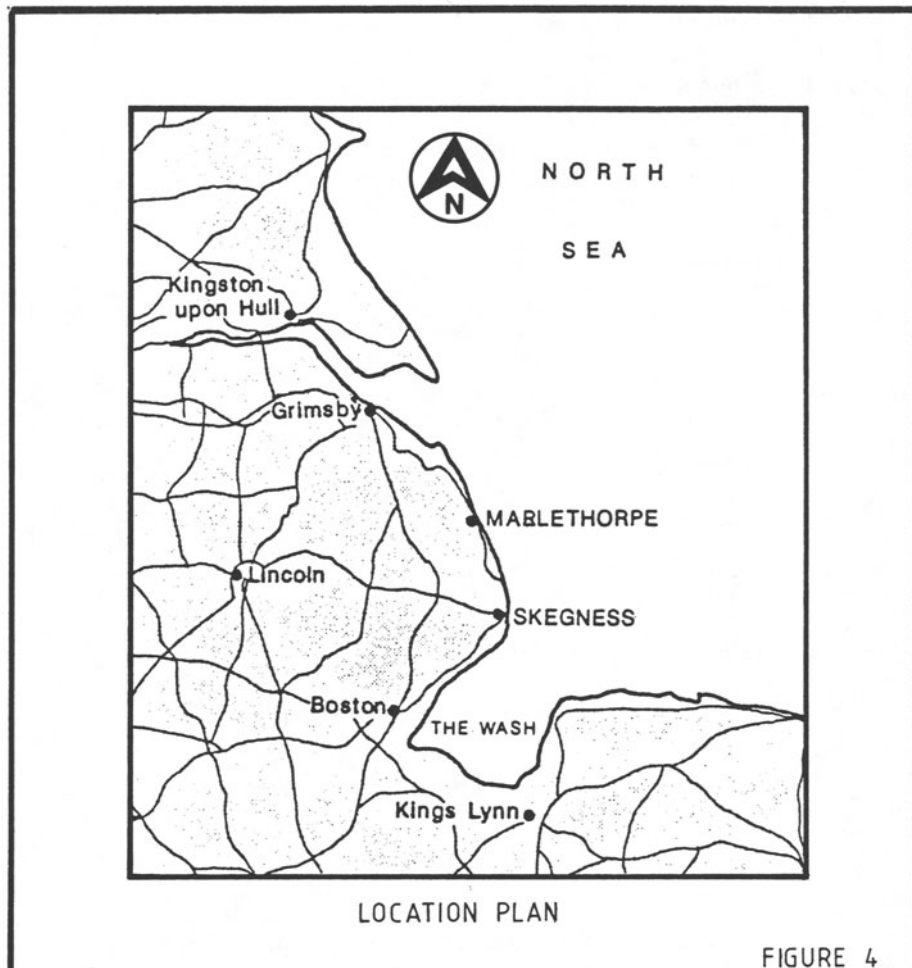
Lincolnshire Sea Defences

The National Rivers Authority (Anglian Region) are responsible for 24km of sea defences extending from Mablethorpe to Skegness (Figure 4) which defend an area of approximately 20,000 hectares of low lying land including some 15,500 residential properties. Together with agricultural, commercial and industrial interests the benefits of flood protection amount to around £700 million.

In 1953 the sea defences were breached resulting in extensive damage and the loss of 41 lives. The present defences originate largely from the rebuilding which followed and comprise seawalls and groynes (270 in total), but reconstruction and improvement of the sea defences has been a continuous process since 1953, and will continue for some years.

The NRA commissioned a major study to examine a strategic approach for the defence of the Mablethorpe to Skegness coast. Briefly the main findings of the study were:

- the majority of the beaches in the central area are narrow, steep and lack beach material.
- the potential drift of sand southwards along the coast is considerable
- there is a long term erosion of clay in some places which is likely to increase
- wave action at the defences will increase due to lowering of beaches and sea level rise
- many of the existing defences will need rebuilding within 10 years
- there is a high risk of many defences failing due to seawater and spray coming over the top of them.



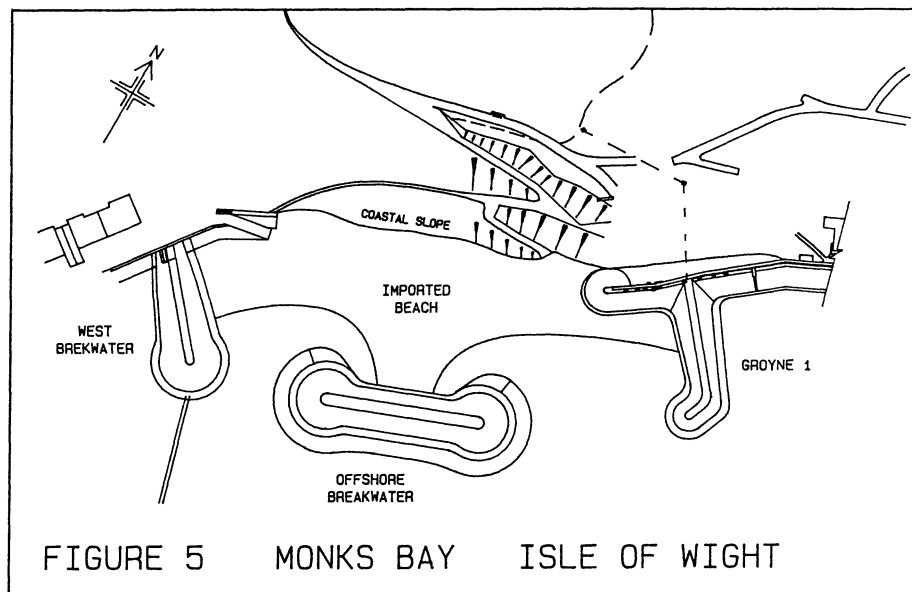
The erosion of the clay beneath the sand and the consequent long term lowering of the beach was a significant factor in determining the solution on the Lincolnshire coast. The new strategy was therefore directed at providing a healthier beach.

Having examined in detail the engineering, environmental and economic issues involved, beach nourishment using sand was selected as the most suitable solution. This will entail raising the level of the beaches by pumping sand ashore. The studies showed that there was no economic advantage in building beach control structures such as groynes.

Following extensive design studies it is now calculated that the scheme will involve some 26 million m³ of sand over a 50 years scheme life, of which 10 million m³ will be placed during the first 4 years. The total estimated scheme cost is £40M.

Monks Bay, Bonchurch, Isle of Wight

Monks Bay lies within the Ventnor Undercliff complex. One of the main influencing factors here was the almost total lack of natural beach feed. In this case the foreshore consisted mainly of soft erodible clay. A further factor was a requirement within the terms of reference to investigate the possibility of providing an amenity beach.



A system of concrete sea walls and groynes constructed in the latter half of the 19th Century had been collapsing progressively over the past 20 years and the cliff had receded since by some 15 metres from the position of the failed wall. The severe storms of winter 1989/90 caused further toe erosion and promoted a major slip in the cliff.

The absence of beach material and natural re-supply precluded the use of conventional groynes without a requirement for a large amount of beach material and the commitment to periodic recharge.

The main options considered were therefore:

- Concrete seawall
- Rock armoured revetment
- Offshore breakwater and beach nourishment

The concrete seawall would have had to be designed to accommodate the foreshore lowering which would have continued without any beach control. Such a scheme would not have provided an amenity beach. A rock armoured revetment would have largely avoided the problem of scour since wave energy would have been absorbed rather than reflected off the structure, although again without the benefit of a beach. A scheme with an offshore breakwater and beach nourishment was shown at initial study stage to be a potentially viable scheme, albeit at a slightly higher cost. However, an economic assessment was carried out which identified that there was sufficient additional benefit from the amenity aspect to justify in economic terms the slight additional costs of this option.

Since the natural supply of beach material to this frontage was very small, the scheme was designed to retain the imported material without significant loss.

In order to develop the offshore breakwater concept from the initial study stage, a 1:80 physical model was commissioned at HR Wallingford. The availability and grading of beach material from licensed dredging areas was investigated. A grading compatible with local sources was chosen and included with appropriate scale allowance in the model.

Wave conditions for the model were derived from data collected at the Owers Light Vessel over a 1 year period 1968/69 and compared with hindcast wave conditions analysed from wind data. Extreme water levels were determined for Ventnor based on extreme levels at Portsmouth derived by Blackman and Graff (Ref. 9). Extreme wave heights offshore were in excess of 6 metres but because of the water depth at the structure were limited to a significant wave height of a little over 2 metres at extreme water levels.

The layout was tested first with waves from the dominant S.S.W direction and further proved with waves from the S.S.E.. The final arrangement is shown in Figure 5.

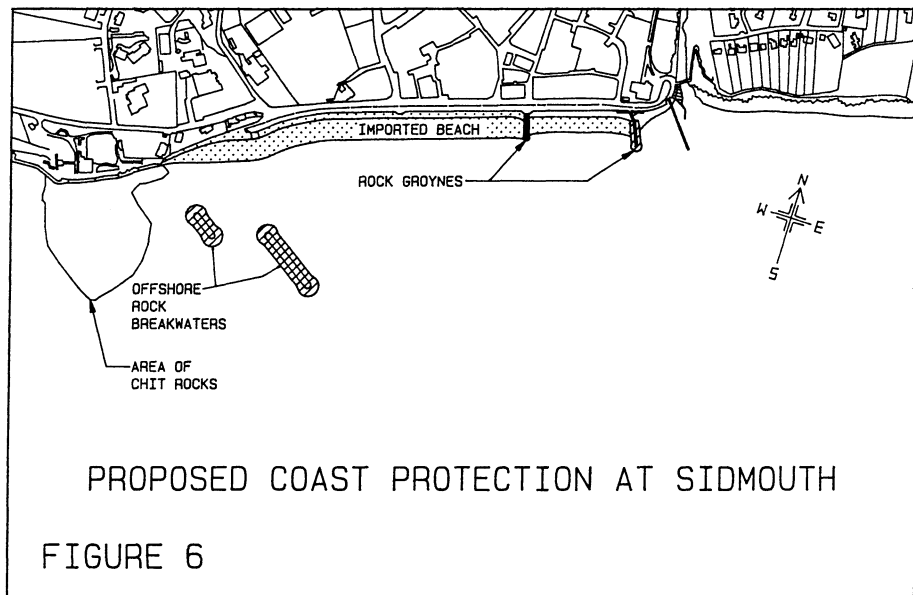
The offshore breakwater has a crest height of 0.74 metres above MHWS and is constructed with 5 to 7 tonne rocks. The model tests indicated the possibility of scour at either end of the breakwater; a rock scour platform has been included accordingly. The associated groynes also are constructed with 5 to 7 tonne rocks and the remaining 19th Century sea walls have been encased in concrete and haunched with rock.

The work was completed in November 1992 at an overall cost of approximately £1.1 million.

Sidmouth, Devon, UK

Sidmouth lies within the valley of the River Sid in Lyme Bay bounded on either side by cliffs in Keuper Marl and sandstone.

Until the early 19th Century the few properties in Sidmouth had been protected from the sea by a wide shingle bank. A very severe storm in 1824 resulted in major erosion of the Chit Rocks (Figure 6) which were providing protection to the town from the south west storms.



A seawall was constructed on the shingle ridge in the 1830's and with the progressive loss of shingle on the frontage the foundations were extended down to the marl bedrock in the 1920's by which time major breaches occurred.

Erosion of the cliffs on either side of the Sidmouth frontage has continued such that the seawall is now some 7 to 10 metres seaward of the adjacent coastline. The frontage has, therefore, become increasingly vulnerable with time, both in terms of the ability to retain beach material and wave attack on the wall.

The severe storms of winter 1989/90 resulted in substantial lowering of the beach and the wall foundations were exposed in places.

Research into the history of the frontage indicated that the beach had remained low for considerable periods in the past, evidence of which was provided also by the severe abrasion on the lower wall. It was clear that average conditions were unlikely to restore the beach naturally since analysis had indicated a slight west to east transport. It was considered therefore that the beach would only recover with a period of prolonged easterlies. Recovery would also be inhibited by wave reflections off the seawall. The solution therefore was to restore the beach to an adequate level and seek to retain it on the frontage.

The major factors affecting the choice of scheme were:

- the small net sediment transport to the east under average conditions
- large movements which could occur in a short space of time under extreme conditions
- the lack of natural supply to the frontage from the west where the remaining outcrops of the Chit Rocks had formed a barrier to the littoral drift.

If beach levels were to be raised and controlled then measures had to be taken either to reduce the wave energy impinging on the beach with offshore breakwaters, or to create a barrier (or barriers) to prevent the movement of the beach with a substantial groyne or possibly several such structures along the frontage.

Given the circumstances, a conventional timber groyne field was unlikely to assist in raising the beach levels. Once the beach had been lost to the east following westerly storms, the groynes would tend to hinder rather than assist in recovery.

A further important parameter was the visual impact of the structures from the Sidmouth Esplanade. Consideration was given therefore to siting a breakwater on the Chit Rocks although it was acknowledged that the protection provided would be limited.

Following the initial studies, a physical model was commissioned at HR Wallingford in order to investigate these options. Testing commenced with the least visually intrusive breakwater scheme located on the Chit Rocks. As anticipated this did not provide adequate protection although it gave an indication of how such a concept might be included within the scheme. A system of shore parallel offshore breakwaters was found to be technically satisfactory although it was recognised that the visual intrusion was such that it was unlikely to be environmentally acceptable.

The final arrangement which was developed is shown in Figure 6 and comprises 2 offshore breakwaters to the west of the frontage and 2 groynes to the east together with some 100,000 cubic metres of imported beach sediment. The offshore breakwaters provide protection from the most damaging S.S.W storms although sufficiently offset from the main Sidmouth frontage such that the visual intrusion is minimised. The Groynes provide a barrier to shingle movement beyond the shadow of the breakwater

and also help control movement westwards during easterly storms.

It is anticipated that construction of this scheme will commence in the late Summer/Autumn of 1993.

REFERENCES

1. Delft Hydraulics, December 1989, "Caister Seawall, Recommendations for Protection, Report on Coastal Morphology Study", H919
2. U.S. Army Corps of Engineers, Coastal Engineering Research Center, 1984, "Shore Protection Manual"
3. Thomas R.S. and Hall B., 1992 "Seawall Design", CIRIA Publication, Butterworth Heinemann
4. Hydraulics Research Station, 1973, "Review of Shingle Sea Defences", publication DE7
5. CIRIA/CUR, 1991 "Manual on the Use of Rock in Coastal and Shoreline Engineering", CIRIA special publication 83/CUR Report 154. Bell and Bain Ltd.
6. Bijker, E.W, 1967, "Some considerations about scales for coastal models with moveable beds", Doctorate dissertation, Delft Univ. of Technology, also appeared as Publ. No. 50 Delft Hydraulics, The Netherlands
7. Posford Duvivier, 1992, "Preston Beach Road - Weymouth, Defence Strategy Stage 2, Final Report to NRA/Weymouth and Portland Borough Council/Dorset County Council
8. Bailard, J.A., 1981, "An energetics total load sediment transport model for a plane sloping beach", Journal of Geophysical Research, Vol. 86. No. C11, November 1981
9. Graff, J., 1981, "An investigation of the frequency distributions of Annual sea level Maxima at Ports around Great Britain", Estuarine, Coastal and Shelf Science 12.

FULL FIELD STUDY OF POST BREAKING VORTICITY

S. Lloyd, C. Created and W. Easson
Fluid Dynamics Unit
University of Edinburgh, JCMB
Mayfield Road, Edinburgh, EH9 3JZ
UK

The use of PIV to analyse post breaking flow fields is presented. A method to resolve the problems of directional ambiguity and very small or zero velocities is discussed. An instantaneous record of a post breaking vortex has been obtained. From this record a vorticity map has been calculated along with the map of the streamlines in the flow. The calculation of energy in the flow field is discussed.

1 INTRODUCTION

Knowledge of the post breaking process is limited, however it is clear that large amounts of energy are dissipated when a wave breaks. Instrumental in this process of dissipation are vortices, visible in the water after the passage of a breaking wave. An understanding of the movement and spread of these vortices will help us to determine more accurately how the wave energy is dissipated. Similarly such an understanding will help us to predict the spread and mixing of pollutants released into the sea and assist with the problems of containment. It is also possible that energy, in the form of a vortex may be swept up into an oncoming wave following a breaking wave and so may contribute to a changed set of conditions for that wave perhaps forcing it to break prematurely and thus altering the forces that it may exert [1].

As Basco [1] pointed out only a few papers have been written on this subject. More often than not papers jumped straight to the turbulence following breaking without recognising the existence of an organised intermediary state - that of the vortex. Sawaragi and Iwata [14] noticed in their experiments that a vortex motion descended towards the bed. The early work carried out by Miller [9] in 1976 showed that a vortex was formed by the breaking wave which could be seen if the entrained bubbles were observed. Further vortices were also formed, up to five in total, by the splash-up from the plunging jet entering the water. Miller traced the motion of the vortices and noted that they traveled slower than the wave velocity and drifted downwards whilst expanding. He also observed that there was a graduation in vortex magnitude from spilling through to steeply plunging breakers.

Sawaragi and Iwata [14] in 1974, estimated that the energy in the vortex motion contained between 15% and 30% of the energy dissipated in breaking. In 1982 Nadaoka and Kondoh [11] also observed, from the entrainment of air bubbles, that there were definite 'large scale eddies' associated with breaking waves. In 1985 Hattori and Aono [5] noted that long lived vortex-like motion is formed under both spilling and plunging breakers and that the strength of this motion appears to be related to the breaker type. Also the size of the vortex motion was related to the breaking height. They confirmed these observations using a flow visualisation technique.

Papers by Okayasu, Shibayama and Mimura [12], and Mizuguchi [10] are less qualitative and studied the plunging vortex in the surf zone using two-component LDA and hot film velocimetry. Both papers contain results for vorticity under a breaking wave but were both done on sloping beaches where the motion is restricted in its depth and is relatively short lived.

Using Particle Image Velocimetry (PIV) it is possible to gain a clearer picture of the vortex that occurs after a wave breaks in deep water. The velocity field generated by the processing of a PIV photograph can be used to determine the vorticity present in the frame, the energy in the frame, the streamlines across the frame and to link the size of the vortex to a length scale.

2 WAVE GENERATION

2.1 Experimental apparatus

The experiments were performed in the 9.75m wave flume at Edinburgh University. The flume is 0.4m wide and has walls and base of 25mm thick glass to enable optical access to the P.I.V. measurement region. The laser illumination system is mounted on rails beneath the tank and allows measurements to be made anywhere in the two 3.25m sections furthest from the wavemaker. This is shown in figure 2. The wavemaker is a hinged paddle device containing a force feedback monitor which is controlled by a microcomputer enabling waves to be generated and reflections to be absorbed simultaneously [13]. The microcomputer also samples two resistance type wave gauges and triggers the camera when necessary. At the opposite end to the wavemaker the waves are absorbed by a wedge type vertical beach made of expanded plastic.

2.2 Wave type

The wave used in the experiment was of the deep water plunging breaker type. This wave was generated by decomposing a desired wave at a chosen location into linear components which, when superimposed, form the wave. The components are then worked back to the wavemaker to establish the emission time to achieve the correct phase at the breaking point. The microcomputer calculates the superimposed waves and varies the voltage to the wavemaker accordingly. The frequencies chosen are all

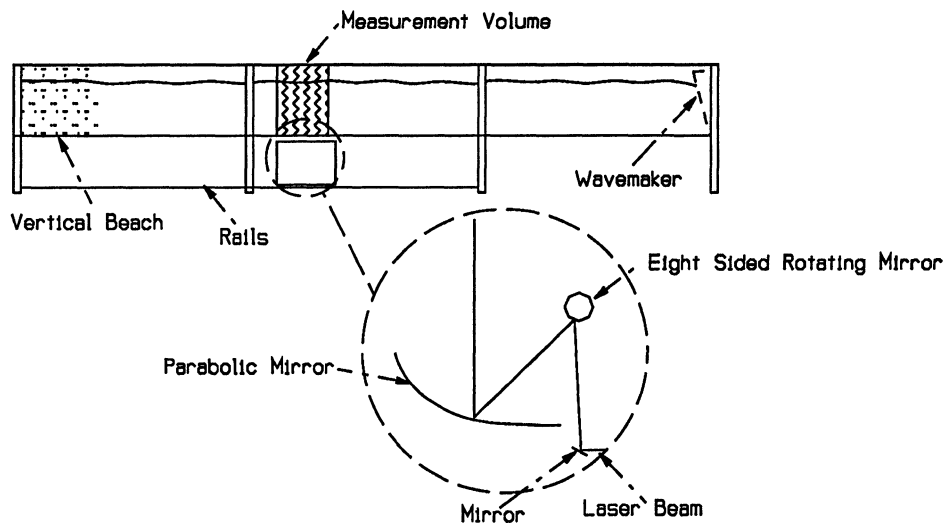


Figure 2: The wave tank and associated optics

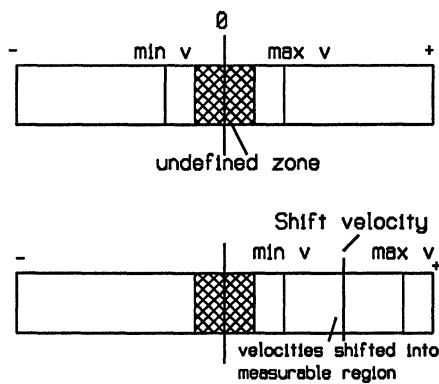


Figure 3: The theory of image shifting

of size $n/25.6$, where n is an integer, and the whole wave packet cycles every 25.6 seconds. This is designed to enable fast fourier transforms of wave gauge records to be easily performed because each frequency has an integer number of cycles in the standard sampling time.

3 FLOW MAPPING TECHNIQUES

3.1 Particle Image Velocimetry

Particle Image Velocimetry (PIV) is a non-intrusive technique involving the multiple exposure of particles in a flow. A photograph is taken of the particles in a plane parallel to the tank walls. The photograph is developed and the separation of the images of the particles can be determined. From this a flow field for that instant can be generated. The particles used are conifer pollen which have neutral buoyancy and are small enough to follow local flow variations.

The particles are illuminated by a scanning beam system [4] which uses a 15W continuous wave Argon Ion laser. The camera shutter is held open long enough for the particles to be illuminated two or more times by the laser beam with the scanning time being chosen to suit the speed of the particles being photographed. The photograph is then analysed by the Young's fringe method [6] which generates a velocity vector field.

3.2 Image shifting

PIV suffers from 180 degree directional ambiguity. This is because the images of the particles are identical in either direction - all that is seen by the system is a set of evenly spaced particles. Also, due to the nature of the flow, velocities at and around zero need to be analysed. This presents a further problem because very closely spaced particles give fringes with very large separations which cannot be analysed.

To overcome this, Edinburgh University has developed an image shifting system. This adds an artificial velocity to the whole velocity field and thus makes all the velocities in that field of the same direction. This is done at the first stage of PIV when the photograph is taken, in this case by rotating the camera on a turntable. This imparts a known velocity or image shift to all the particles, static water will appear to be moving at a constant velocity. Water with a velocity either side of zero will appear to have velocities slightly more or less than the shift velocity but all in the same direction (See figure 3). When the photographic negative is analysed the particles appear to be moving at velocities around the shift velocity. The shift velocity can then be removed from all the particles by simple subtraction and the true velocities are left with no directional ambiguity [2].

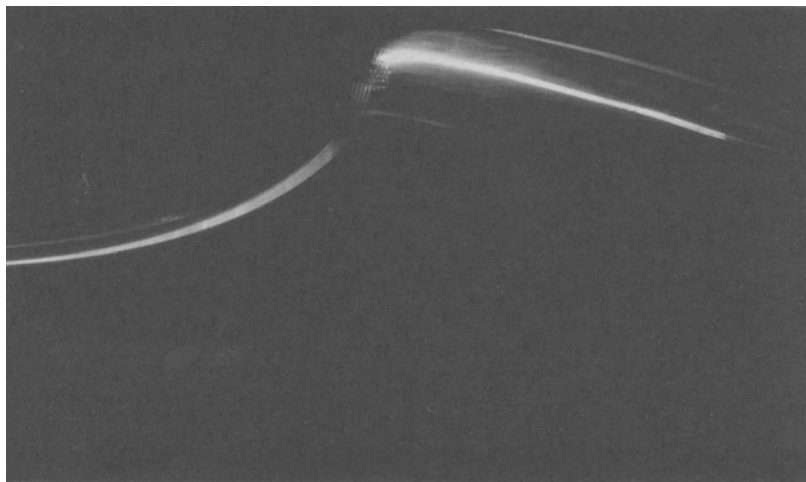


Figure 4: The experimental wave just prior to breaking

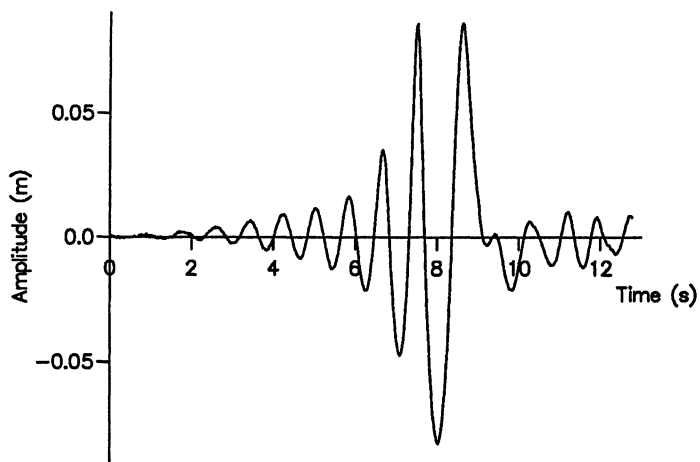


Figure 5: Amplitude record ahead of the breaking point

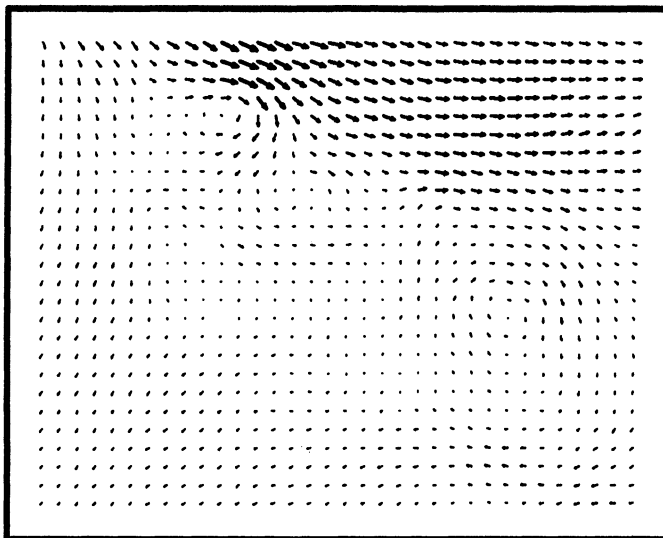


Figure 6: Vector field for a post breaking vortex

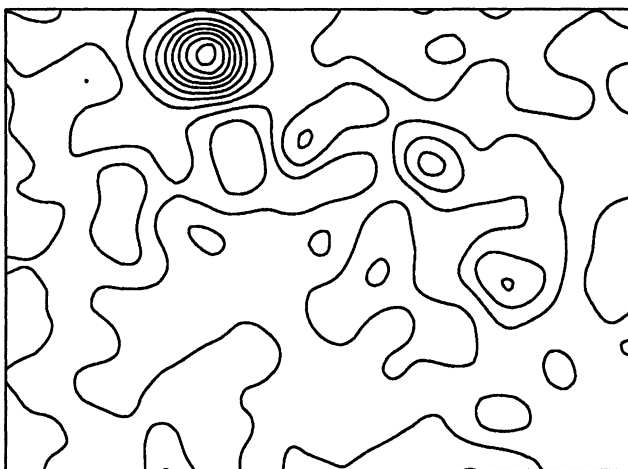


Figure 7: Vorticity map generated from the vector field

4 RESULTS

4.1 Wave height and energy

Figure 4 shows the wave used for this experiment just prior to breaking. From this the wave height can be measured, compared to the still water level, and an estimate for the energy in the wave can also be made. This can be done by calculating the potential energy and the kinetic energy for the wave. The potential energy is calculated by comparing the amount of water above and below the still water level. The kinetic energy is calculated for each vector in the field between the still water crossing points with each vector considered to be a packet of water with dimensions the same as the grid size.

The energy for the wave was also calculated from the wave gauge records. See figure 5 for a typical record. These are numerically transformed using a fast fourier transform routine to yield the amplitude of each frequency used to create the breaking wave. The energy for each frequency is then calculated and the total is considered to be in the breaking wave. A record was also taken of the waves that passed the breaking point, before and after breaking, on the assumption that these were not contributing to the energy of the breaking wave. The energy remaining in the tank due to wave motion was calculated and this was used to modify the energy figure for the breaking wave.

4.2 PIV vector field and vorticity

Figure 6 shows the velocity vector field for a wave shortly after breaking. Three vortices can clearly be seen. Figure 7 shows a vorticity contour map generated from the velocity vector field. The vorticity is calculated from the equation:

$$\omega = \frac{\partial u_2}{\partial x_1} - \frac{\partial u_1}{\partial x_2} \quad (1)$$

This is done by looking at the grid of vectors where each node has two components of velocity as in the figure 1.

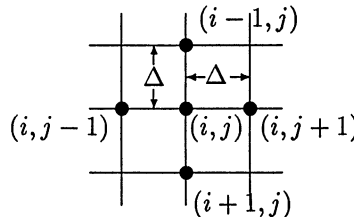


Figure 1: Velocity Grid

The vorticity at each node is then computed by using the difference formula:

$$\omega = \frac{1}{2\Delta}(u_2(i, j+1) + u_1(i+1, j) - u_2(i, j-1) - u_1(i-1, j)) \quad (2)$$

4.3 Energy of vector field

The energy in the vector field after breaking is calculated assuming that the water surface has settled to the still water level and thus the potential energy is zero. Each vector is considered to be a packet of water around its location with dimensions the same as the grid size. This square of water is considered to move with the same direction and velocity as the vector. The kinetic energy for each packet is then calculated. Additionally the rotational energy of the packet is calculated by considering the velocities of the surrounding packets of water and thus the rotation that these impart to the packet. The linear and rotational kinetic energies are then added together to give the total energy.

4.4 Streamlines

The streamlines for the velocity field are shown in figure 8. The local velocity vectors are everywhere tangential to the streamlines, where the stream function ψ is related to the velocities in the flow by the equation:

$$\psi = \int u_1 dx_2 - \int u_2 dx_1 \quad (3)$$

A constant ψ value was assumed at the base of the flow and then the stream function at each point was found by integrating the velocity components across the grid from this streamline.

Using the integration approach, cumulative errors are introduced. Various techniques for reducing these have been considered. One of these is to utilise the Poisson relationship:

$$\nabla^2 \psi = -\omega \quad (4)$$

This can be solved iteratively with the known ω values at the internal grid points and the computed values of ψ on the boundaries.

5 DISCUSSION

It can be seen that the image shifting technique shows the structure and position of the vortices caused by the breaking wave. From the resulting instantaneous vector field plot the vorticity can be derived and the streamlines in the flow plotted. This ability to plot the instantaneous flow field is the main advantage of this technique over previous work using LDA. The system does however introduce extra errors when compared to standard PIV results without image shifting. The error for the

PIV without frequency shift measurements is in the region of 1%-2% relative to the maximum measured velocity [3] [7]. At present the system used has to shift at a minimum of 1m/s to maintain stability and if the flow fluctuations are small then the analysis errors, once the shifting velocities have been removed, can become quite large.

A method to determine the Taylor microscale for the flow is being derived although the fact that the flow does not have a constant mean velocity causes a problem in the calculation. However experiments using PIV to measure the turbulent fluctuations in a flow downstream from a grid have shown PIV to be accurate in determining Taylor microscales in the order of a few millimetres. This was comparable to the result obtained from LDA equipment [8]

6 ACKNOWLEDGMENTS

This work was undertaken as part of the MAST G6 Coastal Morphodynamics research programme. It was funded jointly by the Science and Engineering Research Council, and by the Commission of the European Communities Directorate General for Science, Research and Development under contract N°. MAST 0035C.

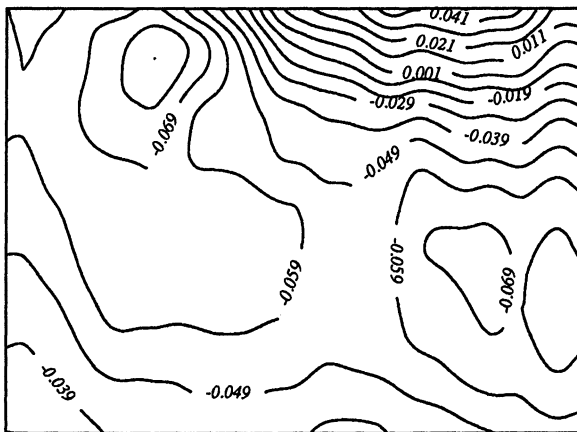


Figure 8: Streamlines calculated from the vector plot

References

- [1] D.R. Basco. A qualitative description of wave breaking. *Journal of Waterway, Port, Coastal & Ocean Engineering Division*, 1985.
- [2] C. Elgaard. Report on methods to resolve directional ambiguity in piv measurements. Internal department document, Dec 1990.
- [3] C. Gray. *The Development of PIV for Water Wave Studies*. PhD thesis, Edinburgh University, 1989.
- [4] C. Gray, C.A. Greated, D.R. McCluskey, and W.J. Easson. An analysis of the scanning beam piv illumination system. *Journal of Phys. Measurement Science and Technology* 2, pages 717–24, 1991.
- [5] M. Hattori and T. Aono. Experimental study on turbulence structure under breaking waves. *Coastal Engineering in Japan*, 28:97–116, 1985.
- [6] J.M. Huntley. An image processing system for the analysis of speckle photographs. *Journal of Physics E: Scientific Instrumentation*, (19):43–49, 1986.
- [7] R.D. Keane and R.D. Adrian. Optimisation of particle image velocimeters. part i: Double pulsed systems. *Journal of Measurement Science and Technology*, 1, pages 1202–15, 1990.
- [8] D.R. McCluskey, C. Elgaard, W.J. Easson, and C.A. Greated. The application of piv to two-phase flows. *Applied Scientific Research*, To be published. Special Publication.
- [9] R.L. Miller. The role of vortices in surf zone prediction : Sedimentation and wave forces. *The Society of Economic Paleontologists and Mineralogists*, (24):48–53, 1976. Special Publication.
- [10] M. Mizuguchi. Experimental study on kinematics and dynamics of wave breaking. *Proceedings 20th Coastal Engineering Conference*, pages 589–603, 1987.
- [11] T. Nadaoka and T. Kondoh. Laboratory measurements of velocity field structure in the surf zone by ldv. *Coastal Engineering in Japan*, 25:125–45, 1982.
- [12] A. Okayasu, T. Shibayama, and N. Mimura. Velocity field under plunging waves. *Coastal Engineering*, (50):660–74, 1986.
- [13] S.H. Salter. Absorbing wavemakers and wide tanks. *Proc. Conf. Directional Wave Spectra Applications (A.S.C.E)*, pages 185–200, 1982.
- [14] T. Sawaragi and K. Iwata. Turbulence effect on wave deformation after breaking. *Coastal Engineering Japan*, 17:39–49, 1974.

MULTIGRID MODEL OF WAVE-CURRENT INTERACTION

B. Li and Dr C.A. Fleming
Sir William Halcrow & Partners Ltd
Burderop Park, Swindon, Wiltshire, SN4 0QD
U.K.

ABSTRACT The multigrid technique is used to solve a variant of the mild-slope equation which takes into account wave-current interaction. The different versions of wave-current interaction equations are first compared with each other and then the governing equation is recast into a form suitable for treatment by the multigrid technique. Experimental data are used to test the model. Results from the present model as well as from a hyperbolic solution of the same governing equation are presented for the case examined by Liu (1983).

INTRODUCTION

The mild-slope equation (Berkhoff, 1972) is valid over the complete range of water depths for pure wave problem subject to slope limitations. This means that the effects of bottom inhomogeneities are included in the equation. The effect of a current is neglected. In practical coastal engineering problems significant tidal currents can occur near a river inlet or a harbour entrance. When currents and waves are in the same direction, this results in the lengthening of waves and reduction of wave heights. However, waves are shortened and steepened by opposing currents, often to the extent of inducing breaking. Therefore, a valuable contribution would be to add terms to the mild slope equation representing the effect of a current.

For the purpose of computing practical cases, where slow variations of depth and current can be both taken into account, Booij (1981) has generalized the original mild slope equation (Berkhoff, 1972) using Lagrangian theory. As he pointed out, the derivation is only valid for current fields with zero rotation. However, in practical applications these conditions rarely occur and rotational current fields should be considered. Booij also compared his wave-current equation with the wave-action equation which is defined as the basic equation of pure wave refraction. By neglecting higher order terms, his equation can be split into two equations corresponding to real part and imaginary part. The imaginary part is the same as the wave-action equation. In order to apply his equation to large area, he derived a parabolic equation from the original wave-current interaction equation.

Liu (1983) derived a similar equation to Booij's model for wave-current interaction. A parabolic method was then used to solve the equation. To demonstrate the application of the parabolic approximation to wave-current interactions, numerical calculations were performed for a problem that was originally studied by Arthur (1950). The case is that of a current system existing on a uniform beach with a slope of 1/50.

Kirby (1984) presented a careful study to wave-current interactions. He derived a new equation by using the Lagrangian formulation which was also used before by Booij (1981). His investigation demonstrated that Booij's equation, after neglecting the second order terms, represents the correct mild-slope equation for linear wave-current interaction motion, although the dynamic free surface boundary condition which Booij applied to derive the equation was incorrect. Due to limitations in the procedure used to derive the equation, Liu's model is not a complete version as also pointed out by Kirby. All three models, Booij's, Liu's and Kirby's, were compared by Kirby with the equation of conservation of wave-action. Both Kirby's and Booij's equation can be reduced to this equation, but Liu's cannot.

The difficulty of application of a wave-current model to the practical situation is the same as that of solving the pure wave mild-slope equation. The parabolic approximation had to be adopted by Booij and Liu to obtain the numerical solutions to reduce computational effort. The multigrid technique provides same significant advantages over these methods.

The multigrid technique is used to solve a variant of the mild-slope equation which takes into account wave-current interaction. Here we adopt Kirby's (1984) governing equation, using a solution scheme that imposes no restrictions on the angle of wave propagation. The governing equation is first recast into a form suitable for treatment by the multigrid technique. Modifications to the basic solution procedure are also necessary in order to deal with the non-linearity of the governing equation. Results from the present model as well as from a hyperbolic solution of the same governing equation (Dong, 1988) are presented for the case examined by Liu (1983). The comparisons show that the present scheme is as at least as accurate as Liu's model, but without the angular restrictions of that scheme, while it is much more efficient computationally than the hyperbolic solver. The case presented by Author is used to test the model and results are compared against those obtained by Liu (1983)

GOVERNING EQUATION

The different versions of the wave-current interaction equations are first compared with each other. Booij (1981), Liu (1983) and Kirby (1984), all produced parabolic models from the elliptic form of wave-current interaction equations. No matter what orders they used, the limitation of the incident wave angle applies to these models. This is because the reductions from the elliptic form to the parabolic form are based on the same principles used for the pure wave problems. Therefore the same angle restrictions will apply for these parabolic versions of wave-current interaction. However, in this section we only concentrate on the elliptical model of wave-current interaction.

Firstly, the available mild-slope equation based models which take into account wave-current interaction are presented. We then proceed with choosing the most suitable for the purposes of this work, and finally transform the adopted model so that it can readily be solved by the multigrid technique.

As previously mentioned, there are currently three models available:

i) Booij's model (1981)

$$\frac{D^2\Phi}{Dt^2} + (\nabla \cdot U) \frac{D\Phi}{Dt} + \left(\frac{D}{Dt} (\nabla \cdot U) \right) \Phi - \nabla \cdot (cc_g \nabla \Phi) + (\sigma^2 - k^2 cc_g) \Phi = 0 \quad (1)$$

ii) Liu's model (1983)

$$\frac{D^2\Phi}{Dt^2} + \nabla \cdot (cc_g \nabla \Phi) + (\sigma^2 - k^2 cc_g) \Phi = 0 \quad (2)$$

iii) Kirby's model (1984)

$$\frac{D^2\Phi}{Dt^2} + (\nabla \cdot U) \frac{D\Phi}{Dt} - \nabla \cdot (cc_g \nabla \Phi) + (\sigma^2 - k^2 cc_g) \Phi = 0 \quad (3)$$

where

$$\sigma^2 = gk \tanh(kh), \quad k = |\bar{k}|,$$

$$\omega = \sigma + \bar{k} \cdot U, \quad U \text{ is the current vector,}$$

$$c = \sigma/k, \quad c_g = \frac{\partial \sigma}{\partial k}, \quad \text{and} \quad \frac{D}{Dt} = \left(\frac{\partial}{\partial t} + U \cdot \nabla \right).$$

Kirby (1984) pointed out that his equation differs slightly from Booij's (1981) due to errors in Booij's derivation, and also differs in a crucial manner from Liu's (1983) due to limitations in the procedure used by Liu to derive the governing equation.

If we consider periodic monochromatic waves of frequency ω , we can write

$$\Phi = \varphi e^{-i\omega t}$$

and equations (1), (2) and (3) become equations (4), (5) and (6), respectively, as shown below

$$\nabla \cdot (cc_g \nabla \varphi) + 2i\omega U \cdot \nabla \varphi - (U \cdot \nabla) \nabla \cdot (U \varphi) + (k^2 cc_g - \sigma^2 + \omega^2 + i\omega \nabla \cdot U) \varphi = 0 \quad (4)$$

$$\nabla \cdot (cc_g \nabla \varphi) + 2i\omega U \cdot \nabla \varphi - U \cdot \nabla (U \cdot \nabla \varphi) + (k^2 cc_g - \sigma^2 + \omega^2) \varphi = 0 \quad (5)$$

$$\nabla \cdot (cc_g \nabla \varphi) + 2i\omega U \cdot \nabla \varphi - U \cdot \nabla (U \cdot \nabla \varphi) - (\nabla \cdot U) (U \cdot \nabla \varphi) + (k^2 cc_g - \sigma^2 + \omega^2 + i\omega \nabla \cdot U) \varphi = 0 \quad (6)$$

Considering realistic cases where the current speed is smaller than the phase velocity and the group velocity of the waves, viz

$$\alpha \left(\frac{cc_g}{|U|^2} \right) \gg 1$$

then equation (6) can be simplified as

$$\nabla \cdot (cc_g \nabla \varphi) + 2i\omega U \cdot \nabla \varphi + (k^2 cc_g - \sigma^2 + \omega^2 + i\omega \nabla \cdot U) \varphi = 0 \quad (7)$$

It should be noted that equation (4) can be reduced to equation (7) but equation (5) cannot. In this paper equation (7) is adopted as the governing equation owing to the rigorous nature of its derivation.

Set

$$\varphi' = \varphi (cc_g)^{\frac{1}{2}}$$

then equation (7) can be rewritten as

$$\frac{\nabla^2 \varphi' + 2i\omega U \cdot \nabla \varphi'}{cc_g} + (k_c^2 + d) \varphi' = 0 \quad (8)$$

where

$$d = \frac{1}{cc_g} (-\sigma^2 - \omega^2 + 3i\omega \nabla \cdot U - \frac{2i\omega}{(cc_g)^{\frac{1}{2}}} \nabla \cdot [U(cc_g)^{\frac{1}{2}}])$$

and

$$k_c^2 = k^2 - \frac{\nabla^2 (cc_g)^{\frac{1}{2}}}{(cc_g)^{\frac{1}{2}}}$$

By taking into account identity

$$\frac{1}{\varphi'} \nabla^2 \varphi' = \nabla^2 (\ln \varphi') + (\nabla \ln \varphi')^2$$

equation (8) can be written as

$$\nabla^2 \Psi + (\nabla \Psi + \frac{2i\omega}{cc_g} U) \cdot \nabla \Psi + (k_c^2 + d) \Psi = 0 \quad (9)$$

where

$$\phi' = \theta^{\Psi}$$

Equation (9) is now in a form suitable for treatment by the multigrid technique. Results from numerical tests carried out by the authors using both the multigrid wave-current interaction model based on equation (9) and Liu's model based on equation (5) will be presented in later sections.

APPLICATION OF MULTIGRID TECHNIQUE TO THE MODEL

The multigrid method has attracted a lot of attention since publication of the original paper by Brandt (1977). It has been applied to a large range of problems, but it is especially suited to equations of the elliptic type. Brandt (1980) applied the multigrid method to the so called Singular Perturbation Difference Equations which have the form

$$\epsilon \nabla^2 U + aU_x + bU_y = F \quad (10)$$

where ϵ , a , b and F are known coefficients (real or complex, depending on the problem) and U , U_x , U_y are the unknown and its derivatives in the x and y directions, respectively. From previous section it has been shown that the model of wave-current interaction has a similar form as equation (10), except that the coefficients a and b are functions of the unknown. This leads to a non-linear equation but the multigrid method can still be applied to it.

With regard to the application of the technique, suppose there is a set of uniform square grids,

$$G^0, G^1, \dots, G^m$$

all approximating the same domain Ω with corresponding mesh sizes

$$h_0 > h_1 > \dots > h_k > h_{k+1}$$

and for simplicity set

$$h_{k+1} : h_k = 1 : 2$$

For a general boundary-value differential equation of the form

$$LU(x)=F(x) \quad \text{for } x \in \Omega, \quad \Lambda U(x)=P(x) \quad \text{for } x \text{ on boundary } \partial\Omega$$

we use standard finite difference approximations to the derivatives on each grid G^k , viz.

$$L^k U^k(x)=F^k(x) \quad \text{for } x \in G^k, \quad \Lambda^k U^k=P^k(x) \quad \text{for } x \in \partial\Omega^k$$

Although we are only interested in solving this discrete problem on the finest grid, G^m , we can exploit the fact that the discrete problem on the coarser grid, G^k , approximates the same differential equation and hence can be used as a certain approximation to the problem (and solution) as defined at the G^m level.

Let u^m be an approximate solution at the grid level G^m and also let

$$L^m u^m = F^m - f^m, \quad \Lambda^m u^m = P^m - p^m$$

where f^m and p^m represent the residual functions. By further assuming L and Λ to be linear, the exact discrete solution is $U^m = u^m + V^m$, where the correction V^m satisfies the residual equations

$$L^m V^m = f^m, \quad \Lambda^m V^m = p^m$$

Using the approximate solution of the residual equations on a coarser grid

$$L^k V^k = f^k, \quad \Lambda^k V^k = p^k$$

where f^k and p^k are the residuals left by V^{k+1} , it can be shown that the residual of the original equation at the $+m$ th grid level may be smoothed out more quickly by using residuals corresponding to coarser grids. Thus

$$f^k = I_{k+1}^k (f^{k+1} - L^{k+1} V^{k+1}), \quad p^k = I_{k+1}^k (p^{k+1} - \Lambda^{k+1} V^{k+1})$$

where I_{k+1}^k represents interpolation from the G^{k+1} to the G^k level; this operation is termed transfer of residuals. For more details on the multigrid technique the reader is encouraged to study the original reference by Brandt (1977) which is an excellent exposition of the subject.

An effective way for solving the residual equations is by the usual relaxation procedures, the Gauss-Seidel relaxation method being an obvious candidate. If the governing equation produces a positive definite square matrix, then the relaxation method can be used successfully. If, however, this matrix is not of the positive definite type, the problem may still be solved directly at the coarsest grid level using Gauss elimination. This approach is very economical in terms of computer resources and makes the application of the multigrid method to the solution of equations (9) very attractive.

When wave-current interaction is taken into account the "constants" a and b are given by the following expressions

$$a = h_k^2 [(\Psi_{i+1,j}^{n-1} - \Psi_{i-1,j}^{n-1}) / (2h_m) + \frac{2i\omega}{cc_g} U_x]$$

$$b = h_k^2 [(\Psi_{i,j+1}^{n-1} - \Psi_{i,j-1}^{n-1}) / (2h_m) + \frac{2i\omega}{cc_g} U_y]$$

With the constants a and b so defined, the numerical solution of equation (9) proceeds along exactly similar lines as the solution procedure for equation (10). It should be noted that when solving equation (9), the parameter k should be determined in advance, which is equivalent to specifying that the direction of wave propagation should be known a priori.

If for an engineering application no information of this kind is available, one could estimate the coefficient in equation (9) by using the expression for k that is valid for zero mean velocity. This approach, which is adopted for the purposes of this work, has also been used by Booij (1981) who analysed the resulting error, concluding that the above assumption is acceptable, the error being of order $O(U/c)$.

An alternative approach involves applying an iterative procedure, whereby the coefficient in the dispersion equation is initially estimated as for the non-current case, a solution is obtained, the coefficient is then adjusted using directional information from the solution, and the process repeated until convergence is achieved. This technique has been tested and it has been found that it does not produce appreciably different results from those obtained using the approach described in the previous paragraph. Taking also into account the fact that it incurs a heavy computational penalty in terms of run times required, it is clear the first approach is more attractive.

MODEL TEST

As a first case, the flume experiments carried out by Brevik and Aas (1980), Brevik and Luftkrigsskolen (1980) are used to test the model. The aim of their experiments were to test the theoretically predicted wave deformation when waves on still water propagate into a current, either following or opposing, fed from below. First experiment was on rippled bed while second one was on smooth bed. To compare the numerical model against the experiment, only the second experiment is considered, due to bottom friction is not included in the wave-current interaction model at moment.

There are two experimental results presented. First is under condition of $h=45\text{cm}$, $t=1.8\text{s}$, $k_0 h_0 = 0.825$, and second is under condition of $h=30\text{cm}$, $t=1.8\text{s}$, $k_0 h_0 = 0.65$. The corresponding comparison of these results and the solutions of numerical model is shown in figure 1 and figure 2. The test confirms that the present model can predict wave height quite accurately under condition of wave-current interaction. However, the model can be further improved if the bottom friction is taken into account (Li, 1992).

As second case, the applicability of the model is demonstrated for a more general and complicated wave-current interaction situation where the conventional ray method is invalid due to the existence of cusped caustics. An ideal case for such a test concerns the wave interaction with an analytical rip current system, which is a problem originally studied by Arthur (1950) using the ray method and by Liu (1983) using a parabolic equation.

Arthur (1950) constructed a set of wave rays for a train of monochromatic waves with the wave period being 8 seconds. Along the centre line many caustics appear

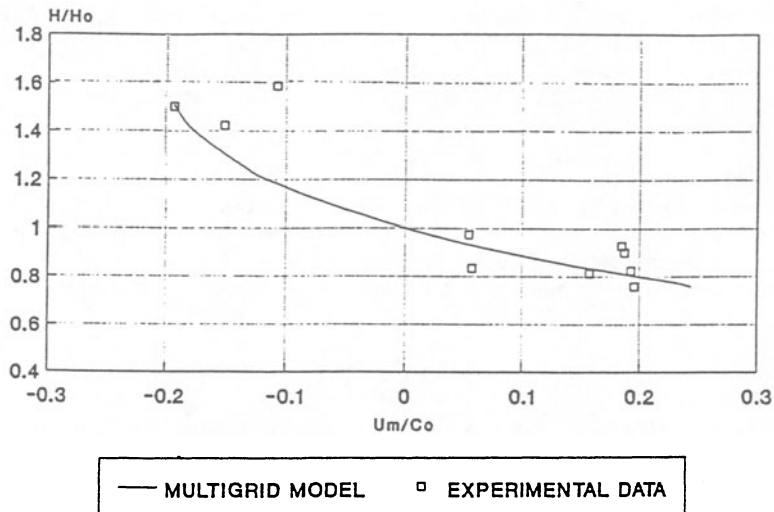


Fig. 1. Comparison of multigrid model of wave-current interaction against experimental data. $K_0H_0=0.825$

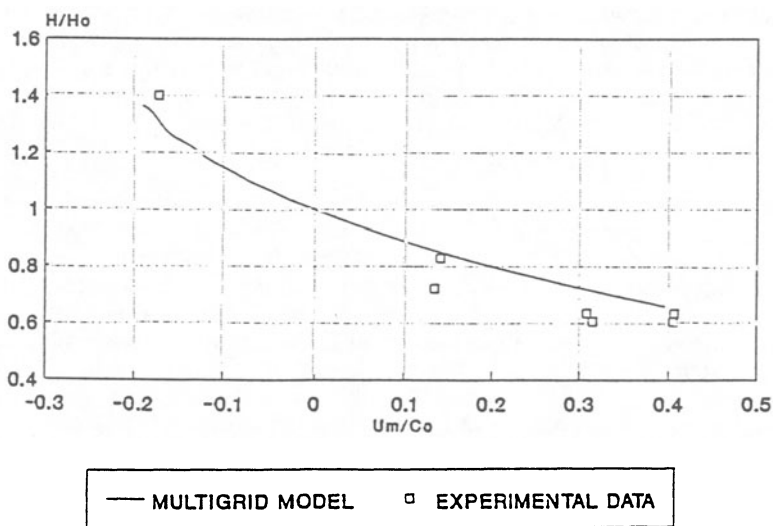


Fig. 2. Comparison of multigrid model of wave-current interaction against experimental data. $K_0H_0=0.65$

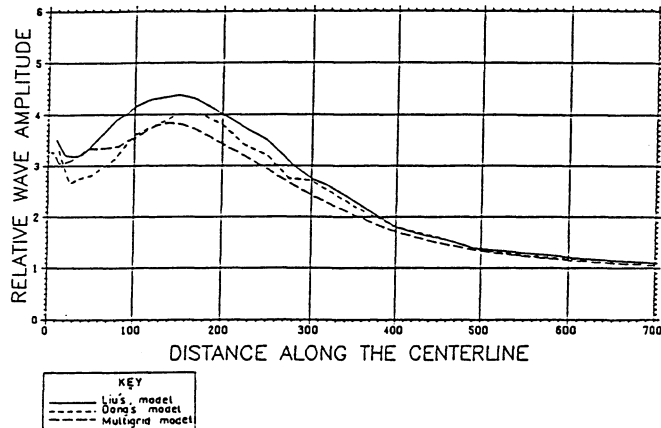


Fig. 3. Comparison between computational results from three models of mild-slope equation, taking into account wave-current interaction.

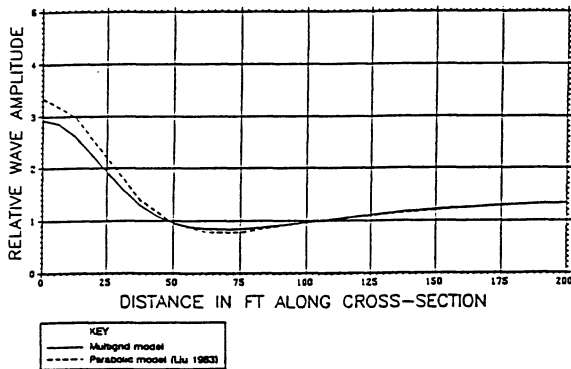


Fig. 4. Comparison between computational result from the Multigrid model and Liu's (1983) model. $X=250$ ft

and the classic ray theory fails there since it will give an infinite wave amplitude. Although at or near the ray focusing points the non-linearity may be important the linear mild-slope equation is expected to be able to give a reasonable first order approximation. This problem relates to a uniformly sloping beach with a slope of $1/50$ on which a current system exists. Taking the positive x axis in the offshore direction and the y axis in the alongshore direction, the current velocity is described as

$$U_y = -3.60[2 - (\frac{x}{250})^2] \mathcal{F}(\frac{x}{250}) \int_0^{\frac{y}{25}} \mathcal{F}(\alpha) d\alpha$$

$$U_x = 0.1442x \mathcal{F}(\frac{x}{250}) \mathcal{F}(\frac{y}{25})$$

where

$$\mathcal{F}(\alpha) = \frac{1}{\sqrt{2\pi}} e^{-\frac{\alpha^2}{2}}$$

where the length and the time units are in feet and seconds, respectively. Figures 3 and 4 show computational results for this test case derived from equation (9), from Liu's (1983) scheme, and from a hyperbolic solution of the mild slope equation proposed by Dong (1988) who presented results for the center line only (which corresponds to the positive x axis). It is evident from Figure 3 that the results from the three models are in close agreement, with differences being at most of the order of 10% in the region close to the shoreline. It is interesting to note that for most of the range the results from Liu's (1983) and the present model fall either side of the full hyperbolic solution of the mild-slope equation.

CONCLUSION

Comparison between Liu's and the present model as shown in Figures 4 indicates that agreement is quite close for the cross section. However, taking into account the fact that the present model considers the combined effects of refraction, diffraction and wave-current interaction without imposing any restrictions on the wave propagation direction, the present model can be applied to the situation where incident wave angle is very large.

References

- Berkhoff, J.C.W., (1972) 'Computation of combined refraction-diffraction', Proc. 13th Coastal Eng. Conf., Vancouver, Canada, A.S.C.E. 1 (1973), 471-490.
- Berkhoff, J.C.W., (1976) 'Mathematical models for simple harmonic linear water waves', Report on Mathematical Investigation, Delft Hydraulics Laboratory, Report W 154-IV.
- Berkhoff, J.C.W., (1982) 'Refraction and diffraction of water waves; wave deformation by a shoal, comparison between computations and measurements', Report on Mathematical Investigation, Delft Hydraulics Laboratory, Report W 154 part III.
- Berkhoff, J.C.W., Booij, N. and Radder, A.C., (1982) 'Verification of numerical wave propagation models for simple harmonic water waves', Coastal Eng., 6: 255-279.

Bettess, P. and Zienkiewicz, O.C., (1977) 'Diffraction and refraction of surface waves using finite and infinite elements', Int. Jnl. Num. Methods in Engng., Vol II, 1271-1290.

Booij, N., (1981) 'Gravity waves on water with non-uniform depth and current', Report No. 81-1, Delft University of Tech., Dept. Civil Eng.

Brandt, A., (1977) 'Multi-level adaptive solutions to boundary-value problems', Math. Comp. 31: 333-390.

Brandt, A., (1980) 'Numerical stability and fast solutions of boundary-value problems', Boundary and Interior Layers - Computational and Asymptotic Methods, (J. J. H. Miller, Ed.) Boole Press, Dublin.

Brevik, I. and B. Aas, (1980) Flume Experiment On Wave And Current. I. Rippled Bed. Coastal Engineering, 3(1980) 149-177.

Brevik, I. and T. Luftkrigsskolen, (1980) Flume Experiment On Wave And Current. II. Smooth Bed. Coastal Engineering, 4(1980) 89-110

Copeland, G.J.M., (1985) 'A practical alternative to the "mild-slope" wave equation', Coastal Eng., 9: 125-149.

Dong, P., (1988) 'The computation of wave-induced circulations with wave-current interaction and refined turbulence modelling', Ph. D thesis, University of London.

Kirby, J.T., (1984) 'A note on linear surface wave-current interaction over slowly varying topography', J. Geophys. Res., Vol. 89, No C1: 745-747.

Li, B. (1992) Efficient Water Wave And Current Propagation Modelling. Ph.D Thesis, Imperial College, London. (To appear)

Li, B. and K. Anastasiou, (1992) Efficient Elliptic Solvers For Mild-slope Equation Using The Multigrid Technique. Coastal Engineering, 16(1992) 245-266.

Liu, P.L-F., (1983) 'Wave-current interactions on a slowly varying topography', J. Geophys. Res., Vol. 88, No C7: 4421-4426.

VARIATION OF BEACH PROFILES IN HELL'S MOUTH BAY, LLYN PENINSULA
FOR THE PERIOD 1979-1981

J. DARBYSHIRE
U.C.E.S., School of Ocean Sciences,
University of Wales, Bangor.

ABSTRACT. An investigation was made into the changes in topography in Hell's Mouth Bay in the Llyn Peninsula in North Wales. It has a very active beach and there has been considerable erosion over the past hundred years. Beach profiles were surveyed along three lines normal to the shoreline down to low springs level at fortnightly intervals at low spring tide times from February 1979 to April 1981.

Comparison of successive profiles showed considerable changes in topography. There was usually a substantial net gain or loss along each line. There were in addition substantial changes at various points along each line from one survey to the one before, the variations having a "wavy" appearance.

From the net results, it was possible to calculate the amount of build-up or erosion along the lines from February 1979 to the time of any survey. The results showed, as might be expected, a build-up during the summer months and an erosion during the winter months.

Some wave data were taken at the site and use was also made of wave data taken near Aberporth in the southern part of Cardigan Bay. It became clear that low amplitude waves with very little breaking caused the build-up whilst the erosion was caused by large breaking waves. As shown by Longuet-Higgins (1953), low non-breaking progressive waves produce a shoreward bottom current whilst the backwash of breaking waves flows along the bottom to give a seaward current. The direction of the current would thus depend on the height of the waves and the net effect of waves over a long period of time could be found by giving weight factors to each height value from 0.5 to over 2.5 metres and then summing up the weighted heights over the period required. By adjusting the weights good agreement could be found between the sum and the observed net differences. The weights given varied from 0.75 for 0.5 metres to -1.5 for over 2.5 metres. There is a conflict between the large breaking waves and the low waves, which have a smaller individual effect but are much more frequent.

Longuet-Higgins's theory can also be applied to stationary waves. Here there is a variation of bottom current from seaward to shoreward in the space of a quarter wavelength. There is also a similar variation with vertical velocity, this being maximum downward at the node position and maximum upward at the antinode position. As the solutions for the progressive and stationary case are independent, the case of a partially reflected wave can be dealt with by taking the sum of the two solutions as the wave can be considered as a mixture of a progressive wave and a stationary wave. In the case of the stationary wave and the partially reflected wave, the suspended particles would tend to fall to the bottom with the downward velocity at the node while suspension would be enhanced by the upward velocity at the anti-node.

In view of these results, it was decided to calculate from the profile concerned, the reflection coefficient and hence the combined wave amplitude for a wide range of frequencies over all stages of the tide for a 14 day interval. The result for each frequency was multiplied by the power spectral density for that frequency for the day concerned. All these values were then summed up together. The sum showed that there was a net variation from point to point which was not unlike the observed changes.

INTRODUCTION.

Hells' Mouth Bay is a wide bay extending over 4 miles and is situated between Mynydd Rhiw to the west and Mynydd Cilan to the east. It is completely unspoilt and has not been affected by any human agency. There is however, considerable beach erosion and the coastline recedes at approximately 0.3 metres per year,Darbyshire,(1977).The location of the beach and the measuring site is shown in Figure 1.

As the beach was a very active one, it was decided to make a thorough investigation of it and in the course of this, beach profiles were taken at fortnightly intervals at low springs from February 1979 to April 1881 along three lines E,F, and D as shown in Figure 2. Line E was the most westerly and the most exposed and surveys on it were discontinued in November 1979 as this part of the beach had been so eroded that it was all rocky.

Some of the profiles are shown in Figures 3 and 4. Figure 3 for lines D and E from 9.2.79 to 24.7.79 and Figure 4 for lines D and F from 4.10.79 to 17.3.80 in figure 4. The levels were taken at 5 metre intervals along each line and were referred to a standard level. Figure 3 and 4 also show the level differences at each point between the profile shown and the preceding one. From these differences it was possible to calculate the net overall gain or loss of material over all the line since the previous survey. By adding these up from the beginning , it was possible to calculate the cumulative change in the amount of material beneath the line from February 1979 to the time in question.These changes are shown in Figure 5 and show, as might be expected, a periodic change from winter to summer. The level differences in Figures 3 and 4 also show a variation along the line often varying from positive to negative and having a wavelike appearance.This characteristic is shown in Figure 2 which shows a plan view of the beach corresponding to the profile taken on 24.9.7.79.

Wave measurements were taken at the site for some of the period involved but due to difficulties in maintaining the apparatus in a rather hostile environment, there were many breaks and the only reasonably continuous run was from January 1979 to July 1979. There were three pressure transducer recorders situated at low springs level and set at the vertices of a right angled isosceles triangle with one side of 10 metre length parallel to the shoreline and the other 10 metre side was normal to the shoreline,(see Figure 2). The equipment is described further by

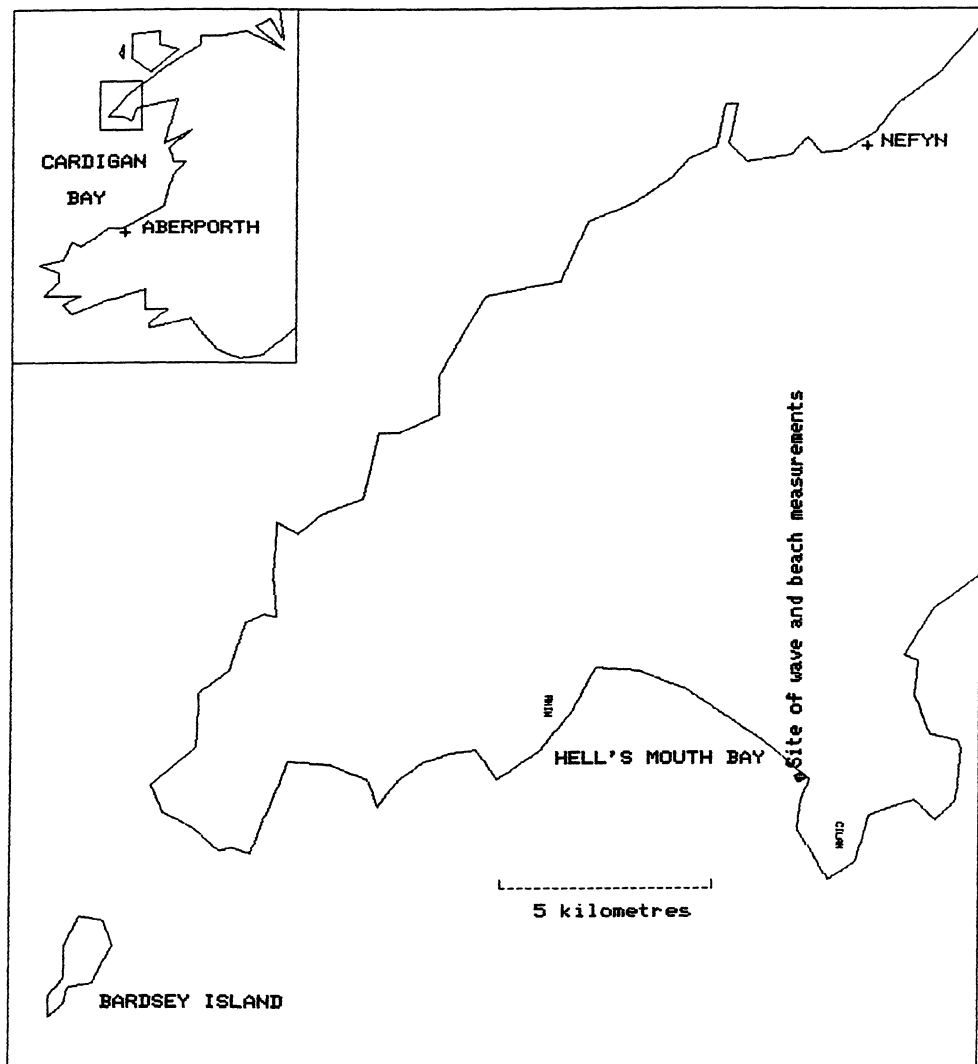


Figure 1. Map of Hell's Mouth Bay and surrounding sea areas.

NANT BEACH, HELL'S MOUTH BAY, 24.7.79

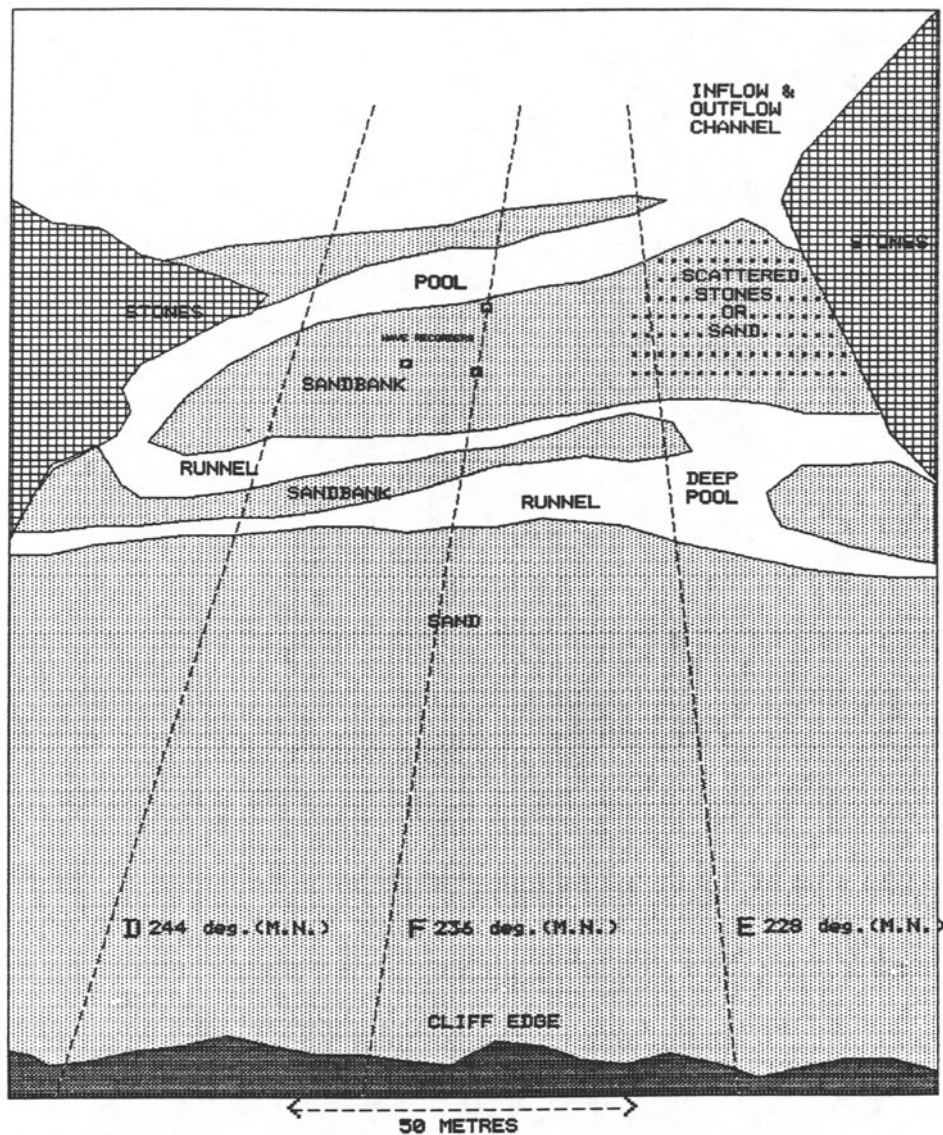


Figure 2. Plan of measuring site, 24.7.79, showing transect lines, wave recorders, and beach features.

PROFILES AND SUCCESSIVE PROFILE DIFFERENCES FOR D AND E

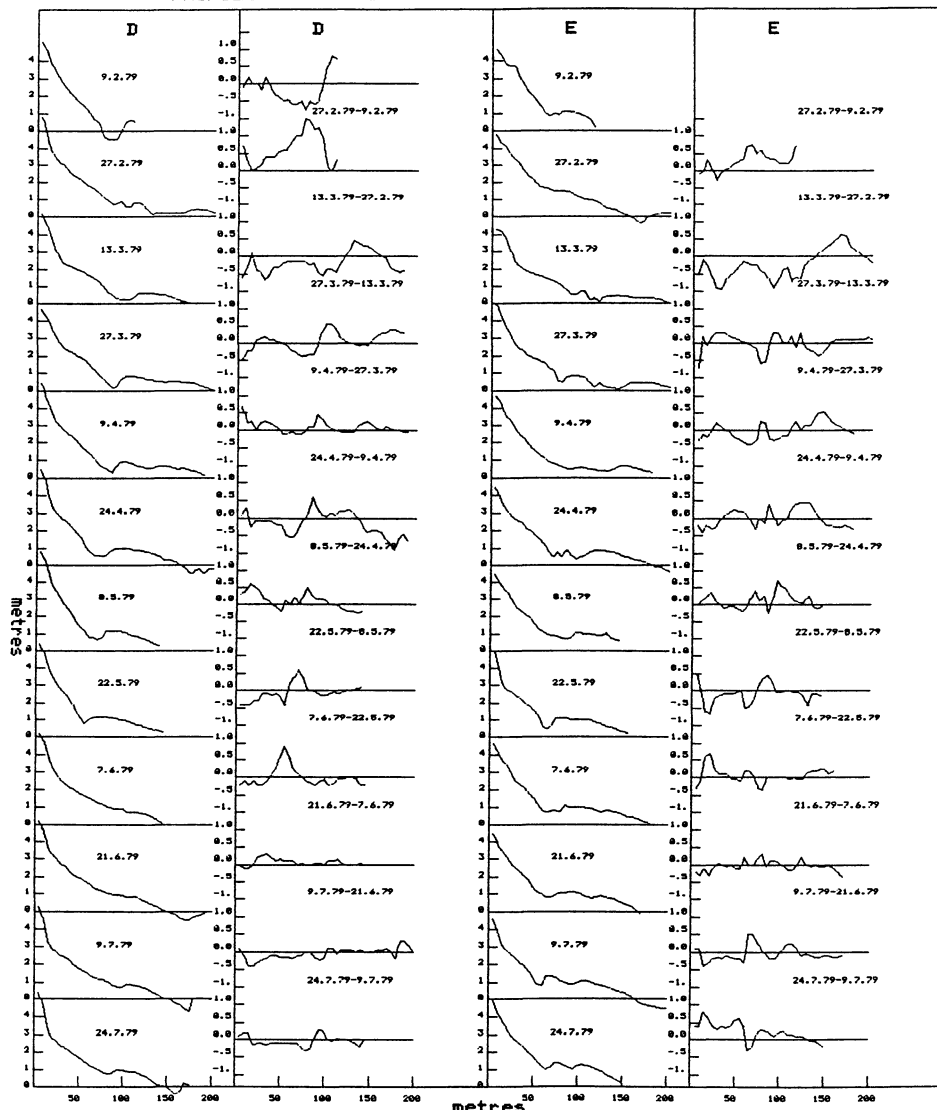


Figure 3. Profiles and successive profile differences for lines D and E, 9.2.79 to 24.7.79.

PROFILES AND SUCCESSIVE PROFILE DIFFERENCES FOR D AND F

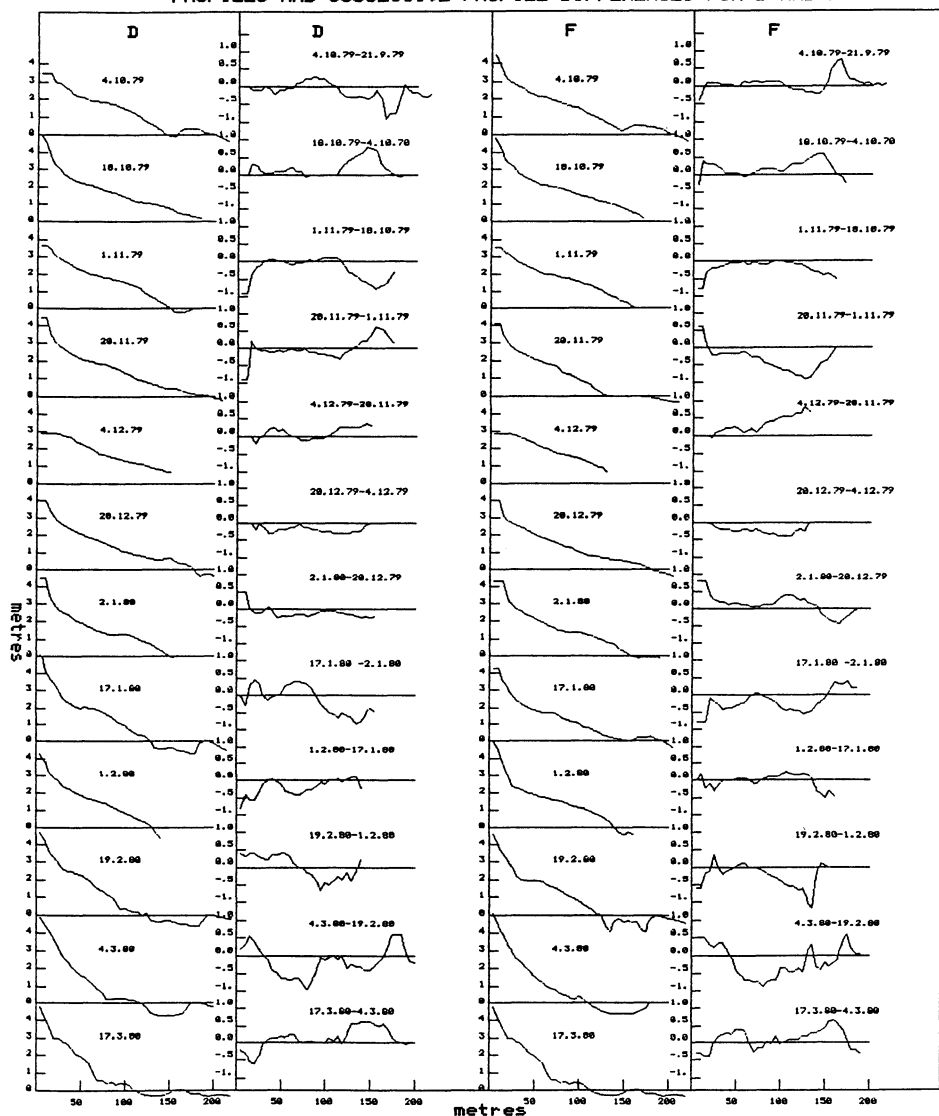


Figure 4. Profiles and successive profile differences for lines D and F, 4.10.79 to 17.3.80.

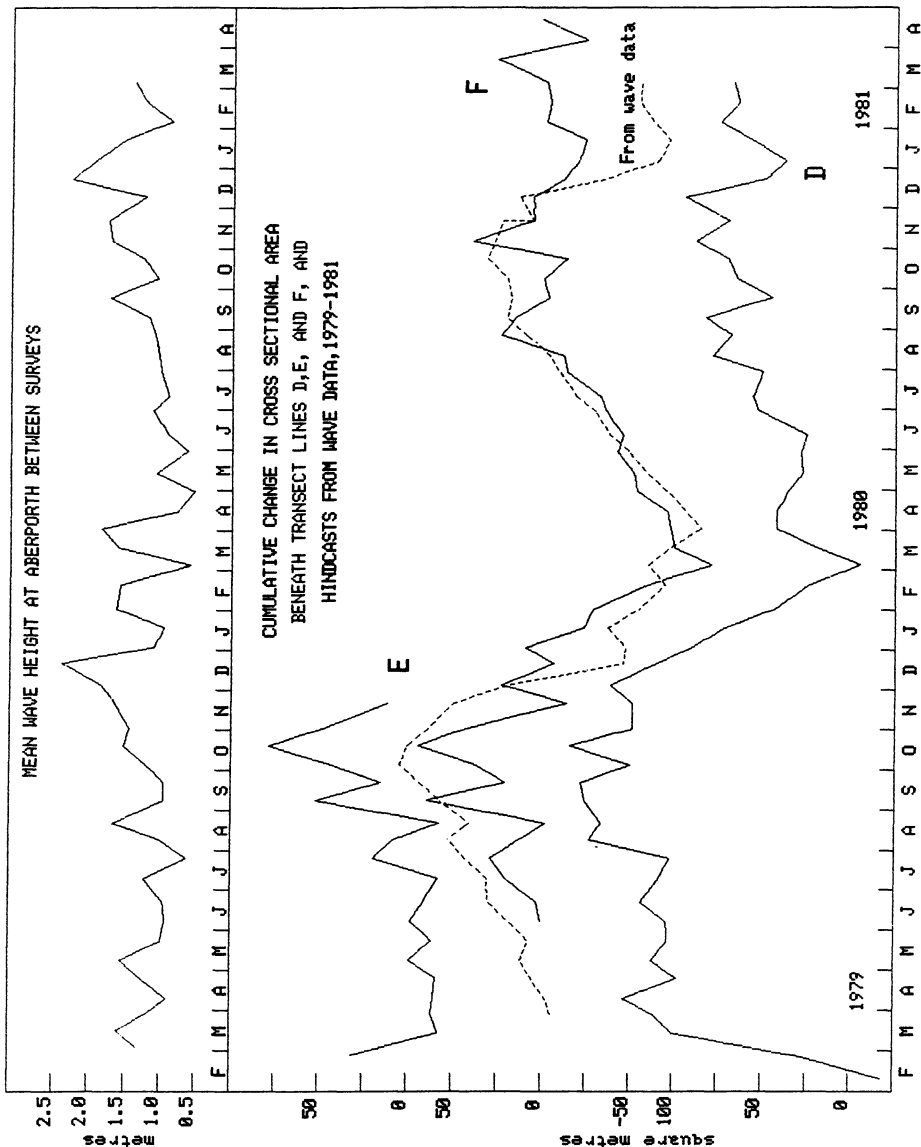


Figure 5. Observed cumulative change in cross sectional area beneath transect lines and estimated change from wave data, and mean wave height between surveys, February 1979 to April 1981.

Darbyshire (1991) where it is shown that by frequency and correlation analysis of the three records, it is possible to calculate the wave direction.

The local wave data were thus insufficient to cover all the surveys and recourse had to be had to wave data taken by the Meteorological Office at the St. Gowan lightship off Aberporth in the southern part of the Cardigan Bay and about 80 km. south of Hell's Mouth Bay. The data consisted of significant wave heights taken every 12 hours for all the three years 1979-1981. Comparison of contemporary data indicated that these values were about 50% higher than the corresponding ones for Hell's Mouth. Tidal measurements were not available but it was possible to calculate the tidal height for every hour at Nefyn (also in the LLyn Peninsula, see Figure 1) from the known tidal constants.

Effect of tides and waves.

The beach profiles could be affected by both tidal currents and by wave currents and these will be discussed in turn.

(a) Tides.

Figure 6 shows profiles taken along line E for three successive days, 19th., 20th., and 21st. September 1979. These were taken at the time of springs and the wave activity as given by Aberporth was moderate, the wave height being 1 metre on the 19th., 1.5 metres on the 20th. and 1.25 metres on the 21st. The successive profiles are superimposed in Figure 6 and show very little change except near the bottom of the beach but this could be attributed to wave action as there is a pronounced difference between the 20th. and 21st. in agreement with the greater wave activity on the 20th.

For all practical purposes, it would appear that the direct effect of tidal currents can be ignored as their effect seem to cancel out. There may, however, be an indirect effect due to non-linear interaction with wave currents.

(b) Wave currents.

We are concerned with the mean wave currents over a considerable period of time over which the ordinary orbital currents cancel out. These mean currents have been studied by Longuet-Higgins (1953) who showed that in the case when the depth was much smaller than the wavelength that the stream function for a non-breaking progressive wave was given by

PROFILES FOR 19-21.9.79

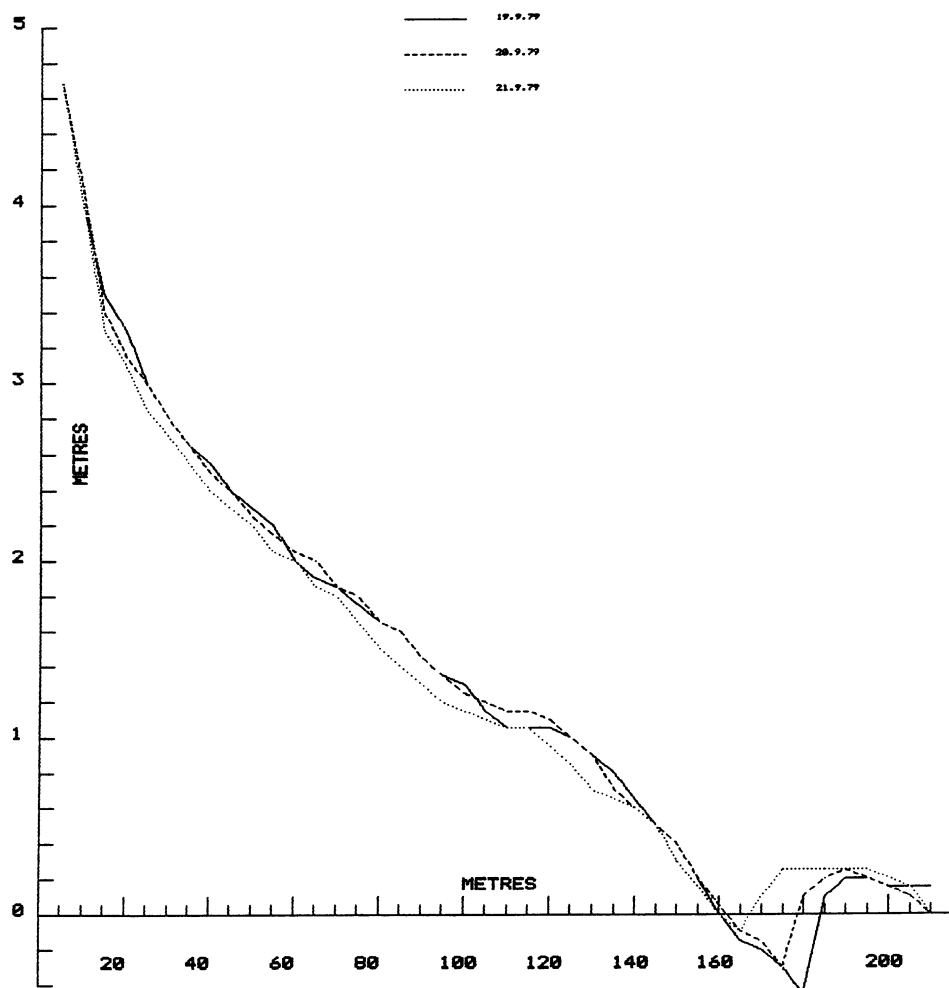


Figure 6. Profiles along line E, 19, 20, and 21.9.79.

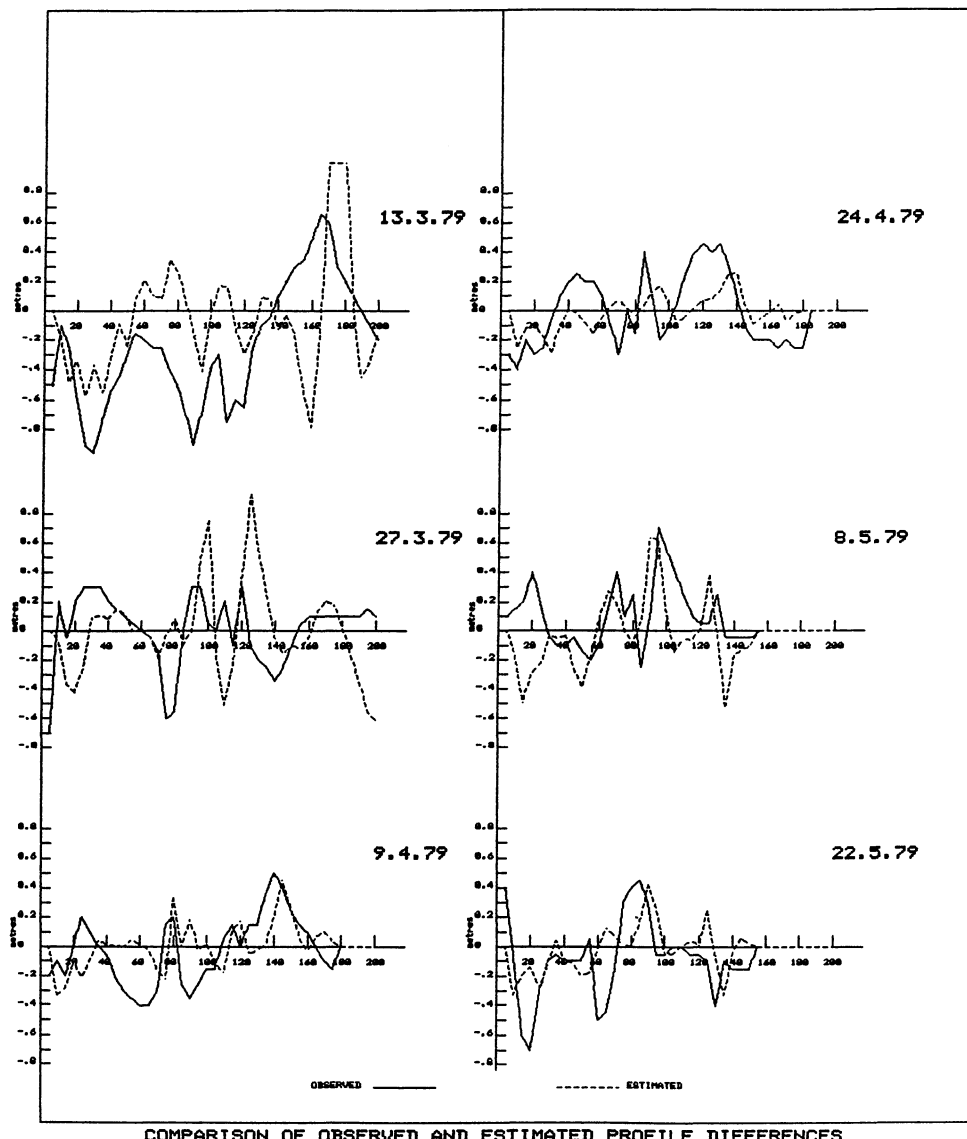


Figure 7. Observed and estimated profile differences between successive surveys for 13.3.79-27.2.79, 27.3.79-13.3.79, 9.4.79-27.3.79, 24.4.79-9.4.79, 8.5.79-24.4.79, and 22.5.79-8.5.79.

$$\Psi = \left\{ (5a^2/g)/8h \right\} (z^3/h^3 - z/h) \quad (1)$$

which gives a horizontal velocity

$$\partial\Psi/\partial z = u = \left\{ (5a^2/g)/8h^{3/2} \right\} (3z^2/h^2 - 1) \quad (1a)$$

where k is the wave number, σ is the angular frequency, h is the depth, a the amplitude and z the height of any point above the bottom.

This solution only applies when $a \ll h$. The solution implies that there is a shoreward current at the bottom

$$u = 10a^2/g/8h^{3/2} \quad (2)$$

and a seaward current at the surface

$$u = -5a^2/g/8h^{3/2} \quad (3)$$

With larger values of kh , there is a shoreward current at the surface, a seaward current at middle depths and again a shoreward current at the bottom. There is then a less severe restriction on the value of a/h .

Longuet-Higgins also considered the case of a non-breaking stationary wave. If the elevation is given by

$$\eta = 2a \cos kx \cos \sigma t \quad (4)$$

then for small values of kh , the stream function is given by

$$\Psi = - \left\{ (3a^2/g/4h) \right\} (z^3/h^2 - z/h) \sin 2kx \quad (5)$$

and the horizontal velocity is given by

$$u = \partial\Psi/\partial z = - \left\{ (3a^2/g/4h^{3/2}) \right\} (3z^2/h^2 - 1) \sin 2kx \quad (6)$$

Thus the horizontal velocity is zero at

$$x = (\frac{1}{2}m + 1/4)\lambda, \text{ or } z = \sqrt{3} h \quad (7)$$

The vertical velocity is given by

$$v = -\frac{\partial \Psi}{\partial x} = \left(\frac{3a^2/g}{4h^{3/2}} \right) \left(3z^2/h^2 - 1 \right) 2k \cos 2kx \quad (8)$$

Thus the motion consists of eddy cells of wavelength half the water wavelength, the first half having an anti-clockwise motion with the horizontal velocity being seaward at the bottom and shoreward at the surface and this half is separated by a line of zero horizontal velocity from the second half where the motion is clockwise with the horizontal velocity being seaward at the bottom and shoreward at the surface.

When there is partial reflection, the situation is the same as superimposing a smaller amplitude stationary wave on a progressive wave. The solutions given above are independent and so if R is the reflection coefficient, the stream function becomes

$$\Psi = \left(z^3/h^3 - z/h \right) \left(\frac{a^2/g}{h^{3/2}} \right) \left(\frac{5}{8} - \frac{(3R^2 \sin 2kx)}{4} \right) \quad (9)$$

Hence the horizontal velocity becomes

$$u = \left(3z^2/h^2 - 1 \right) \left(\frac{a^2/g}{h^{3/2}} \right) \left(\frac{5}{8} - \frac{(3R^2 \sin 2kx)}{4} \right) \quad (10)$$

and the vertical velocity becomes

$$v = - \left(z^3/h^3 - z/h \right) \left(\frac{a^2/g}{h^{3/2}} \right) \left(-\frac{(3kR^2 \cos 2kx)}{2} \right) \quad (11)$$

In all cases the velocity is proportional to the square of the amplitude and in the case of standing waves the vertical velocity is also proportional to the wave number and so to the frequency as the depth is small compared to the wavelength.

In the case of breaking waves, the motion is much simpler as the water is carried forward at the surface and the backwash flows along the bottom, so that there is a net seaward current there.

Application to the present investigation.

These results can be applied to the present investigation. Breaking conditions depend on both the amplitude and the wavelength. Unfortunately,

the periods are not given very accurately in the data and we have to assume that the amount of breaking depends on the amplitude. This is not unreasonable as low waves are often associated with long swell.

It is assumed that wave action loosens the beach material so that some can be transported by entrainment from the bed and a large amount would go into suspension and be directly transported by the current.

In the circumstances, as the direction of the current and the movement of material depends on the wave amplitude, it was decided to multiply the wave heights by factors and sum the products up from the beginning to the time of each survey.

Thus the sum

$$H = \sum w_i a_i \quad (12)$$

where the a_i s are the heights and the w_i s the factors. These factors were found by trial and error so that the sum corresponded with the ones observed for the lines. Thus

```
If height < 0.5 metre then w=0.75
If 0.5 < height < 1.0 metre then w=0.5
If 1.0 < height < 1.5 metre then w=0.2
If 1.5 < height < 2.0 metre then w=0
If 2.0 < height < 2.5 metre then w=-1
If height > 2.5 metre then w=-1.5
```

A regression equation was obtained with 42 corresponding values of the weighted sum of the wave heights and the mean of the cumulative differences for D and F, from 9.7.79 to 5.3.81. It was given by:

$$0.5(\text{cumul diff. D} + \text{cumul. diff. F}) = 2.05(\text{weighted sum of wave heights})$$

sq. metres	metres	(13)
------------	--------	------

The correlation coefficient was 0.80 and the results are shown by the dotted line in Figure 5. The equation was extended to February 1979. The agreement is very good. The result shows that there is a conflict between the effect of large breaking waves giving a seaward current and much smaller but more frequent waves which give a shoreward current.

The mean value of the wave height during the preceeding two weeks is shown in the upper part of the diagram.

Ideally from the theory, the squares of the heights should have been integrated but the simpler procedure appears to be adequate. It is possible that by using different weighting factors, that a satisfactory result would have been obtained with the squares but in view of the successful use of the linear values such a complication seems unnecessary.

Variations along the profiles.

Mention has been made of the wavelike character of the variations in level changes along the lines. These are of the same order of magnitude as the water-wave wavelengths. These can be explained by Longuet-Higgins's theory as applied to partial reflection.

Reference to equation (11) shows that the vertical velocity is maximum positive when $\cos 2kx=1$ and maximum negative when $\cos 2kx=-1$. Thus there is a maximum downward velocity at $x=(2m+1)\pi$ i.e. where the amplitude is least. A downward velocity would increase the deposition of suspended beach material whereas an upward current would enhance suspension. One would therefore expect an increase in deposition at the amplitude minima

It was decided to investigate along these lines. It was necessary first to determine the reflection coefficient from the observed profile. A method of doing this has been described in detail by Darbyshire (1991) and is an extension of Lamb's formula for reflection at a discontinuous depth to the case of a continuously varying depth.

If x^0 refers to the distance of the water-line from the origin and x^1 refers to any point between them, then the reflected wave at x^1 will be contributed to from all positions x from it to the water-line. The phase of the contribution will depend on the time taken by the wave to travel from x^1 to x and back. Thus the reflection coefficient will be given by

$$\int_{x^1}^{x^0} (1/2c) (dc/dx) \exp(i \int_0^x 2kd\lambda) \quad (14)$$

The integration is carried out numerically and the square of the combined amplitude at each point along the line in question is obtained. The program allows for refraction if the beach is assumed to be uniform along the

shoreline direction, which is not unreasonable for the small area involved.

The problem becomes complicated because of the tidal variation. It was thus decided to start with a profile at a given date and then work out the variation for 17 wave frequency values from 0.011 to 0.182 s^{-1} at intervals of 0.01 s^{-1} . From the wave spectra, each result was multiplied by the power density corresponding to the frequency involved, and by the frequency. The process was repeated one hour later, allowing for the different tidal height and the different area immersed. This was continued for 13 hours using the same wave power density values. This was repeated for the 14 days until the next survey, using the appropriate wave spectral values for each day. To save calculating time, only one tide per day was considered as the wave data were only available once per day. In all, $17 \times 13 \times 14$ wave reflection calculations were done. All the individual sets were reduced to variations about the mean and then negated. All 3094 sets were then added together to give the required result.

As there was some variation in the sensitivity of the wave recorders, it was decided to allow for this by using factors to adjust the mean r.m.s. amplitude over each fortnightly period to be proportional to the corresponding mean height at Aberporth. The wave spectra and hence the final result for each example would have to be multiplied by the square of the factor involved. All the calculated results are then divided by a constant factor to obtain a suitable comparison with the observed values. The observed and estimated variations are shown superimposed in Figure 7 for six surveys from 27.2.79 to 22.5.79, the estimates being shown with the broken line. In view of the complexity of the calculation and some uncertainty in the data, one would not expect a point to point correspondence but the estimates and the observations are similar enough as regards both wavelength and amplitude to suggest that the right mechanism has been considered. The resemblance would definitely be not so good if the results had not been negated. The theory only applies strictly to non-breaking conditions but there would be some breaking, particularly, at low periods. For this reason wave periods lower than 5 seconds have not been included in the calculations.

Conclusions.

An investigation of the changes in beach profiles over fortnightly

intervals over a two year period has shown that the beach is built up by low non-breaking waves which produce a shoreward bottom current as suggested by Longuet-Higgins (1953) and is eroded by large breaking waves where the backwash produces a seaward bottom current. It has been possible to describe these processes quantitatively by using wave data and show how the beach builds up during the summer months and is eroded over the winter months.

It has also been shown that between each survey the changes in level between various points along a line normal to the the shorelin have a wavelike appearance with a wavelength of about half a water wavelength. This appears to be due to the waves being partially reflected as they move up the beach. This would produce a smaller stationary wave on top of the incident progressive wave. Again, according to Longuet-Higgins, a stationary non-breaking wave sets up eddy cells half a wavelength long with a maximum downward velocity at the node position and a maximum upward velocity at the antinode position. The downward current would aid deposition of suspended material whilst the upward motion would aid suspension. There should thus be a rise in level due to extra deposition at the node position and a lowering in level due to increased suspension at the antinode position. Calculation of the reflection coefficients from the profile and the calculation of the resulting stationary waves for a wide range of frequencies over all stages of the tide for a 14 day interval and summing the results has suggested that such variations could be caused by this mechanism.

Acknowledgements.

The author wishes to thank Mrs.Eileen Pritchard and the late W.R. Davis without whose invaluable assistance and dedication ,this paper could not have been written. He also wishes to thank Dr. T. Sherwin for calculating the tidal heights for Nefyn.

Finally, thanks are also given to the Meteorological Office for supplying the Aberporth wave data.

References.

- Darbyshire, J. 1977. The restless shores of Hell's Mouth Bay. *Maritime Wales*, No. 2. July. pp 67-71.
- Darbyshire, J. 1991. The reflection of waves off beaches. pp. 377-405 in, *Dynamics and exchange in estuaries and coastal zones*. (ed. D. Prandle). New York: American Geophysical Union, 647 pp. (Coastal and Estuarine Studies, 40).
- Longuet-Higgins, M. S. 1953 Mass transport in water waves
Phil. Trans. Roy. Soc. A, No. 9034 Vol. 245, pp. 535-581